UNIVERSITÀ DI PARMA

UNIVERSITA' DEGLI STUDI DI PARMA

DOTTORATO DI RICERCA IN

Scienza e Tecnologia dei Materiali

CICLO XXXIV

Fabrication and characterization of polymer-derived Ultra-High Temperature Ceramic Matrix Composites (UHTCMCs) for applications in severe environments

Coordinatore:
Chiar.mo Prof. Enrico Dalcanale

Tutore:
Chiar.ma Dott.ssa Diletta Sciti

Co-tutore:
Chiar.mo Dott. Luca Zoli

Dottorando: Francesca Servadei

Anni Accademici 2018/2019 – 2020/2021

A chi ha creduto in me più di me stessa.

A me stessa, per la determinazione.

Abstract

There is an increasing demand for advanced materials with enhanced temperature capability in highly corrosive environments. A new class of materials called Ultra-High Temperature Ceramics (UHTCMCs) have emerged as they combine the toughness of a composite with the high temperature stability of ultra-high temperature ceramics. This thesis deals with the fabrication and characterization of continuous fibre-reinforced UHTCMCs, using the Polymer Infiltration and Pyrolysis (PIP) technique re-adapted from the traditional CMC manufacturing technologies.

The first part is aimed at the development of carbon fibre-reinforced ZrB_2/SiC composites via aqueous slurry impregnation coupled with polymer infiltration and pyrolysis, using a allyl-hydrido polycarbosilane precursor. Ultra-high modulus pitch-based carbon fibres were selected for the first time for the PIP process investigating three different architectures (0/0°, 0/90°, and 2D), besides the cheaper and wider available high strength PAN-based carbon fibres, using simple (0/0°) and complex (2D and 2.5D) carbon fibre architectures. Microstructure and mechanical properties were investigated. As expected, the mechanical properties showed the tendency to decrease with increase of the preforms complexity, due to the higher amount of flaws and residual stresses. Moreover, the oxidation behaviour was investigated through short term oxidation tests in air performed for 1 min and 5 min at 1500 °C and 1650 °C in a bottom loading furnace. Microstructure, oxide scale thickness and composition were analysed by SEM/EDS/XRD. Results indicated that a good dispersion of ZrB_2 particles in the polymer-derived SiC(O) matrix promoted the formation of compact scales of a viscous borosilicate glass filling surface holes left by fibre oxidation.

The second part was focused on the improvement of performance at elevated temperature of PIP-ed UHTCMCs at mild conditions. A baseline ZrB_2/SiC reinforced with 0/0° pitch-based C_f composite consolidated by PIP at 1000 °C was subjected to post-consolidation thermal treatments from 1100 to 1900 °C to explore the thermal stability. Microstructural characterization was performed to evaluate evolution of the matrix, highlighting the crucial aspects about crystallization and porosity. Mechanical properties at room and elevated temperature were investigated through bending tests up to 1500 °C. The composite consolidated at mild conditions exhibited good flexural strength up to

1400 °C, but at 1500 °C it showed a loss of performance. Post-treated composites resulted in a performance deterioration at room temperature, nevertheless at 1500 °C an improvement of the bending resistance was achieved after pyrolysis at temperature ≥ 1400 °C.

The third part deals with the preparation of UHTCMCs by coupling water-based powder slurry infiltration, Polymer Infiltration and Pyrolysis (PIP) and Hot Pressing (HP) techniques. The best sequence of consolidation techniques to better integrate the carbon fibre cloths into an ultra-refractory sintered ceramic matrix of ZrB_2-SiC was identified. Infiltrated preforms with UHTC powder slurry were densified via: a) a pre-sintering step by HP followed by two PIP cycles with polycarbosilane, and vice versa, b) two PIP cycles followed by a cycle of HP. Flexural strengths at room temperature and at 1500 °C were found to be significantly higher for composites obtained by the second route, suggesting that sintering of polymer-derived SiC during HP improves the structural properties of C_f/ZrB_2-SiC composites. This represents an effective method for UHTCMC manufacturing in a shorter time than traditional PIP process.

The fourth part is addressed to the development of simple ways to prepare polymer-derived ceramics (PDCs) with high thermal stability. Firstly, the effect pre-curing treatment and catalysts on the ceramic yield of commercial allyl-hydrido polycarbosilane was studied to understand its curing and pyrolysis behaviour. Then, a tentative of synthetise SiBCN(O) ceramic was carried out by coupling polycarbosilane, used as Si and C precursor, with ammonia borane, source of boron and nitrogen at the same time. The as-prepared precursor and obtained ceramic were investigated to identify chemical composition (FTIR, SEM-EDS and XRD). SEM analysis highlighted that the boron and nitrogen were not preferentially incorporated into the silicon carbide lattice but entered the SiC(O) forming segregated BNO-reach areas. Finally, a simple route was proposed for the synthesis of polymer precursors for zirconium carbide (ZrC), using zirconium tetrachloride ($ZrCl_4$) as zirconium source and three different carbon sources: two phenolic resins and a type of bitumen. The results indicated that obtained organometallic compounds could be a Zr-O-C polymer. They were heat treated up to 1800 °C to achieve ZrC via carbo-thermal reaction. The pyrolysis behaviour and structural evolution of the carbon sources and the prepared precursors were analysed.

Keywords

- Ultra-High Temperature Ceramic Matrix Composites
- Polymer-derived Ceramics
- Polymer Infiltration and Pyrolysis
- Microstructure
- Mechanical properties
- Oxidation resistance

List of publications

1. F. Servadei, L. Zoli, P. Galizia, A. Vinci, D. Sciti, Development of UHTCMCs via water based ZrB_2 powder slurry infiltration and polymer infiltration and pyrolysis, J. Eur. Ceram. Soc. 40 (2020) 5076–5084.
   https://doi.org/10.1016/j.jeurceramsoc.2020.05.054
   IF 5.302

2. F. Servadei, L. Zoli, A. Vinci, P. Galizia, D. Sciti, Significant improvement of the self-protection capability of ultra-high temperature ceramic matrix composites, Corros. Sci. 189 (2021) 109575. https://doi.org/10.1016/j.corsci.2021.109575.
   IF 7.205

3. F. Servadei, L. Zoli, P. Galizia, C. Melandri, D. Sciti, Preparation of UHTCMCs by hybrid processes coupling Polymer Infiltration and Pyrolysis with Hot Pressing and vice versa, J. Eur. Ceram. Soc. 42 (2022) 2118–2126.
   https://doi.org/10.1016/j.jeurceramsoc.2021.12.039.
   IF 5.302

Table of contents

1. Aim of the work

Ceramic Matrix Composites (CMCs) are currently used for components in transportation, defence, nuclear and aerospace fields such as brake systems, gas turbine, facing materials, combustion chambers, thrusters, rocket nozzles, and the noses or leading edges of re-entry vehicles, because of their higher strength-to-weight ratio, good toughness and thermal shock resistance at high temperature. However, Carbon/Silicon Carbide (C/SiC) and Silicon Carbide/Silicon Carbide (SiC/SiC) composites display an excellent behaviour below 1600 °C, but over such temperature their oxidation resistance is limited due to the active oxidation of SiC in SiO phase. Actually, the only available solution to protect space vehicles during Earth re-entry at Mach 25 is the use of non-reusable, ablative materials (e.g. Carbon/Carbon (C/C) composites), which dissipate energy consuming themselves. Therefore, more demanding applications invoke the introduction of Ultra-High Temperature Ceramic (UHTC) phases in the matrix to overcome the main limitations of current CMCs in term of maximum temperature of service.

Ultra-High Temperature Ceramic Matrix Composites (UHTCMCs) are a novel class of materials designed to couple the best features of CMCs, such as damage tolerance, and those of UHTCs, such as oxidation and ablation resistance. They have been identified as promising candidates for operating beyond the limits of the currently used composites, thus paving the way for a next generation of reusable materials for aerospace, military, defence and nuclear applications that will have to bear a combination of high temperature (2000 °C), thermal shocks and strong heat fluxes. To date, the research is still focused on the design and processing of these composites. Several published works report the fabrication of UHTCMCs using many approaches, such as Chemical Vapour Infiltration (CVI), Polymer Infiltration and Pyrolysis (PIP), Reactive Melt Infiltration (RMI), and Slurry Infiltration and Hot Pressing (SI-HP). Among these, the PIP technique is featured by relatively low processing temperatures, no fibre damage, opportunity of using complex architecture preforms, and near-net shape capability. Commercial UHTC polymer precursors are apparently non-existent, while basic science research is limited. Currently, the most practiced way of introducing UHTC phases is by infiltrating fibre preforms with a slurry containing the preceramic polymers and the ceramic powders.

However, simply adding UHTC powders to a non-UHTC precursor often results in a inhomogeneous distribution of the ultra-refractory phase in final composite. Despite such drawback, the PIP process remains one of the most viable techniques for the production of UHTCMCs.

This PhD thesis aims to explore the fabrication and characterization of continuous fibre-reinforced Ultra-High Temperature Ceramic Matrix Composites (UHTCMCs), with the objective of providing novel processing routes that integrate the Polymer Infiltration and Pyrolysis processing technique re-adapted from the traditional CMC manufacturing technologies. This work can be divided in four main parts:

1) The first part is aimed at the development of UHTCMCs using uncoated pitch-based carbon fibre cloths via a two-step process, that involves impregnation with a water-based ZrB_2 powder slurry, and consolidation in mild conditions by repeated PIP using a polycarbosilane. The correlation between microstructural features, mechanical properties and oxidation resistance up to 1650 °C of composites with increased fibre preforms complexity were studied. Then, the application of the developed process to prepare composites using uncoated PAN-based carbon fibres was explored.
2) In the second part, post-consolidation thermal treatments from 1100 to 1900 °C were carried out on pitch-based C_f/ZrB_2-SiC composite consolidated by PIP process at mild conditions to evaluate the microstructural evolution of the matrix and the effect on the mechanical properties at elevated temperature.
3) In the third part, the potential of two hybrid processes for the manufacturing of UHTCMCs by coupling water-based powder slurry infiltration, Polymer Infiltration and Pyrolysis (PIP) and Hot Pressing techniques (HP) was studied to identify the best sequence of consolidation techniques to better integrate the carbon fibre cloths into an ultra-refractory sintered ceramic matrix.
4) The fourth part proposes novel routes for the synthesis of polymer precursors for SiBCN and ZrC, addressed to a future development in the preparation of UHTCMCs by the PIP method using UHTC precursors.

This work was carried out at the Institute of Science and Technology for Ceramics of the National Research Council (CNR-ISTEC) in Faenza (Ravenna, Italy).

2. State of the art

2.1 Ceramic Matrix Composites

Ceramic Matrix Composites (CMCs) are a class of structural materials, consisting of carbon or SiC fibres embedded in a ceramic matrix (oxide or non-oxide) [1]. These materials have been designed to overcome the main drawbacks of monolithic ceramics, mainly their brittleness. Indeed, the inclusion of fibres as reinforcement has the function to improve the resistance to crack propagation and fracture toughness, causing the material to fail gradually preventing catastrophic failure that typically occurs in conventional ceramics.

In addition, CMCs possess excellent high-temperature strength, high thermal conductivity, low coefficient of thermal expansion, and good thermal shock resistance. Moreover, they have low density, about a third of superalloys, resulting in mass-specific properties which are unsurpassed by any other structural material beyond 1000 °C [2] (see Figure 2.1). These composites are also more resistant to high-temperature oxidation compared to superalloys [3,4].

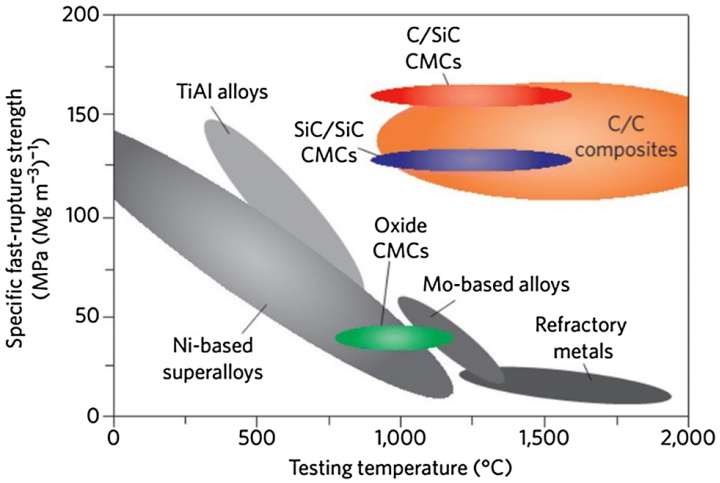

Figure 2.1. Specific fast-rupture strength as a function of the testing temperature of various metals and composites [2].

Until now, the most commonly used CMCs are non-oxide ones, based on carbon or SiC matrices, namely carbon/carbon (C/C), carbon/silicon carbide (C/SiC), and silicon carbide/silicon carbide (SiC/SiC) composites [5]. Generally, labels indicate the fibre type first and secondly the matrix (e.g. C/SiC means carbon-fibre reinforces silicon carbide).

C/C composites retain their properties at ultra-high temperature of 2000 °C or higher in an inert atmosphere or vacuum [6], but they are highly sensitive to oxidative environments and the carbon fibres undergo oxidation already at 500 °C [1].

C/SiC and SiC/SiC composites have an excellent oxidation and ablation resistance [7–9], thanks to the beneficial effect of a highly viscous film of silica, originating from the oxidation of SiC matrix at 1100 °C. This layer acts as oxidation barrier limiting the diffusion of oxygen, also continues to adsorb a significant amount of heat due to the phase transitions of SiO_2 [10]. SiC matrix is able to offer protection against oxidation at least up to 1600 °C in an oxygen-rich atmosphere. Unfortunately, oxidation resistance is compromised at temperatures above 1650 °C and in low-oxygen atmosphere [ref].

Due to their better oxidation resistance than C/C and better high-temperature performance than SiC/SiC, mostly C/SiC composites have a great potential as high-temperature structural materials.

2.1.1 Manufacturing methods

The main processes for fabricating CMCs include Chemical Vapor Infiltration (CVI), Polymer Infiltration and Pyrolysis (PIP), also called Liquid Polymer Infiltration (LPI), Melt Infiltration (MI), also called Liquid Silicon Infiltration (LSI) [1,8]:

- Chemical Vapor Infiltration (CVI) [11–14] involves the deposition of a ceramic matrix from gaseous reactants, which diffuse in a porous fibre preform. This technique was originally developed for the production of C/C composites. Carbon fibre preform is treated in a mixture of argon and light hydrocarbons at high temperature (~1000 °C) under pressure, such that gaseous precursors decompose forming C on the surface of the fibres. Later on, CVI process has been also adopted for the deposition of SiC matrix using a mixture of methyltrichlorosilane and H_2 (Figure 2.2). One main advantage of this process was the highly pure matrix obtained, leading to excellent mechanical properties. However, process rate is slow (may continue up to several weeks) and is very difficult to obtain fully dense composites.
- Polymer Infiltration and Pyrolysis (PIP) [15–17] is based on the infiltration of a carbon fibre preform with a liquid precursor which is then pyrolysed to form a matrix reinforced with fibres. PIP is well established for the manufacture of C/C composites, whereby phenolic resin is converted into a graphitic matrix. For the production of SiC-based as

well as SiCN- and SiCO-based composites, the matrix is obtained by infiltration of low viscosity preceramic polymers (see subparagraph 2.1.2.1) into fibre preform followed by pyrolysis (Figure 2.2). Infiltration and pyrolysis steps are repeated several times until near full density is achieved, requiring long manufacturing times.

- Liquid Silicon Infiltration (LSI), or Reactive Melt Infiltration (RMI), [18–20] consists of a preliminary infiltration of a carbon preform with phenolic resin, followed by an infiltration with melt silicon that reacts with the solid carbon and forms SiC in-situ (Figure 2.2). This process allows to produce fully dense composites, since the liquid silicon fills any voids left in C matrix. On the other hand, the molten silicon is highly reactive with C and can damage the carbon fibres.

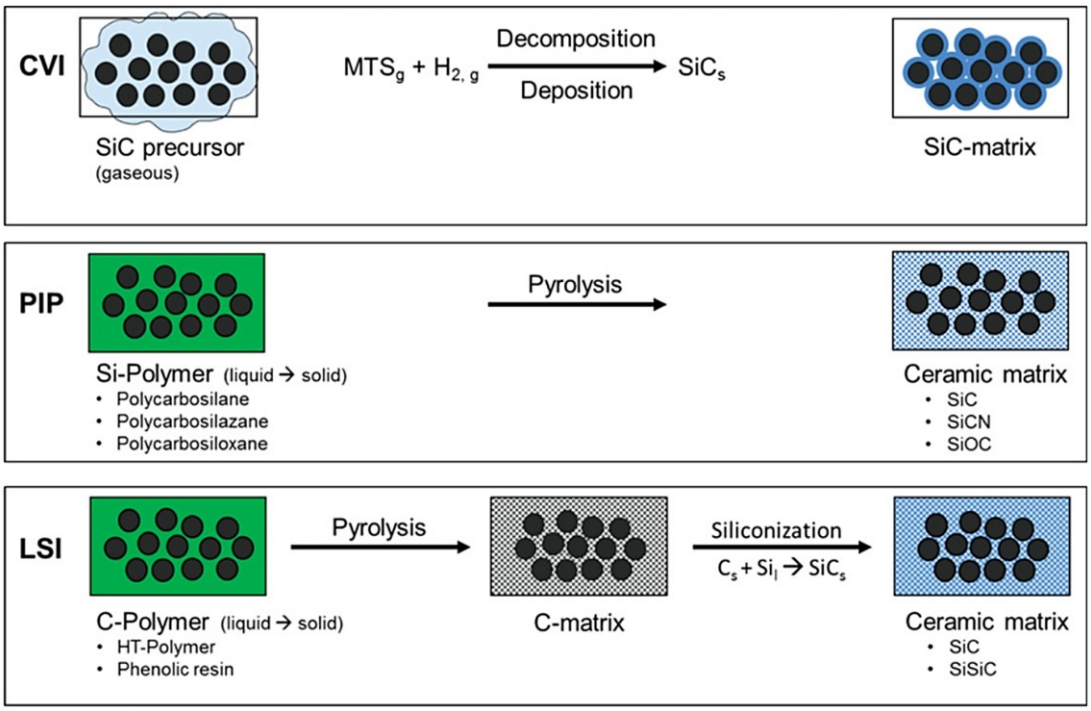

Figure 2.2. Schematic overview of the different methods for matrix build-up in fibre-reinforced SiC materials: Chemical Vapor Infiltration (CVI), Polymer Infiltration and Pyrolysis (PIP), and Liquid Silicon Infiltration (LSI) [8].

2.1.1.1 Polymer-derived ceramics

Polymer-Derived Ceramics (PDCs) represent a class of ceramics that are prepared from inorganic polymers, also called preceramic polymers [21,22].

Silicon-based PDCs are synthetised directly by pyrolysis of organosilicon polymers, polymers based on a backbone of Si atoms combined with other atoms such as C, O, N,

and B, resulting in different classes of silicon-based polymers. Starting from different classes of Si-based polymers, such as poly(organocarbosilanes), poly(organosiloxanes), poly(organosilazanes) and poly(organosilylcarbodiimides), ceramics as SiC, $Si_xC_yO_z$, and $Si_xC_yN_z$, respectively, can be obtained after thermal treatment under inert atmosphere [21] (Figure 2.3).

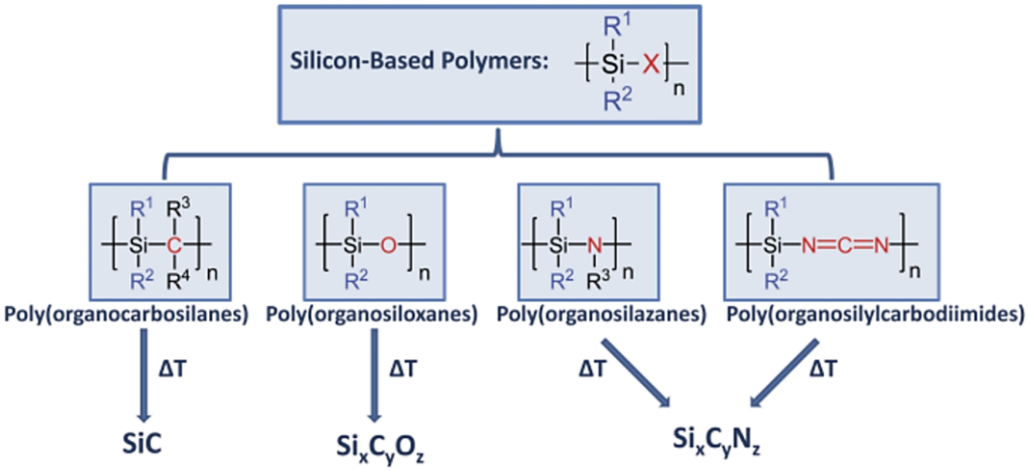

Figure 2.3. Silicon-based polymers (with simplified representation of the molecular structure) and respectively Polymer-Derived Ceramics (PDCs) obtained via thermal decomposition [21].

Preceramic polymers can be liquid or solid and, if solid, they can be molten at low temperature (< 150 °C) or solved in common organic solvents. Hence, preceramic polymers can be shaped adopting conventional polymer-forming techniques. After shaping, they must be converted by proper thermal treatment (curing and pyrolysis) to a ceramic. The presence of functional groups (e.g. Si–H, Si–OH, or Si-vynil) leads to cross-linking, which occurs spontaneously via condensation and addition reactions at temperature below 200 °C, forming a thermoset capable of maintaining its shape at higher temperature. Therefore, polymer-to-ceramic conversion (also called ceramization) leads to the decomposition of Si–H, Si–OH, or $Si–NH_x$ groups and organic moieties to obtain an amorphous or crystalline ceramic [21] (Figure 2.4).

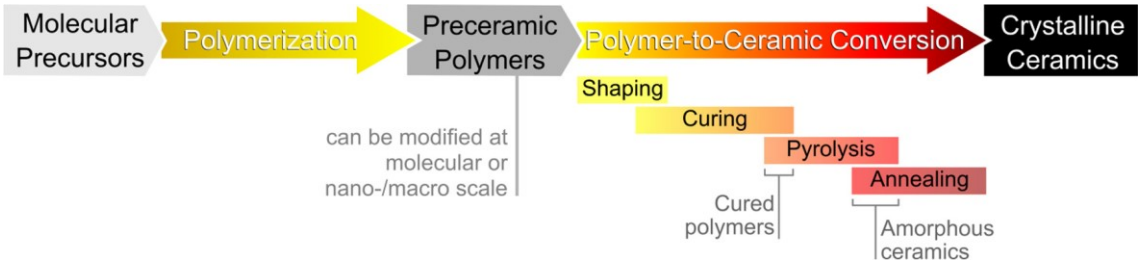

Figure 2.4. Polymer-to-ceramic conversion of polymer-derived ceramics (PDCs) [23].

In general, PDCs are thermally stable at very high temperature and show enhanced thermo-mechanical properties [24]. Moreover, the synthesis and the processing of PDCs is an excellent way to design ceramics with tailored features and consequently properties [22]. Therefore, in the last few year PDCs have gained interest to produce ceramic-based composite materials with adjusted chemical, physical and mechanical properties by polymer infiltration and pyrolysis (PIP).

For the production of C/SiC composites, polycarbosilane with high yields of SiC are typically used, such as polymethylsilane and allylhydridopolycarbosilane, characterized by a chain of alternating Si and C atoms [ref]. Polycarbosilanes form an amorphous SiC matrix during pyrolysis at relatively low temperature (850–1050 °C), while a crystalline β-SiC with increased density and temperature stability can be obtained by heat treatment at temperatures of 1500–1600 °C).

A brief overview of polytypes for SiC is given in Figure 2.5. Silicon carbide is known to have more than 200 polytypes [25], such as 2H, 3C, 4H, 6H, 15R, where number refers to the number of Si-C layers in the stacking sequence, and the letter indicates the crystal system (C for cubic, H for hexagonal and R for rhombohedral). The 3C polytype, which corresponds to β-SiC, is the first structure that forms during crystallization of SiC, since the cubic polytype is the most kinetically favoured structure due to the high symmetry of the cubic lattice. β-SiC is usually observed at relatively low temperatures (below 1700 °C) [26]. Above such temperature, β-SiC converts to polymorph α-SiC, which has a hexagonal crystal structure [27].

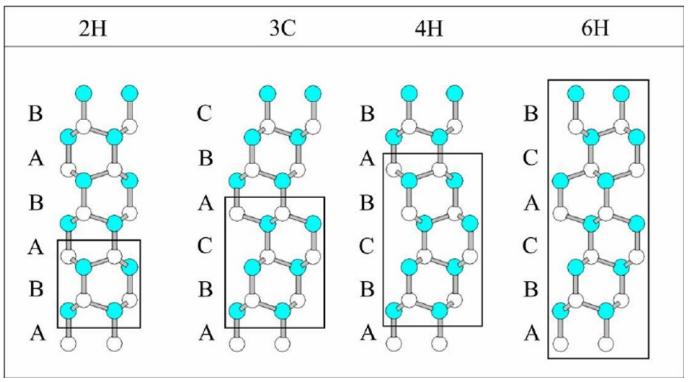

Figure 2.5. Some of the main polytypes of silicon carbide: crystal structures 3C, 4H, 6H [28].

2.1.2 Applications

The impelling demand for components able to withstand extreme conditions has been an important driving force for the continuous research of highly performing materials possessing unique properties. Monolithic ceramics can be suitable for several applications due to their high hardness, stiffness and chemical resistance at high temperatures, but their brittle nature has prevented their implementation in critical structural applications. Due to their higher strength-to-weight ratio, good toughness and thermal shock resistance at high temperature, Ceramic Matrix Composites are good candidates for working under high temperatures, harsh corrosive environments, and extreme loading. CMCs have more promising properties also compared to other structural materials, such as steels, aluminium or titanium alloys, nickel-based superalloys.

Currently used thermal protection systems and rocket motor components of hypersonic space vehicles, satellite launchers (e.g. VEGA, ARIANE) and brake systems of hyper speed vehicles, such as Formula 1 cars, are made of CMCs. Recently, other sectors such as aviation and metallurgy are replacing refractory metals with CMCs [1].

Carbon/Carbon (C/C) composites are mainly employed for rocket nozzles and hot parts. However, they are plagued by severe erosion because of their poor oxidation resistance and low wear resistance. These drawbacks reduce material durability and restrict application in air elevated temperatures.

Silicon-based composites (C/SiC and SiC/SiC) are largely used for aeronautical and space application thanks to their superior oxidation resistance. However, the capability of SiC matrix to protect carbon fibres is not effective in a wide range of conditions of temperatures and heat fluxes [29–32]. Above 1650 °C and in low-oxygen atmospheres SiO_2 surface layer becomes chemically active, leading to sublimation of its constituents and high erosion rates, thus compromising the life of the material [33].

Therefore, more demanding applications invoke the introduction of Ultra-High Temperature Cercamic (UHTC) phases in the matrix to overcome the main limitations of current CMCs in term of maximum temperature of service [34].

2.2 Ultra-high temperature ceramics

Several different definitions have been proposed to identify ultra-high temperature ceramics (UHTCs). The three main classification factors are melting temperature, ultimate use temperature and chemical composition. Most commonly, UHTCs are defined as materials that have melting points of 3000 °C or higher. As shown in Figure 2.6 materials that melt at temperatures above 3000 °C are limited to very few elements or compounds from any class of materials: most of these are borides, carbides, and nitrides of early transition metals, while only three metals (W, Re, and Ta) and one oxide ceramic (ThO_2) have so high melting temperature [35]. An alternative definition for UHTCs relates to materials capable of use in air at temperatures higher than those possible for typical high-temperature ceramics [36,37]. The latter, such as alumina, magnesia, silicon carbide and silicon nitride, withstand temperatures up to 1600 °C, hence the ultra-high temperature regime is arbitrary defined above that level [35]. Chemically, nearly all UHTCs are binary compounds in which boron, carbon or nitrogen combine with one of the early transition metals, such as Zr, Hf, Ti and Ta [37].

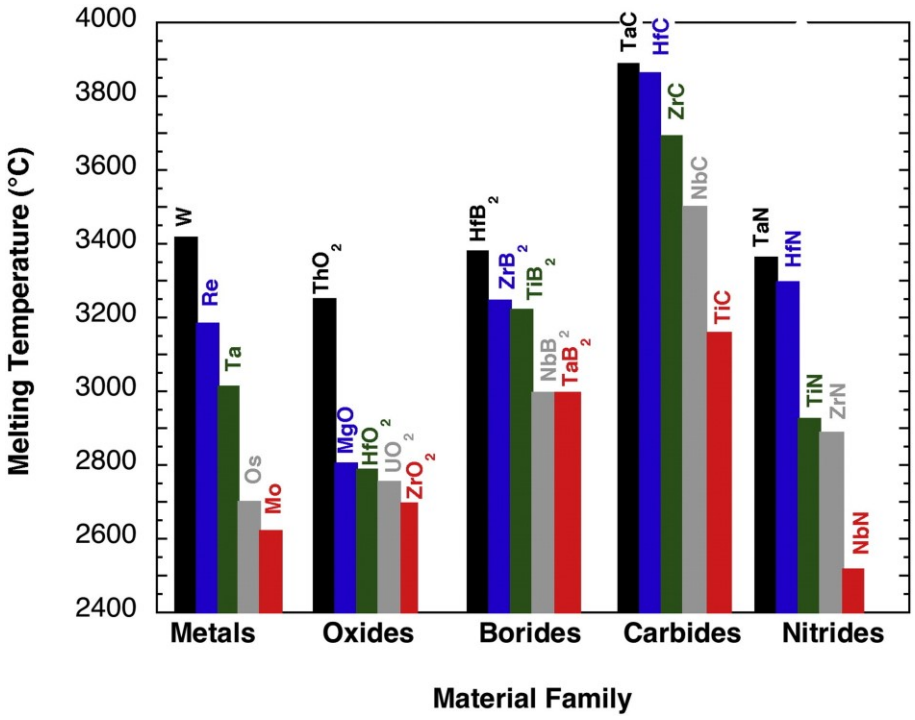

Figure 2.6. Elements and compounds, grouped by material family, with the highest reported melting temperature [35]. Several borides, carbides, and nitrides have melting temperature above 3000 °C and are considered ultra-high temperature ceramics (UHTCs).

Reports of the synthesis of UHTCs date back to the late 1800s [38,39], but it was not until the seminal works sponsored by the U.S. Air Force [40] and the work of Samsonov [41] in the 1960s that these materials became more widely known. At that time due to the space race, NASA (and its predecessor agency NACA) as well as groups in the Soviet Union were searching for materials that could be used in the extreme environments associated with rocket propulsion and atmospheric re-entry for the first generation of spacecraft [42,43]. After the space race, interest on UHTCs waned for several decades, until it renewed in the late 1980s again due to aerospace applications such as hypersonic aerospace vehicles, scramjet propulsion and advanced rocket motors [44–47].

Research on this class of materials during the last 30 years has furthered knowledge in several areas including synthesis, processing, densification, thermal properties, mechanical behaviour, and oxidation resistance.

2.2.1 Crystal structure

Crystal structure determines the chemical, physical, and thermal properties of materials. Transition metals form strong covalent bonds with boron, carbon or nitrogen, lending the UHTC compounds a unique combination of ceramic-like and metal-like properties: high melting temperature, hardness, stiffness, electrical and thermal conductivity [37,48–51].

The most common crystal structure for Group IV-VI transition metal diborides is primitive hexagonal (AlB_2-type, belonging to the *P6/mmm* space group symmetry) [52], as shown in Figure 2.7.

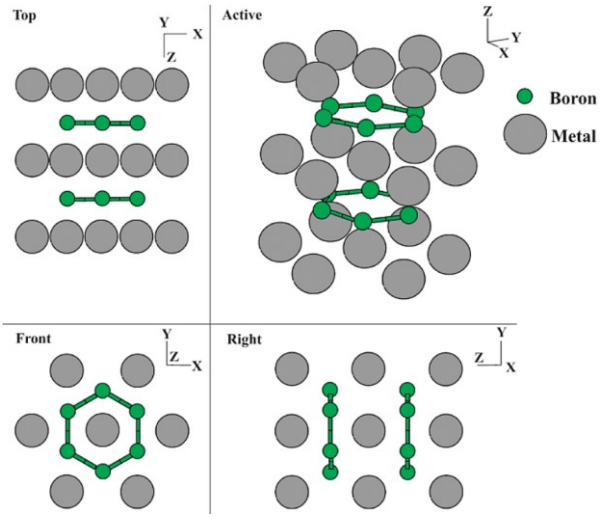

Figure 2.7. Projections of the AlB_2-type structure of transition metal diborides [52].

The crystal structure is composed of layers of B atoms in 2D graphite-like sheets alternating with planes of hexagonally close-packed metal atoms, that held together by bonds with mixed ionic and covalent characters because of the metal-boron (M-B) donor-acceptor interactions and the partial excitation of metal *d* electrons [52]. The M-B and B-B bonds length and strength vary depending on the metal atom [52–54]. Zr and Hf are very chemically similar elements, so the borides of these elements are also very similar. Both compounds are characterized by very high strengths of the B-B rings and M-B bonds, which provide high hardness and temperature stability [36,52].

Carbides exhibit extremely high melting points and hardness, exceeding those of the aforementioned borides. In particular, the monocarbides of Ta and Hf (TaC and HfC) possess the highest melting temperatures (3980 °C and 3928 °C, respectively) of any known compounds [36]. This is attributed to their interatomic bonding, which is a complex mixture of metallic, covalent and ionic characters [55–57]. The interaction between the *d*-band of the metal atoms and *p*-band of the carbon atoms (which produce sp^3 hybridization [58]) leads to very strong covalent bonding, higher than those in the boron complexes [52]. The group IVB and VB monocarbides all crystallise in the NaCl-type face-centred cubic (FCC) structure (*Fm-3m* space group), with carbon atoms in the octahedral sites [59] (Figure 2.8).

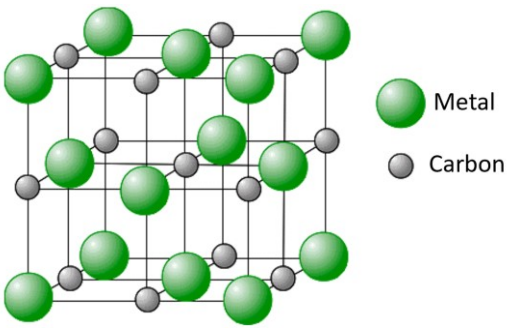

Figure 2.8. NaCl-type face-centred cubic (FCC) crystal structure of transition metal monocarbides, where the metal atoms form a FCC lattice and the carbon atoms occupy the octahedral interstitials.

Even though the chemical formula for the monocarbides is generally written as MeC, they are often found in substoichiometric mixture due to vacancies in the C sublattice, therefore MeC_x (where *x* is the C/Me ratio) is a more appropriate formula. Notably, the substoichiometric phase stability field allow to tailor their thermophysical and thermomechanical properties [35].

The nitrides of groups IV-VI are similar in structure and composition and have similar properties to the respective carbides. Among the nitrides belonging to UHTCs, the most common are ZrN, HfN and TaN. These mononitrides adopt the rocksalt (NaCl-type FCC) structure. Such structure may show significant variation in composition, but unlike carbides, due to vacancies of both nonmetal and metal atoms [60,61]. Their complex combination of metallic, covalent, and ionic bonding leads to high hardness, high melting points and chemical inertness, even though they are not as refractory as the carbides because of the weaker bonding [50,51]. Nitrides of groups IV and V have melting points above 2000 °C, whereas those of group VI dissociate rapidly at high temperature [62].

2.2.2 Synthesis

Borides can be synthesized by different approaches [35]. The simplest reaction synthesis method for producing MeB_2 powder consists in the reaction of elemental constituents of the desired borides (Reaction 1):

$$Me + B_2 \rightarrow MeB_2 \quad (1)$$

Since the high oxygen affinity of transitional metals such as Zr and Hf, the synthesis is carried out in inert or reducing atmosphere to prevent the formation of oxide impurities. Reaction 1 is extremely exothermic, so it can sustain itself once initiated. Also, the large generated heat can promote local melting of the metal, which further accelerates the reaction.

Another method is the reduction process, based on the reaction between the transition metals oxides and boron-containing materials, that are used as the metal and boron source respectively. Boron sources can act directly as reducing agents, such as B and B_4C, or combined with carbon.

Carbothermal reduction (Reaction 2) is commonly used to produce commercial MeB_2 powders, specifically ZrB_2 an HfB_2.

$$MeO_2 + B_2O_3 + 5C \rightarrow MeB_2 + 5CO_{(g)} \quad (2)$$

Due to its volatility, an excess B_2O_3 is required to minimize unreacted carbon contamination [ref]. Commercially, synthesis of ZrB_2 uses an excess B_2O_3 content of 10–30 wt%, that result in ZrB_2 powder with low C content.

Carbo/borothermal reduction involves B_4C as boron source and reducing agent (Reaction 3):

$$2MeO_2 + B_4C + 3C \rightarrow 2MeB_2 + 4CO_{(g)} \quad (3)$$

In the synthesis of ZrB_2, the loss of B_2O_3 can result in the formation of ZrC in the final product (Reaction 4). Using excess B_4C allows to decrease the amount of C; even if ZrC forms as an intermediate product, it can be removed thanks to excess B_2O_3 by Reaction 5. By this process, as in the case of carbothermal reduction, carbon may remain in the final product as an impurity.

$$ZrO_2 + 3C \rightarrow ZrC + 2CO_{(g)} \quad (4)$$

$$ZrC + B_2O_3 + 2C \rightarrow ZrB_2 + 3CO_{(g)} \quad (5)$$

Borothermal reduction employs elemental B as raw material, which can help to eliminate carbon or carbides impurities in final MeB2. Common borothermal processes are represented by the general reaction (6):

$$3MeO_2 + 10B \rightarrow 3MeB_2 + 2B_2O_{3(g)} \quad (6)$$

B_2O_3 reacts with excess B to form boron-rich gaseous species, such as B_2O_2 and BO (Reactions 7 and 8):

$$2B_2O_{3(l)} + 2B \rightarrow 3B_2O_{2(g)} \quad (7)$$

$$B_2O_{3(l)} + B \rightarrow 3BO_{(g)} \quad (8)$$

However, boron oxides will be source of oxygen impurities. In order to obtain a pure product, B_2O_3 can be removed by washing or vaporization with hot water at temperature above 1500 °C.

Similarly to the borides, the carbides can be prepared by the reaction of elemental precursor powders (Reaction 9), which causes the direct carburization of the metal, or the carbothermal reduction of the corresponding oxide (Reaction 10). This latter method is the most widely used way due to the low production cost [35,63].

$$Me + C \rightarrow MeC \quad (9)$$

$$MeO_2 + 3C \rightarrow MeC + 2CO_{(g)} \quad (10)$$

2.2.3 Densification

Ceramics are typically made by sintering, a process used to transform the initial powders into dense solids by forming bonds between particles and removing porosity. Such step involves heating a "green" body (pre-consolidated object with shape similar to the final one) at a temperature that usually exceeds 70% of the melting point. The high temperature activates the diffusion of atoms at the grain boundaries, that ultimately bonds the particles together [64].

Sintering of UHTCs is difficult due to their strong covalent bonds between atoms and low intrinsic self-diffusivity [65]. In order to achieve full densification in monolithic UHTCs, sintering processes are normally carried out at temperatures over 2000 °C. However, at high temperature the grain coarsening prevails on densification, leading to a depletion of mechanical properties compared to ceramics with refined microstructures. Hence, different strategies to achieve better densification have been developed:

- pure and ultrafine powders, since oxide impurities on the particle surfaces promote grain coarsening [66,67];
- refinement of powder particle sized and increasing the defect concentrations by mechanical activation (i.e. high-energy milling) [68];
- high-temperature reactive sintering of solid precursors [69];
- use of additives which generate a liquid phase at sintering temperature [52,70].

The latter is the most widely used approach. For instance, several additives have been investigated to improve sinterability of borides such as ZrB_2 and HfB_2 [71–76]. Silicon carbide (SiC) is the most popular additive for these compounds, as it acts as sintering aid, prevents grain growth and improves oxidation resistance [77–86]. Similar sintering issues affect transition metal carbides, for whose it has been demonstrated that additives such as metal, carbides and silicides (e.g. $MoSi_2$) [87–91] can be useful.

Different techniques can be used to prepare dense shapes of UHTCs, including pressureless sintering and hot pressing, that are traditionally used for various ceramic materials [92]:

– Pressureless sintering (PS): [71,73,81,84,87,93–96] very simple and economic technique, usually chosen to fabricate near-net shape component and thus reducing subsequent diamond machining. Due to the poor sinterability of UHTC compounds, manufacturing

of dense shapes of UHTCs requires very high temperature and long holding times, that are detrimental to the mechanical properties. Hence, this technique is prevalently used incorporating additives to UHTC powders to decrease the severity of the processing conditions.

- Hot pressing (HP): [69,72,97] pressure-assisted technique that allows ceramics to be sintered at lower temperature and shorter times than pressureless technique. It is often employed also using sintering aids to reduce the processing temperature as much as possible. HP is the most common method for fabricating dense UHTC bodies, despite it is more expensive than PS, also generally production is limited to simple shapes due to the uniaxial applied pressure.
- Spark plasma sintering (SPS): [98–105] is employs a pulsed DC current to activate and improve sintering kinetics allowing higher heating rates, lower sintering temperatures and shorter dwelling times in comparison with conventional sintering techniques (hot-pressing, pressureless sintering, etc.). As a result, higher densities, refined microstructures, overall improvement in the materials performance is achieved.

2.2.4 Mechanical properties

Besides high melting temperature, the strong covalent bonding between the transition metals and B, C, or N results in high stiffness, hardness, and strength. The mechanical properties, including elastic modulus, hardness, flexural strength and fracture toughness, of common UHTCs are reported in Table 2.1.

Table 2.1. Basic physical and mechanical properties at room temperature possessed by common UHTCs. Data taken from ref. [52,57,106,107].

Material	Density (g/cm^3)	Melting temperature (°C)	Elastic Modulus (GPa)	Hardness (GPa)	Flexural Strength (MPa)	Fracture Toughness ($MPa \cdot m^{0.5}$)
ZrB_2	6.2	3245	489	23	300–400	2–4
HfB_2	11.2	3380	480	28	350–450	4–5
ZrC	6.5	3420	350	25	400	2
HfC	12.3	3930	420	20	250–350	2–3
ZrN	7.3	3000	460	15	-	-
HfN	13.8	3330	380	18	-	-

Elastic modulus ranges from 350 to 489 MPa, while hardness can be up to 30 MPa, notably superior compared to most ceramics (e.g. hardness for Al_2O_3 ~19 GPa, ZrO_2 ~12 GPa) and other material classes, such as metals and alloys [108].

Among UHTCs, zirconium diboride (ZrB_2), due to its relatively low density (Table 2.1), has been considered the most suitable for ultra-high temperature applications [109]. Hence, in recent years mechanical behaviour of ZrB_2-based ceramics has been extensively investigated. Properties values for ZrB_2 with and without SiC additive are summarized in Table 2.2.

Table 2.2. Elastic modulus, Vickers hardness, fracture toughness and flexure strength at room temperature of ZrB_2-based ceramics. Data taken from ref [35].

Composition (vol%)	Elastic modulus (GPa)	Hardness (GPa)	Fracture toughness ($MPa \cdot m^{0.5}$)	Flexural strength (MPa)
ZrB_2	346–498	9–23	1.9–4.8	300–565
ZrB_2 + 10 SiC	450–507	18–24	3.8–5.7	393–835
ZrB_2 + 20 SiC	466–506	21–24	3.9–6.8	487–1009
ZrB_2 + 30 SiC	487–541	20–27	4.4–5.9	425–1150

Published data in literature have a wide range, because mechanical properties are strictly dependent on processing conditions and final microstructure. Stoichiometry, presence of impurities (oxygen, free carbon), grain size, dispersion and cluster size of second phases affect the properties.

Single-phase ZrB_2 showed elastic modulus ranging approximately from 345 to 500 GPa and flexural strength from 300 to 565 MPa (Table 2.2), depending on porosity and grain size. Higher strengths were obtained for materials with finer grain sizes [110,111]. Factors as large starting particle size, presence of impurity, processing temperatures above 2000 °C, which resulted in grain growth, reduced mechanical strength [112]. ZrB_2-SiC composites exhibited enhanced properties: room temperature flexural strength above 1000 MPa [110,111,113], fracture toughness as high as 5.5 $MPa \cdot m^{0.5}$ [110,111,114], and hardness exceeding 22 GPa [111,113,114]. This is due to the SiC added as sintering aid for improving densification, that may also inhibit grain growth and thus enhance strength. Although ZrB_2 grain size is affected by the SiC content, in ZrB_2-SiC ceramics the strength is controlled by the size of SiC particles. Watts et al. [113] found that the critical grain size was between 6.5 and 13.8 μm. Since SiC grain size is the determining factor for the strength,

uniform dispersion of SiC is required to maximize resistance. The effect of SiC content on the strength of ZrB_2/SiC ceramics was also studied. Chamberlain et al. [110] found that the strength of 560 MPa of pure ZrB_2 increased to 1090 MPa with the addition of SiC content up to 30 vol%. Even in this case the strength was controlled by the size of SiC inclusions. Indeed, Liu et al. [115] found that for SiC contents above 30 vol%, SiC particles began to aggregate forming clusters that reduced the strength. The fracture toughness of pure ZrB_2 is generally around 3.5 MPa·$m^{0.5}$, considerably lower compared to other materials classes [35,108]. It was found that the addition of 30 vol% SiC led to an increase in fracture toughness up to 5.3 MPa·$m^{0.5}$ [110]. The cause of toughness improvement was attributed to the higher tortuosity of the crack path induced by SiC particles, promoting inter-granular fracture.

One of the more important aspects that have gained the interest for UHTCs is the retention of hardness and strength at high temperature. Generally elastic modulus tends to decrease rapidly with the increase of temperature due to the weakening of covalent bonding. Okamoto et al. [116] reported for ZrB_2 bulk a decrease of elastic modulus from 525 GPa at room temperature to 490 GPa at 1100 °C. Other works [117,118] reported lower values, nevertheless up to 1200 °C elastic modulus decreased linearly keeping a value of 450 MPa. Above this temperature, modulus decreased more rapidly, because of grain boundary sliding and diffusional creep mechanisms. ZrB_2/SiC ceramics showed similar trend: elastic modulus decreased steadily from 530 GPa at room temperature to 420 GPa at 1400°C, then it drastically decreased down to 100 GPa at 1600 °C [119]. A different behaviour can be observed for high temperature strength. Fully dense pure ZrB_2 with strength of 325 MPa at room temperature reached a value of 420 MPa at 800°C due to relief of thermal stresses; then strength decreased to 145 MPa at 1400 °C, but increased again to 200 MPa at 1900°C due to stress relief coupled with creep mechanisms, and finally fell down to 50 MPa at 2200 °C [119]. Studies on ZrB_2 ceramics containing 20–30 vol% showed that strength is generally retained, or even increased, from room temperature up to 1000 °C. Strength can be maintained between 500 and 700 MPa due to formation of a silica glass capable of healing surface flaws. For instance, Zou et al. [120] reported for ZrB_2-20 vol% SiC an increase of strength from 550 MPa at room temperature to 680 MPa at 1000 °C, then decreased to 460 MPa at 1600 °C.

As far as the carbides, the mechanical properties are more difficult to determine due to the intrinsic obstacle in obtaining fully dense materials. Some works on HfC reported

values of flexural strength at room temperature of 235 MPa which decreased to 109 MPa at 1315 °C [48], while works from Fahrenholtz et al. [121] on cermets based on tungsten doped with ZrC exhibited strength of about 400 MPa. Carbides showed plastic deformation only at very elevated temperature, above 2000 °C [48].

2.2.5 Thermal properties

The values of coefficients of thermal expansion (CTE) and thermal conductivity of common UHTCs are reported in Table 2.3.

Table 2.3. Coefficients of thermal expansion (CTE) and thermal conductivity at room temperature of common UHTCs. Data taken from ref. [52,57].

Material	CTE (ppm/K)	Thermal Conductivity (W/mK)
ZrB_2	5.9	60
HfB_2	6.3	104
ZrC	7.5	24.6
HfC	6.1	25.1
ZrN	7.8	11
HfN	8.5	11

Borides, such as ZrB_2 and HfB_2, have significant higher thermal conductivities compared to carbides or nitrides, due to their crystal structure [57]. The intrinsic thermal conductivities of ZrB_2 and HfB_2 at room temperature approach copper [36]. Thermal properties depend on temperature, tending to decrease increasing temperature, nevertheless borides exhibit higher values than those of nitrides and carbides also at high temperature [ref]. For instance, ZrB_2 registered a little dropoff up to 2500 °C [36].

Generally, a high thermal conductivity provides a smaller thermal gradient, allowing to reduce thermal stresses within the material. This property makes borides very appealing for applications where thermal stress response is an important issue.

2.2.6 Oxidation resistance

Unfortunately, bulk UHTCs exhibit rather poor oxidation resistance. Thus, despite the unique combination of properties that has attracted increasing attention in particular on ZrB_2 and HfB_2, this shortcoming is the main barrier to their more extensive applications.

The oxidation behaviour of diborides has been thoroughly studied and modelled over a wide temperature range [122,123]. The low resistance is the result of the lack of the formation of a stable and protective scale during high-temperature oxidation [52,124,125]. For instance, monolithic ZrB_2 during oxidation forms porous ZrO_2 crystals and B_2O_3, according to Reaction 11. The latter above 450 °C is liquid and surrounds the ZrO_2 grains providing partial protection, until its volatilization at temperature around 1100 °C that leaves the porous scale susceptible to further oxygen attack.

$$ZrB_2 + 5/2\ O_2 \rightarrow ZrO_{2(s)} + B_2O_{3(l/g)} \quad (11)$$

In this regard, the development of UHTCs moved toward composite formulations enriched with phases which improve performance in oxidative environment, such as SiC or metal silicides [48,126–129].

SiC phase combined to ZrB_2 leads to the formation of a borosilicate glass (Reaction 12), which is more viscous and less volatile than pure B_2O_3 and hinders oxygen diffusion within the material up at least 1600 °C (Figure 2.9). At the same time borosilicate glass is less viscous than pure silica (SiO_2) and spreads better along the surface, sealing cracks and defects [114]. Moreover, above 1600 °C borosilicate scale has enhanced durability, since ZrO_2 solid particles embedded into the glass induce a physical modification while their partial dissolution promotes a chemical modification of Si-O bonds [130].

$$ZrB_2 + SiC + 4O_2 \rightarrow ZrO_{2(s)} + SiO_2{\cdot}B_2O_{3(l)} + CO_{(g)} \quad (12)$$

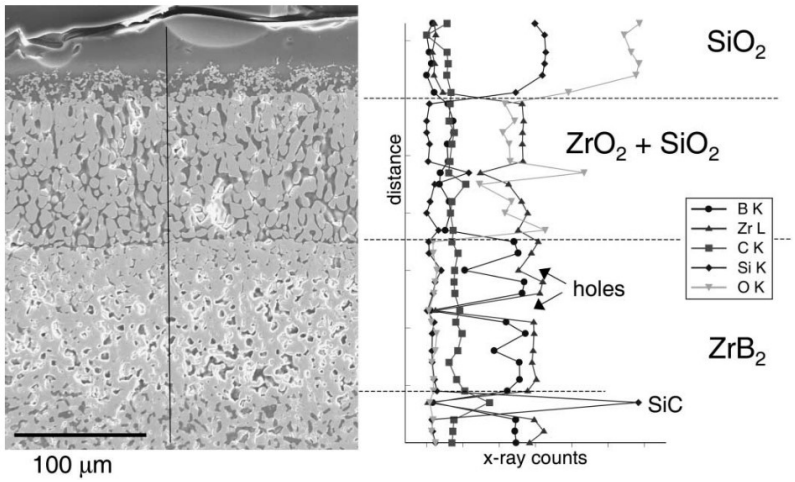

Figure 2.9. Scanning Electron Microscope (SEM) image and composition profile of a cross section of ZrB_2-SiC material after 10-minute cycles at 1627 °C in air. From the surface: outer glass layer, ZrO_2-based interlayer, SiC depleted zone, and unreacted bulk ceramic [131].

Among metal silicides, $MoSi_2$ was demonstrated to be one of the most effective greatly improving the oxidation resistance of ZrB_2 or HfB_2-based ceramics [93,95,127]. The beneficial effect of $MoSi_2$ during oxidation was due to the formation of a glassy SiO_2 layer on the outer surface, that acts as oxygen diffusion barrier, and stable condensed phases in the subsurface layer, for instance MoB and Mo_5Si_3, thus leading to the suppression of volatile species. The combination of these factors has been considered the responsible for hindering the evolution of columnar ZrO_2 grains in the subsurface, which is detrimental for the fast oxygen diffusion inward into the ceramic matrix. The oxidation route of ZrB_2 doped with $MoSi_2$ has been indicated as follows (Reactions 13 and 14) [132]:

$$ZrB_2 + 5MoSi_2 + 19/2\ O_2 \rightarrow ZrO_2 + 7SiO_2 + Mo_5Si_3 + B_2O_3 \quad (13)$$

$$2MoSi_2 + B_2O_3 + 5/2\ O_2 \rightarrow 4SiO_2 + 2MoB \quad (14)$$

Different oxidation behaviour is observed for the carbides. Most of the carbides are resistant to oxidation below 800 °C and above 1800 °C. At temperature beyond 800 °C, a crystalline oxide scale is formed on the surface, according to reaction (15):

$$MeC + O_2 \rightarrow MO_{2(s)} + C \quad (15)$$

Further oxidation of the formed elemental carbon (see Reaction 13) leads to evolution of gaseous species such as CO_2 and CO, resulting in the formation of porous oxide scales. Moreover, until 1800 °C the scale has no good adherence due to high sintering temperature of oxides species and falls off, not providing protection. For this reason, generally carbides can be used for applications involving very rapid heating to temperature above 1800 °C. Also in this case, the addition of SiC or metal silicides can be beneficial for improving oxidation resistance because they form a dense SiO_2 protective layer between 1300 and 1500 °C [90,133].

2.2.7 Applications

The combination of properties such as high melting point (> 3000 °C), strength at high temperature, high thermal conductivity, low thermal expansion coefficient, oxidation resistance and erosion resistance enable UHTCs to survive extreme conditions that are beyond the capabilities of current materials.

Structural materials for use in oxidizing environments at temperature above 2000 °C are of great interest to the aerospace sector. UHTCs have been extensively investigated for applications as Thermal Protection Systems (TPSs) [109,134], sharp-leading edges [77,131,135] and rocket motor nozzles [134,136,137] of hypersonic re-entry vehicles. For these applications, oxidation resistance as well as high thermal conductivity are desirable, since temperature can rise over 2000 °C on the operating surface very rapidly (less than a second) while cool temperature is still present on the opposite one, generating compressive and tensile stresses at the respective surfaces [36].

Borides typically have much higher thermal conductivity than carbides and nitrides, thus they can readily dissipate the heat through the component reducing thermal gradient and thermal stresses [49,138]. ZrB_2 and HfB_2 are also potential candidates for use in applications as neutron-shielding material [139], electrodes for metal refining [140], microelectronics [141], and many others.

Carbides and nitrides are characterized by their extremely high melting points, high hardness and good chemical inertness, thus they have received more interest in applications where higher thermal and mechanical loads are faced, such as nozzle throats and liners [137], control thrusters [142], and also cutting tools, in microelectronic industry [143] and nuclear field [35].

However, bulk UHTCs suffer from fracture toughness and poor thermal shock resistance. Consequently, exposure to extreme temperature and heat fluxes may cause a catastrophic failure. One approach to overcome these disadvantages is to introduce carbon fibres as reinforcement.

2.3 Ultra-high temperature ceramic matrix composites

Nowadays, the hypersonic flight regime continues to attract a great deal of attention from scientific community. Therefore, the scientific research is pushed towards a continuous search of highly performing materials able to operate in extreme conditions for aerospace applications [144]. For instance, Thermal Protection Systems (TPSs) of hypersonic re-entry vehicles are exposed to temperatures above 2000 °C while heat fluxes and highly reactive gases hit the surfaces [145]. Such extremely hot conditions are beyond the feature of currently commercial metals, metal matrix composites [146,147] and even the majorities of Ceramic Matrix Composites (CMCs), such as C/SiC and SiC/SiC

[ref5,6]. SiC-based materials are able to withstand mechanical stresses and thermal shocks during satellite launch and Earth re-entry [147–150], but their oxidation resistance is limited to temperature below 1600 °C due to the active oxidation of SiC phase to SiO gas [9,151,152]. Ultra-high temperature ceramics (UHTCs), in particular the transition metal di-borides, have gained interest for use in extreme environments [ref5]. ZrB_2 has been extensively investigated as a potential candidate for the development of TPS, because of its relatively low density and high thermal conductivity [ref6]. However, these materials suffer from catastrophic failure due to their low fracture toughness and poor thermal shock resistance [ref1].

Ultra-High Temperature Ceramic Matrix Composites (UHTCMCs) are a novel class of materials constituted of carbon or silicon carbide fibre and an ultra-high temperature (UHTC) matrix. They are designed to combine the best features of pure CMCs with those of UHTCs. The integration of these two classes of materials should mitigate the limits from each and reach the goal of an improved erosion/ablation resistance compared to CMCs, improved damage tolerance and thermal shock compared to UHTCs [144] (Figure 2.10).

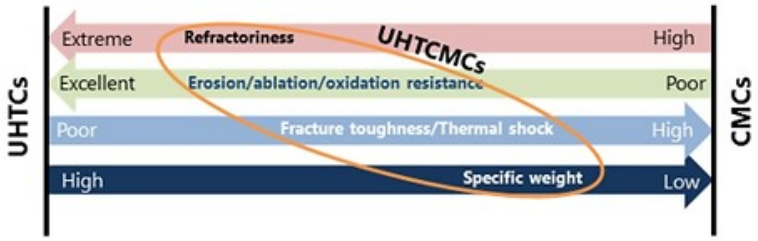

Figure 2.10. Concept of the Ultra-High Temperature Ceramic Matrix Composites (UHTCMCs) class [144].

2.3.1 Manufacturing methods

Sintering is an essential step for the consolidation of bulk ceramics, and pressure-assisted techniques such as Hot Pressing (HP) and Spark Plasma Sintering (SPS) are well-known and largely used for UHTCs. They are rarely applied to the manufacturing of CMCs because of the consequence of the applied pressure combined with the elevated temperature (e.g. fibre damage). There are few works concerning the sintering of CMCs and they are mainly focused on SiC fibre-reinforced SiC matrix composites [153–156], since these fibres are less reactive than carbon ones. Nevertheless, sintering process have been rethought for UHTCMC manufacturing [157]. If short fibres are used as reinforcement, composites can be produced by conventional ceramic technology (i.e. ball milling,

shaping, sintering) [158–160]. Differently, preparation of UHTCMCs with continuous carbon fibres consists of impregnation of the fibres, which can occur by direct immersion of the preform into the UHTC slurry or by filament winding, and densification by HP or SPS [161,162,171,172,163–170]. Sintering route is typically characterized by short manufacturing time (e.g. hours) and allows to create a sintered UHTC matrix that can contribute to the structural properties in extremely hot environments. However, an accurate setting of the pressure and heating is required to produce a pore and crack-free matrix, conserve the integrity of the reinforcement, and avoid a strong fibre/matrix interface that leads to fibre failure without toughening mechanisms. In addition, the use of pressure-assisted techniques is limited to simple shapes and fabrication of complex shape as well as processing of complex fibre architectures is still challenging.

In the literature, several published works report the fabrication of Ultra-High Temperature Ceramic Matrix Composites (UHTCMCs) by the introduction of UHTC phases into the matrix, using many processing techniques re-adapted from the CMC manufacturing technologies such as:

- Reactive Melt Infiltration (RMI) [173–178], which produces near fully dense matrix via infiltration of a porous CMC with a molten metal. The technology has the potential to be very quick (few days) and cost effective. However, the proposed examples with Zr showed severe degradation of carbon fibres, due to the reaction at 1900 °C with the aggressive molten metal, and the presence of unreacted residual metallic phases in the final matrix, which may lead to a drop of mechanical properties at elevated temperature [157,179];
- Chemical Vapour Infiltration (CVI) [180,181], which is a layer-by-layer technique, versatile and low-temperature process, making it possible to achieve excellent mechanical properties with no fibre damage. However, it requires the highest processing times (weeks to months) and production costs among the cited technologies [157,179];
- Polymer Infiltration and Pyrolysis (PIP), whose advantages include: near-neat shape manufacturing, low temperature processing and tuning of matrix microstructure through proper setting of the pyrolysis cycle [157,179]. Currently, the most feasible way to introduce UHTC phase is infiltration of the preforms with SiC preceramic polymer doped with UHTC powders [182–185], even though this method does not always result in a uniform distribution of the matrix phases. The use of UHTC preceramic polymers

should be advantageous for a more homogenous distribution in the matrix and higher UHTC content [186,187]. For instance, Hu et al. [182] fabricated 2D C_f/SiC-ZrB_2 using a ZrB_2 powder based slurry containing polycarbosilane and divinyl benzene, followed by thermal treatment at 1200 °C, achieving composites with a final UHTC content of 19% and porosity of 23%. Uhlmann et al. [184] prepared 2D C_f/SiC-ZrB_2-TaC composites by adding ZrB_2 and Ta powder within the pre-ceramic slurry of C/SiC, followed by thermal treatment at 1600 °C; these materials exhibited an excellent thermo-chemical resistance despite open porosity was above 20%. Recently, Ran et al. [188] have prepared C_f/C-ZrB_2-SiC through a method of high-solid-loading slurry impregnation and further densified by PIP with a polycarbosilane as SiC precursor, reaching an open porosity of 7% after the eighth pyrolysis carried out at 1400 °C. Unfortunately, commercial products are almost non-existent, while reported studies are mostly about carbide compounds (see subparagraph 2.3.1.1). It should be noted that several cycles are required for infiltration and densification of the matrix [179] and each cycle can be time consuming since typical heating rates of 1-2 °C/min are required [189]. Consequently, on the one hand PIP technique is attractive for the relatively low processing temperature and no complex experimental system, on the other hand it is disadvantageous from a time/cost perspective [34,157,179,190]. Despite these drawbacks, PIP is one of the most viable techniques for production of UHTCMCs, hence the combination of the PIP process with other techniques has been recently investigated to obtain a dense matrix in a fast and cost-effective manner [157,190].

2.3.1.1 Preceramic polymers as precursors of UHTCs

Most commercially available polymers are polycarbosilane, polysilazane and polyxilosane for manufacturing SiC, SiCN(O) and SiCO-based composites, respectively. Contrarily, there is a lack of polymer precursors to UHTCs. Only few companies provide HfC and TaC precursors, while metal borides are not available on the market [157]. Therefore, researchers have begun studying synthesis of new metal-containing polymers.

Two strategies may be applied for the synthesis of polymeric precursors of UHTC phases: 1) methods via chemical modification of metal alkoxides with, e.g. (poly)alcohols, (poly)acetates or other compounds such as acetylacetone, salicylic acid, etc.; and 2)

methods via chemical modification of organometallic compounds such as metallocene-type compounds or other metal complexes with alkyl, alkenyl, alkynyl, or aryl ligands [186].

Many examples of precursors for ZrC are reported in the literature. Zhao et al. [191] made a precursor for ZrC by just blending zirconium butoxide and divinylbenzene. Sacks et al. [192] synthesised nano ZrC powders using mixed solutions of zirconium n-propoxide/n-propanol and phenolic resin or glycerol. Several researchers went for zirconium oxychloride octahydrate as zirconium source, less toxic than zirconium alkoxides. For instance, from the reaction between it and acetylacetone and salicylic alcohol Tao et al. [193] synthesised a new polymer precursor, polyzirconoxanesal, soluble in common organic solvents; similarly, Yan et al. [194] obtained a polymer by chelation of acetylacetone to Zr, which combined with phenolic resin as carbon source. Dong et al. [195] synthesised a polymer precursor for ultra-fine ZrC using zirconium tetrachloride, acetylacetone, and phenol as starting materials. Some authors [196] developed an environmentally friendly aqueous solution-based processing using zirconium acetate and sucrose, combined with polyvinyl pyrrolidone. Also, to take an example of the second preparative tool, Xie et al. [197] used a polymeric zirconium cyclopentadienyl/boron hydride species to obtain ZrB_2/ZrC ceramic.

Due to the relatively poor oxidation stability of pure UHTCs, precursors which enable mixed ceramic phases containing silica formers (e.g. SiC) were developed for high-temperature applications. Si-containing and UHTC precursors are combined to form either blends, to produce nanocomposites with low content of silica former (10–20 vol%), or single-source polymeric precursors, which are used for preparing nanocomposites with high content of silica former (80–90 vol%) [186]. The same synthesis methods used for UHTCs were reported for the former, whereas for the latter the most common approach is the chemical modification of the silica former (such as polysilane and polycarbosilane) at molecular scale by metal-containing compounds. Then, the single-source precursor is thermally converted (~1000 °C) in a single-phase amorphous ceramic, which upon heat treatment at higher temperature undergoes phase separation and crystallization forming bi- or multiphase nanocomposites consisting of highly refractory secondary phases dispersed within a silicon-based PDC-based matrix (such as SiOC, SiCN, SiBCN) [22,186,198–201] (Figure 2.11).

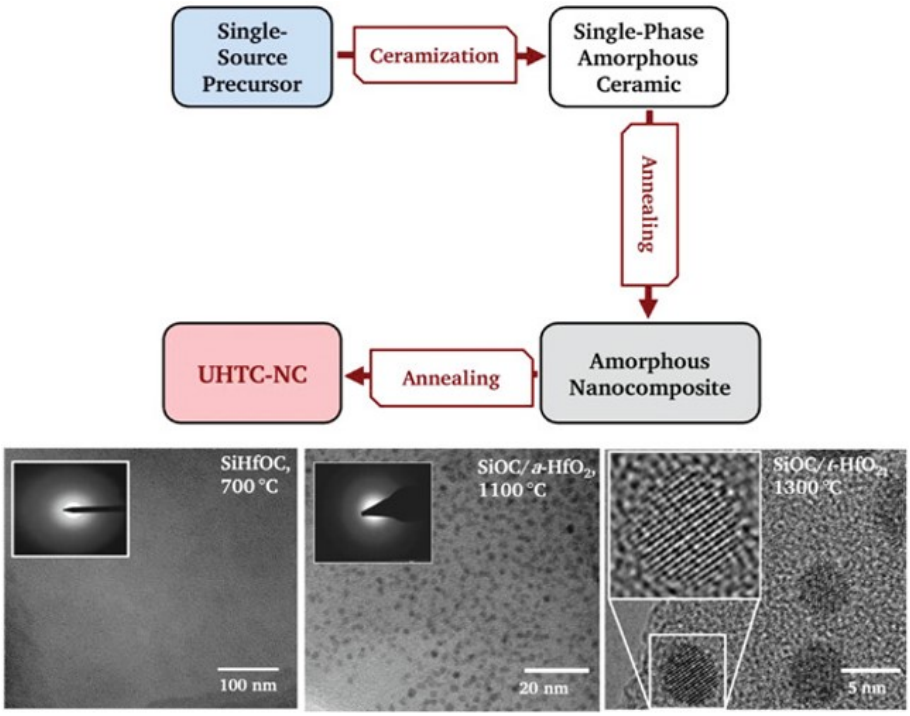

Figure 2.11. Typical preparative approach of polymer-derived ceramic nanocomposites starting from single-source precursors [186].

There are several advantages of the polymeric-precursor-based synthesis methods of UHTCs and their nanocomposites, such as materials with tailored composition, nanoscopic particle size, relatively low synthesis temperatures. Moreover, this synthetic approach may have high relevance for the preparation of UHTCMCs via polymer infiltration and pyrolysis (PIP). However, to date, preceramic polymers are often lacking in desirable polymeric properties, air stability, and high ceramic yield [190]. Moreover, producing pure UHTC phases from PIP route is complicated by the thermodynamic proclivity for the formation of other carbide, nitride and oxide phases because of the precursors frequently used [202]. Also, some authors [203,204] have reported that significant degradation of the carbon fibres occurs due to the reaction with the precursors.

2.3.2 Mechanical properties

The last few years have seen a large escalation of publications on UHTCMCs, much of these concerning composites reinforced with continuous fibre for maximum load transfer and strain to failure. Unfortunately, available mechanical data are still poorly reported to allow for a clear understanding of the mechanical behaviour of UHTCMCs. Indeed, in the published works there is plenty of different microstructural features that

strongly influence the mechanical response, but often they are not reported in detail limiting the possibility to correlate properties with microstructure. Moreover, it is hard to make direct comparison of values, due to the different testing methods. In general, UHTCMCs exhibit enhanced mechanical behaviour over current materials. Research on UHTCMCs has led to successful fabrication of materials possessing a good strength even at 2100 °C [165,168,170,205], a good fracture toughness (e.g. 15.7 $MPa \cdot m^{1/2}$) [168], and an excellent thermal shock resistance (> 1500 °C) [168,206].

2.3.3 Oxidation resistance

Many approaches have been investigated to implement the self-protection capability of UHTCs into conventional CMCs. The diborides of the transition metals have proven to be the best candidate UHTCs to date. Specifically, it is well-known the beneficial effect of the combination ZrB_2/SiC for improved oxidation and ablation resistance, without being detrimental to the high temperature stability [32,207].

Some authors applied an environmental barrier coating (EBC), made of UHTCs, on conventional C/C composites [208–210] and tested the material from 1500 to 2600 °C. The adhesion between the composite and the coating could be compromised due to the different chemistry of the materials and the thermal expansion mismatch under severe thermal stresses. Other authors introduced ZrB_2 powders into fibre preforms via slurry impregnation and consolidated the material using non-sintering routes, such as chemical vapour infiltration (CVI) with methane gas [211] or polymer infiltration and pyrolysis (PIP) with polycarbosilane [182,183,212,213], and sintering approaches, such as pack cementation (PC) [209] and hot pressing (HP) [164,214,215]. All the non-sintering approaches introduce relatively little amounts of UHTC phases, that were found to significantly improve the oxidation and ablation resistance of CMCs as a result of the formation of a protective scale. Investigations were carried out also on fibre-reinforced UHTCs fabricated by HP, where the UHTC phase is the main constituent. Also in this case, it was demonstrated the efficacy of a matrix of ZrB_2-SiC (with a content of SiC above 10 vol%) in protecting fibres from oxidation [164,214,215].

Also, testing in relevant conditions (e.g. arc jet, high velocity oxyflame and oxyacetylene torch) showed promising results. UHTCMs benefit from a damage tolerant

body thanks to the large fraction of fibres like CMCs and the ablation resistance typical of UHTC [179,216–220].

2.3.4 Potential impact

Ultra-High Temperature Ceramics (UHTCMCs), due to their very challenging properties, will no doubt play a useful role in aerospace field. These new materials, capable of providing structural integrity, thermal protection, and low erosion rates can be used in potential applications as near-zero erosion rocket nozzles and near-zero ablation thermal protection systems (TPSs) [221]. Thus, UHTCMCs will foster the implementation of new propellants for boost and thrust applications and reusable components, where neither C/C nor C/SiC can be used since they undergo severe oxidation and ablation. UTCMCs will potentially be a breakthrough not only for aerospace, but also for other fields with similar severe conditions, such as defence, transports, combustion, nuclear environments or concentrating solar power system, paving the way for enormous innovations.

However, a number of issues remain to date. For instance, the thermal mismatch between fibre and matrix can lead to the formation of cracks upon cooling, which then can act as mechanical defects and paths for corrosive/oxidative gases [190]. The choice of the best manufacturing technique is still under debate. A sintered matrix is desired for high density, mechanical and oxidation performance; however, it can become detrimental if it is much stiffer than reinforcement. Polymer infiltration and pyrolysis (PIP) remains one of the most viable techniques for production of near-net shaped components, but the lack of polymer precursor chemistries limits its success.

Research continues to deal with such issues, with a great effort on manufacturing process, precursors synthesis and microstructure/properties correlation. Indeed, although UHTCMCs are still at infancy state, their initial success is promising for the increasing demand for advanced materials with enhanced temperature capability in highly corrosive environments.

2.4 References

1. Krenkel, W. *Ceramic Matrix Composites: Fiber Reinforced Ceramics and their Applications*. (Wiley-VCH, 2008). doi:10.1002/9783527622412.

2. Padture, N. P. Advanced structural ceramics in aerospace propulsion. *Nat. Mater.* **15**, 804–809 (2016).

3. Marshall, D. B. & Cox, B. N. Integral Textile Ceramic Structures. *Annu. Rev. Mater. Res.* **38**, 425–443 (2008).

4. Dever, J. A., Nathal, M. V. & DiCarlo, J. A. Research on High-Temperature Aerospace Materials at NASA Glenn Research Center. *J. Aerosp. Eng.* **26**, 500–514 (2013).

5. Naslain, R. R. & Pomeroy, M. Ceramic Matrix Composites: Matrices and Processing. in *Reference Module in Materials Science and Materials Engineering* (Elsevier, 2016). doi:10.1016/b978-0-12-803581-8.02317-1.

6. Ferreira, J. R., Coppini, N. L. & Levy Neto, F. Characteristics of carbon–carbon composite turning. *J. Mater. Process. Technol.* **109**, 65–71 (2001).

7. Kumar, S., Shekar, K. C., Jana, B., Manocha, L. M. & Eswara Prasad, N. C/C and C/SiC Composites for Aerospace Applications. in *Aerospace Materials and Material Technologies* (eds. Kumar, S., Shekar, K. C., Jana, B., Manocha, L. M. & Prasad, N. E.) 343–369 (Springer Singapore, 2017). doi:10.1007/978-981-10-2134-3_15.

8. Heidenreich, B. C/SiC and C/C-SiC Composites. in *Ceramic Matrix Composites* (eds. Bansal, N. P. & Lamon, J.) vol. 9781118231 147–216 (John Wiley & Sons, Inc., 2014).

9. Wang, Y., Chen, Z. & Yu, S. Ablation behavior and mechanism analysis of C/SiC composites. *J. Mater. Res. Technol.* **5**, 170–182 (2016).

10. Natali, M., Monti, M., Kenny, J. M. & Torre, L. A nanostructured ablative bulk molding compound: Development and characterization. *Compos. Part A Appl. Sci. Manuf.* **42**, 1197–1204 (2011).

11. Besmann, T. M., Stinton, D. P., Lowden, R. A. & Lee, W. Y. Chemical Vapor Deposition (CVD) and Infiltration (CVI). in *Carbide, Nitride and Boride Materials Synthesis and Processing* (ed. A.W., W.) 547–577 (Springer, 1997). doi:10.1007/978-94-009-0071-4_22.

12. Naslain, R., Langlais, F. & Fedou, R. The CVI-processing of Ceramic Matrix Composites. *Le J. Phys. Colloq.* **50**, C5-191-C5-207 (1989).

13. Naslain, R. & Langlais, F. CVD-Processing of Ceramic-Ceramic Composite Materials. in *Tailoring Multiphase and Composite Ceramics* (ed. Tressler R.E., Messing G.L., Pantano C.G., N. R. E.) 145–164 (Springer, Boston, MA, 1986). doi:10.1007/978-1-4613-2233-7_12.

14. Stinton, D. P., Besmann, T. M. & Lowden, R. A. Advanced ceramics by chemical vapor deposition techniques. *Am. Ceram. Soc. Bull.* **67**, 350–355 (1988).

15. Motz, G., Schmidt, S. & Beyer, S. The PIP-Process: Precursor Properties and Applications. in *Ceramic Matrix Composites: Fiber Reinforced Ceramics and their Applications* (ed. Krenkel, W.) 165–186 (John Wiley & Sons, Ltd, 2008). doi:10.1002/9783527622412.CH7.

16. Rak, Z. S. A Process for C_f/SiC Composites Using Liquid Polymer Infiltration. *J. Am. Ceram. Soc.* **84**, 2235–2239 (2001).

17. Santhosh, U., Ahmad, J., Easler, T. & Gowayed, Y. A polymer infiltration and pyrolysis (PIP) process model for ceramic matrix composites (CMCs). *J. Am. Ceram. Soc.* **104**, 6108–6130 (2021).

18. Li, Y. *et al.* Mechanical behavior of LSI based C/C-SiC composites subjected to flexural loadings. *Compos. Part A Appl. Sci. Manuf.* **95**, 315–324 (2017).

19. Krenkel, W. & Schanz, P. Fiber ceramic structures based on liquid impregnation technique. *Acta Astronaut.* **28**, 159–169 (1992).

20. Heidenreich, B., Koch, D., Kraft, H. & Klett, Y. C/C–SiC sandwich structures manufactured via liquid silicon infiltration. *J. Mater. Res. 2017 3217* **32**, 3383–3393 (2017).

21. Colombo, P., Mera, G., Riedel, R. & Sorarù, G. D. Polymer-derived ceramics: 40 Years of research and innovation in advanced ceramics. *J. Am. Ceram. Soc.* **93**, 1805–1837 (2010).

22. Mera, G. & Ionescu, E. Polymer-Derived Ceramics. *Encyclopedia of Inorganic and Bioinorganic Chemistry* 1–26 (2019) doi:10.1002/9781119951438.EIBC2705.

23. Hotza, D. *et al.* Tape casting of preceramic polymers toward advanced ceramics: A review. *Int. J. Ceram. Eng. Sci.* **1**, 21–41 (2019).

24. Shanmugam, P., Krishnan, S., Devapal, D. & Balasubramanian, S. Polymer-Derived Ceramics and Their Space Applications. in *Handbook of Advanced Ceramics and Composites* (ed. Mahajan Y., R. J.) 1–107 (Springer, 2020). doi:10.1007/978-3-319-73255-8_31-1.

25. Ramsdell, L. S. Studies on silicon carbide. *Am. Mineral.* **32**, 64–82 (1947).

26. Muranaka, T., Kikuchi, Y., Yoshizawa, T., Shirakawa, N. & Akimitsu, J. Superconductivity in carrier-doped silicon carbide. *Sci. Technol. Adv. Mater.* **9**, 044204 (2008).

27. Shaw, J. J. A. & Heine, V. The nature of interplanar interactions in SiC polytypes. *J. Phys. Condens. Matter* **2**, 4351 (1990).

28. Mitridis, S. Determination of lattice site location of impurities in compound semiconductors by TEM. (2008).

29. Xiang, Y., Li, W., Wang, S. & Chen, Z. H. Oxidation behavior of oxidation protective coatings for PIP-C/SiC composites at 1500 °C. *Ceram. Int.* **38**, 9–13 (2012).

30. Yang, X., Feng, C., Peng, Z. hang, Yi, W. & Li, G. de. Evolution of microstructure and mechanical properties of PIP-C/SiC composites after high-temperature oxidation. *J. Asian Ceram. Soc.* **5**, 370–376 (2017).

31. Yan, B., Chen, Z., Zhu, J., Zhang, J. & Jiang, Y. Effects of ablation at different regions in three-dimensional orthogonal C/SiC composites ablated by oxyacetylene torch at 1800 °C. *J. Mater. Process. Technol.* **209**, 3438–3443 (2009).

32. Tang, S., Deng, J., Wang, S., Liu, W. & Yang, K. Ablation behaviors of ultra-high temperature ceramic composites. *Mater. Sci. Eng. A* **465**, 1–7 (2007).

33. Hald, H. Operational limits for reusable space transportation systems due to physical boundaries of C/SiC materials. *Aerosp. Sci. Technol.* **7**, 551–559 (2003).

34. Arai, Y., Inoue, R., Goto, K. & Kogo, Y. Carbon fiber reinforced ultra-high temperature ceramic matrix composites: A review. *Ceram. Int.* **45**, 14481–14489 (2019).

35. Fahrenholtz, W. G., Wuchina, E. J., Lee, W. E. & Zhou, Y. *Ultra-High Temperature Ceramics: Materials for Extreme Environment Applications*. vol. 9781118700 (John Wiley & Sons, Inc., 2014).

36. Wuchina, E., Opila, E., Opeka, M., Fahrenholtz, W. & Talmy, I. UHTCs: Ultra-High Temperature Ceramic materials for extreme environment applications. *Electrochem. Soc. Interface* **16**, 30–36 (2007).

37. Fahrenholtz, W. G. & Hilmas, G. E. Ultra-high temperature ceramics: Materials for extreme environments. *Scr. Mater.* **129**, 94–99 (2017).

38. Moissan, H. Sur un nouveau carbure de zirconium. *C. R. Hebd. Seances Acad. Sci.* **122**, (1896).

39. Tucker, S. A. & Moody, H. R. II.—The production of hitherto unknown metallic borides. *J. Chem. Soc. Trans.* **81**, 14–17 (1902).

40. Rudy, E. *TERNARY PHASE EQUILIBRIA IN TRANSITION METAL-BORON-CARBON-SILICON SYSTEMS. PART V. COMPENDIUM OF PHASE DIAGRAM DATA*. (1969).

41. Samsonov, G. V. & Vinit͡skiĭ, I. M. *Handbook of refractory compounds*. (IFI/Plenum, 1980).

42. Love, E. S. Introductory Considerations of Manned Reentry Orbital Vehicles. in *Joint Conf. on Lifting Manned Hypervelocity and Reentry vehicles, part 1* (ed. U.S.Air Force - National Aeronautics and Space Administration) (1960).

43. Mathauser, E. E. Materials for Application to Manned Reentry Vehicles. in *Joint Conference on Manned Hypervelocity and Reentry Vehicles: A Compilation of Papers Presented* (ed. U.S.Air Force - National Aeronautics and Space Administration) 559–570 (1960).

44. Vedula, V. M. *Ultra-High Temperature Ceramic-Ceramic Composites, Final Report on Project WRDC-TR-89-4089*. (1989).

45. Courtright, E. L., Graham, H. C., Katz, A. P. & Kerans, R. J. *Ultrahigh temperature Assessment Sudy - Ceramic Matrix Compsites, Final Report WL-TR-91-4061*. *Composites* (1992).

46. Mehrotra, G. M. *Chemical compatibility and oxidation resistance of potential matrix and reinforcement materials in ceramic composites for ultra-high temperature applications*. (1991).

47. Rasky, D., Bull, J. & Bull, J. *Ultra-High Temperature Ceramics*. (1994).

48. Opeka, M. M., Talmy, I. G., Wuchina, E. J., Zaykoski, J. A. & Causey, S. J. Mechanical, Thermal, and Oxidation Properties of Refractory Hafnium and zirconium Compounds. *J. Eur. Ceram. Soc.* **19**, 2405–2414 (1999).

49. Cutler, R. A. Engineering properties of borides. in *Ceramics and glasses, engineered materials handbook* vol. 4 787–803 (ASM International, Materials Park, 1991).

50. Hampshire, S. Engineering Properties of Nitrides. in *Engineered Materials Handbook.* vol. 4 812–820 (ASM International, 1991).

51. Shaffer, P. T. B. Engineering Properties of Carbides. in *Engineered Materials Handbook, Vol.4, Ceramics and Glasses* 804–811 (ASM International, 1991).

52. Fahrenholtz, W. G., Hilmas, G. E., Talmy, I. G. & Zaykoski, J. A. Refractory diborides of zirconium and hafnium. *J. Am. Ceram. Soc.* **90**, 1347–1364 (2007).

53. Heid, R. *et al.* Lattice dynamics and electron-phonon coupling in transition-metal diborides. *Phys. Rev. B* **67**, 180510 (2003).

54. Vajeeston, P., Ravindran, P., Ravi, C. & Asokamani, R. Electronic structure, bonding, and ground-state properties of AlB_2-type transition-metal diborides. *Phys. Rev. B - Condens. Matter Mater. Phys.* **63**, 045115 (2001).

55. Cottrell, A. H. Transition metal carbides with NaCl structure. *Mater. Sci. Technol.* **10**, 788–792 (2013).

56. Cottrell, A. H. Crystal structures of transition metal carbides. *Mater. Sci. Technol.* **11**, 329–333 (2013).

57. Lengauer, W. Transition Metal Carbides, Nitrides, and Carbonitrides. in *Handbook of Ceramic Hard Materials* (ed. Riedel, R.) 202–252 (Wiley-VCH Verlag GmbH, 2000). doi:10.1002/9783527618217.ch7.

58. Xu, C. *et al.* Revealing unusual rigid diamond net analogues in superhard titanium carbides. *RSC Adv.* **8**, 14479–14487 (2018).

59. Weinberger, C. R. & Thompson, G. B. Review of phase stability in the group IVB and VB transition-metal carbides. *J. Am. Ceram. Soc.* **101**, 4401–4424 (2018).

60. Bazhenov, A. S. & Honkala, K. Understanding Structure and Stability of Monoclinic Zirconia Surfaces from First-Principles Calculations. *Top. Catal. 2016 606* **60**, 382–391 (2016).

61. Yu, S. *et al.* First-principles study of Zr–N crystalline phases: phase stability, electronic and mechanical properties. *RSC Adv.* **7**, 4697–4703 (2017).

62. Friedrich, A., Winkler, B., Juarez-Arellano, E. A. & Bayarjargal, L. Synthesis of Binary Transition Metal Nitrides, Carbides and Borides from the Elements in the Laser-Heated Diamond Anvil Cell and Their Structure-Property Relations. *Materials (Basel).* **4**, 1648 (2011).

63. Wu, K. H., Jiang, Y., Jiao, S., Chou, K. C. & Zhang, G. H. Synthesis of high purity nano-sized transition-metal carbides. *J. Mater. Res. Technol.* **9**, 11778–11790 (2020).

64. Fang, Z. Z. *Sintering of Advanced Materials*. (Woodhead Publishing, 2010).

65. Sonber, J. K. & Suri, A. K. Synthesis and consolidation of zirconium diboride: review. *Adv. Appl. Ceram. Struct. Funct. Bioceram.* **110**, 321–334 (2013).

66. Kravchenko, S. E., Torbov, V. I. & Shilkin, S. P. Nanosized zirconium diboride: Synthesis and properties. *Russ. J. Inorg. Chem. 2011 564* **56**, 506–509 (2011).

67. Jung, E. Y., Kim, J. H., Jung, S. H. & Choi, S. C. Synthesis of ZrB_2 powders by carbothermal and borothermal reduction. *J. Alloys Compd.* **538**, 164–168 (2012).

68. Ortiz, A. L., Zamora, V. & Rodríguez-Rojas, F. A study of the oxidation of ZrB_2 powders during high-energy ball-milling in air. *Ceram. Int.* **38**, 2857–2863 (2012).

69. Chamberlain, A. L., Fahrenholtz, W. G. & Hilmas, G. E. Reactive hot pressing of zirconium diboride. *J. Eur. Ceram. Soc.* **29**, 3401–3408 (2009).

70. Guo, S. Q. Densification of ZrB_2-based composites and their mechanical and physical properties: A review. *J. Eur. Ceram. Soc.* **29**, 995–1011 (2009).

71. Sciti, D., Guicciardi, S., Bellosi, A. & Pezzotti, G. Properties of a pressureless-sintered ZrB_2-$MoSi_2$ ceramic composite. *J. Am. Ceram. Soc.* **89**, 2320–2322 (2006).

72. Sciti, D., Monteverde, F., Guicciardi, S., Pezzotti, G. & Bellosi, A. Microstructure and mechanical properties of ZrB_2-$MoSi_2$ ceramic composites produced by different sintering techniques. *Mater. Sci. Eng. A* **434**, 303–309 (2006).

73. Silvestroni, L. & Sciti, D. Effects of $MoSi_2$ additions on the properties of Hf- and Zr-B_2 composites produced by pressureless sintering. *Scr. Mater.* **57**, 165–168 (2007).

74. Silvestroni, L. & Sciti, D. Densification of ZrB_2-$TaSi_2$ and HfB_2-$TaSi_2$ ultra-high-temperature ceramic composites. *J. Am. Ceram. Soc.* **94**, 1920–1930 (2011).

75. Sciti, D., Silvestroni, L., Celotti, G., Melandri, C. & Guicciardi, S. Sintering and mechanical properties of ZrB_2-$TaSi_2$ and HfB_2-$TaSi_2$ ceramic composites. *J. Am.*

Ceram. Soc. **91**, 3285–3291 (2008).

76. Silvestroni, L., Kleebe, H. J., Lauterbach, S., Müllet, M. & Sciti, D. Transmission electron microscopy on Zr- and Hf-borldes with $MoSi_2$ addition: Densification mechanisms. *J. Mater. Res.* **25**, 828–834 (2010).

77. Gasch, M. *et al.* Processing, properties and arc jet oxidation of hafnium diboride/silicon carbide ultra high temperature ceramics. *J. Mater. Sci. 2004 3919* **39**, 5925–5937 (2004).

78. Monteverde, F. & Bellosi, A. Microstructure and Properties of an HfB_2-SiC Composite for Ultra High Temperature Applications. *Adv. Eng. Mater.* **6**, 331–336 (2004).

79. Monteverde, F. Beneficial effects of an ultra-fine α-SiC incorporation on the sinterability and mechanical properties of ZrB_2. *Appl. Phys. A 2005 822* **82**, 329–337 (2005).

80. Guicciardi, S., Sciti, D., Melandri, C. & Bellosi, A. Nanoindentation Characterization of Submicro- and Nano-Sized Liquid-Phase-Sintered SiC Ceramics. *J. Am. Ceram. Soc.* **87**, 2101–2107 (2004).

81. Sciti, D., Silvestroni, L., Medri, V. & Guicciardi, S. Pressureless sintered in situ toughened ZrB_2–SiC platelets ceramics. *J. Eur. Ceram. Soc.* **31**, 2145–2153 (2011).

82. Sciti, D., Melandri, C. & Bellosi, A. Properties of ZrB_2-Reinforced Ternary Composites. *Adv. Eng. Mater.* **6**, 775–781 (2004).

83. Medri, V., Sciti, D., Dalle Fabbriche, D., Piancastelli, A. & Landi, E. Ice templating of ZrB_2-SiC systems. *Ceram. Int.* **41**, 10324–10330 (2015).

84. Sciti, D., Winterhalter, F. & Bellosi, A. Oxidation behaviour of a pressureless sintered AlN-SiC composite. *J. Mater. Sci. 2004 3923* **39**, 6965–6973 (2004).

85. Sciti, D., Guicciardi, S. & Silvestroni, L. Are short Hi-Nicalon SiC fibers a secondary or a toughening phase for ultra-high temperature ceramics? *Mater. Des.* **55**, 821–829 (2014).

86. Silvestroni, L. & Sciti, D. Oxidation of ZrB_2 ceramics containing SiC as particles, whiskers, or short fibers. *J. Am. Ceram. Soc.* **94**, 2796–2799 (2011).

87. Silvestroni, L. & Sciti, D. Microstructure and properties of pressureless sintered ZrC-based materials. *J. Mater. Res. 2008 237* **23**, 1882–1889 (2008).

88. Silvestroni, L., Sciti, D., Kling, J., Lauterbach, S. & Kleebe, H. J. Sintering mechanisms of zirconium and hafnium carbides doped with $MoSi_2$. *J. Am. Ceram. Soc.* **92**, 1574–1579 (2009).

89. Silvestroni, L. & Sciti, D. Transmission electron microscopy on Hf- and Ta-carbides sintered with $TaSi_2$. *J. Eur. Ceram. Soc.* **31**, 3033–3043 (2011).

90. Sciti, D., Silvestroni, L., Guicciardi, S., Fabbriche, D. D. & Bellosi, A. Processing,

mechanical properties and oxidation behavior of TaC and HfC composites containing 15 vol% $TaSi_2$ or $MoSi_2$. *J. Mater. Res.* **24**, 2056–2065 (2009).

91. Charpentier, L., Balat-Pichelin, M., Bêche, E., Sciti, D. & Silvestroni, L. Microstructural characterization of ZrC-$MoSi_2$ composites oxidized in air at high temperatures. *Appl. Surf. Sci.* **283**, 751–758 (2013).

92. Sonber, J. K., Murthy, T. S. R. C., Subramanian, C., Hubli, R. C. & Suri, A. K. Processing methods for ultra-high temperature ceramics. in *MAX Phases and Ultra-High Temperature Ceramics for Extreme Environments* 180–202 (2013). doi:10.4018/978-1-4666-4066-5.ch006.

93. Sciti, D., Brach, M. & Bellosi, A. Oxidation behavior of a pressureless sintered ZrB2-MoSi2 ceramic composite. *J. Mater. Res.* **20**, 922–930 (2005).

94. Sciti, D., Silvestroni, L. & Bellosi, A. High-density pressureless-sintered HfC-based composites. *J. Am. Ceram. Soc.* **89**, 2668–2670 (2006).

95. Sciti, D., Balbo, A. & Bellosi, A. Oxidation behaviour of a pressureless sintered HfB_2-$MoSi_2$ composite. *J. Eur. Ceram. Soc.* **29**, 1809–1815 (2009).

96. Silvestroni, L., Sciti, D. & Bellosi, A. Microstructure and properties of pressureless sintered HfB_2-based composites with additions of ZrB_2 or HfC. *Adv. Eng. Mater.* **9**, 915–920 (2007).

97. Balbo, A. & Sciti, D. Spark plasma sintering and hot pressing of ZrB_2-$MoSi_2$ ultra-high-temperature ceramics. *Mater. Sci. Eng. A* **475**, 108–112 (2008).

98. Sciti, D., Guicciardi, S. & Nygren, M. Spark plasma sintering and mechanical behaviour of ZrC-based composites. *Scr. Mater.* **59**, 638–641 (2008).

99. Bellosi, A., Monteverde, F. & Sciti, D. Fast densification of ultra-high-temperature ceramics by spark plasma sintering. *Int. J. Appl. Ceram. Technol.* **3**, 32–40 (2006).

100. Sciti, D., Silvestroni, L. & Nygren, M. Spark plasma sintering of Zr- and Hf-borides with decreasing amounts of $MoSi_2$ as sintering aid. *J. Eur. Ceram. Soc.* **28**, 1287–1296 (2008).

101. Sciti, D., Bonnefont, G., Fantozzi, G. & Silvestroni, L. Spark plasma sintering of HfB_2 with low additions of silicides of molybdenum and tantalum. *J. Eur. Ceram. Soc.* **30**, 3253–3258 (2010).

102. Grasso, S. *et al.* Flash Spark Plasma Sintering (FSPS) of Pure ZrB_2. *J. Am. Ceram. Soc.* **97**, 2405–2408 (2014).

103. Licheri, R., Orrù, R., Musa, C., Locci, A. M. & Cao, G. Spark plasma sintering of UHTC powders obtained by self-propagating high-temperature synthesis. *J. Mater. Sci. 2008 4319* **43**, 6406–6413 (2008).

104. Ghaffari, S. A., Faghihi-Sani, M. A., Golestani-Fard, F. & Mandal, H. Spark plasma sintering of TaC–HfC UHTC via disilicides sintering aids. *J. Eur. Ceram. Soc.* **33**, 1479–1484 (2013).

105. Failla, S., Fu, S., Sciti, D. & Grasso, S. Flash spark plasma sintering of pure TiB_2. *Open Ceram.* **5**, 100075 (2021).

106. Sciti, D., Guicciardi, S. & Nygren, M. Densification and mechanical behavior of HfC and HfB_2 fabricated by spark plasma sintering. *J. Am. Ceram. Soc.* **91**, 1433–1440 (2008).

107. Sciti, D. & Nygren, M. Spark plasma sintering of ultra refractory compounds. *J. Mater. Sci.* **43**, 6414–6421 (2008).

108. Low, I. M., Sakka, Y. & Hu, C. F. *MAX phases and ultra-high temperature ceramics for extreme environments*. (IGI Global, 2013). doi:10.4018/978-1-4666-4066-5.

109. Chamberlain, A. L., Fahrenholtz, W. G., Hilmas, G. E. & Ellerby, D. T. Characterization of zirconium diboride for thermal protection systems. *Key Eng. Mater.* **264**–**268**, 493–496 (2004).

110. Chamberlain, A. L., Fahrenholtz, W. G., Hilmas, G. E. & Ellerby, D. T. High-Strength Zirconium Diboride-Based Ceramics. *J. Am. Ceram. Soc.* **87**, 1170–1172 (2004).

111. Rezaie, A., Fahrenholtz, W. G. & Hilmas, G. E. Effect of hot pressing time and temperature on the microstructure and mechanical properties of ZrB_2–SiC. *J. Mater. Sci. 2006 428* **42**, 2735–2744 (2007).

112. Telle, R., Sigl, L. S. & Takagi, K. Boride-Based Hard Materials. in *Handbook of Ceramic Hard Materials* 802–945 (John Wiley & Sons, Ltd, 2008). doi:10.1002/9783527618217.CH22.

113. Watts, J., Hilmas, G. & Fahrenholtz, W. G. Mechanical Characterization of ZrB_2–SiC Composites with Varying SiC Particle Sizes. *J. Am. Ceram. Soc.* **94**, 4410–4418 (2011).

114. Zhu, S., Fahrenholtz, W. G. & Hilmas, G. E. Influence of silicon carbide particle size on the microstructure and mechanical properties of zirconium diboride–silicon carbide ceramics. *J. Eur. Ceram. Soc.* **27**, 2077–2083 (2007).

115. Liu, Q., Han, W. & Han, J. Influence of SiCnp content on the microstructure and mechanical properties of ZrB_2–SiC nanocomposite. *Scr. Mater.* **63**, 581–584 (2010).

116. Okamoto, N. L. *et al.* Temperature dependence of thermal expansion and elastic constants of single crystals of ZrB_2 and the suitability of ZrB2 as a substrate for GaN film. *J. Appl. Phys.* **93**, 88–93 (2003).

117. Zhu, S. Densification, microstructure, and mechanical properties of zirconium diboride based ultra-high temperature ceramics. *PhD Thesis* (Missouri University of Science and Technology, Rolla (MO), 2008). doi:10.2/JQUERY.MIN.JS.

118. Neuman, E. W., Hilmas, G. E. & Fahrenholtz, W. G. Strength of Zirconium Diboride to 2300°C. *J. Am. Ceram. Soc.* **96**, 47–50 (2013).

119. Rhodes, W. H., Clougherty, E. V. & Kalish, D. *Research and Development of*

Refractory Oxidation-Resistant Diborides. Part II, Volume IV: Mechanical Properties. https://apps.dtic.mil/sti/citations/AD0865809 (1970).

120. Zou, J. *et al.* High-temperature bending strength, internal friction and stiffness of ZrB_2–20 vol% SiC ceramics. *J. Eur. Ceram. Soc.* **32**, 2519–2527 (2012).

121. Zhang, S. C., Hilmas, G. E. & Fahrenholtz, W. G. Zirconium Carbide–Tungsten Cermets Prepared by In Situ Reaction Sintering. *J. Am. Ceram. Soc.* **90**, 1930–1933 (2007).

122. Parthasarathy, T. A., Rapp, R. A., Opeka, M. & Kerans, R. J. A Model for Transitions in Oxidation Regimes of ZrB_2. *Mater. Sci. Forum* **595**–**598**, 595–832 (2008).

123. Parthasarathy, T. A., Rapp, R. A., Opeka, M. & Kerans, R. J. A model for the oxidation of ZrB_2, HfB_2 and TiB_2. *Acta Mater.* **55**, 5999–6010 (2007).

124. Sarin, P. *et al.* In situ studies of oxidation of ZrB_2 and ZrB_2-SiC composites at high temperatures. *J. Eur. Ceram. Soc.* **30**, 2375–2386 (2010).

125. Gangireddy, S., Karlsdottir, S. N., Norton, S. J., Tucker, J. C. & Halloran, J. W. In situ microscopy observation of liquid flow, zirconia growth, and CO bubble formation during high temperature oxidation of zirconium diboride-silicon carbide. *J. Eur. Ceram. Soc.* **30**, 2365–2374 (2010).

126. Hu, P., Zhang, X. H., Han, J. C., Luo, X. G. & Du, S. Y. Effect of Various Additives on the Oxidation Behavior of ZrB_2-Based Ultra-High-Temperature Ceramics at 1800°C. *J. Am. Ceram. Soc.* **93**, 345–349 (2010).

127. Silvestroni, L., Meriggi, G. & Sciti, D. Oxidation behavior of ZrB_2 composites doped with various transition metal silicides. *Corros. Sci.* **83**, 281–291 (2014).

128. Pastor, H. & Meyer, R. An investigation of the effect of additions of metal silicides on titanium and zirconium borides from the point of view of their sintering behaviour and their resistance to oxidation at high temperature. *Rev. Int. des Hautes Temp. des Refract.* **11**, 41–54 (1974).

129. Talmy, I. G., Zaykoski, J. A. & Opeka, M. M. High-Temperature Chemistry and Oxidation of ZrB_2 Ceramics Containing SiC, Si_3N_4, Ta_5Si_3, and $TaSi_2$. *J. Am. Ceram. Soc.* **91**, 2250–2257 (2008).

130. Cissel, K. S. & Opila, E. Oxygen diffusion mechanisms during high-temperature oxidation of ZrB_2-SiC. *J. Am. Ceram. Soc.* **101**, 1765–1779 (2018).

131. Levine, S. R. *et al.* Evaluation of ultra-high temperature ceramics for aeropropulsion use. *J. Eur. Ceram. Soc.* **22**, 2757–2767 (2002).

132. Silvestroni, L., Stricker, K., Sciti, D. & Kleebe, H. J. Understanding the oxidation behavior of a ZrB_2–$MoSi_2$ composite at ultra-high temperatures. *Acta Mater.* **151**, 216–228 (2018).

133. Zhao, L., Jia, D., Duan, X., Yang, Z. & Zhou, Y. Oxidation of ZrC–30 vol% SiC

composite in air from low to ultrahigh temperature. *J. Eur. Ceram. Soc.* **32**, 947–954 (2012).

134. Savino, R., De Stefano Fumo, M., Silvestroni, L. & Sciti, D. Arc-jet testing on HfB_2 and HfC-based ultra-high temperature ceramic materials. *J. Eur. Ceram. Soc.* **28**, 1899–1907 (2008).

135. Zhang, X., Hu, P., Han, J. & Meng, S. Ablation behavior of ZrB_2–SiC ultra high temperature ceramics under simulated atmospheric re-entry conditions. *Compos. Sci. Technol.* **68**, 1718–1726 (2008).

136. Savino, R., Festa, G., Cecere, A., Pienti, L. & Sciti, D. Experimental set up for characterization of carbide-based materials in propulsion environment. *J. Eur. Ceram. Soc.* **35**, 1715–1723 (2015).

137. Pienti, L., Sciti, D., Silvestroni, L., Cecere, A. & Savino, R. Ablation tests on HfC- and TaC-based ceramics for aeropropulsive applications. *J. Eur. Ceram. Soc.* **35**, 1401–1411 (2015).

138. Grimvall, G. & Guillermet, A. F. Phase stability properties of transition metal diborides. in *AIP Conference Proceedings* vol. 231 423 (American Institute of PhysicsAIP, 2008).

139. Chant, I. & Murty, K. L. Structural materials issues for the next generation fission reactors. *JOM* **62**, 67–74 (2010).

140. Basu, B., Raju, G. B. & Suri, A. K. Processing and properties of monolithic TiB_2 based materials. *Int. Mater. Rev.* **51**, 352–374 (2006).

141. Hou, Y. T. *et al.* High performance tantalum carbide metal gate stacks for nMOSFET application. in *Technical Digest - International Electron Devices Meeting, IEDM* vol. 2005 31–34 (2005).

142. Wuchina, E. *et al.* Designing for ultrahigh-temperature applications: The mechanical and thermal properties of HfB_2, HfC_x , HfN_x and αHf(N). *J. Mater. Sci. 2004 3919* **39**, 5939–5949 (2004).

143. Milek, J. T. Silicon Nitride for Microelectronic Applications. in *Silicon Nitride for Microelectronic Applications* (ed. Milek, J. T.) (Springer US, 1971). doi:10.1007/978-1-4684-6162-6.

144. Sciti, D., Silvestroni, L., Monteverde, F., Vinci, A. & Zoli, L. Introduction to H2020 project C3HARME–next generation ceramic composites for combustion harsh environment and space. *Adv. Appl. Ceram.* **117**, s70–s75 (2018).

145. Van Wie, D. M., Drewry, D. G., King, D. E. & Hudson, C. M. The hypersonic environment: Required operating conditions and design challenges. *J. Mater. Sci. 2004 3919* **39**, 5915–5924 (2004).

146. Shirvanimoghaddam, K. *et al.* Carbon fiber reinforced metal matrix composites: Fabrication processes and properties. *Compos. Part A Appl. Sci. Manuf.* **92**, 70–96

(2017).

147. May, M., Rupakula, G. D. & Matura, P. Non-polymer-matrix composite materials for space applications. *Compos. Part C Open Access* **3**, 100057 (2020).

148. Wang, X. *et al.* Advances in modifications and high-temperature applications of silicon carbide ceramic matrix composites in aerospace: A focused review. *J. Eur. Ceram. Soc.* **41**, 4671–4688 (2021).

149. Triantou, K. *et al.* Thermo-mechanical performance of an ablative/ceramic composite hybrid thermal protection structure for re-entry applications. *Compos. Part B Eng.* **82**, 159–165 (2015).

150. Triantou, K. I. *et al.* Thermal shock performance of carbon-bonded carbon fiber composite and ceramic matrix composite joints for thermal protection re-entry applications. *Compos. Part B Eng.* **111**, 270–278 (2017).

151. Yang, X., Wei, L., Song, W., Bi-Feng, Z. & Zhao-Hui, C. ZrB2/SiC as a protective coating for C/SiC composites: Effect of high temperature oxidation on mechanical properties and anti-ablation property. *Compos. Part B Eng.* **45**, 1391–1396 (2013).

152. Luo, L. *et al.* Carbon fiber reinforced silicon carbide composite-based sharp leading edges in high enthalpy plasma flows. *Compos. Part B Eng.* **135**, 35–42 (2018).

153. Dassios, K. G., Aggelis, D. G., Kordatos, E. Z. & Matikas, T. E. Cyclic loading of a SiC-fiber reinforced ceramic matrix composite reveals damage mechanisms and thermal residual stress state. *Compos. Part A Appl. Sci. Manuf.* **44**, 105–113 (2013).

154. Shimoda, K., Hinoki, T. & Park, Y. H. Development of non-brittle fracture in SiCf/SiC composites without a fiber/matrix interface due to the porous structure of the matrix. *Compos. Part A Appl. Sci. Manuf.* **115**, 397–404 (2018).

155. Al-Dawery, I. A. H. & Butler, E. G. Fabrication of high-temperature resistant oxide ceramic matrix composites. *Compos. - Part A Appl. Sci. Manuf.* **32**, 1007–1012 (2001).

156. Naslain, R. R. The design of the fibre-matrix interfacial zone in ceramic matrix composites. *Compos. Part A Appl. Sci. Manuf.* **29**, 1145–1155 (1998).

157. Zoli, L. *et al.* Ultra-High Temperature Ceramic Matrix Composites. *Encyclopedia of Materials: Technical Ceramics and Glasses* 340–352 (2021) doi:10.1016/b978-0-12-818542-1.00023-0.

158. Pienti, L., Sciti, D., Silvestroni, L. & Guicciardi, S. Effect of milling on the mechanical properties of chopped SiC fiber-reinforced ZrB_2. *Materials (Basel).* **6**, 1980–1993 (2013).

159. Sciti, D., Pienti, L., Fabbriche, D. D., Guicciardi, S. & Silvestroni, L. Combined effect

of SiC chopped fibers and SiC whiskers on the toughening of ZrB_2. *Ceram. Int.* **40**, 4819–4826 (2014).

160. Sciti, D. & Silvestroni, L. Processing, sintering and oxidation behavior of SiC fibers reinforced ZrB_2 composites. *J. Eur. Ceram. Soc.* **32**, 1933–1940 (2012).

161. Sciti, D. *et al.* From random chopped to oriented continuous SiC fibers-ZrB_2 composites. *Mater. Des.* **63**, 464–470 (2014).

162. Sciti, D., Natali Murri, A., Medri, V. & Zoli, L. Continuous C fibre composites with a porous ZrB_2 Matrix. *Mater. Des.* **85**, 127–134 (2015).

163. Zoli, L., Medri, V., Melandri, C. & Sciti, D. Continuous SiC fibers-ZrB_2 composites. *J. Eur. Ceram. Soc.* **35**, 4371–4376 (2015).

164. Zoli, L. & Sciti, D. Efficacy of a ZrB_2–SiC matrix in protecting C fibres from oxidation in novel UHTCMC materials. *Mater. Des.* **113**, 207–213 (2017).

165. Sciti, D. *et al.* Effect of PAN-based and pitch-based carbon fibres on microstructure and properties of continuous C_f/ZrB_2-SiC UHTCMCs. *J. Eur. Ceram. Soc.* **41**, 3045–3050 (2021).

166. Zoli, L. *et al.* Rapid spark plasma sintering to produce dense UHTCs reinforced with undamaged carbon fibres. *Mater. Des.* **130**, 1–7 (2017).

167. Zoli, L. *et al.* Is spark plasma sintering suitable for the densification of continuous carbon fibre - UHTCMCs? *J. Eur. Ceram. Soc.* **40**, 2597–2603 (2020).

168. Sciti, D. *et al.* Properties of large scale ultra-high temperature ceramic matrix composites made by filament winding and spark plasma sintering. *Compos. Part B Eng.* **216**, 108839 (2021).

169. Vinci, A., Zoli, L., Sciti, D., Melandri, C. & Guicciardi, S. Understanding the mechanical properties of novel UHTCMCs through random forest and regression tree analysis. *Mater. Des.* **145**, 97–107 (2018).

170. Vinci, A. *et al.* Mechanical behaviour of carbon fibre reinforced TaC/SiC and ZrC/SiC composites up to 2100°C. *J. Eur. Ceram. Soc.* **39**, 780–787 (2019).

171. Vinci, A. *et al.* Influence of fibre content on the strength of carbon fibre reinforced HfC/SiC composites up to 2100 °C. *J. Eur. Ceram. Soc.* **39**, 3594–3603 (2019).

172. Vinci, A., Zoli, L., Galizia, P. & Sciti, D. Influence of Y_2O_3 addition on the mechanical and oxidation behaviour of carbon fibre reinforced ZrB_2/SiC composites. *J. Eur. Ceram. Soc.* **40**, 5067–5075 (2020).

173. Chen, B. W. *et al.* Ablation behavior of C_f/ZrC-SiC-based composites fabricated by an improved reactive melt infiltration. *J. Eur. Ceram. Soc.* **39**, 4617–4624 (2019).

174. Xu, Y. *et al.* Ablation properties of C/C-UHTCs and their preparation by reactive infiltration of K_2MeF_6 (Me = Zr, Ti) molten salt. *J. Eur. Ceram. Soc.* **41**, 5405–5416

(2021).

175. Kütemeyer, M., Schomer, L., Helmreich, T., Rosiwal, S. & Koch, D. Fabrication of ultra high temperature ceramic matrix composites using a reactive melt infiltration process. *J. Eur. Ceram. Soc.* **36**, 3647–3655 (2016).

176. Vinci, A. *et al.* Reactive melt infiltration of carbon fibre reinforced ZrB_2/B composites with Zr_2Cu. *Compos. Part A Appl. Sci. Manuf.* **137**, (2020).

177. Chen, X. *et al.* Microstructure and mechanical properties of three dimensional C_f/SiC-ZrC-ZrB_2 composites prepared by reactive melt infiltration method. *J. Eur. Ceram. Soc.* **36**, 3969–3976 (2016).

178. Tatarko, P. *et al.* Design of Lu_2O_3-reinforced C_f/SiC-ZrB_2-ZrC ultra-high temperature ceramic matrix composites: Wetting and interfacial reactivity by ZrSi2 based alloys. *J. Eur. Ceram. Soc.* **41**, 3051–3060 (2021).

179. Binner, J. *et al.* Selection, processing, properties and applications of ultra-high temperature ceramic matrix composites, UHTCMCs–a review. *Int. Mater. Rev.* **0**, 1–56 (2019).

180. Rubio, V. *et al.* Materials characterisation and mechanical properties of C_f-UHTC powder composites. *J. Eur. Ceram. Soc.* **39**, 813–824 (2019).

181. Paul, A. *et al.* UHTC-carbon fibre composites: Preparation, oxyacetylene torch testing and characterisation. *J. Eur. Ceram. Soc.* **33**, 423–432 (2013).

182. Hu, H. *et al.* Preparation and characterization of C/SiC-ZrB_2 composites by precursor infiltration and pyrolysis process. *Ceram. Int.* **36**, 1011–1016 (2010).

183. Li, Q., Dong, S., Wang, Z. & Shi, G. Fabrication and properties of 3-D C_f/ZrB_2-ZrC-SiC composites via polymer infiltration and pyrolysis. *Ceram. Int.* **39**, 5937–5941 (2013).

184. Uhlmann, F. *et al.* Preparation and characterization of ZrB_2 and TaC containing C_f/SiC composites via Polymer-Infiltration-Pyrolysis process. *J. Eur. Ceram. Soc.* **37**, 1955–1960 (2017).

185. Galizia, P., Sciti, D. & Jain, N. Insight into microstructure and flexural strength of ultra-high temperature ceramics enriched SICARBON^{TM} composite. *Mater. Des.* **208**, 109888 (2021).

186. Ionescu, E. *et al.* Polymer-Derived Ultra-High Temperature Ceramics (UHTCs) and Related Materials. *Adv. Eng. Mater.* **21**, 1900269 (2019).

187. Li, K. Z., Jing, X., Qian-Gang, F., He-Jun, L. & Ling-Jun, G. Effects of porous C/C density on the densification behavior and ablation property of C/C–ZrC–SiC composites. *Carbon N. Y.* **57**, 161–168 (2013).

188. RAN, L. ping, RAO, F., PENG, K., YIN, H. & YI, M. zhong. Preparation and properties of C/C−ZrB_2−SiC composites by high-solid-loading slurry impregnation and polymer infiltration and pyrolysis (PIP). *Trans. Nonferrous Met. Soc. China* **29**,

2141–2150 (2019).

189. Gu, J. *et al.* Fast fabrication of SiC particulate-reinforced SiC composites by modified PIP process using spark plasma sintering – effects of green density and heating rate. *J. Eur. Ceram. Soc.* **41**, 4037–4047 (2021).

190. Rueschhoff, L. M., Carney, C. M., Apostolov, Z. D. & Cinibulk, M. K. Processing of fiber-reinforced ultra-high temperature ceramic composites: A review. *Int. J. Ceram. Eng. Sci.* **2**, 22–37 (2020).

191. Zhao, D., Hu, H., Zhang, C., Zhang, Y. & Wang, J. A simple way to prepare precursors for zirconium carbide. *J. Mater. Sci. 2010 4523* **45**, 6401–6405 (2010).

192. Sacks, M. D., Wang, C. A., Yang, Z. & Jain, A. Carbothermal reduction synthesis of nanocrystalline zirconium carbide and hafnium carbide powders using solution-derived precursors. *J. Mater. Sci. 2004 3919* **39**, 6057–6066 (2004).

193. Tao, X. Y., Qiu, W. F., Li, H. & Zhao, T. One pot synthesis of a soluble polymer for zirconium carbide. *Chinese Chem. Lett.* **21**, 620–623 (2010).

194. Yan, C., Liu, R., Cao, Y., Zhang, C. & Zhang, D. Carbothermal Synthesis of Submicrometer Zirconium Carbide from Polyzirconoxane and Phenolic Resin by the Facile One-Pot Reaction. *J. Am. Ceram. Soc.* **95**, 3366–3369 (2012).

195. Dong, Z. *et al.* Synthesis and pyrolysis behavior of a soluble polymer precursor for ultra-fine zirconium carbide powders. *Ceram. Int.* **41**, 7359–7365 (2015).

196. Wang, J. X. *et al.* Synthesis of nanocrystallized zirconium carbide based on an aqueous solution-derived precursor. *RSC Adv.* **7**, 22722–22727 (2017).

197. Xie, Z., Zhou, T. & Gou, Y. Synthesis and characterization of zirconium diboride ceramic precursor. *Ceram. Int.* **41**, 6226–6231 (2015).

198. Ionescu, E. *et al.* Phase separation of a hafnium alkoxide-modified polysilazane upon polymer-to-ceramic transformation-A case study. *J. Eur. Ceram. Soc.* **32**, 1873–1881 (2012).

199. Yuan, J. *et al.* Single-source-precursor synthesis of hafnium-containing ultrahigh-temperature ceramic nanocomposites (UHTC-NCs). *Inorg. Chem.* **53**, 10443–10455 (2014).

200. Feng, B. *et al.* High-temperature phase and microstructure evolution of polymer-derived SiZrCN and SiZrBCN ceramic nanocomposites. *J. Am. Ceram. Soc.* **103**, 7001–7013 (2020).

201. Mera, G., Gallei, M., Bernard, S. & Ionescu, E. Ceramic Nanocomposites from Tailor-Made Preceramic Polymers. *Nanomaterials* **5**, 468 (2015).

202. Binner, J. *et al.* Selection, processing, properties and applications of ultra-high temperature ceramic matrix composites, UHTCMCs–a review. *Int. Mater. Rev.* **65**, 389–444 (2020).

203. Xie, J., Li, K., Li, H., Fu, Q. & Guo, L. Ablation behavior and mechanism of C/C–ZrC–SiC composites under an oxyacetylene torch at 3000 °C. *Ceram. Int.* **39**, 4171–4178 (2013).

204. Huang, D., Zhang, M., Huang, Q., Wang, L. & Tong, K. Mechanical Property, Oxidation and Ablation Resistance of C/C–ZrB_2–ZrC–SiC Composite Fabricated by Polymer Infiltration and Pyrolysis with Preform of Cf/ZrB2. *J. Mater. Sci. Technol.* **33**, 481–486 (2017).

205. Galizia, P. *et al.* Retained strength of UHTCMCs after oxidation at 2278 K. *Compos. Part A Appl. Sci. Manuf.* **149**, 106523 (2021).

206. Zoli, L., Vinci, A., Galizia, P., Melandri, C. & Sciti, Di. On the thermal shock resistance and mechanical properties of novel unidirectional UHTCMCs for extreme environments. *Sci. Rep.* **8**, 1–9 (2018).

207. Hu, P., Gui, K., Yang, Y., Dong, S. & Zhang, X. Effect of SiC Content on the Ablation and Oxidation Behavior of ZrB_2-Based Ultra High Temperature Ceramic Composites. *Materials (Basel).* **6**, 1730 (2013).

208. Zhou, H., Gao, L., Wang, Z. & Dong, S. ZrB_2 -SiC Oxidation Protective Coating on C/C Composites Prepared by Vapor Silicon Infiltration Process. *J. Am. Ceram. Soc.* **93**, 915–919 (2010).

209. Haibo, O. *et al.* Self-healing ZrB_2–SiO_2 oxidation resistance coating for SiC coated carbon/carbon composites. *Corros. Sci.* **110**, 265–272 (2016).

210. Corral, E. L. & Loehman, R. E. Ultra-high-temperature ceramic coatings for oxidation protection of carbon-carbon composites. *J. Am. Ceram. Soc.* **91**, 1495–1502 (2008).

211. Tang, S., Deng, J., Wang, S. & Liu, W. Fabrication and Characterization of an Ultra-High-Temperature Carbon Fiber-Reinforced ZrB_2-SiC Matrix Composite. *J. Am. Ceram. Soc.* **90**, 3320–3322 (2007).

212. Liu, L. *et al.* Ablation in different heat fluxes of C/C composites modified by ZrB_2-ZrC and ZrB_2-ZrC-SiC particles. *Corros. Sci.* **74**, 159–167 (2013).

213. Wang, Y., Liu, W., Cheng, L. & Zhang, L. Preparation and properties of 2D C/ZrB_2-SiC ultra high temperature ceramic composites. *Mater. Sci. Eng. A* **524**, 129–133 (2009).

214. Vinci, A., Zoli, L., Landi, E. & Sciti, D. Oxidation behaviour of a continuous carbon fibre reinforced ZrB_2–SiC composite. *Corros. Sci.* **123**, 129–138 (2017).

215. Vinci, A., Zoli, L. & Sciti, D. Influence of SiC content on the oxidation of carbon fibre reinforced ZrB_2/SiC composites at 1500 and 1650 °C in air. *J. Eur. Ceram. Soc.* **38**, 3767–3776 (2018).

216. Mungiguerra, S. *et al.* Arc-jet wind tunnel characterization of ultra-high-temperature ceramic matrix composites. *Corros. Sci.* **149**, 18–28 (2019).

217. Mungiguerra, S. *et al.* Ultra-high-temperature testing of sintered ZrB_2-based ceramic composites in atmospheric re-entry environment. *Int. J. Heat Mass Transf.* **156**, (2020).

218. Mungiguerra, S. *et al.* Characterization of novel ceramic composites for rocket nozzles in high-temperature harsh environments. *Int. J. Heat Mass Transf.* **163**, 120492 (2020).

219. Sciti, D. *et al.* Design, fabrication and high velocity oxy-fuel torch tests of a C_f-ZrB_2- fiber nozzle to evaluate its potential in rocket motors. *Mater. Des.* **109**, 709–717 (2016).

220. Baker, B. *et al.* Ablation behaviour of carbon fibre ultra-high temperature composites at oblique angles of attack. *Mater. Des.* **212**, 110199 (2021).

221. Savino, R., Mungiguerra, S. & Di Martino, G. D. Testing ultra-high-temperature ceramics for thermal protection and rocket applications. *Adv. Appl. Ceram. Struct. Funct. Bioceram.* **117**, s9–s18 (2018).

3. Experimental

3.1 Manufacturing of UHTCMCs

CNR-ISTEC possesses facilities and know-how for the design, manufacturing and characterization of Ultra-High Temperature Ceramic Matrix Composites (UHTCMCs). In these last few years, the fabrication of UHTCMCs performed at ISTEC has relied on slurry infiltration and consolidation by sintering [1–10].

This Ph.D. research was focused on the development of novel processing routes based on Polymer Infiltration and Pyrolysis (PIP) technique to produce continuous carbon fibre-reinforced ZrB_2/SiC composites. Two different processing approaches were studied: i) a water-based UHTC powder slurry infiltration followed by polymer infiltration and pyrolysis (PIP) cycles, ii) a water-based UHTC powder slurry infiltration, then consolidation by coupling Polymer Infiltration and Pyrolysis (PIP) and Hot Pressing (HP) techniques. Both processing modes require several separate stages which will be explained in detail below in this chapter. Experimental procedures of some of these steps (i.e. powder treatment, preparation of the slurry, slurry infiltration and sintering) are the result of previous studies conducted at ISTEC and will be illustrated on the basis of previous works [1–3,5,11–13].

3.1.1 Materials

Commercial products were used as raw materials for the preparation of ceramic matrix composites.

Ceramic powders:

- ZrB_2 (Grade B, H.C. Starck, Germany; specific surface area 1.0 m^2/g, particle size range 0.5–6 µm, impurities (wt%): 0.25 C, 2 O, 0.25 N, 0.1 Fe, 0.2 Hf);
- α-SiC (Grade UF-25, H.C. Starck, Germany; specific surface area 23–26 m^2/g, D_{50} 0.45 µm, impurities (wt%): 2.5 O).

Preceramic polymer of SiC:

- allyl-hydrido polycarbosilane (StarPCS™ SMP-10, Starfire System Inc., U.S.A; density 0.998 g/cm^3, viscosity 40–100 cPs at 25 °C).

Part of the content of this chapter has been published in Journal of the European Ceramic Society 40 (2020) 5076–5084 as "*F. Servadei, L. Zoli, P. Galizia, A. Vinci, D. Sciti, Development of UHTCMCs via water based ZrB_2 powder slurry infiltration and polymer infiltration and pyrolysis*" and in Journal of the European Ceramic Society 42 (2022) 2118–2126 as "*F. Servadei, L. Zoli, P. Galizia, A. Vinci, D. Sciti, Development of UHTCMCs via water based ZrB_2 powder slurry infiltration and polymer infiltration and pyrolysis*".

Catalyst:

- trimethyl(methylcyclopentadienyl)platinum(IV), $MePtCpMe_3$ (Sigma Aldrich; purity 98%);
- dicumyl peroxide (DCP), $[C_6H_5C(CH_3)_2]_2O_2$ (Sigma Aldrich; purity 98%).

Fibres:

- unidirectional (UD) pitch based ultra-high modulus carbon fibre fabrics (UF-XN80-300, Granoc, Japan; fabric areal weight 330 g/m^2; yarn: XN80-60S, tensile modulus 780 GPa, tensile strength 3.4 GPa, fibre diameter 10 µm, density 2.17 g/cm^3);
- plain-woven (2D) pitch-based ultra-high modulus carbon fibre fabrics (PF-XN80-240, Granoc, Japan; fabric areal weight 240 g/m^2; yarn: XN80-60S, tensile modulus 780 GPa, tensile strength 3.4 GPa, fibre diameter 10 µm, density 2.17 g/cm^3);
- twill-woven (2D) PAN-based carbon fibre fabrics (GG 301 T, 2x2 Twill, Angeloni, Italy; fabric areal weight 300 g/m^2, 6 K);
- plain-woven (2D) pitch-based ultra-high modulus carbon fibre and PAN-based carbon fibre fabrics (custom made for ISTEC, Angeloni, Italy; Granoc XN80/12K Tenax);
- 2.5D needled PANOX carbon fibre preform (Surface Transforms, UK; fibre volume fraction 23%, density 0.37 g cm^{-3}).

Solvents:

- ethanol, CH_3CH_2OH (Merck; absolute, purity: ≥ 99.5 %);
- tetrahydrofuran (THF), $(CH_2)_3CH_2O$ (Sigma Aldrich; anhydrous, purity: ≥ 99.9 %, inhibitor-free).

3.1.1.1 Allyl-hydrido polycarbosilane

A commercially available allyl-hydrido polycarbosilane (AHPCS), StarPCS™ SMP-10 acquired from Starfire® Systems Inc. (Schenectady, NY, U.S.A.), was used for the preparation of continuous fibre-reinforced ZrB_2-SiC composites. SMP-10 is in the form of clear, amber-coloured, viscous liquid at room temperature (see properties in Table 3.1 [14]). It is the only commercial liquid precursor of SiC ceramics which requires no solvents or the need to be melted for processing, thus offering ease of use and reduction in manufacturing cycle times.

Table 3.1. Properties of allyl-hydrido polycarbosilane StarPCS™ SMP-10 as obtained from Starfire Systems datasheet [14].

Properties of StarPCS™ SMP-10	
Density	0.998 g/cm^3
Appearance	Clear, amber liquid
Viscosity	40 to 100 cPs at 25 °C
Compatible solvents	Hexanes, Tetrahydrofuran, Toluene; Insoluble in water
Flash Point	89 °C
Moisture absorption	<0.1% in 24 hours at room temperature
Surface tension	30 dynes/cm^2
Odour	None
DOT/IATA Regulations	Non hazardous
Storage	Vacuum container or inert environment; Refrigerated

This highly branched allyl-substituted hydrido polycarbosilane [15] with a nominal composition which comprises 10% of allyl moieties [16] (Figure 3.1) produces high purity near-stoichiometric SiC (1:1 silicon to carbon atomic ratio) with high ceramic yields (72-78%) [14].

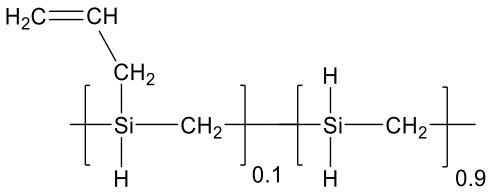

Figure 3.1. Nominal composition of allyl-hydrido polycarbosilane StarPCS™ SMP-10 [16].

Data sheet [14] for SMP-10 reports that the preceramic polymer undergoes a low temperature green cure from 180 °C to 400 °C, resulting in the hardening and irreversible conversion of the liquid to an insoluble and infusible solid, due to the crosslinking of the polymer chains. Two main mechanisms can contribute to its thermal crosslinking process: hydrosilylation and dehydrocoupling reactions [16–18] (Figure 3.2). Small amounts of additives can also be used to promote crosslinking and increase the ceramic yield of SMP-10, such as organic peroxide initiators (dicumyl peroxide [19–21]) and platinum catalysts ($MeCpPtMe_3$ [22,23]).

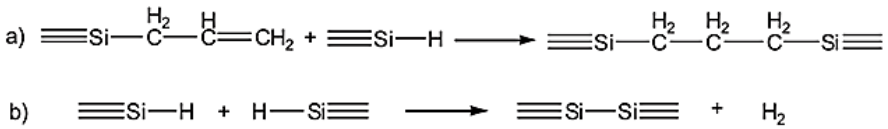

Figure 3.2. Hydrosilylation between the allyl and silane groups (a) and dehydrocoupling of the silane groups (b) reactions occurring upon thermal cross-linking of SMP-10 [16].

The resin is converted into a ceramic material upon pyrolysis at above 800 °C in inert environment in an atmospheric pressure. When it is processed at temperatures up to 1200 °C, the product is amorphous SiC. Nano-crystalline beta-SiC is formed from 1250 to 1700 °C, and it converts to alpha-SiC with temperatures in the range 1800–2000 °C [14,24].

3.1.1.2 Carbon fibres

Carbon fibres (C_f) can be defined as fibres with a carbon content of at least 92 wt%. They can be prepared using any precursor with a carbon backbone that can yield carbonaceous residue on pyrolysis [25]. Several organic polymeric materials have been investigated as starting materials for the preparation of carbon fibres [26]. Moreover, in the last few years new fibre types with nearly 100% carbon have been generated from carbon allotropes such as carbon nanotubes [27] or graphene [28]. However, for large scale production and application the choice is narrowed down to carbon fibres made by carbonizing precursors, and in particular to three main types: PAN-based, pitch-based and rayon-based according to the type of precursor used [25]. At present, more than 90% of commercial carbon fibres produced globally are made from polyacrylonitrile (PAN) precursors. The reason for the popularity of PAN-based carbon fibres is their superiority in balancing performance (high strength and reasonably high modulus) and production cost [29,30]. Carbon fibres made from pitch are adopted in high stiffness components where ultra-high modulus is required and various uses by exploiting their high thermal and/or electrical conductivity [31]. Currently less than 1% of the commercial carbon fibres are rayon-based fibres, as they find few applications in the market due to their low performance and productivity [29].

In this work of thesis, the choice of the carbon fibre type fell on commercially available PAN- and pitch-based carbon fibres. Thus, only an overview of these types of fibre are presented below.

Polyacrylonitrile (PAN)-based Carbon fibres

The manufacturing process of PAN-based carbon fibres is outlined in Figure 3.3.

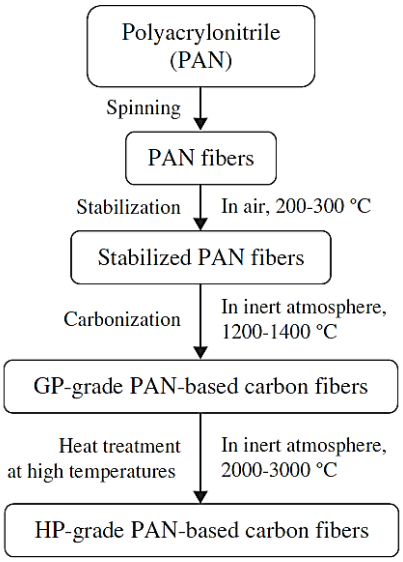

Figure 3.3. Basic steps required for the production of PAN-based carbon fibres [32].

Production begins with the polymerization of PAN homopolymer or PAN copolymer, followed by fibre spinning and drawing to increase polymer chain alignment in the fibre axial direction. Conversion of the PAN fibre into a carbonized structure involves two heat treatment processes, namely stabilization and carbonization [32] (Figure 3.3). The precursor fibre is first treated under tension in an oxidative environment at temperatures between 200 and 300 °C, that leads to a transformation of the linear polyacrylonitrile macromolecules in a rigid, thermally stable ladder structure [30] (Figure 3.4). The stabilized fibre tows are subsequently subjected to the carbonization process in inert environment at temperatures in the range 1200–1400 °C [32] up to 1700 °C [30,33]. During this heat treatment process, non-carbon elements are released while the carbon content increases [30,34] (Figure 3.4), thereby forming a turbostratic carbon structure. This generally consists of an imperfect graphitic (sp^2-carbon units) structure (Figure 3.5a), in which graphitic layers are not neatly stacked but have a random arrangement and are also not planar [25,35,36]. As shown in Figure 3.5b, the applied tension ensures the carbon hexagonal segments oriented in the axial direction of fibre, while perpendicular to the fibre axis there is not usually orientation. A high alignment of the graphitic basal planes is obtained parallel to the surface layer, contrarily in the internal turbostratic structure the graphite-type carbon layers are folded showing a low crystallite orientation [36,37]. An additional treatment (Figure 3.3), called graphitization, can be conducted by heat-treating the fibre up to 3000 °C to improve the ordering and orientation of the small crystallites in the direction of the fibre axis. Increasing the treatment temperature results in an increase in

the tensile strength and modulus, but simultaneously leads to lower tensile strength of the final carbon fibres [30,34]. The final step of C_f production involves oxidative surface treatment and sizing, generally with epoxy resin, to protect fibre surface, improve the manageability, and to increase the interfacial bonding between the fibre and matrix of a composite material [38].

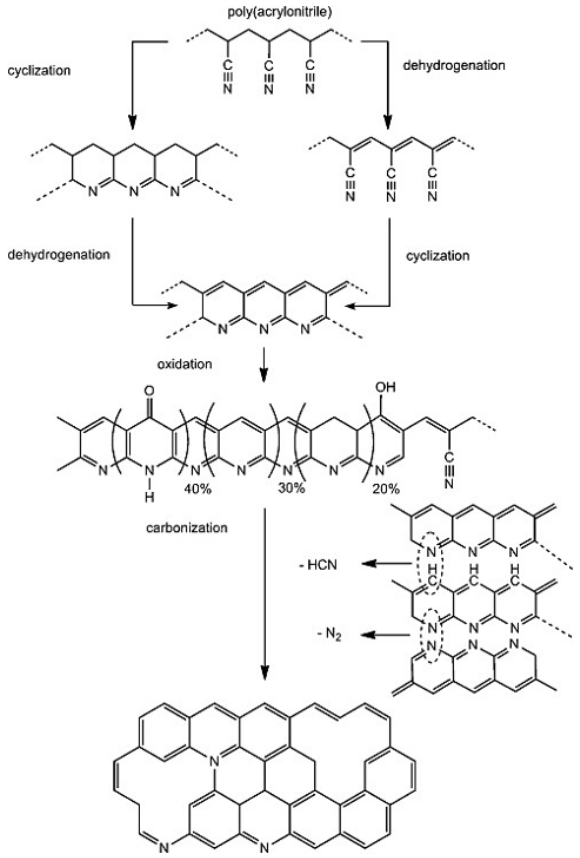

Figure 3.4. Model reaction paths from PAN to a carbon phase [34].

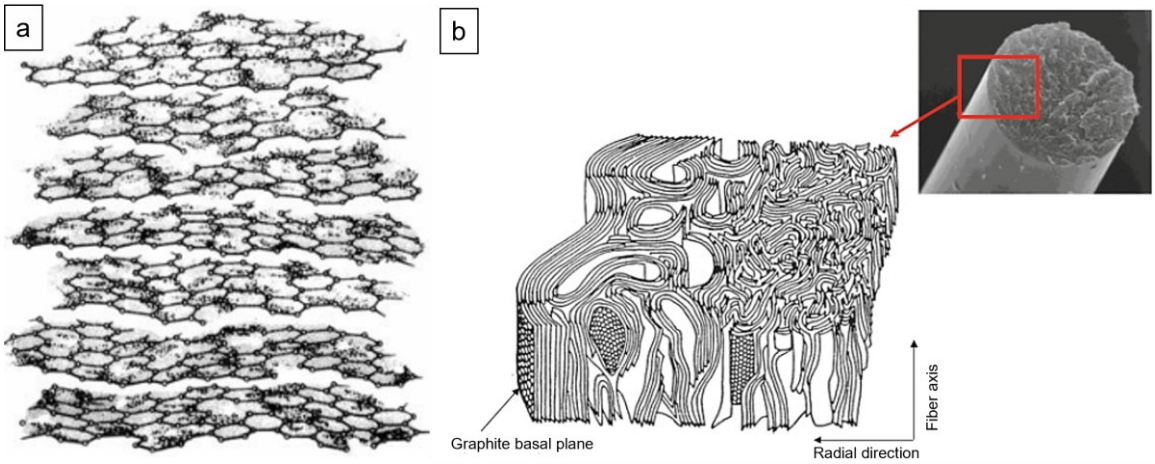

Figure 3.5. Structure of PAN-derived carbon fibre. (a) Schematic illustration of turbostratic structure of carbon. (b) Typical structural model of fibre showing folded graphitic-type carbon layers in the internal.

Pitch-based Carbon fibres

Pitch is the name for tarry substances that are almost solid or highly viscous at room temperature, and with a very high carbon content. It can be derived from natural resources (petroleum fraction, coal hydration, asphalt) or from synthetic materials (pyrolysis of polyaromatic compounds and polymers) [25]. As a result of the wide variety of precursors materials and chemical and physical treatments, there are typically two classes of pitch-based carbon fibre: i) general purpose grade pitch-based C_f, manufactured from petroleum and coal tar pitch which is isotropic in nature; ii) high-performance pitch-based C_f, for which isotropic pitch must undergo thorough treatment in order to convert to anisotropic pitch, also called mesophase pitch [30].

Similarly to the PAN-based carbon fibres, pitch-based carbon fibre production requires four main steps: spinning, stabilization, carbonization and graphitization (Figure 3.6).

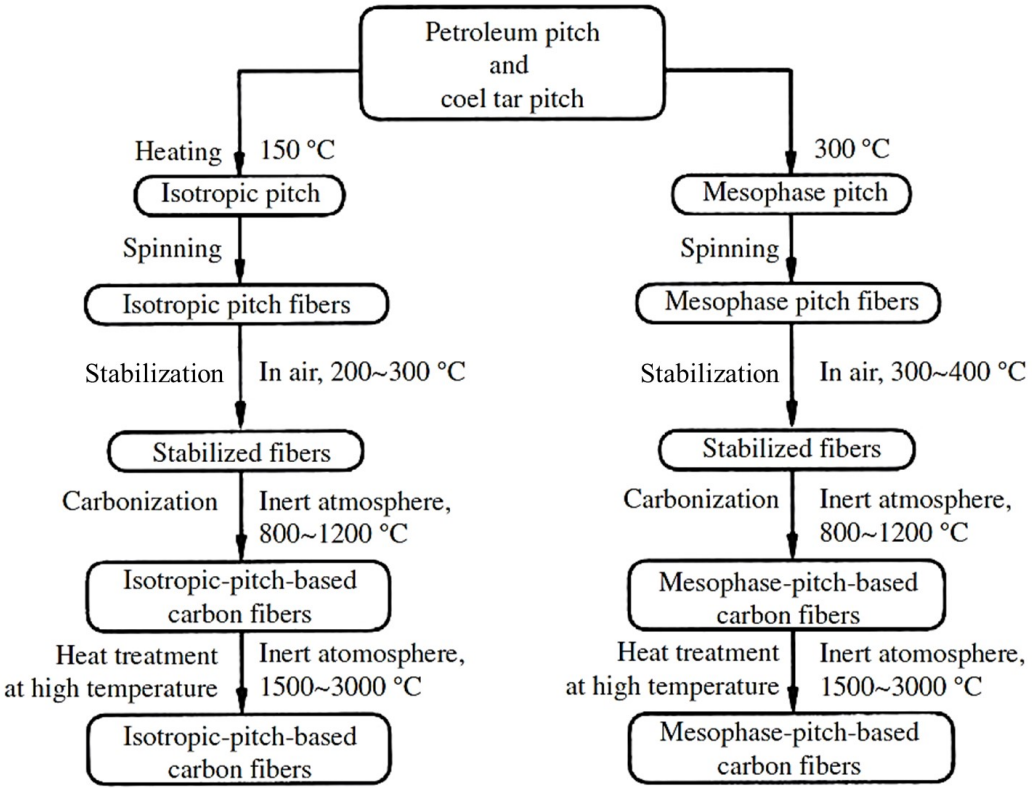

Figure 3.6. Basic steps for the production of carbon fibres from pitch (isotropic, mesophase) [32].

Both isotropic and mesophase-pitch can be spun into fibres using melt spinning. Processing parameters must be carefully controlled during the spinning of mesophase-pitch because of the extreme sensitivity to temperature variations of the precursor fibre

texture, which in turn has a great influence on the structural changes due to the high temperature treatments and the properties of resultant carbon fibre. For instance, the fibre texture in cross-section has been shown to transition from a cracked radial structure at lower melt spinning temperatures to an onion-skin texture (concentric around the fibre axis at the highest ones [39–42] (Figure 3.7), which offers the best performance [40,41,43].

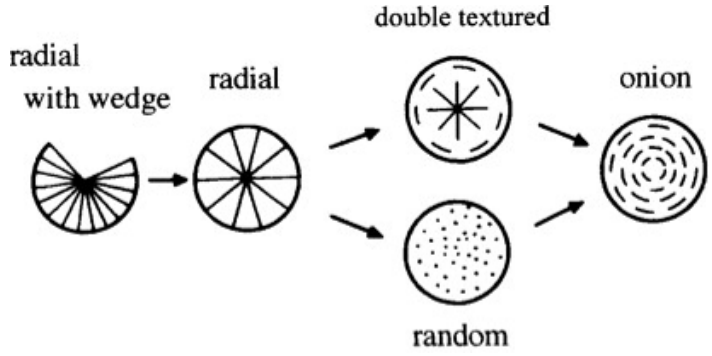

Figure 3.7. Schematic representation of textures in cross-section of mesophase pitch-based carbon fibres.

Then, pitch precursor fibres are stabilized in air at temperatures below its softening point so they do not melt during the carbonisation process. Immediately following the stabilization, the fibres undergo carbonization in nitrogen or argon, and graphitization in argon up to 3000 °C to increase the final carbon fibre tensile strength and tensile modulus [44]. The sizing process to further improve the bonding property is similar to the PAN-based carbon fibres.

The fundamental reaction path for the carbonization of a polyaromatic mesophase pitch precursor is shown in Figure 3.8 [34]. At temperatures over 350 °C, a condensation reaction based on the elimination of hydrogen establishes additional covalent bonds. Above 1500 °C, the structure eliminates further hydrogen, and in the case of pitch from natural resources also nitrogen and oxygen. Atomic structures of carbon fibres made from pitch are mostly hexagonal in shape and are composed of entirely carbon, leading to a more regular arrangement of the carbon atoms than that obtained from PAN precursor [45].

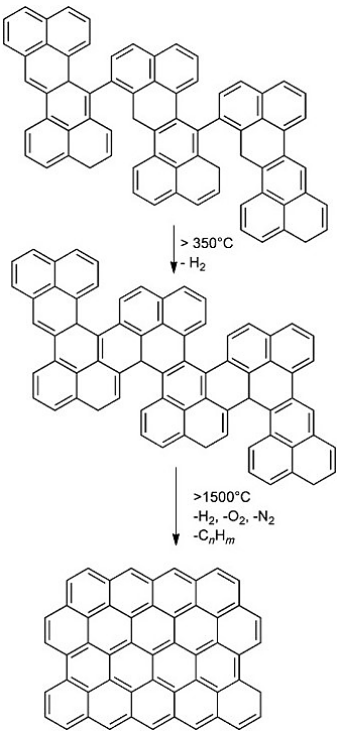

Figure 3.8. Reaction path for the carbonization of a polyaromatic mesophase pitch precursor [34].

The carbon fibres are also classified according to their mechanical performance. Figure 3.9 displays the relationships between the tensile strength and the modulus over a diverse range of carbon fibres from PAN and pitch. Some PAN-based and isotropic-pitch-based carbon fibres have low tensile strength and modulus, around 1 and 100 GPa respectively, and they are defined as general purpose grade (GP-grade). Carbon fibres with higher strength and modulus than GP grade are generally defined as high-performance grade (HP-grade), further divided into high-strength type (HT type) and high-modulus type (HM type) [32]. Most PAN-based carbon fibres produced in industry are HT type, reaching tensile strengths up to 6500 MPa while the tensile modulus is in the range 200–300 GPa [45,46]. Great effort has been paid to obtain PAN-based carbon fibres with a high modulus (the highest limit is 600 GPa [45]) but a lower strength. Mesophase-pitch-based carbon fibres are classified as high modulus (HM) or ultra-high modulus (UHM) reaching 900 MPa [46] at the highest-modulus grade. This extremely high modulus property is due to mesophase pitch, which leads to oriented graphite layers in the direction of the fibre axis reflecting on the strength and rigidity of final product. Contrarily, when an isotropic pitch is used as a starting material the orientation of graphite layers is not sufficient, hence carbon fibres with low tensile modulus and strength are produced.

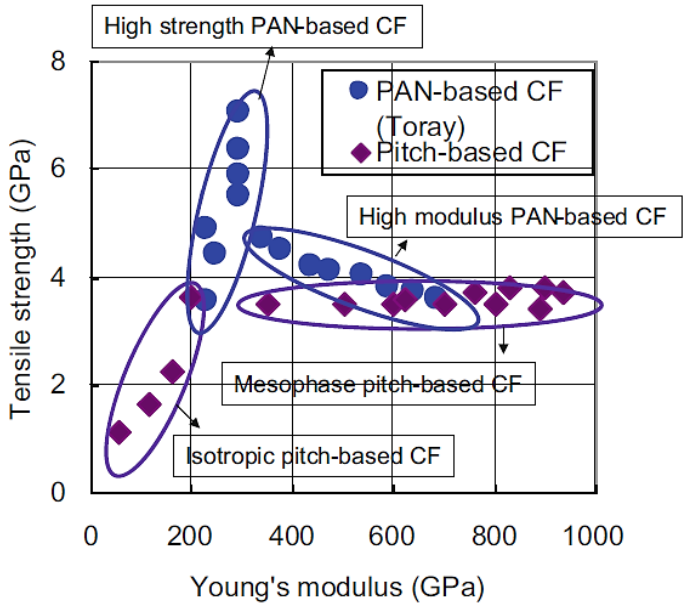

Figure 3.9. Mechanical properties of PAN-based and pitch-based carbon fibres [47].

3.1.2 Development of UHTCMCs via water-based ZrB_2 powder slurry infiltration and polymer infiltration and pyrolysis

The manufacturing of UHTCMCs consisted in a multi-step process that combined impregnation with a water-based slurry containing UHTC particles and consolidation through repetitive cycles of polymer infiltration and pyrolysis (PIP) with SMP-10, see Figure 3.10.

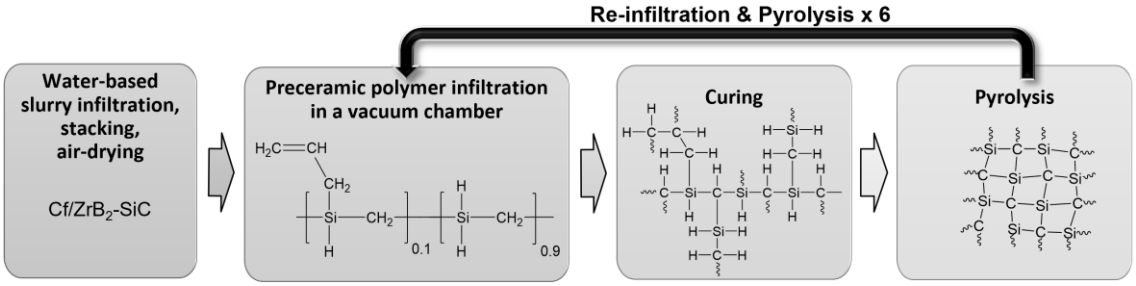

Figure 3.10. Multi-step process diagram showing UHTCMC manufacturing: 1st step, powder slurry infiltration and stacking of infiltrated fabrics; 2nd step, polymer infiltration of the green composite; 3rd step, crosslinking of polymeric chains (curing); 4th step, conversion of cross-linked resin into ceramic (pyrolysis).

3.1.2.1 Slurry infiltration

Firstly, a powder mixture of ZrB_2-10 vol% SiC was prepared by wet ball milling. "Ball milling technique is based on the capability of hard materials (such as SiC or Si_3N_4) to grind relatively softer powders and allows for the reduction of the starting particle size and

their homogenization. The presence of a solvent, such as ethanol, aids the mixing of the powders and minimizes heat production and oxidation of the particles [48]. The raw ZrB_2 and α-SiC powders were milled in ethanol with SiC grinding media into a HDPE bottle for 24 h at 60 rpm. Weight ratio of the powder to solvent to grinding media was 1:1:1. Absolute ethanol (water content < 0.05%) was chosen as solvent to limit the presence of water and minimize the surface oxidation of the powders during milling. Then, the powder mixture was completely dried using rotary evaporator at 90 °C and sieved (250 µm mesh) to breakdown the agglomerates. An aqueous slurry was prepared by dispersing the sieved powders in deionized water with polyacrylates according to previous studies[1].

C_f preforms with different architectures (unidirectional, 2D and 2.5D) with approximate dimensions 60 mm × 100 mm were infiltrated with the suspension. Subsequently, infiltrated fabrics were stacked (UD fabrics were stacked in 0/0° and 0/90° configurations). Finally, as obtained materials were air-dried at 100 °C for 2 h to remove water in the slurry. Green samples (that mean not consolidated) with a thickness ranging from 2 mm to 6 mm in composites prepared by stacking layers, and 17 mm using 2.5D preform were produced.

3.1.2.2 Polymer infiltration

Green plates were introduced in a glovebox (LabStar, MBraun, Germany) under argon atmosphere (Figure 3.11) for further processing. Inside the glovebox, allyl-hydrido polycarbosilane SMP-10 was mixed with 1.0 wt% of catalyst ($MePtCpMe_3$ was put directly into SMP, whilst DCP was dissolved previously into THF) which acts as a cross-linker during curing step, using a magnetic stirrer for 15 min; the resulting 1 wt% amber-coloured liquid was used for polymer infiltration.

Each plate was placed in a vessel inside a desiccator, located in the glovebox. Argon was evacuated by a vacuum pump and the composite was subsequently infiltrated by pouring the polymer on the sample until the latter was completely covered (see the scheme of apparatus used for infiltration in Figure 3.12). The vacuum was kept for 1 min. After that, the ambient pressure was recovered. Infiltrated plates were placed between graphite foils and sealed into plastic bags, finally taken out from the glovebox.

Figure 3.11. Glovebox (LabStar, MBraun, Germany) under Ar atmosphere used for infiltration with air and moisture sensitive preceramic precursor.

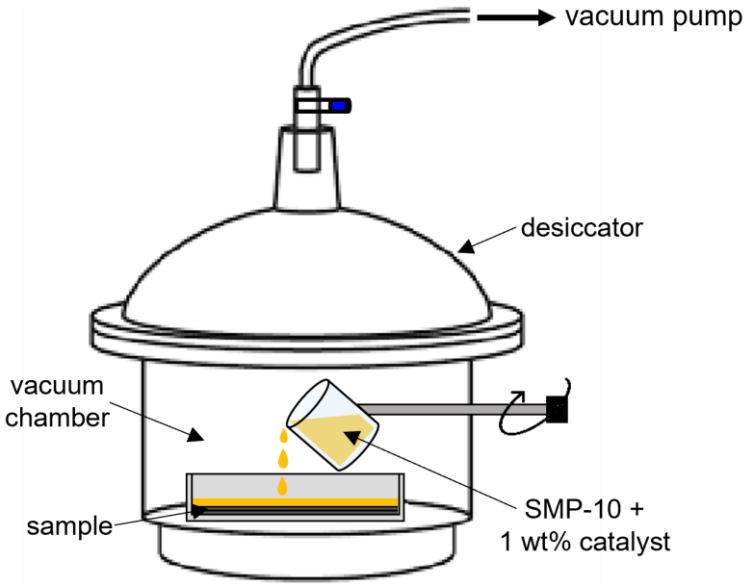

Figure 3.12. Scheme of apparatus used for polymer infiltration.

3.1.2.3 Curing and pyrolysis

Samples were transferred in a tube furnace (HST 12/600, Carbolite Gero, Germany - Verder Scientific, Italy) under an argon flow of 1 mL/min for curing and pyrolysis. Pictures and a scheme of the tubular furnace are reported in Figure 3.13.

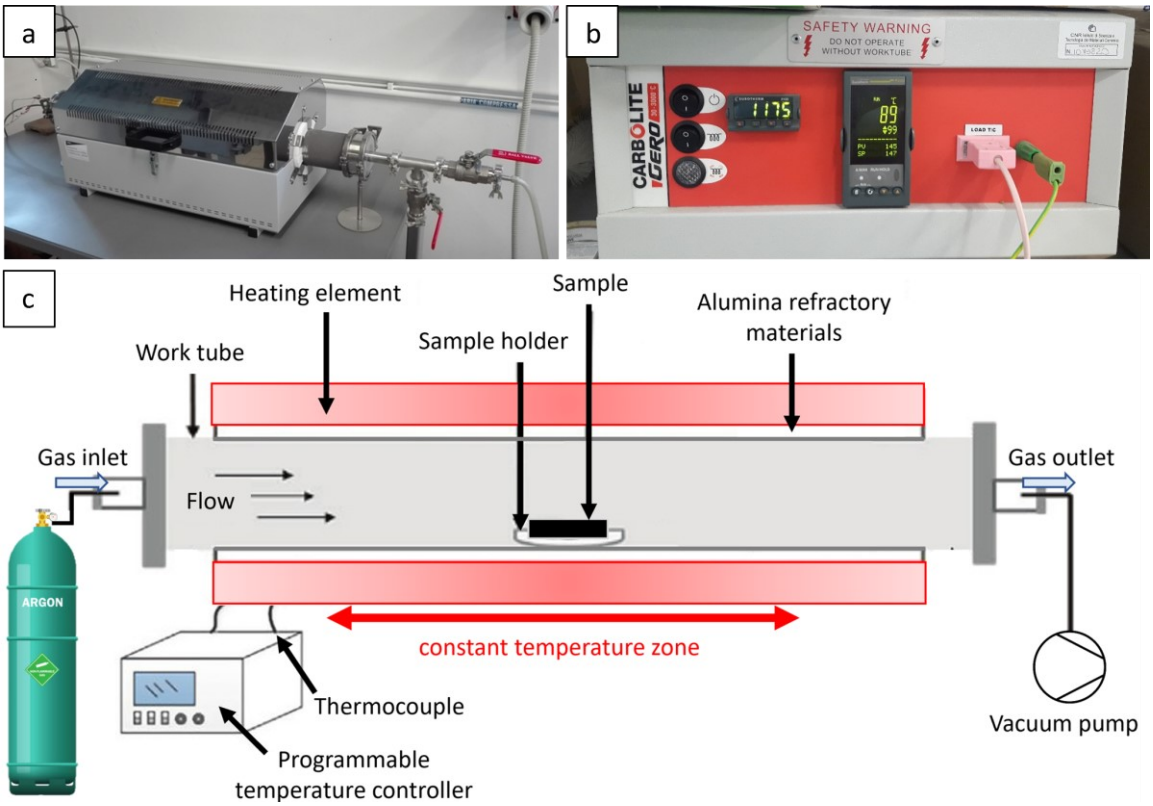

Figure 3.13. Tube furnace (HST 12/600, Carbolite Gero, Germany) used for curing and pyrolysis cycles: (a) furnace, (b) separate control module with programmable temperature controller (Eurotherm 3508), (c) Schematic illustration of experimental apparatus.

Curing was carried out at 300 °C for 4 h, in order to cross-link the functional groups and convert liquid polymer into a rigid resin, then pyrolysis was carried out at 1000 °C for 2 h, in order to obtain an amorphous ceramic (see profile of thermal cycle in Figure 3.14).

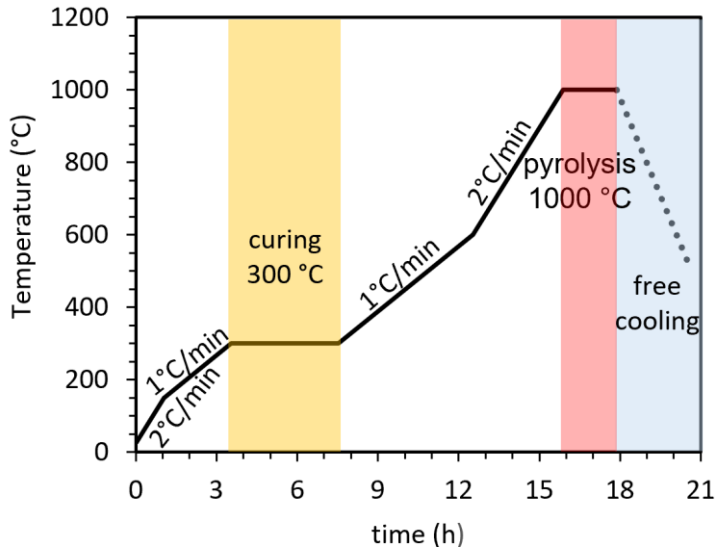

Figure 3.14. Temperature (°C) vs. time (h) profile of thermal cycle.

A total of 6 cycles of infiltration with modified SMP-10 (with catalyst) and heat treatment until 1000 °C were carried out to achieve the final materials, both reinforced with pitch-based carbon fibres (labelled as **0/0°**, **0/90°**, **2D** in the Chapter 4) and PAN-based carbon fibres (labelled as **0/0°_t**, **2D_tw**, **2D_pl**, **2.5D** in the Chapter 5).

3.1.2.4 Pyrolysis at higher temperature

After the sixth cycle of pyrolysis at 1000 °C under Ar flow, a heat treatment at higher temperature was experienced to convert polycarbosilane-derived amorphous SiC in crystalline SiC. The further pyrolysis cycle was performed in a resistance-heated graphite furnace (1000-3060-FP12, Astro Industries Inc., U.S.A., Figure 3.15) under a flowing Ar atmosphere, testing different temperatures ranging from 1100 to 1900 °C (ramp 600 °C/h up to target temperature and dwell for 2h, free cooling in Ar environment).

Considering the high processing temperatures, pitch-based carbon fibre-reinforced UHTCMC with 0/0° carbon fibre architecture was chosen (sample labelled as **0/0°**) among those consolidated by 6 PIP cycles at 1000 °C under Ar flow (see Section 3.1.2.3) as reference material. Heat treatments were carried out on 25 mm × 2.5 mm × 2 mm sized bars and 10 mm × 10 mm × 2 mm cut from a reference material.

Figure 3.15. Resistance-heated graphite furnace (1000-3060-FP12, Astro Industries Inc.) used for pyrolysis cycles at temperature in the range 1100-1900 °C under Ar atmosphere.

3.1.3 Development of UHTCMCs by hybrid processes coupling water-based ZrB_2 powder slurry infiltration, polymer infiltration and pyrolysis with hot pressing

The manufacturing of UHTCMCs consisted in a four-step hybrid processes coupling water-based UHTC powder slurry infiltration, PIP and HP techniques.

A mixture of ZrB_2-10 vol% SiC powders was homogenised by ball milling in ethanol, dried by rotary evaporator and sieved (as reported in detail in Section 3.1.2.1). Then, a water-based slurry was prepared according to previous studies [11] and used to impregnate the pitch-based carbon fibre cloths. Infiltrated unidirectional cloths were cut with dimensions 30 mm × 30 mm and stacked in a 0/90° configuration. As shown in the schematic overview in Figure 3.16, at least 34 layers were piled-up to produce 16 mm thick green samples. Subsequently, in order to consolidate the materials, two multistep processes combining polymer infiltration and pyrolysis (PIP) followed by hot pressing (HP) and vice versa were carried out.

Sample HPP: Green samples were consolidated by a cycle of hot pressing (HP) followed by two cycles of polymer infiltration and pyrolysis (PIP), see "route **(a)**" in Figure 3.16. Hot pressing (MP 20(II), SIATEM, Ing. Allaria Alto Vuoto, Italy) cycles were set in agreement with typical densification curve of previously densified C_f/ZrB_2-SiC composites [49], in order to reduce the starting porosity by about half. The pre-sintering step carried out at 1850 °C with no dwell time was considered the best compromise to compact the green pellet halving the starting open porosity without compromising the integrity of fibres. Further details about Hot Pressing technique are reported below (see Section 3.1.3.1).

Repetitive cycles of infiltration with polycarbosilane and pyrolysis at 1000 °C were carried out to further reduce the porosity following the PIP process described in Section 3.1.2.3. In detail, the green sample was air-dried at 100 °C for 2 h and introduced in a glovebox (LabStar, MBraun, Germany) under argon atmosphere. Inside the glovebox, allyl-hydrido polycarbosilane SMP-10 was mixed with 1.0 wt% of DCP catalyst (0.25 g dissolved previously into 10 mL of THF), which acts as a cross-linker during curing step, using a magnetic stirrer for 15 min. As described in Section 3.1.2.2, the infiltration was carried out in vacuum environment by pouring the modified polymer on the sample until this was completely covered. The sample was cured at 300 °C for 4 h and pyrolysed at

1000 °C for 2 h under an argon flux of 1 mL/min into a tube furnace (HST 12/600 Carbolite Gero, Verder scientific, Italy). More than two PIP cycles were not effective to reduce porosity since the obtained material did not allow a significant further penetration of the polycarbosilane.

Sample PHP: Green samples were consolidated through two repetitive cycles of polymer infiltration and pyrolysis (PIP) followed by a hot pressing (HP) cycle, indicated as "route **(b)**" in Figure 3.16. See conditions reported above for sample HPP for PIP and HP parameters. For the sake of comparison, the same number of PIP cycles were performed for manufacturing samples HPP and PHP. Hot pressing was carried out according to previous studies at 1900 °C for 15 min under 40 MPa [50] to reduce the porosity at the same level of HPP sample.

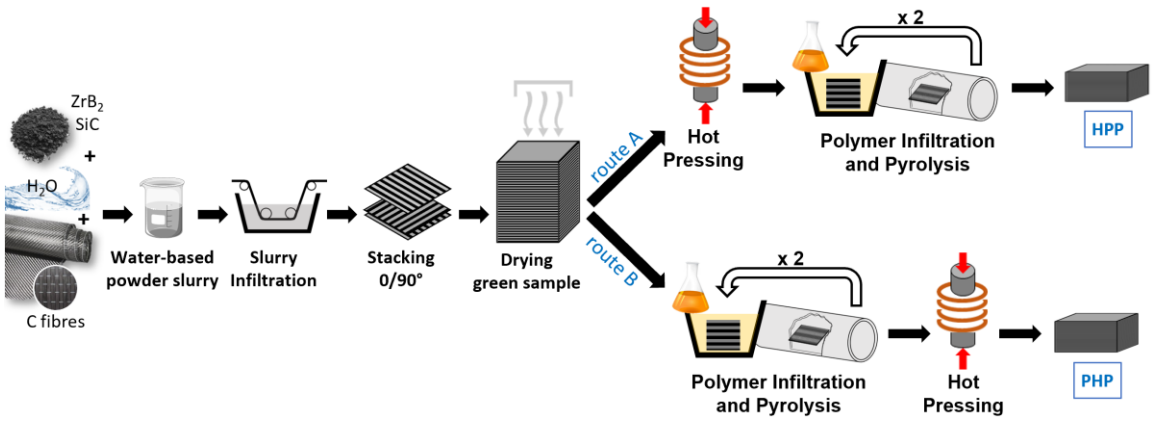

Figure 3.16. Schematic flowchart of UHTCMC manufacturing by two reversed paths: production of a green sample by slurry infiltration and stacking of infiltrated fabrics; consolidation via: route A, a cycle of HP followed by two PIP cycles, and route B, two PIP cycles followed by HP.

3.1.3.1 Hot pressing

Cycles of hot pressing were carried out in low vacuum (about 10^{-5} bar), in a graphite oven heated by induction heating with a heating rate of 80 °C/min [48,51]. Uniaxial pressure is applied to the sample through two rigid rams which enter the die opening. Both die and rams are made of graphite, allowing to apply simultaneously heat and pressure. Figure 3.17 illustrates the vacuum furnace for HP with induction heating system (MP 20(II), SIATEM, Ing. Allaria Alto Vuoto, Italy) [51].

An initial low pressure was applied starting at 900 °C and then it was progressively increased to 40 MPa at the target temperature (i.e. 1900 °C for sample PIP/HP and 1850 °C for sample HP/PIP). At 1900 °C the pressure was kept for 10 min for sample PIP/HP,

whilst for sample HP/PIP no holding time under pressure was executed. Finally, the load was removed, and the samples were cooled down to room temperature.

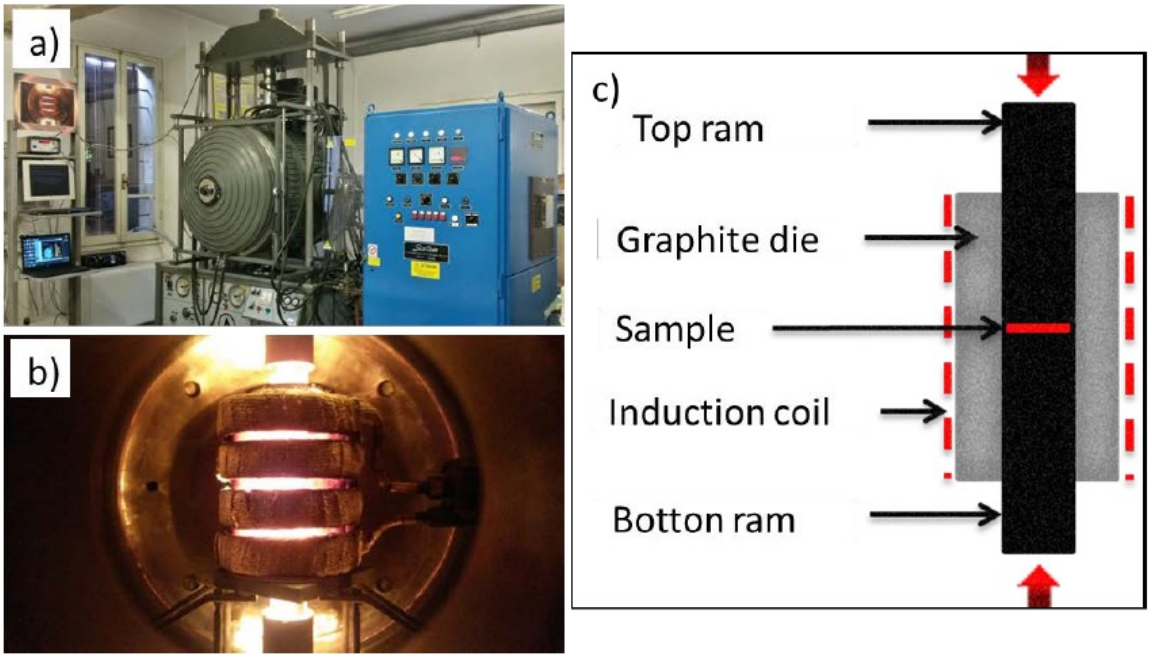

Figure 3.17. (a) Vacuum hot pressing (HP) with induction heating system (Ing. Allaria MP20/II Alto Vuoto, IT); (b) induction coil (internal chamber of the oven, working condition 1900 °C); (c) simplifying scheme of the hot pressing process [51].

3.2 Preparation of polymer-derived ceramics

Polymer-derived ceramics are an attractive route for manufacturing structural materials with unique microstructural features and very desirable high temperature properties. In this part of the thesis, the overall goal was to investigate the synthesis, processing, and properties of polymer-derived SiC-based and UHTC phases.

Polymer preceramic precursors can be integrated in manufacturing of UHTCMCs by Polymer Infiltration and Pyrolysis (PIP) technique through the developed processes reported in Section 3.2 from a forward-looking perspective.

3.2.1 Materials

The following materials were used for the synthesis of polymeric precursors:

- allyl-hydrido polycarbosilane (StarPCS^{TM} SMP-10, Starfire System Inc., U.S.A; density 0.998 g/cm^3, viscosity 40–100 cPs at 25 °C);
- dicumyl peroxide (DCP), $[C_6H_5C(CH_3)_2]_2O_2$ (Sigma Aldrich; purity 98%);
- trimethyl(methylcyclopentadienyl)platinum(IV), $MePtCpMe_3$ (Sigma Aldrich; purity 98%);
- borane-ammonia complex, $H_3N{\cdot}BH_3$ (Sigma Aldrich; technical grade 90%);
- zirconium tetrachloride, $ZrCl_4$ (Sigma Aldrich; anhydrous, powder, 99.99% trace metals basis);
- novolac-type phenolic resin (BAKELITE® PF 8978 FL 01, Hexion GmbH, Germany; liquid, containing furfuryl alcohol and ethanol);
- novolac-type phenolic resin (GP® 2074, Georgia-Pacific Chemicals, U.S.A.; solid);
- bitumen (ENI, Italy; solid pellets);
- tetrahydrofuran (THF), $(CH_2)_3CH_2O$ (Sigma Aldrich; anhydrous, purity: ≥ 99.9%, inhibitor-free);
- cyclohexane, C_6H_{12} (Sigma Aldrich; anhydrous, purity: 99.5%);
- ethanol, CH_3CH_2OH (Merck; absolute, purity: ≥ 99.5%);
- acetone, CH_3COCH_3 (Merck; analytical standard, purity: ≥ 99.5%);
- petroleum ether (Sigma Aldrich; anhydrous).

3.2.2 Study for improving yield of polymer ceramic precursors

Optimal processing of PIPed Ceramic Matrix Composites should focus on maximizing ceramic yield of the polymer precursors. Indeed, volumetric yield and volatile release rates strongly affect the degree of cracks due to shrinkage and the porosity, and consequently manufacturing time. The goal of the study presented herein was to increase the mass yield of commercially available allyl-hydrido polycarbosilane SMP-10. Different strategies were evaluated: i) use of polymer catalysts, and ii) heat pre-treatment.

Two different catalysts were used with the aim to promote cross-linking during curing step: a free-radical initiator, dicumyl peroxide (DCP), and a catalyst based on cyclopentadienyl complexes of platinum(IV), such as trimethyl(methylcyclopentadienyl)platinum(IV). Several authors used DCP with concentration varying from 0.01 to 5 wt% of the Si-based precursor [52]. Commonly 1 wt% DCP is added as cross-linking agent for polymer precursor for PIP purposes [20,53–56], thus the effect of such catalyst on SMP-10 conversion was examined by preparing a 1wt% mixture. SMP-10 was mixed with 1 wt% DCP catalyst in THF solution (0.25 g of solid DCP in 10 mL of THF), by stirring for 15 min at room temperature using a magnetic stirrer. Differently, a mixture containing 1 wt% $MeCpPtMe_3$ was prepared by directly adding the solid catalyst to liquid SMP-10 and stirring at room temperature for 15 min.

It was demonstrated that heat treatments on polycarbosilane SMP-10 before cross-linking begins (> 90 °C) [57] lead to an increase in cured mass yield, which can be translated in enhanced SiC mass yield [58]. In this study, heat treatment of as-received SMP-10 was performed in a conical flask connected to a vacuum pump (ultimate vacuum 0.03 mbar), holding at ~50 °C for 3 h then at ~90 °C for 5 h. The effect of such treatment was study both on treated SMP-10 only and on treated SMP-10 subsequently modified with 1 wt% $MeCpPtMe_3$. The latter was prepared by mixing treated SMP-10 and solid $MeCpPtMe_3$ (without adding solvent) and stirring for 20 min using a magnetic stirrer.

The sample preparation was carried out in an argon-filled glovebox (LabStar, MBraun, Germany) to minimize oxidation and contamination of atmospheric moisture. Mixtures (~ 0.9–1.0 g) were put in alumina crucibles, which were covered with graphite sheets before taken out from the glovebox. Curing and pyrolysis were carried out in a

tube furnace (HST 12/600, Carbolite Gero, Germany) at 300 °C for 4 h and at 1000 °C for 2 h respectively (see the thermal cycle reported in Section 3.1.2.3) under argon flow.

For comparison, a sample of as-received SMP-10 was prepared following the same procedure.

3.2.3 Synthesis of polymer-derived ceramic SiBCN(O)

The commercially available allyl-hydrido polycarbosilane SMP-10 was used as Si and C precursor. For the incorporation of B and N on the polymer chain, ammonia borane (AB) was chosen since it is source of boron and nitrogen at the same time, also it has an higher solubility in THF than BH_3. All reactants were handled in argon-filled glovebox (LabStar, MBraun, Germany). The amount of AB and SMP-10 was calculated in order to obtain a single source precursor with a theoretical Si:B:C:N atomic ratio close to 1.

Considering the solubilities of the starting materials [14,59–61] (see Table 3.2), AB was dissolved in THF and stirred at 60 °C using a hotplate magnetic stirrer, by adding solvent occasionally.

Table 3.2. Properties of raw materials used for the synthesis of SiBCN(O).

Code	Appearance	Density (g/cm^3)	Solubility
StarPCS^{TM} SMP-10	clear, amber liquid	0.998	Hexanes, THF, Toluene; insoluble in water
Ammonia Borane	colorless or white solid	0.26	Soluble in NH_3, water (33.6 g/100 g), THF (25 g/100 g), methanol (23 g/100 g)
THF	colorless liquid	0.89	Solvent; miscible in water

The prepared solution was filtered using a filtering syringe to remove unsolved fractions, which were attributable to boric acid. Then, AB solution in THF was added dropwise to SMP-10 at room temperature under stirring.

Evolution of gases was observed for some minutes, and a clear pale-yellow solution, noticeably paler than amber-coloured SMP-10, formed. Then, the solution was kept at room temperature under stirring and single drops of solution (about 0.1 mL) were collected at regular time intervals of: 5, 15, 120, 240 min and then were quickly heated at ~66 °C to evaporate the solvent. The resulting solid precursors were analysed by FT-IR spectrometer equipped with ATR tip to evaluate reaction evolution.

A new fresh solution of AB and SMP-10 was prepared in similar way and heated under reflux. Again, single drops of solution (about 0.1 mL) were collected at regular time intervals of: 5, 15 and 30 min, then each drop was evaporated at ~66 °C on hot plate to collect the solid precursor for FT-IR analysis.

Table 3.3 reports a summary of experiments, parameters and characterizations carried out on single source precursors and related PDCs.

Table 3.3. Experiments carried out in function of different reaction conditions (time, temperature), processing and characterizations.

Lable	Time (min)	Temperature (°C)	Chemical analysis	Pyrolysis conditions T (°C), t (h)	Post characterization
SMP_AB, 0.08h	5	Room temperature	FTIR	- -	-
SMP_AB, 0.25h	15	Room temperature	FTIR	- -	-
SMP_AB, 2h	120	Room temperature	FTIR	- -	-
SMP_AB, 4h	240	Room temperature	FTIR	- -	-
SMP_AB, R0.08h	5	Reflux of THF	FTIR	- -	-
SMP_AB, R0.25h	15	Reflux of THF	FTIR	- -	-
SMP_AB, R0.5h	30	Reflux of THF	FTIR	800, 0.5; 800, 12	SEM, XRD

Single-source precursor obtained from Exp#7 was dried, then transferred in an alumina crucible sealed in a plastic bag and transported in a tube furnace (HST 12/600, Carbolite Gero, Germany). Two experiments of polymer-to-ceramic conversion were performed by pyrolysis of the precursor at 800 °C for 30 min and 12 h under argon flow (1 L/min).

3.2.4 Synthesis of Zirconium Carbide precursors

Zirconium chloride, $ZrCl_4$, was used as Zr source, while two types of phenolic resin (novolac-type) and bitumen (unknown) were used as carbon source. According to reaction $ZrO_2 + 3C = ZrC + 2CO_{(g)}$, 1:3 Zr:C atomic ratio was obtained taking into account the yield of conversion of Phenolic resins and bitumen into carbon after pyrolysis of them at 1000°C under argon flow.

Phenolic resin Bakelite PF® 8978 FL 01 (here called “resin PF”), kindly furnished by DLR (Stuttgart) is in liquid form so was subjected to a partial curing process forming a brownish rubber, in such a way to have all C sources in solid form for the purpose to determine the carbon yield of conversion. Rubbery resin PF was chopped, while phenolic

resin GP 2074 (here called “resin GP”) and bitumen, in form of flakes and pellets respectively, were ground to coarse powders with mortar and pestle.

Firstly, amounts (~5 g) of resin PF, resin GP and bitumen were put in zirconia crucibles and pyrolysed under Ar flow at 1000 °C in a tube furnace (HST 12/600, Carbolite Gero, Germany). From the pyrolysed char of each C source, corresponding moles of C were determined for synthesis of ZrC precursors using a C/Zr molar ratio 3:1.

Samples of ZrC precursors were prepared inside a glovebox with inert (Ar) environment (LabStar, MBraun, Germany) since $ZrCl_4$ hydrolyses rapidly in humid air. 1 g of resin PF, resin GP and bitumen were put in separate beakers and dispersed in 10 mL of a solvent mixture of THF/cyclohexane (solvent ratio 1:1) through magnetic stirring at room temperature for 2 h. Then, solid $ZrCl_4$ was added to each mixture (2.55 g to resin PF, 2.70 g to resin GP and 3.90 g to bitumen solutions, respectively) a little at a time. For the possible evolution of HCl gas, a home-made hood connected to a condensation trap containing sodium bicarbonate was assembled. The reaction mixtures were stirred at room temperature for 2 h, by adding solvent as needed because of its evaporation. After solvent removal on hotplate (T ~100 °C), solid precursors were transferred into zirconia crucibles and transported in a container closed in inert environment to the tube furnace. Pyrolysis was carried out at 1000 °C for 2 h under Ar flow, with low heating rate (see thermal cycle reported in Section 3.1.2.3). A graphite furnace (1000-3060-FP12, Astro Industries Inc., U.S.A) was used for high-temperature treatments at 1400, 1600 and 1800 °C for 2 h (heating ramp 600 °C/h) with flowing argon atmosphere.

For comparison, synthesis of ZrC precursors was also conducted via dry-method. Three batches of ~0.5 g were prepared by mixing $ZrCl_4$ powder with each of carbon sources previously crushed into powder. The same Zr:C atomic ratio of previous synthesis was kept for those experiments. As-prepared samples were heat treated following the same procedure of the previous samples.

3.3 Characterization

Characterization is a fundamental step in material science that forms the basis for knowing the potential of a material.

Knowledge of the microstructure of a material becomes essential because it plays a key role on understanding of the relationship between processing and chemical, electrical, thermal, and mechanical properties. By the term “microstructure”, we include the whole compositional, crystallographic, and morphological characteristics of a material; thus, studying microstructure means analysing chemical composition, crystallographic phases, spatial distributions of the constituting phases, density and the presence of defects into a material. In this work of thesis, beyond physical measurements (i.e. density, weight loss, yield, etc.) and quantifications of the phases constituting the material, several analytical techniques were employed for the microstructural characterization of the fabricated composites and the products resulting from the syntheses. The principal techniques include Mercury Intrusion Porosimetry (MIP), X-Ray Diffraction (XRD), Fourier Transform Infrared Spectroscopy (FTIR), optical profilometry, digital microscopy, Scanning Electron Microscopy (SEM) and Energy Dispersive X-ray Spectroscopy (EDS).

In order to evaluate if the prepared composites can be considered suitable for structural applications, an extensive mechanical characterization was carried out to investigate thermo-mechanical properties, such as Young’s and shear modulus, flexural strength and fracture toughness at room and elevated temperature. Moreover, oxidation experiments were performed using a thermogravimetric analyser (TGA) and a bottom loading furnace to investigate the behaviour of these composites in oxidizing environment and their resistance.

A brief description of the employed techniques and the principles on which they rely on is furnished below. Also, experimental procedures for the preparation and analysis of the characterized samples are reported in each corresponding paragraph.

3.3.1 Microstructural characterization

3.3.1.1 Mercury Intrusion Porosimetry

Mercury Intrusion Porosimetry (MIP) provides information about total accessible pore volume, pore size and volumetric distribution, bulk and skeletal densities for solid and powder materials [62].

This technique basically relies on the non-wetting property of mercury (chemical symbol Hg) to most solids combined with its high surface tension [63,64] (Figure 3.18a). Hg does not penetrate the pores by capillary action but only as a result of externally applied pressure [63,64] (Figure 3.18b). MIP analysis is the progressive intrusion of Hg into a porous medium under increasingly controlled pressures. The largest pores which are directly accessible at the surface are intruded into first, followed, as the pressure increases, by ever-smaller pores accessible at the surface or connected to pores already filled [63,64]. The relationship between the applied pressure and the pore size in which Hg has intruded is given by the Washburn equation (1) [65]:

$$PD = -4 \Upsilon \cos \theta \quad (1)$$

where P is the applied pressure, D is the pore diameter, Υ is the surface tension of Hg (480 dyne · cm^{-1}) and θ is the contact angle between the Hg and the pore wall (typically within the range 120°–150°, a value of 140° is commonly used). The assumption is that the pores are perfect cylinders with circular pore openings [62].

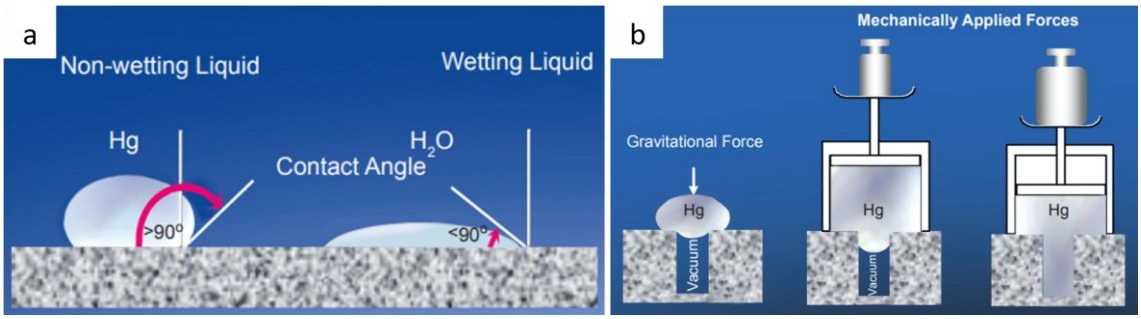

Figure 3.18. (a) Liquid-solid contact angle for wetting (i.e. H_2O) and non-wetting (i.e. Hg) liquids. (b) Hg forced into the pores by the application of external pressure: Hg in equilibrium with and entering an opening under increasing forces.

The volume of pores in the corresponding size class is determined by measuring at each pressure change the volume of Hg that intrudes into the sample. This is monitored

by a penetrometer (Figure 3.19), which consists of a sample holder cup connected to a stem, which is a glass capillary plated with metal acting as a reservoir for the analytical mercury; as pressure forces liquid out of the capillary and then into the sample during intrusion, a decrease in capacitance between the Hg column in the stem and the metal plating on the outer surface proportional to the volume of Hg leaving the capillary is detected [63,64,66].

MIP technique offers an unrivalled dynamic range for detailed investigation of the porosity since it covers pore sizes over a range of 5 orders of magnitude [62,67]. It could be used also on materials characterized by small pore sizes and low porosity, such as ceramics [68]. However, one of the key limitations to mercury porosimetry is that it cannot be used to analyse closed pores, which are isolated from the external surface and inside which fluids are not able to penetrate [69].

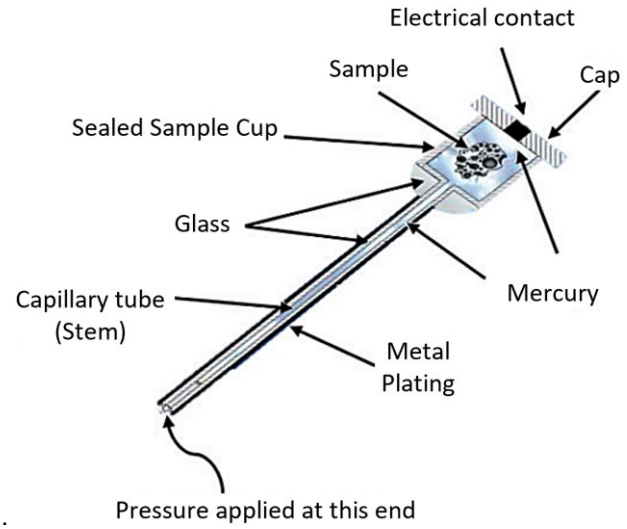

Figure 3.19. Cross-sectional view of a Mercury penetrometer.

In this work, a low pressure (max P 4 bar) and a high pressure (max P 2000 bar) porosimetric station (respectively Pascal 140 and Pascal 240 series, Thermo Finnigan, U.S.A.) were used to determine the open porosity in the range 0.0058–100 µm in the prepared composite materials. The analysis was carried out directly on bulk specimens with dimensions about 20 mm x 10 mm x 0.2 mm cut from fabricated plates, due to the limit of the porosimeter cell.

3.3.1.2 X-ray diffraction

X-ray diffraction (XRD) is a non-destructive analytical technique for characterizing crystalline materials. XRD analysis is primarily used for the identification of crystalline phases present in a material; it can also provide information about the crystallographic structure, preferential crystal orientations, and other structural parameters, such as crystallite size, crystallinity, strain, and reticular defects [70]. X-ray diffraction principle is also applicable on single crystal (Single Crystal X-ray Diffraction, SC-XRD), giving information about the internal lattice, including unit cell dimensions, bond-lengths, bond-angles, details of site-ordering, and on electronic density [71,72]; however, the difficulty of obtaining single crystals makes it a less widespread technique.

XRD techniques are based on observing the elastic scattering of X-rays from structures that have long range order. X-rays are high-energy electromagnetic radiation with short wavelengths ranging from 10 nm to 1 pm, that fall in the electromagnetic spectrum in the region between ultraviolet light and gamma-rays. Typically, XRD analysis operates with a wavelength of about 1 Å, which is in the order of interatomic spacing in solids. Since the distances between crystallographic planes and the wavelength are comparable, a X-ray beam which hits a solid material is diffracted by the electrons of the atoms that are in the beam path. The diffracted X-rays interfere with each other constructively, destructively, or giving rise to partial reinforcement of the wave amplitudes if the difference between the phases is intermediate between these two extremes. Constructive interference occurs only when the path difference between two incident rays on the crystallographic planes (express as equation 2) is equal to an integer multiple of the wavelength of the X-ray beam, as summarized in the Bragg's law (equation 3, Figure 3.20) [70].

$$AB + BC = 2\,d\sin\theta \quad (2)$$

$$n\lambda = 2\,d\sin\theta \quad (3)$$

where n is an integer (1,2,3…n), λ is the wavelength, d is the distance between the atomic planes, θ is the angle of incident X-ray beam. As the λ is known and θ at which constructive interference are measured during XRD analysis, the Bragg's equation allows determining the distance between lattice planes, characteristic of each crystalline cell.

Thus, it is possible to identify the phases present by comparison with known diffractograms (JCPDS standard) [73].

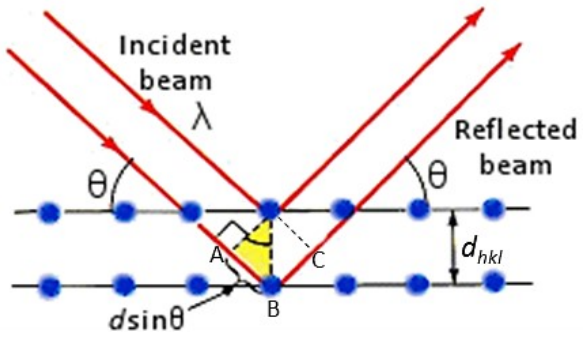

Figure 3.20. Bragg's law: X-ray diffraction in a crystal lattice.

Most of X-ray powder diffractometers work in Bragg-Brentano parafocusing geometry, in which the incident and diffracted beams move on a circle that is centred on the sample (Figure 3.21). This type of diffractometer is constituted by: i) a X-ray tube, containing a cathode (tungsten filament) that heated by electric current emits electrons, which bombard the metal anode (target) causing emission of X-rays; ii) a sample holder; iii) a detector, where the interaction between X-rays with a gas produces ions that generates a current, which is a function of the intensity of the X-rays. Two different goniometer configurations are used: θ-θ configuration, with fixed sample while the tube and the detector rotate around it, and θ-2θ configuration, where the sample is tilted by an angle θ and the X-ray tube is fixed [74].

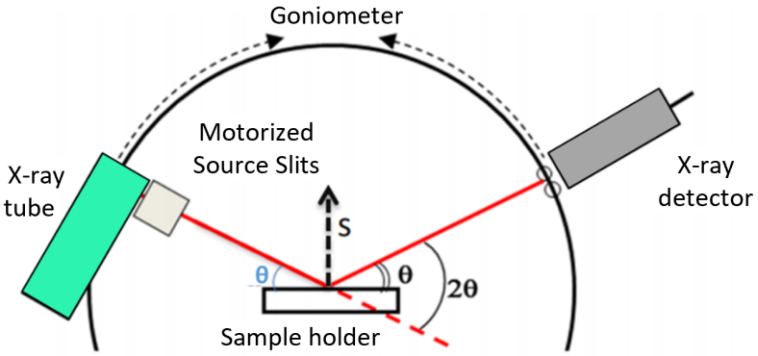

Figure 3.21. Schematic of an X-ray powder diffractometer with Bragg-Brentano geometry.

In this work, X-ray diffraction analysis was performed using an apparatus with Bragg-Brentano θ-θ geometry (D8 Advance, Bruker, Germany) equipped with a LYNXEYE detector, using Cu Kα radiation (λ = 1.54178 Å) as X-ray source. Analyses were carried out

both on bulk sample (on surface or on cross section) cut from tiles of prepared UHTCMCs, both on powder for polymer-derived ceramics. Spectra were collected from 10 to 80° with a step of 0.02 and a step time 0.5 s.

3.3.1.3 Fourier transform infrared (FTIR) spectroscopy

Fourier transform infrared (FTIR) spectroscopy is the most common method of infrared spectroscopy, since it is faster, more sensitive and precise than older techniques [75]. Infrared (IR) spectroscopy is an analytical technique based on the interaction of infrared radiation with matter, which causes vibrational transitions in chemical bonds.

IR light is the electromagnetic radiation with wavelengths longer than those of visible light but shorter than those of radio waves, ranging from 700 nm to 1 mm. The region of greatest interest for spectroscopy is between 2.5 and 25 μm for the study of fundamental vibrations and the rotation-vibration of small molecules [76]. In this spectral region, molecules involve several vibration modes: symmetric or asymmetric stretching alters the bond length, whilst bending vibrations consist of changing the bond angle, through twisting, rocking, wagging, and scissoring [77] (Figure 3.22). A vibrational mode absorbs light if a periodic change in the dipole moment of the molecule occurs; such vibrations are said to be infrared active [78].

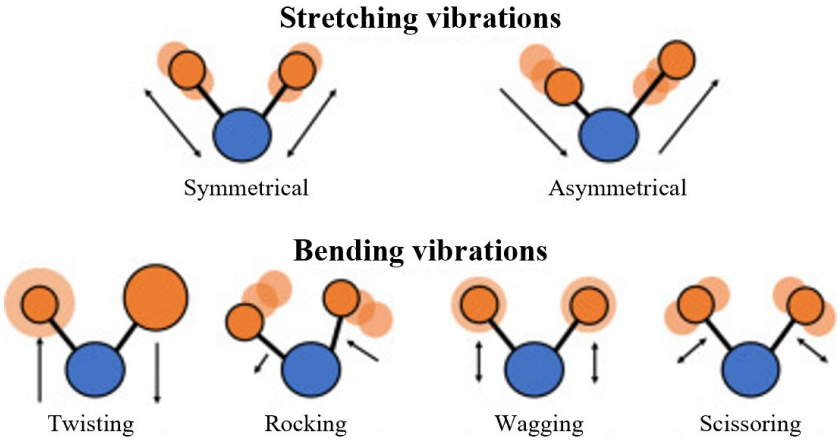

Figure 3.22. Vibrational modes of bonds [77].

IR spectroscopy is used to study and identify functional groups within a sample, since different functional group absorbs different frequency of IR radiation, determined by the strengths of the bonds involved and the mass of the component atoms. Each molecule has a characteristic spectrum often referred to as the “fingerprint”, thus a molecule can be identified by comparing it to a spectra data bank [79]. IR spectroscopy is very useful in

the identification and structure analysis of a variety of substances, including both organic and inorganic compounds.

In a FTIR spectrometer, IR light emitted by source passes through a Michelson interferometer, which is constituted by three mirrors, and the sample; since the position of the moving mirror varies over time, and consequently the distribution of light, the transmittance of the sample will vary over time. Light output us recorded as a function of mirror position in a "interferogram", that is turned into a spectrum thanks to Fourier transform (Figure 3.23). An IR spectrum is reported in a graph of IR light absorbance/transmittance on the vertical axis vs. wavenumber or frequency on the horizontal axis (expressed as cm^{-1}) [80].

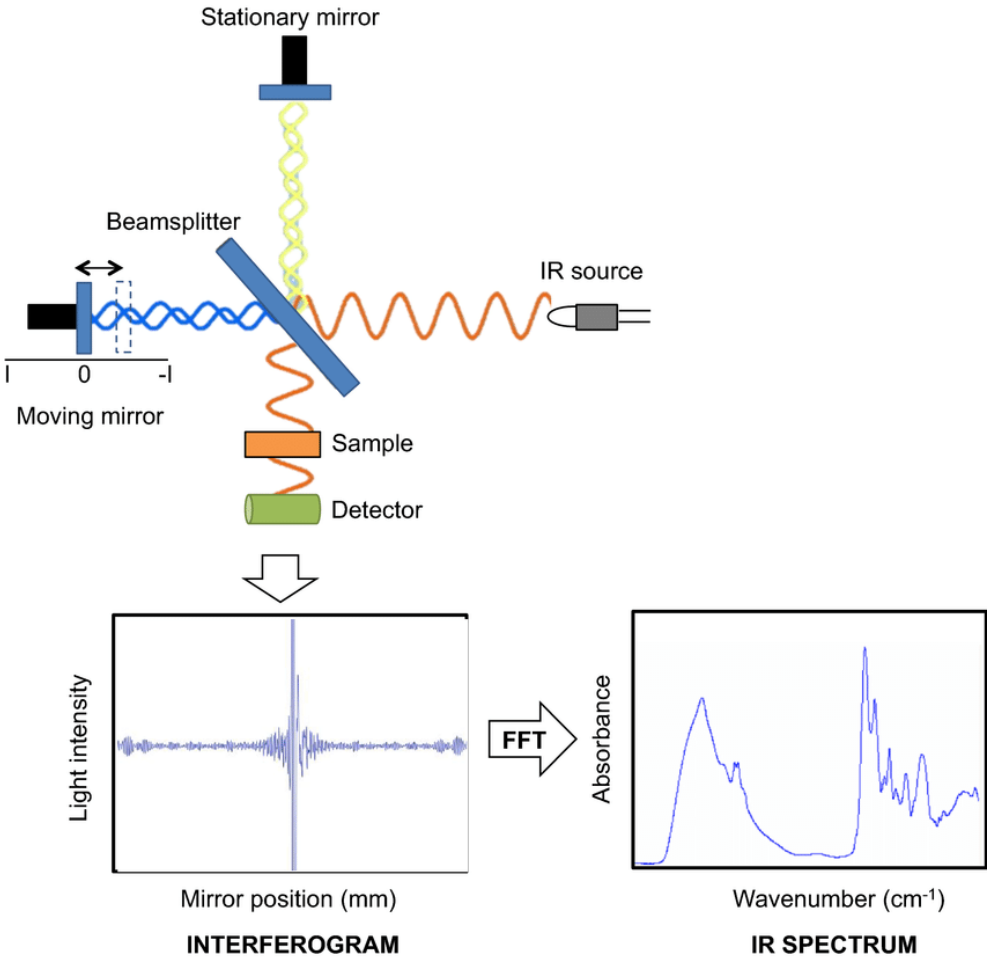

Figure 3.23. Scheme of a FT-IR spectrometer, highlighting the conversion of interferogram to IR spectrum through Fourier transform [80].

In addition to the classic absorption/transmission infrared spectroscopy, there is a technique based on the principle of attenuated total reflectance (ATR). In this case, the

IR light passes through a crystal with a high refractive index, transparent to the IR, and undergoes multiple internal reflections. This internal reflectance creates an evanescent wave that extends beyond the surface of the crystal into the sample, which is in contact with the crystal (Figure 3.24). After interacting with sample, the wave returns to the crystal and will be attenuated in regions of IR light in which the sample absorbs energy, finally exits the opposite end of the ATR crystal and is directed to the detector [81].

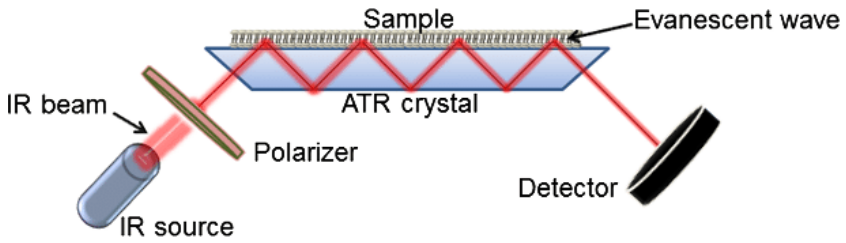

Figure 3.24. Schematic representation of an ATR-FTIR system [82].

The instrument employed in this work was a FTIR spectrometer (Nicolet IS5, Thermo Fisher Scientific, U.S.A.) equipped with the accessory for ATR analysis with a monolithic diamond crystal (iD7, Thermo Fisher Scientific, U.S.A.). By using this equipment through the ATR technique, it is possible to analyse liquid, bulk solids and powder samples avoiding long preparation times and the common problems related to hygroscopicity of the materials (e.g. KBr) typically used for FTIR analysis, also the main causes of error due to the poor reproducibility of the preparation methods can be limited. ATR-FTIR analyses were carried out on raw materials, polymer precursors and pyrolysis products in order to investigate the structural modification. All the spectra were acquired by accumulation of 16 scans covering the 4000 to 400 cm^{-1} range at a resolution of 2 cm^{-1}.

3.3.1.4 Non-contact profilometry

Profilometry is a technique used to scan and map the surface of an object. In conventional contact profilometry, a mechanical stylus comes in contact with the surface to trace the surface features, however this method tends to alter or even damage the surface features. On contrary, non-contact optical profilometer is able to get the surface morphology without damaging it since this type uses a light.

Optical profilometers can be based on very different measurement principles, including the interferometric measurement mode. This method is based on the principle of interferometry: the light beam source is split into two identical rays that follow two

different paths, a beam strikes the samples while the other strikes a mirror, until recombining at the beam splitter and then focusing on the detector (CCD sensor); the difference of the optical path followed by each ray generates a phase change, which results in the interference figure [83,84]. A simplified schematic of an interferometric profilometer is shown in Figure 3.25.

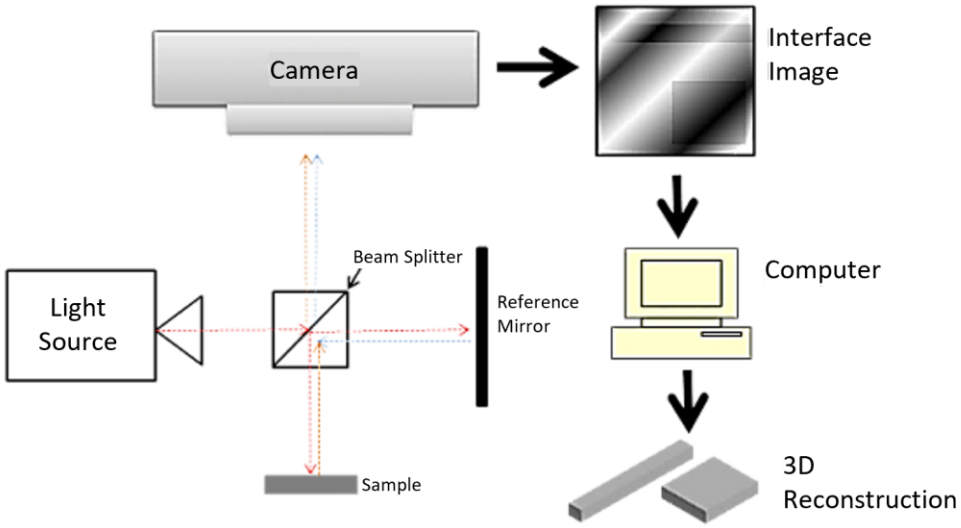

Figure 3.25. Schematic of an interferometric profilometer (from www.nanoscience.com).

In this thesis, the topological characterization of the surface of the as-obtained samples fabricated via slurry infiltration and six PIP cycles was performed with the interferometric profilometer Contour GT-K 3D (Bruker, Germany) on 8 × 8 mm^2 areas of the surface of 2D carbon fibre-reinforced composites. Then the data were analysed using the commercial software Vision64 Map.

3.3.1.5 Digital microscopy

A digital microscope is a variation of a traditional optical microscope that uses optics and a digital camera to output captured images to a computer monitor. In this type of microscopes, the optics for the human eye are omitted and observation, image capture and measurement are executed through an on-screen interface.

A digital microscope can perform the same tasks as an optical microscope, but with extra benefits. A primary difference between these microscopes is the magnification: while optical microscopes determine the magnification by multiplying the lens magnification by the eyepiece magnification, digital microscopes use the computer monitor leading to higher magnification. Digital microscopes provide better-quality

images since they project the images directly to the camera, besides features such as anti-halation to reduce glare, HDR for better contrast and colour, and lighting options to provide more texture. Moreover, many digital microscopes use computer software that can perform advanced tasks, such as measuring the distance from pixel to pixel in 2D and in 3D for length, width, diagonal, and circle measurement, or 2D and 3D tiling to create panoramic [85–87].

In this work, a digital microscope (RH-2000, Hirox Europe, France) (Figure 3.26) was used for failure analysis observing the deformation of specimens after bending tests at RT and 1500 °C, and for evaluation of fracture toughness of fibre-reinforced composites. Furthermore, this instrument was particularly suitable for capturing high-resolution images of modified surfaces after oxidation tests.

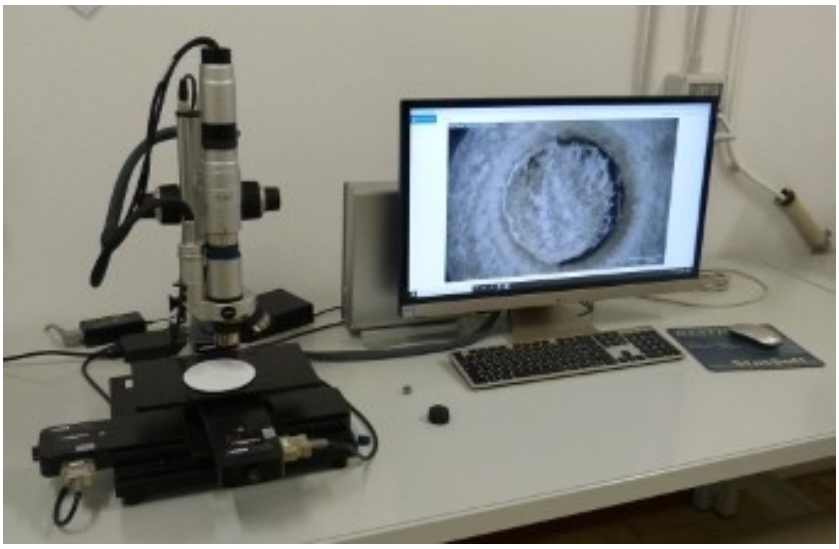

Figure 3.26. Digital microscope Hirox RH-2000 at CNR-ISTEC.

3.3.1.6 Scanning electron microscopy

Scanning electron microscopy (SEM) is one of the most employed imaging techniques in material science because it allows the observation of objects with magnifications and resolution over 1000 times higher than optical microscopy. The acronym SEM is used interchangeably to designate the technique and the instrument itself.

A scanning electron microscope (SEM) is a microscope that uses a focused beam of electrons to scan the surface of a sample in a raster pattern to create a high-resolution image.

Essential components of a typical SEM [88–90] (Figure 3.27) include:

- electron source (gun), constituted by a cathode and an anode, at the top of the column, that produces the electron beam. Electron sources are broadly divided into thermionic and field emission. In the former the beam is emitted thermionically, thanks to an applied current to the cathode that causes it to heat up until its electrons have enough energy to escape the surface. Tungsten filaments are typically used in thermionic gun because it has the highest melting point and lowest vapor pressure of all metals; other emitters can be single crystals of LaB_6 and CeB_6 but they require higher vacuum, thereby increasing the overall cost. Field emission guns (FEGs) use a strong electrostatic field applied to the sharp tip of a tungsten wire to induce electron emission. These sources are divided in cold-cathode type (using single crystal emitters) and Schottky type, which uses as emitters tungsten single crystals coated with ZrO_2 and is thermally assisted, combining the benefits of field emission and thermionic effect. FEG sources develop a smaller emission area than thermionic sources, resulting in enhanced image quality, however the use of electrostatic field in ultra-high vacuum makes them more expensive. Anode, placed nearby the cathode, attracts the electrons and accelerates them down the column;
- electromagnetic lenses, constituted by two condenser lenses, which reduce the electron beam dimension into a spot, scanning coils that deflect the beam in the x and y directions in order to scan a rectangular area, and a final objective lens which focuses the beam on the sample surface making a further reduction of the spot [91,92];
- analysis chamber, where the interaction between the electron beam and the sample takes place under vacuum;
- detectors for collecting the several signals resulting from the electron – matter interaction;
- software for the reconstruction of image. Each pixel of the resulting image is synchronized with the position of the beam on the analysed specimen, thus the resulting image in grey scale is a distribution map of the intensity of the signals emitted from the scanned area.

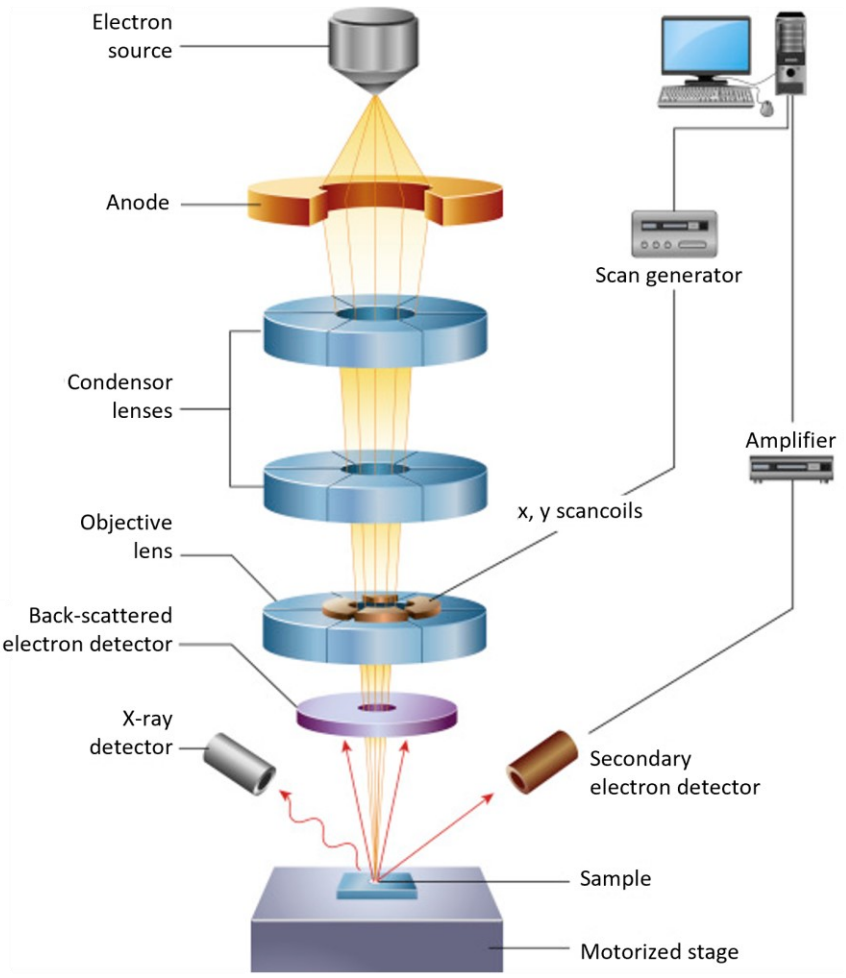

Figure 3.27. Schematic of a Scanning Electron Microscope (SEM), showing the principal components [89].

When the primary electron beam hits the sample, the electrons generate scattering phenomena and absorption within a teardrop-shaped volume of interaction (Figure 3.28). The interaction volume may extend from less than 100 nm to approximately 5 µm into the material; its depth and diameter depends on the beam energy as well as the specimen's density of the specimen, for instance it will be larger for a higher accelerating voltage, smaller for samples containing elements with a higher atomic number Z [90].

The electron-matter interaction causes several signals [89,90,93] (Figure 3.28), among these the most commonly analysed are secondary electrons, backscattered electrons (BSEs) and X-rays:

- Secondary electrons (SEs) are formed as a result of inelastic interactions with electron clouds of sample atoms, causing emission of electrons from the sample. They have low energy (< 50 eV) and originate few nanometres in deep from the surface, thus they provide information on the sample morphology;

- Backscattered electrons (BSEs) are high-energy (> 50 eV) electrons reflected back after elastic interaction between the electrons of the beam and the atomic nuclei in the specimen. They come from deeper regions in the volume interaction. BSEs do not allow a detailed morphological analysis but are useful for revealing chemical compositional differences, since heavy element (high atomic number) backscatter electrons more strongly than light elements and consequently they appear brighter in the resulting image;
- X-rays are high-energy photons due to the excitation of deep electrons. They are used for elemental microanalysis (see Section 3.3.7).

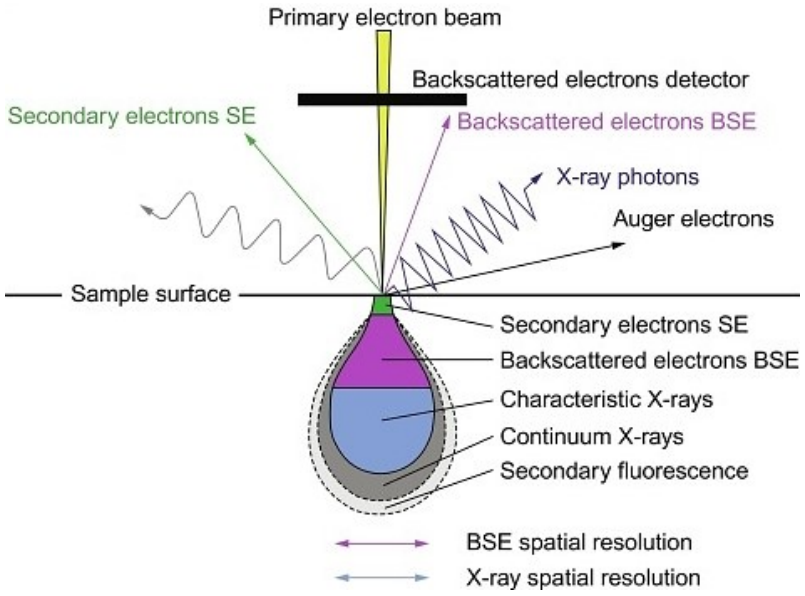

Figure 3.28. Electron volume interaction with matter and various type of generated signals [93].

The SEM has unique advantages, for instance it allows to acquire high resolution images even at high magnification, obtaining continuous enlargements without using separate objectives, it has a high depth of field which allows focusing on a large area of the sample despite irregular surfaces; also, the preparation of the specimens is quite simple. However, conventional SEMs require conductive solid materials stable in vacuum in the order of 10^{-5}-10^{-6} representing application limits. In the case of insulating materials, the surface can be made electrically conductive by graphite tape or glue, or by applying a conductive coating on the surface. In addition, instruments operating in low vacuum or environmental exist that enable also unstable and wet materials to be observed by electron microscopy.

The equipment employed in this work was a FE-SEM, i.e. field emission gun-scanning electron microscope, with W-ZrO_2 source with Schottky effect and hot cathode gun (Zeiss Sigma, Carl Zeiss Microscopy Gmbh, Germany) equipped with detectors for secondary electrons SE2, low energy electrons SE1 and backscattered electrons BSE. Polished specimens for microscopy were prepared by cutting cross sections from samples, mounting them in epoxy resin and polishing them using semi-automatic polishing machine (Tegramin-25, Struers, Italy); then, they washed with ethanol and acetone in an ultrasonic bath and finally cleaned with a plasma cleaner (Colibrì Plasma RF 50 KHz, Gambetti, Italy) at 40 W for 5 min. For SEM analysis, all the samples were mounted on aluminium stubs with carbon tape. Non-conductive samples required carbon or metal coating; oxidized samples were coated with a thin layer of carbon using a turbo-pumped sputter coater (Q150T ES, Quorum Technologies Ltd, UK).

Image analysis with a commercial software package (Image-Pro Plus® Analyzer 7.0, Media Cybernetics, U.S.A.) was carried out onto SEM micrographs of polished sections to determine the amounts and the mean grain size (m.g.s.) of the phases (C_f, ZrB_2, SiC).

3.3.1.7 Energy dispersive X-ray spectroscopy

Energy dispersive X-ray spectroscopy (EDS or EDX), also called energy dispersive X-ray microanalysis (EDXMA), is a technique used for the elemental analysis or chemical characterization of materials [90].

EDS system is typically integrated with an electron microscopy instrument such as scanning electron microscope (SEM) or transmission electron microscope (TEM). EDS technique analyses X-rays that are emitted by the sample during interaction with the electron beam of the electron microscope. When the incident beam hits the sample, an electron in the inner shell bound to the nucleus is ejected from the shell creating a vacancy, which is filled by an electron from the outer shell. The energy difference between the higher-energy shell and the lower-energy shell may be released in the form of X-ray fluorescence. As shown in Figure 3.29, the movement of an electron to the K shell from the L and M orbitals produces K_α and K_β emission respectively, while L_α X-ray is generated when an electron from the M shell fills a vacancy in the L shell. The cumulative spectrum of the emission energies is characteristic of the chemical element from which

the X-ray was emitted, thus it can be used to identify the elemental composition of the sample [90].

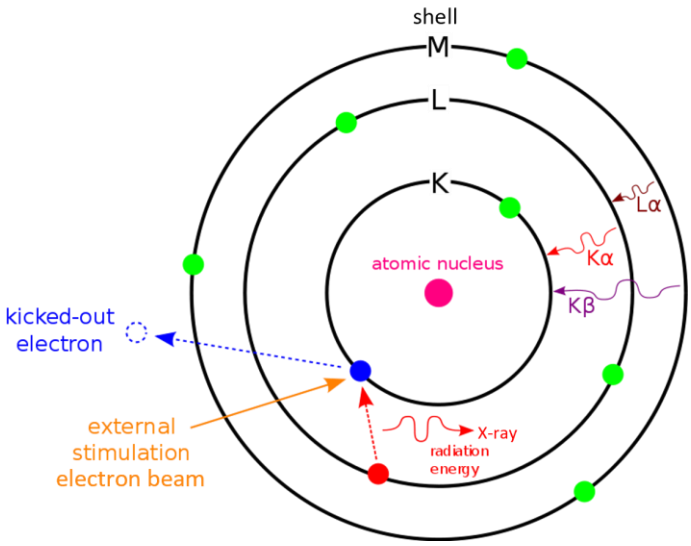

Figure 3.29. Illustration of the emission mechanism of X-rays.

EDS probe allows precise qualitative analysis of very small components. It can provide also quantitative analysis, even though accurate results are difficult to obtain for light elements [94]. Heavy metal targets require high energy incident beam to emit X-rays, however higher accelerating voltages lead to a larger depth of penetration of the electronic beam, negatively affecting the accuracy on elements with lower atomic weight.

In this work, EDS (Oxford Energy X-act, Oxford Instruments, UK, interfaced by INCA software) coupled to FE-SEM was used for qualitative and semiquantitative analysis. Since different elements that spanning from light to heavy atomic weight (B < C < Si < Zr) were present in prepared materials, the operating voltage was set between 5 and 10 keV. EDS microanalysis was performed by using an aperture of 60 µm and a working distance of 8.0 mm. To optimize the semiquantitative measurements, the detector was calibrated with cobalt standard element.

3.3.2 Mechanical testing

3.3.2.1 Elastic modulus

A solid material under tension or compression undergoes strain in the direction of the applied load. When the stress is relatively low, elastic deformation occurs, meaning that the material returns to its original shape after the load is removed.

Elastic modulus (E), also known as Young's modulus, is the measurement of a material's resistance to elastic deformation when stress is applied [95]. It is defined through the Hooke's law [95] as (4):

$$E = \sigma/\varepsilon \quad (4)$$

where σ is stress, which is the force causing the deformation divided by the area on which the force is applied, and ε is strain, that is given by the ratio of the change due to the deformation in some parameter to the original value [96]. Elastic moduli are typically so large that they are expressed in gigapascals (GPa).

In a stress-strain curve of an object, in the elastic deformation region the strain is proportional to the applied stress and elastic modulus represents the slope of the linear part [95] (Figure 3.30).

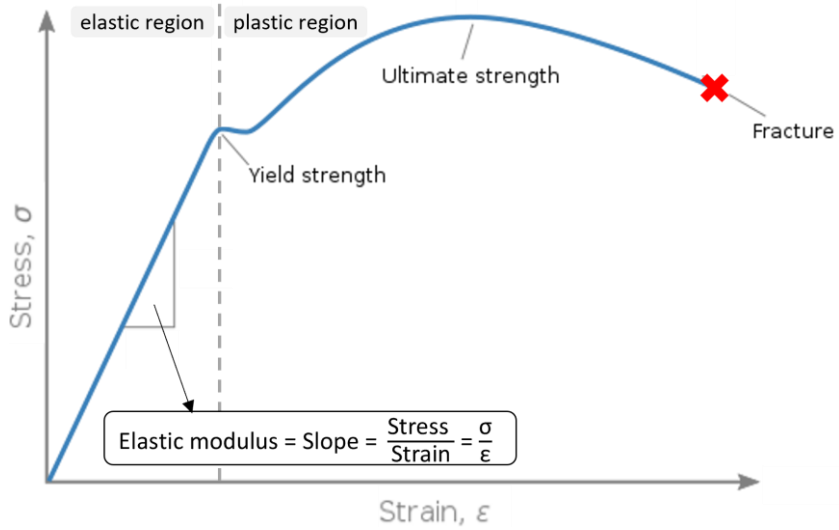

Figure 3.30. Typical stress-strain curve of a ductile material. The elastic modulus is defined as the slope of the curve in the elastic deformation region.

The methods used to measure the elastic modulus are divided in two groups: static and dynamic. In static methods, a known static load is applied on the specimen by a dynamometer and the induced deformation is measured with strain gauges. These methods give reliable results for ductile materials, but they are not recommended for rigid materials, such as ceramics, which necessitate high loads to induce a little deformation before rupturing the specimen [97]. Dynamic methods have the advantage that the stresses used to measure the moduli are far below those at the elastic limit, thus the specimens are not altered by the stresses and different measurements can be made

on the same sample [98]. Two types of dynamic tests are commonly conducted to measure the elastic constants:

- ultrasonic wave technique, based on the measurement of the propagations speed of ultrasounds through a specimen of known geometry, that is correlated to elastic properties;
- resonant frequencies, in which oscillations are induced on the specimen, allowing to identify the resonant frequency of the material and from it calculate the modulus. Specimens are excited mechanically, either by an impulse or continuously through the rod supports, and in different ways in such a way to favour the measurement of the elastic modulus or the shear modulus [98]. The elastic modulus (E) and the shear modulus (G) can be calculated through the equations (5) and (6), respectively:

$$E = 0.946\left(\frac{m{f_n}^2}{b}\right)\left(\frac{L}{t}\right)^3\left[1 + 6.585\left(\frac{t}{L}\right)^2\right]10^{-9} \quad (5)$$

$$G = \frac{4Lm{f_t}^2}{bt}\left[\frac{1+\left(\frac{b}{t}\right)^2}{4-2.521\frac{t}{b}\left(1-\frac{1.991}{e^{\pi\frac{b}{t}}+1}\right)}\right]\left[1+\frac{0.00851b^2}{L^2}\right] - 0.060\left(\frac{b}{L}\right)^{\frac{3}{2}}\left(\frac{b}{t}-1\right)^2 \quad (6)$$

where f_n is the natural frequency (Hz), f_t is the torsional frequency (Hz), m is the mass (g), and b, L and t are the width, length and thickness (mm) respectively [99,100].

In this work, continuous resonance technique was used to determine the Young's and shear moduli of the composites prepared via powder slurry infiltration and six PIP cycles. The resonant frequencies were measured on pitch-based carbon fibre-reinforced UHTCMCs on rectangular section bars of 60 mm (length) × 10 mm (width) × as-processed (~2 mm) thickness, and on PAN-based carbon fibre-reinforced UHTCMCs on rectangular section bars of 60 mm × 10 mm × 2.5 mm for sample 0/0°, 60 mm × 10 mm × 2.5 mm and 68 mm x 7 mm x 2.2 mm for sample 2D_tw, 60 mm × 10 mm × 2.5 mm and 60 mm × 5 mm x 1.7 mm for sample 2D_pl, and 105 mm × 16.7 mm x 3.5 mm for sample 2.5D.

Measurements were performed by varying the frequency of the oscillations using an impedance analyser (HP 4194A, USA), see Figure 3.31a. According to ENV 843-2 standard, the test-piece was suspended in loops of cotton threads, using one loop to drive the vibration transmitted by the exciting transducer, and the other which was connected to the detecting transducer to detect it. Different setups were used for measuring the

natural frequency to calculate E (as shown in Figure 3.31b) and the torsional frequency to estimate G (as shown in Figure3.31c).

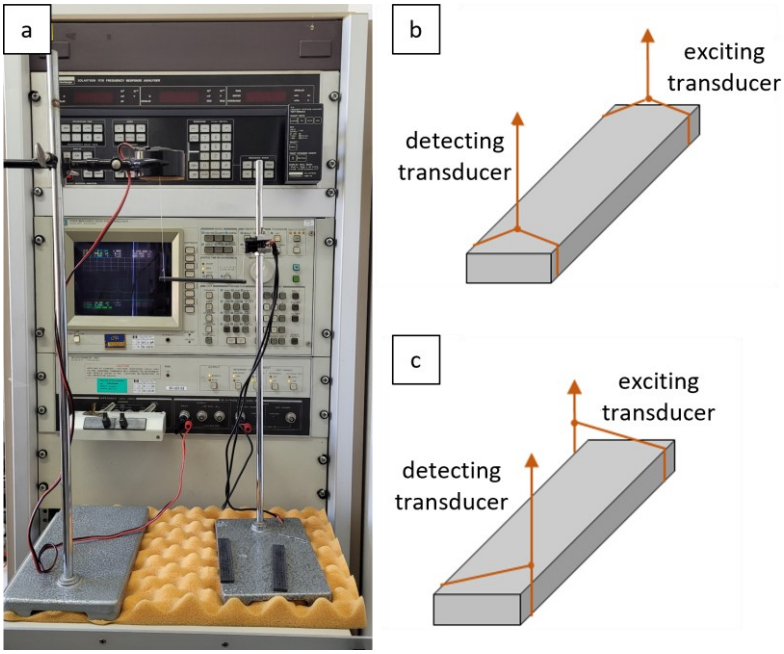

Figure 3.31. (a) Impedance analyser (HP 4194A, USA). Representation of the experimental setups used to determine the (b) elastic modulus and (c) shear modulus by continuous resonance technique.

3.3.2.2 Flexural strength

Flexural strength, or bending strength, is a material property defined as the maximum stress that can be applied to that material before it yields [95]. The most common way of obtaining flexural strength of a material is by employing a bending test, in which a bar having cylindrical or rectangular cross-section is bent until fracture or yielding using three- or four-point flexural setup [101,102].

The flexural strength of monolithic ceramics is dependent on several factors such as size, shape, grain size, density, distribution of flaws and pores. Large grains, surface flaws and residual porosity can degrade mechanical performance, in particular pores are deleterious because they act as defects where stresses are concentrated leading to a catastrophic failure [103].

Determining the bending strength of fibre-reinforced ceramic composites is more difficult due to the synergistic effects between matrix and fibres. Moreover, the strength is strongly influenced by fibre orientation because of the intrinsic anisotropy. For specimens of unidirectional fibre-reinforced composite in bending with the applied load perpendicular to the fibre orientation, the load is fully transferred to the fibres and the

maximum strength value is obtained; differently, when the load is parallel to the fibres, the bar rupture occurs in a brittle mode because the fibres acting as a defect not as a reinforcement [104]. Samples with complex fibre architecture give rise to more complex fracture modes.

In this Thesis, flexural tests were experienced both on large bars and small bars.

Specimens of 60 mm (length) × 10 mm (width) × as-processed thickness were cut from the pitch-based carbon fibre-reinforced composites prepared via powder slurry and six PIP cycles (i.e. 0/0°, 0/90° and 2D samples) and tested at room temperature. Larger specimens allow to work with a higher and consequently more favourable span-to-thickness ratio; in these conditions it is expected to reach an increase of the ultimate stress by limiting the interlaminar shear stresses during bending moment. Large bars of pitch carbon fibre-reinforced samples 0/0°, 0/90° and 2D were fractured with a span-to-thickness ratio (s/t) of 20 and a strain rate ($\dot{\varepsilon}$) of 8×10^{-4} s^{-1} by using a universal testing machine (Z050, Zwick Roell, Germany). According to ASTM C1341-13 standard for continuous fibre-reinforced advanced ceramic composites [105], three-point bending tests were carried on 0/0° and 0/90° composites with a lower span of 50 mm and 44 mm respectively, while 2D composite was tested through four-point bending with a lower span of 51 mm and an upper span of 17 mm (see three-point and four-point-L/3 geometries used in Figure 3.32a and b, respectively). Four-point bending test was chosen instead three-point bending test because the former allowed to expose at least 8 inter-bundle voids (typical critical flaws of 2D composites [106]) to the maximum stress, and so to avoid invalid tests due to fractures outside the section under the maximum stress.

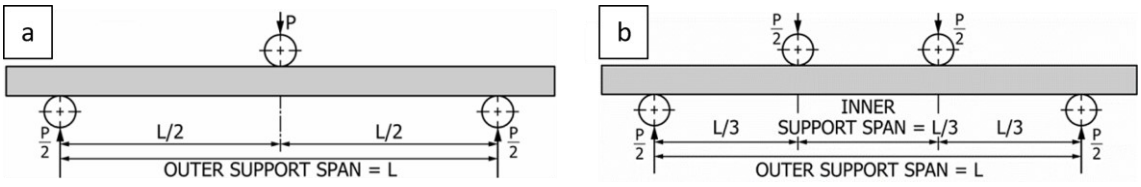

Figure 3.32. Loading geometries reported in ASTM C1341-13 [105] used for the bending tests at R.T. on large specimens cut from composites prepared via powder slurry infiltration and PIP: (a) three-point loading geometry for samples 0/0° and 0/90°, (b) four-point-L/3 loading geometry for sample 2D.

The mechanical behaviour at room temperature of PAN-based carbon fibre-reinforced composites were investigated on bars both with horizontal and vertical skins

were tested, specifically: bars of 60 mm × 10 mm × 2.5 mm (length × width × thickness) with horizontal skins for 0/0°, 2D_tw and 2D_pl samples, and bars with vertical skins 68 mm x 7 mm x 2.2 mm, 60 mm × 5 mm x 1.7 and 105 mm × 16.7 mm x 3.5 mm for samples 2D_tw, 2D_pl and 2.5D, respectively. All the bars were fractured using the three-point fixture. Bars with horizontal skins were tested in the same conditions reported above (i.e. s/t ratio of 20, $\dot{\varepsilon}$ of 8×10^{-4} s^{-1}), while specimens with vertical skins were tested with a ratio of cross-head speed to thickness of 5.8.

Bars with dimensions 25.0 mm × 2.5 mm × 2.0 mm (length by width by thickness, respectively) were cut from the sample 0/0° reinforced with pitch-based C_f and samples prepared via hot pressing to carry out tests both at room temperature and at high temperature. This is because the apparatus working at high temperature is equipped with a semi-articulated fixture that can allocate specimens with maximum length of 30 mm. Hence, same testing conditions at RT and high temperature were chosen in order to enable a direct comparison among flexural strengths. For the tests at R.T., the specimens were fractured by a screw-driven load frame (Z050, Zwick-Roell, Germany) using a fully-articulated steel four-point fixture with a lower span of 20 mm and an upper span of 10 mm (Figure 3.33) and a cross-head rate of 1 mm/min, following the guidelines of advanced technical ceramics ISO 14704:2016(en) [107].

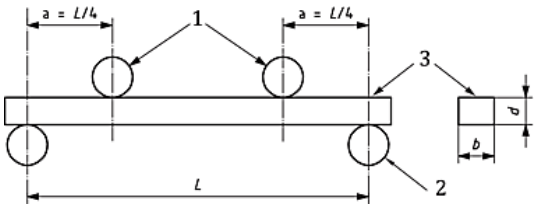

Figure 3.33. Four-point geometry reported in ISO 14704:2016(en) [107].

For the tests at high temperature (1000–1500 °C), bending strength tests were performed using a screw-driven load frame (Instron mod. 1195, Instron, USA) equipped with a furnace (HTTF mod. 924, Severn Furnaces Limited, UK), see Figure 3.34, using a fixture with a lower span of 20 mm and an upper span of 10 mm and at a cross-head rate of 1 mm/min; the specimens were mounted on the four-point alumina fixture and heated up with a rate of 10 °C/min to the target temperature and held for 15 min before the load application.

Figure 3.34. Screw-driven load frame (Instron mod. 1195, Instron, USA) equipped with a furnace (HTTF mod. 924, Severn Furnaces Limited, UK) for bending tests at high temperature.

3.3.2.3 Fracture toughness

Fracture toughness is a property used to describe the ability of a material containing a crack to resist fracture [108]. It is denoted K_{Ic}, which is the plane strain fracture toughness, i.e. the critical value of stress intensity factor K in mode I loading measured under plane strain conditions that leads to brittle fracture [109]. K_{Ic} value is relatively high for ductile materials and low for brittle materials, such as ceramics. Several methods are known for determining this parameter on ceramic materials [110] (Table 3.4).

Table 3.4. Fracture toughness test methods for conventional ceramics [110].

Specimen	Method and fracture surface of specimen	Specimen	Method and fracture surface of specimen
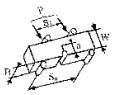	SEPB  (single edge precracked beam)	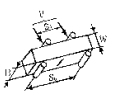	SCF  (surface crack in flexure)
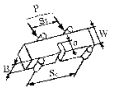	SENB  (single edge notched beam)	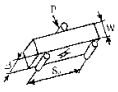	IS  (indentation strength)
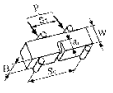	CNB  (chevron notched beam)	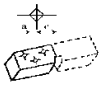	IF (indentation fracture)

Among these, indentation tests (IF in Table 3.4, e.g. Vickers hardness test [111]) have become quite popular for bulk ceramics due to the simplicity of the method. In this method, a hard indenter penetrates the specimen surface and induces the formation of cracks departing from the corners of the indent, which length is correlated to material fracture toughness. However, this method does not enable reliable values to be obtained for fibre-reinforced composites, because crack propagation can be easily stopped due to the presence of fibres. Therefore, techniques based on bending test on beams with a notch, on which all the stresses are concentrated, are preferred for the evaluation of fracture toughness in composite materials. In single edge notched beam (SENB), a flat notch is introduced; however, the difficulty in introducing a notch with a radius below 25 µm, which is needed for a good determination of K_{Ic} [112], tends to give scattered data. Single edge pre-cracked beam (SEPB) states that the flat notch, like SENB, is introduced and the beam is pre-cracked at the notch tip at low loads; this method allows for more accurate results, but it can be difficult to initiate the crack in presence of fibre reinforcement. According to the chevron notched beam (CNB) method, an inverse V-notch is introduced by diamond blades in rectangular bars; when the load is applied during flexural test, the crack starts at the tip of the triangle and propagates initially stable, then it spreads catastrophically. This method has the advantage of a precise notch without problem of curvature radius at the tip, even in fibre-reinforced materials.

By applying CNB method, fracture toughness is calculated starting from the maximum load (P max) measured in a four-point bending test of a V-notched beam with known geometry trough "slice model equations" of Munz [113]. The CNB model and these equations are reported in Figure 3.35.

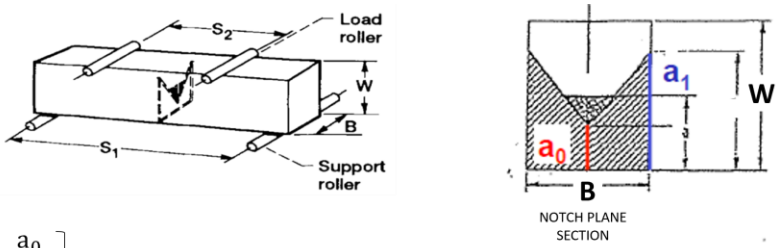

$$\left.\begin{aligned}\alpha_0 &= \frac{a_0}{W}\\ \alpha_1 &= \frac{a_1}{W}\end{aligned}\right\} \rightarrow y^* = (3.08 + 5\alpha_0 + 8.33\alpha_0^2)\frac{(S_1 - S_2)}{W}\left(1 + 0.007\sqrt{\frac{S_1 S_2}{W^2}}\right)\left(\frac{\alpha_1 - \alpha_0}{1 - \alpha_0}\right)$$

$$\downarrow$$

$$K_{Ic} = \frac{P_{max}}{B\sqrt{W}} y^*$$

Figure 3.35. Chevron notched beam (CNB) model and equations for the determination of K_{Ic}.

In this work, the fracture toughness (K_{Ic}) was evaluated by four-point bending test on chevron-notched beams (CNB), following the standard of advanced technical ceramics EN 14425-3:2010. Test bars, with dimensions 25.0 mm × 2.0 mm × 2.5 mm (length by width by thickness, respectively), were notched using a high precision cutting machine (T34, Missimi-Berney, Switzerland) with a 0.1 mm-thick diamond saw; the chevron-notch tip depth and average side length were about 0.12 and 0.80 of the bar thickness, respectively. The subsequent flexural tests were carried out both at room temperature and high temperature (i.e. 1500 °C under Argon flow), using the same machines used for bending tests, but with a cross-head speed of 0.05 mm/min. The specimens, at least three for each test on composites, were fractured using four-point fixtures with lower span of 20 mm and upper span of 10 mm.

3.3.3 Thermal properties

3.3.3.1 Thermogravimetry and Differential scanning calorimetry

Thermogravimetric analysis or thermal gravimetric analysis (TGA) is a thermoanalytical technique that determines changes in sample mass as a function of temperature and time, during a specific temperature program and in a defined atmosphere. TGA analyser involves the use of a thermobalance (a combination of an electronic microbalance with a furnace and appropriate temperature controller) to monitor the weight variation of the sample due to physical or chemical transformations [114], such as dehydration, decomposition with the release of volatiles, oxidation, adsorption or desorption of gas (Figure 3.36).

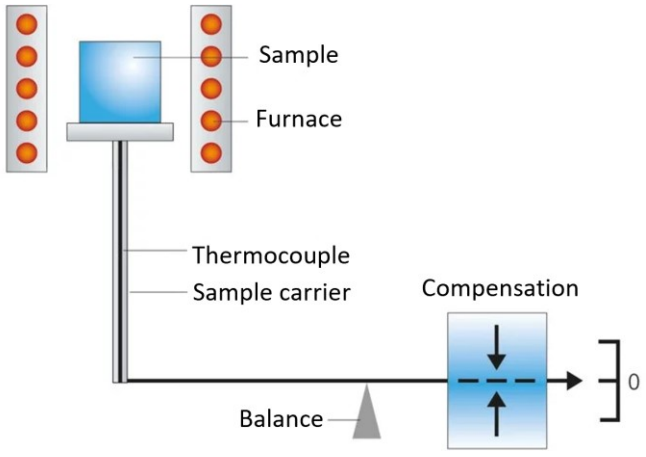

Figure 3.36. Scheme of the measuring principle of thermogravimetric (TGA) analysis (from www.netzsch-thermal-academy.com)[114].

The result is represented as a thermogravigram, a plot which reports in abscissa the temperature or time versus the mass variation as absolute or percentage value.

Differential scanning calorimetry (DSC) measures the heat flux required to keep at the same temperature a sample and a reference material which does not show transitions in the temperature range of analysis, during a controlled thermal program in a controlled atmosphere. The crucibles containing the sample and the reference are connected to two thermocouples and subjected to the same thermal cycle (Figure 3.37), allowing to determine the heat flow difference due to chemical reactions or structural transformations: negative heat changes are associated with exothermic transformations [115], such as crystallization, chemical or physical adsorption, while positive ones indicate endothermic transformations such as melting, sublimation, desorption.

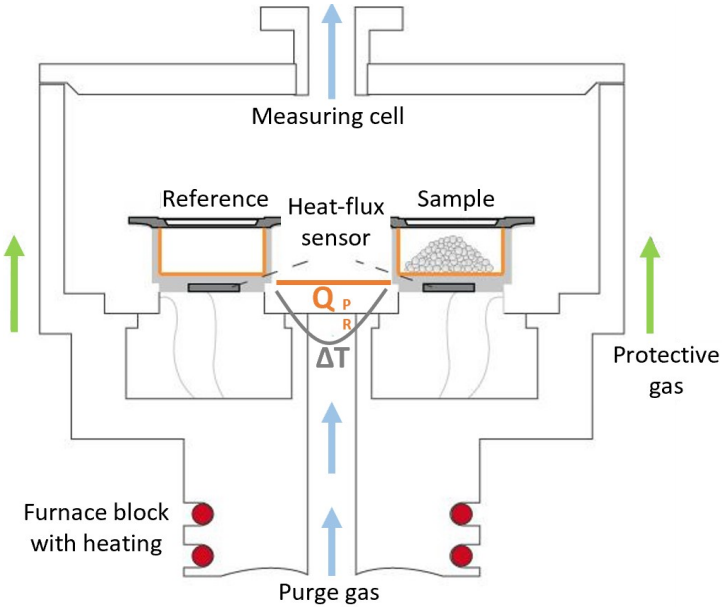

Figure 3.37. Scheme of the measuring principle of differential scanning calorimetry (DSC) analysis (adapted from www.netzsch-thermal-academy.com).

It is possible to apply this technique simultaneously, gathering more information from each test run. The term Simultaneous Thermal Analysis (STA) generally refers to the simultaneous application of TGA and DSC to the same in a single instrument.

In this work, TG and DSC analysis were carried out using a STA analyser (STA 449 C Jupiter, NETZSCH, Geraetebau GmbH, Germany). TGA were conducted to study the behaviour in oxidizing environment and identify the critical oxidation temperatures of composites prepared via slurry infiltration and repetitive PIP cycles. Regular specimens

sized 9 mm × 4 mm × 2 mm were cut from the reference sample, labelled 0/0°, cleaned with acetone in an ultrasonic bath and dried under IR lamp. Oxidation tests were carried out in synthetic air (composition: 80 vol% N2 + 20 vol% O_2, with 30 mL/min gas flow), up to 1350 °C with a heating rate of 10 °C/min. During TGA test, the mass variation was recorded continuously by the analyser (sensitivity 10^{-3} mg).

Simultaneous TG-DSC was carried out on obtained polymer-derived zirconium carbide to monitor the ceramic transformation. Analysis was carried on powders in an argon atmosphere up to 1500 °C at a heating rate of 10 °C/min.

3.3.4 Oxidation resistance

3.3.4.1 Air furnace oxidation testing

Bottom loading furnace is equipped with an electrically motorized elevator table, which as it rises into the furnace chamber, places the load into the heated zone. The all-around heating elements in side walls of the chamber ensures to achieve uniform heating. This type of furnace, thanks to the vertically moving elevator, simplifies the loading of the samples in the high-temperature chamber (Figure 3.38). Therefore, the furnace can be heated to the target temperature and only once it is reached the samples are introduced in the hot zone. In this way it is possible to evaluate the thermal shock resistance of materials which are directly exposed at the target temperature (e.g. 1500 °C or 1650 °C), thus the ability to withstand sudden changes either during heating and cooling are tested, also potential oxidation phenomena that may occur at lower temperature are by-passed.

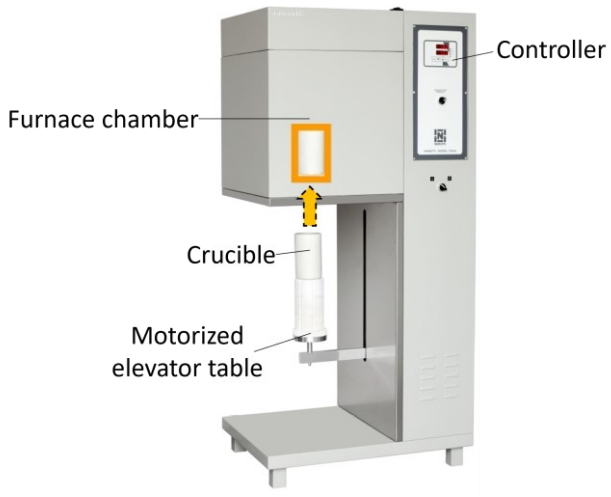

Figure 3.38. Bottom loading furnace (Nannetti S.r.l, Italy) showing principal components.

In the present work, short term oxidation tests were carried out in order to evaluate resistance in extreme environments of composites produced through slurry infiltration and PIP technique. 10 mm × 10 mm × as-processed thickness plates were cut from 0/0°, 0/90° and 2D samples, cleaned with acetone in an ultrasonic bath and dried under a IR lamp. Tests were performed in a bottom loading furnace (FC18-0311281, Nannetti S.r.l., Italy) at 1500 °C and 1650 °C in air for 1 min and 5 min. The plates were put on a porous zirconia sample holder, resting on one of the two largest surfaces, and introduced in the furnace when the target temperature was reached. At the end of the oxidation stage, the samples were removed and left to cool naturally in air.

Specimens were weighed with an analytical balance (accuracy ±0.01 mg) before (w_{in}) and after oxidation test (w_{fin}). Mass variation was normalized over the initial surface area using equation: $\frac{\Delta m}{S} = \frac{w_{fin} - w_{in}}{S}$, in which S is the initial surface area, measured by calliper (accuracy ± 0.05 mm).

3.4 References

1. Sciti, D. *et al.* From random chopped to oriented continuous SiC fibers-ZrB_2 composites. *Mater. Des.* **63**, 464–470 (2014).

2. Sciti, D., Natali Murri, A., Medri, V. & Zoli, L. Continuous C fibre composites with a porous ZrB_2 Matrix. *Mater. Des.* **85**, 127–134 (2015).

3. Zoli, L. & Sciti, D. Efficacy of a ZrB_2–SiC matrix in protecting C fibres from oxidation in novel UHTCMC materials. *Mater. Des.* **113**, 207–213 (2017).

4. Zoli, L., Medri, V., Melandri, C. & Sciti, D. Continuous SiC fibers-ZrB_2 composites. *J. Eur. Ceram. Soc.* **35**, 4371–4376 (2015).

5. Vinci, A., Zoli, L., Sciti, D., Melandri, C. & Guicciardi, S. Understanding the mechanical properties of novel UHTCMCs through random forest and regression tree analysis. *Mater. Des.* **145**, 97–107 (2018).

6. Zoli, L. *et al.* Rapid spark plasma sintering to produce dense UHTCs reinforced with undamaged carbon fibres. *Mater. Des.* **130**, 1–7 (2017).

7. Sciti, D. *et al.* Properties of large scale ultra-high temperature ceramic matrix composites made by filament winding and spark plasma sintering. *Compos. Part B Eng.* **216**, 108839 (2021).

8. Vinci, A., Zoli, L., Galizia, P. & Sciti, D. Influence of Y_2O_3 addition on the mechanical and oxidation behaviour of carbon fibre reinforced ZrB_2/SiC composites. *J. Eur. Ceram. Soc.* **40**, 5067–5075 (2020).

9. Vinci, A. *et al.* Mechanical behaviour of carbon fibre reinforced TaC/SiC and ZrC/SiC composites up to 2100°C. *J. Eur. Ceram. Soc.* **39**, 780–787 (2019).

10. Vinci, A. *et al.* Influence of fibre content on the strength of carbon fibre reinforced HfC/SiC composites up to 2100 °C. *J. Eur. Ceram. Soc.* **39**, 3594–3603 (2019).

11. Medri, V., Capiani, C. & Gardini, D. Slip casting of ZrB_2-SiC composite aqueous suspensions. *Adv. Eng. Mater.* **12**, 210–215 (2010).

12. Medri, V., Mazzocchi, M. & Bellosi, A. ZrB_2-Based Sponges and Lightweight Devices. *Int. J. Appl. Ceram. Technol.* **8**, 815–823 (2011).

13. Vinci, A., Zoli, L. & Sciti, D. Influence of SiC content on the oxidation of carbon fibre reinforced ZrB_2/SiC composites at 1500 and 1650 °C in air. *J. Eur. Ceram. Soc.* **38**, 3767–3776 (2018).

14. Starfire® Systems Inc. StarPCS SMP-10. (2018).

15. Interrante, L. V. *et al.* Silicon-based ceramics from polymer precursors. *Pure Appl. Chem.* **74**, 2111–2117 (2003).

16. Kaur, S., Riedel, R. & Ionescu, E. Pressureless fabrication of dense monolithic SiC ceramics from a polycarbosilane. *J. Eur. Ceram. Soc.* **34**, 3571–3578 (2014).

17. Kaur, S. *et al.* Single-source-precursor synthesis of novel V_8C_7/SiC(O)-based ceramic nanocomposites. *J. Eur. Ceram. Soc.* **36**, 3553–3563 (2016).

18. Kaur, S., Fischer, S., Falta, J., Rezwan, K. & Wilhelm, M. High surface area SiC(O)-based ceramic by pyrolysis of poly (ethylene glycol) methacrylate-modified polycarbosilane. *J. Am. Ceram. Soc.* **102**, 7187–7197 (2019).

19. Konegger, T., Patidar, R. & Bordia, R. K. A novel processing approach for free-standing porous non-oxide ceramic supports from polycarbosilane and polysilazane precursors. *J. Eur. Ceram. Soc.* **35**, 2679–2683 (2015).

20. Süß, F. *et al.* Combination of PIP and LSI processes for SiC/SiC ceramic matrix composites. *Open Ceram.* **5**, (2021).

21. Larson, N. M. & Zok, F. W. In-situ 3D visualization of composite microstructure during polymer-to-ceramic conversion. *Acta Mater.* **144**, 579–589 (2018).

22. Boardman, L. D. (η^5-Cyclopentadienyl)trialkylplatinum Photohydrosilylation Catalysts. Mechanism of Active Catalyst Formation and Preparation of a Novel Bis(silyl)platinum Hydride. *Organometallics* **11**, 4194–4201 (1992).

23. Park, S. *et al.* Fabrication of three-dimensional SiC ceramic microstructures with near-zero shrinkage via dual crosslinking induced stereolithography. *Chem. Commun.* 4880–4882 (2009) doi:10.1039/b907923h.

24. FAQs - Starfire Systems. https://www.starfiresystems.com/faqs/.

25. J. B. Donnet, O. P. Bahl, R. C. Bansal, T. W. Carbon fibers. *Encyclopedia of Physical*

Science and Technology 431–455 (2001).

26. Park, S. J. & Heo, G. Y. *Precursors and Manufacturing of Carbon Fibers*. *Springer Series in Materials Science* vol. 210 (Springer, Dordrecht, 2015).

27. Wu, A. S. & Chou, T. W. Carbon nanotube fibers for advanced composites. *Mater. Today* **15**, 302–310 (2012).

28. Xu, Z. *et al.* Ultrastrong Fibers Assembled from Giant Graphene Oxide Sheets. *Adv. Mater.* **25**, 188–193 (2013).

29. Matsuhisa, Y. & Bunsell, A. R. Tensile failure of carbon fibers. in *Handbook of Tensile Properties of Textile and Technical Fibres* 574–602 (Woodhead Publishing, 2009). doi:10.1533/9781845696801.2.575.

30. Newcomb, B. A. Processing, structure, and properties of carbon fibers. *Compos. Part A Appl. Sci. Manuf.* **91**, 262–282 (2016).

31. Huson, M. G. High-performance pitch-based carbon fibers. in *Structure and Properties of High-Performance Fibers* (ed. Bhat, G.) 31–78 (Woodhead Publishing, 2017). doi:10.1016/B978-0-08-100550-7.00003-6.

32. Inagaki, M. & Kang, F. Engineering and Applications of Carbon Materials. in *Materials Science and Engineering of Carbon: Fundamentals* 219–525 (2014). doi:10.1016/b978-0-12-800858-4.00003-6.

33. Minus, M. L. & Kumar, S. The processing, properties, and structure of carbon fibers. *JOM 2005 572* **57**, 52–58 (2005).

34. Frank, E., Steudle, L. M., Ingildeev, D., Spörl, J. M. & Buchmeiser, M. R. Carbon fibers: Precursor systems, processing, structure, and properties. *Angew. Chemie - Int. Ed.* **53**, 5262–5298 (2014).

35. Dresselhaus, M. S., Dresselhaus, G., Sugihara, K., Spain, I. L. & Goldberg, H. A. *Graphite Fibers and Filaments*. vol. 5 (Springer Berlin Heidelberg, 1988).

36. Buckley, J. D. Carbon-carbon - An overview. *Am. Ceram. Soc. Bull.* **67**, (1988).

37. Bennett, S. C., Johnson, D. J. & Johnson, W. Strength-structure relationships in PAN-based carbon fibres. *J. Mater. Sci. 1983 1811* **18**, 3337–3347 (1983).

38. Strong, A. B. *Fundamentals of composites manufacturing: materials, methods and applications*. (Society of Manufacturing Engineers, 2008).

39. Otani, S. & Oya, A. Progress of Pitch-Based Carbon Fiber in Japan. in *Petroleum-Derived Carbons* (eds. Bacha, J. D., Newman, J. W. & White, J. L.) 323–334 (ACS, 1986). doi:10.1021/BK-1986-0303.CH022.

40. Korai, Y., Hong, S. H. & Mochida, I. Meso-scale texture of mesophase pitch and its spun fiber. *Carbon N. Y.* **36**, 79–85 (1998).

41. Mochida, I. *et al.* Microstructure of mesophase pitch-based carbon fiber and its

control. *Carbon N. Y.* **34**, 941–956 (1996).

42. Mochida, I., Yoon, S. H. & Korai, Y. Control of transversal texture in circular mesophase pitch-based carbon fibre using non-circular spinning nozzles. *J. Mater. Sci. 1993 289* **28**, 2331–2336 (1993).

43. Edie, D. D. The effect of processing on the structure and properties of carbon fibers. *Carbon N. Y.* **36**, 345–362 (1998).

44. Bright, A. A. & Singer, L. S. The electronic and structural characteristics of carbon fibers from mesophase pitch. *Carbon N. Y.* **17**, 59–69 (1979).

45. Bunsell, A. R. *Handbook of tensile properties of textile and technical fibres*. (Woodhead Publishing, 2009).

46. Arai, Y. Pitch-based carbon fibers. in *High-Performance and Specialty Fibers: Concepts, Technology and Modern Applications of Man-Made Fibers for the Future* (ed. Japan The Society of Fiber Science and Techno) 343–354 (Springer Japan, 2016). doi:10.1007/978-4-431-55203-1_21.

47. Endo, M. Carbon fiber. in *High-Performance and Specialty Fibers: Concepts, Technology and Modern Applications of Man-Made Fibers for the Future* (ed. Japan The Society of Fiber Science and Techno) 327–342 (Springer Japan, 2016). doi:10.1007/978-4-431-55203-1_20.

48. Vinci, A. Fabrication and characterization of fibre reinforced UHTC composites. (Universita' degli studi di Parma. Dipartimento di Scienze chimiche, della vita e della sostenibilità ambientale, 2019).

49. Zoli, L. *et al.* Is spark plasma sintering suitable for the densification of continuous carbon fibre - UHTCMCs? *J. Eur. Ceram. Soc.* **40**, 2597–2603 (2020).

50. Kannan, R. & Rangaraj, L. Processing and characterization of C_f/ZrB_2-SiC-ZrC composites produced at moderate pressure and temperature. *Ceram. Int.* **43**, 2625–2631 (2017).

51. Failla, S. Sintering and characterization of high hardness/high toughness/high entropy structural ceramics for severe environments. (2020).

52. D'Elia, R. *et al.* Cure kinetics of a polysilazane system: Experimental characterization and numerical modelling. *Eur. Polym. J.* **76**, 40–52 (2016).

53. Zoli, L. *et al.* Additive Manufacturing of Ceramics Enabled by Flash Pyrolysis of Polymer Precursors with Nanoscale Layers. *J. Am. Ceram. Soc.* **99**, 57–63 (2016).

54. Azarnoush, S., Laubscher, F., Zoli, L. & Raj, R. Additive Manufacturing of SiCN Ceramic Matrix for SiC Fiber Composites by Flash Pyrolysis of Nanoscale Polymer Films. *J. Am. Ceram. Soc.* **99**, 1855–1858 (2016).

55. Mainzer, B. *et al.* Characterization and application of a novel low viscosity polysilazane for the manufacture of C- and SiC-fiber reinforced SiCN ceramic matrix composites by PIP process. *J. Eur. Ceram. Soc.* **39**, 212–221 (2019).

56. Ding, Q. *et al.* 3D C_f/SiBCN composites prepared by an improved polymer infiltration and pyrolysis. *J. Adv. Ceram.* **7**, 266–275 (2018).

57. Key, T. S. *et al.* Process modeling of the low-temperature evolution and yield of polycarbosilanes for ceramic matrix composites. *J. Am. Ceram. Soc.* **101**, 2809–2818 (2018).

58. King, D., Apostolov, Z., Key, T., Carney, C. & Cinibulk, M. Novel processing approach to polymer-derived ceramic matrix composites. *Int. J. Appl. Ceram. Technol.* **15**, 399–408 (2018).

59. Stephens, F. H., Pons, V. & Tom Baker, R. Ammonia–borane: the hydrogen source par excellence? *Dalt. Trans.* 2613–2626 (2007) doi:10.1039/B703053C.

60. Ingram, D. J. *et al.* Dihydrogen vs. hydrogen bonding in the solvation of ammonia borane by tetrahydrofuran and liquid ammonia. *Phys. Chem. Chem. Phys.* **20**, 12200–12209 (2018).

61. Weast, R. C. & Astle, M. J. *CRC handbook of data on organic compounds*. (CRC Press, 1985).

62. Giesche, H. Mercury Porosimetry: A General (Practical) Overview. *Part. Part. Syst. Charact.* **23**, 9–19 (2006).

63. Webb, P. A. An Introduction To The Physical Characterization of Materials by Mercury Intrusion Porosimetry with Emphasis On Reduction And Presentation of Experimental Data. 1–23 (2001).

64. Rouquerol, J. *et al.* Liquid intrusion and alternative methods for the characterization of macroporous materials (IUPAC technical report). *Pure Appl. Chem.* **84**, 107–136 (2012).

65. Washburn, E. W. Note on a Method of Determining the Distribution of Pore Sizes in a Porous Material. *Proc. Natl. Acad. Sci. U. S. A.* **7**, 115 (1921).

66. Staněk, M. & Géraud, Y. Granite microporosity changes due to fracturing and alteration: Secondary mineral phases as proxies for porosity and permeability estimation. *Solid Earth* **10**, 251–274 (2019).

67. Micromeritics Instrument Corp. The Definitive Guide to Porosity Characterization Exploring Theory, Techniques and Practice for Industrial Application. *Whitepaper* 1–10.

68. Haugen, H. J. & Bertoldi, S. Characterization of morphology—3D and porous structure. in *Characterization of Polymeric Biomaterials* (eds. Tanzi, M. & Fare, S.) 21–53 (Woodhead Publishing, 2017). doi:10.1016/B978-0-08-100737-2.00002-9.

69. Friess, K. *et al.* Physical Chemistry Characterization of Polymeric Membranes. in *Comprehensive Membrane Science and Engineering* (eds. Drioli, E., Giorno, L. & Fontananova, E.) 445–482 (Elsevier Science, 2017). doi:10.1016/B978-0-12-409547-2.12230-9.

70. Cullity, B. D. *Elements of x-ray diffraction*. (Addison-Wesley Publishing Company Inc., 1978).

71. Bashir, S. & Liu, J. Nanocharacterization. in *Advanced Nanomaterials and their Applications in Renewable Energy* (eds. Liu, J. L. & Bashir, S.) 117–180 (Elsevier Science, 2015). doi:10.1016/C2013-0-23140-8.

72. Putnis, A. *An Introduction to Mineral Sciences*. (Cambridge University Press, 1992). doi:10.1017/CBO9781139170383.

73. Hubbard, C. R. & McCarthy, G. J. JCPDS-International Centre for Diffraction Data. *Acta Crystallogr. Sect. A Found. Crystallogr.* **37**, C344–C344 (1981).

74. Mittemeijer, E. J. & Welzel, U. *Modern Diffraction Methods*. *Modern Diffraction Methods* (Wiley-VCH, 2013). doi:10.1002/9783527649884.

75. Fadlelmoula, A., Pinho, D., Carvalho, V. H., Catarino, S. O. & Minas, G. Fourier Transform Infrared (FTIR) Spectroscopy to Analyse Human Blood over the Last 20 Years: A Review towards Lab-on-a-Chip Devices. *Micromachines* **13**, (2022).

76. Sherman Hsu, C.-P. Infrared Spectroscopy. in *Handbook of Instrumental Techniques for Analytical Chemistry* (ed. Settle, F. A.) vol. 995 247–283 (Prentice Hall PTR, 1997).

77. Ozaki, Y., Baranska, M., Lednev, I. K. & Wood, B. R. *Vibrational Spectroscopy in Protein Research: From Purified Proteins to Aggregates and Assemblies*. (Elsevier, 2020). doi:10.1016/C2018-0-02644-4.

78. Anon. IR-Active and IR-Inactive Vibrations. *Chemistry LibreTexts* https://chem.libretexts.org/Bookshelves/Organic_Chemistry/Map%3A_Organic_Chemistry_(Wade)/11%3A_Infrared_Spectroscopy_and_Mass_Spectrometry/11.03%3A_IR-Active_and_IR-Inactive_Vibrations (2020).

79. Colthup, N. B., Daly, L. & Wiberley, S. *Introduction to infrared and Raman spectroscopy*. (© Academic Press 1990, 1990).

80. Campanella, B., Palleschi, V. & Legnaioli, S. Introduction to vibrational spectroscopies. *ChemTexts 2021 71* **7**, 1–21 (2021).

81. Greener, J., Abbasi, B. & Kumacheva, E. Attenuated total reflection Fourier transform infrared spectroscopy for on-chip monitoring of solute concentrations. *Lab Chip* **10**, 1561–1566 (2010).

82. Ausili, A., Sánchez, M. & Gómez-Fernández, J. C. Attenuated total reflectance infrared spectroscopy: A powerful method for the simultaneous study of structure and spatial orientation of lipids and membrane proteins. *Biomed. Spectrosc. Imaging* **4**, 159–170 (2015).

83. Heikkinen, V., Nysten, J., Byman, V., Hemming, B. & Lassila, A. Multi-sensor optical profilometer for measurement of large freeforms at nm-level uncertainty. *Surf. Topogr. Metrol. Prop.* **8**, 045030 (2020).

84. Nita, D., Mignot, J., Chuard, M. & Sofa, M. 3-D profilometer using a CCD linear image sensor: application to skin surface topography measurement. *Ski. Res. Technol.* **4**, 121–129 (1998).

85. Grubb, D. T. Optical Microscopy. in *Polymer Science: A Comprehensive Reference* (eds. Matyjaszewski, K. & Möller, M.) vol. 2 465–478 (Elsevier Science, 2012).

86. Masters, B. R. The Optical Microscope: Its Principles, Components, and Limitations. in *Confocal Microscopy and Multiphoton Excitation Microscopy: The Genesis of Live Cell Imaging* (ed. Masters, B. R.) vol. PM161 19–37 (SPIE, 2006).

87. Chen, X., Zheng, B. & Liu, H. Optical and digital microscopic imaging techniques and applications in pathology. *Anal. Cell. Pathol. (Amst).* **34**, 5 (2011).

88. Valdrè, U. *Electron Microscopy in Material Science*. (Academic Press, 1971). doi:10.1016/B978-0-12-780584-9.X5001-6.

89. Inkson, B. J. Scanning electron microscopy (SEM) and transmission electron microscopy (TEM) for materials characterization. in *Materials Characterization Using Nondestructive Evaluation (NDE) Methods* (eds. Hübschen, G., Altpeter, I., Tschuncky, R. & Herrmann, H.-G.) 17–43 (Woodhead Publishing, 2016). doi:10.1016/B978-0-08-100040-3.00002-X.

90. Goldstein, J. I. *et al. Scanning Electron Microscopy and X-ray Microanalysis*. (Springer US, 2003). doi:10.1007/978-1-4615-0215-9.

91. Kruit, P. *Introduction to Charged Particle Optics*. (2007).

92. Reimer, L. *Scanning Electron Microscopy*. vol. 45 (Springer Berlin Heidelberg, 1998).

93. Sharma, V. & Bhardwaj, A. Scanning electron microscopy (SEM) in food quality evaluation. in *Evaluation Technologies for Food Quality* (eds. Zhong, J. & Wang, X.) 743–761 (Woodhead Publishing, 2019). doi:10.1016/B978-0-12-814217-2.00029-9.

94. Konopka, J. Options for quantitative analysis of light elements by SEM/EDS. *Technical Note 52523* 1–4 (2013).

95. Callister, W. D. & Rethwisch, D. G. *Scienza ed ingegneria dei materiali*. (ediSES, 2019).

96. Beer, F. P., Johnston, E. R., DeWolf, J. T. & Mazurek, D. F. *Mechanics of materials*. (McGraw-Hill Education, 2014).

97. Lord, J. D. & Morrell, R. M. Comparison of static and dynamic methods for measuring stiffness of high modulus steels and metal composites. *Can. Metall. Q.* **53**, 292–299 (2014).

98. Wiederhorn, S. *et al.* Mechanical Properties. in *Springer Handbook of Materials Measurement Methods* (eds. Czichos, H., Saito, T. & Smith, L.) 283–397 (Springer, 2006). doi:10.1007/978-3-540-30300-8_7.

99. Standard Test Method for Dynamic Young's Modulus, Shear Modulus, and Poisson's Ratio by Sonic Resonance. https://www.astm.org/e1875-08.html.

100. Quinn, G. D. & Swab, J. J. Elastic Modulus by Resonance of Rectangular Prisms: Corrections for Edge Treatments. *J. Am. Ceram. Soc.* **83**, 317–320 (2000).

101. Davidge, R. W. *Mechanical behaviour of ceramics*. (Cambridge University Press, 1979).

102. Vable, M. *Mechanics of materials*. (Oxford University Press, 2002).

103. Barsoum, M. W. *Fundamentals of Ceramics*. (McGraw Hill, 1997).

104. Campbell, F. C. *Structural composite materials*. (ASM International, 2010).

105. Standard Test Method for Flexural Properties of Continuous Fiber-Reinforced Advanced Ceramic Composites. https://www.astm.org/c1341-13r18.html.

106. Stantschev, G., Frieß, M., Kochendörfer, R. & Krenkel, W. Long fibre reinforced ceramics with active fillers and a modified intra-matrix bond based on the LPI process. *J. Eur. Ceram. Soc.* **25**, 205–209 (2005).

107. ISO - ISO 14704:2016 - Fine ceramics (advanced ceramics, advanced technical ceramics) — Test method for flexural strength of monolithic ceramics at room temperature. https://www.iso.org/standard/65411.html.

108. Askeland, D. R., Fulay, P., Wright, W. J. & Mapelli, C. *Scienza e tecnologie dei materiali*. (CittàStudi, 2017).

109. Suresh, S. *Fatigue of Materials*. *Fatigue of Materials* (Cambridge University Press, 1998). doi:10.1017/CBO9780511806575.

110. Gogotsi, G. A. Fracture toughness of ceramics and ceramic composites. *Ceram. Int.* **29**, 777–784 (2003).

111. Quinn, G. D. & Bradt, R. C. On the Vickers Indentation Fracture Toughness Test. *J. Am. Ceram. Soc.* **90**, 673–680 (2007).

112. Claussen, N. Fracture Toughness of Al2O3 with an Unstabilized ZrO2Dispersed Phase. *J. Am. Ceram. Soc.* **59**, 49–51 (1976).

113. Munz, D. G., Shannon, J. L. & Bubsey, R. T. Fracture toughness calculation from maximum load in four point bend tests of chevron notch specimens. *Int. J. Fract. 1980 163* **16**, R137–R141 (1980).

114. Loganathan, S., Valapa, R. B., Mishra, R. K., Pugazhenthi, G. & Thomas, S. Thermogravimetric Analysis for Characterization of Nanomaterials. in *Thermal and Rheological Measurement Techniques for Nanomaterials Characterization* (eds. Sabu, T., Raju, T., Ajesh, K. Z. & Mishra, R. K.) vol. 3 67–108 (Elsevier, 2017).

115. Gill, P., Moghadam, T. T. & Ranjbar, B. Differential Scanning Calorimetry Techniques: Applications in Biology and Nanoscience. *J. Biomol. Tech.* **21**, 167

(2010).

4. Pitch-based carbon fibre-reinforced UHTCMCs via water-based slurry infiltration and polymer infiltration and pyrolysis

4.1 Introduction

The overwhelming majority of published works has been carried out on PAN-based carbon fibre-reinforced Ceramic Matrix Composites (CMCs), while a limited number of studies are concerned with the use of uncoated pitch-based carbon fibre as reinforcement [1–3]. Nevertheless, the higher graphitization of pitch-based C fibres [4] leads to improved thermal and electrical conductivity, thermal and chemical stability and elevated stiffness. Those characteristics make pitch-derived carbon fibres the best option to realize CMCs able to withstand harsh environments for aerospace applications.
Moreover, a weak fibre-matrix interface is often obtained thanks to coatings on PAN-based carbon fibres, such as pyrolytic carbon or boron nitride, in order to achieve damage tolerant and high strength composites, whereas pitch-based C fibres have been shown to provide intra-fibre pull-out during fracture even without a coating [5–8].

In this chapter, for the first time to the best of our knowledge, the manufacturing and characterization of C_f/ZrB_2-SiC composites was studied using uncoated pitch-based carbon fibre cloths via impregnation with a water-based slurry containing ZrB_2 and SiC particles and consolidation in mild conditions by repeated infiltration and pyrolysis (PIP), six cycles, of a allyl-hydrido polycarbosilane at 1000 °C. This double infiltration step was designed to improve the distribution of ZrB_2 around fibres even in the core of bundles, since one single step infiltration with polymer-based slurries is less effective [3]. Three different carbon fibre architectures, i.e. 0/0°, 0/90° and 2D were investigated. The first purpose was to compare the microstructural features and mechanical properties of composites with increased fibre preforms complexity. Then, an extensive study of the oxidation behaviour of these materials via thermo-gravimetric analysis (TGA) up to 1350 °C and short oxidation tests in air at 1500 °C and 1650 °C for 1 min and 5 min were presented.

Part of the content of this chapter has been published in Journal of the European Ceramic Society 40 (2020) 5076–5084 as "*F. Servadei, L. Zoli, P. Galizia, A. Vinci, D. Sciti, Development of UHTCMCs via water based ZrB_2 powder slurry infiltration and polymer infiltration and pyrolysis*" and in Corrosion Science (2021) 109575 as "*F. Servadei, L. Zoli, A. Vinci, P. Galizia, D. Sciti, Significant improvement of the self-protection capability of ultra-high temperature ceramic matrix composites*".

4.2 Manufactured C_f/ZrB_2-SiC composites

Three C_f/ZrB_2-SiC samples with different fibre architectures were fabricated by a cycle of water-based slurry infiltration of fibre fabrics, using a mixture of ZrB_2-10 vol% SiC powders, followed by repetitive cycles of PIP, according to the procedure previously reported in Chapter 3. Infiltration with SMP-10 (containing 1 wt% of catalyst) and pyrolysis cycles at 1000 °C under argon flux were carried out six times.

A sample was realized by stacking infiltrated plain-woven fabrics (sample labelled as **2D**); a second sample, with an asymmetric orientation of fibres, was prepared by stacking unidirectional infiltrated fabrics with the same orientation (sample labelled as **0/0°**), while a third sample, with symmetric configuration of fibres, was obtained by stacking unidirectional infiltrated fabrics with 0-90° orientation (sample labelled as **0/90°**) (Figure 4.1).

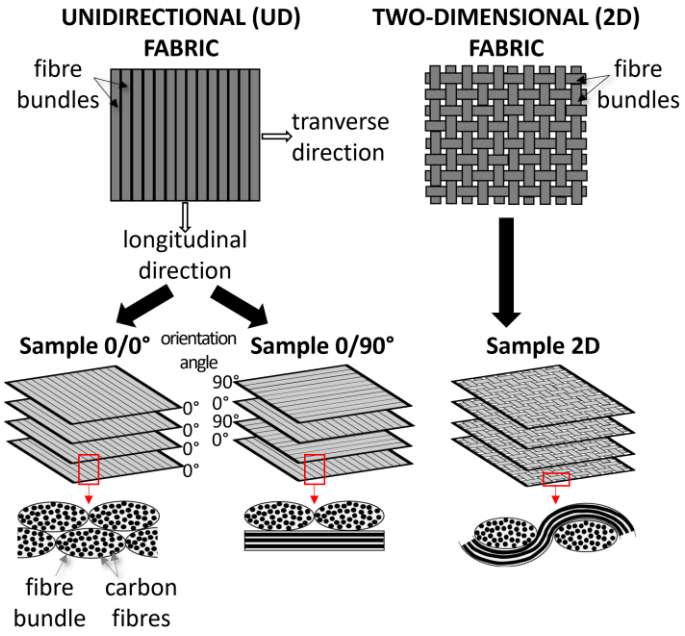

Figure 4.1. Schematic representation of C_f/ZrB_2-SiC samples with different fibre architectures: sample 0/0°, prepared by stacking infiltrated unidirectional (UD) fabrics with the same orientation, sample 0/90°, prepared by stacking infiltrated UD fabrics with the 0-90° orientation, and sample 2D, realized with infiltrated and subsequently piled up plain woven (2D) fabrics.

By stacking four impregnated UD or 2D C_f fabrics, samples with approximate dimensions 100 mm x 60 mm x 2 mm were produced; specifically, the thickness of 0/0°, 0/90° and 2D plates after 6 PIP cycles was ~2.5 mm, 2.2 mm and 1.7 mm respectively. Optical pictures of the as-processed samples are shown in Figure 4.2a-c, where the fibre

textures appear not-altered due to the pressureless manufacturing. On the 2D sample surface (Figure 4.2c), spaces between interlaces typical of plain weave are still visible after the repetitive infiltrations with ceramic phases. Indeed, the water-based ceramic powder slurry leaked through these spaces (~0.5 mm), causing the formation of cavities in correspondence to intersections of the carbon bundles on the surface and in the inner part of the material (see the white arrows in Figure 4.2d). Such macro-voids as well as layer delamination which can occur during shaping step are hardly recoverable by PIP cycles, thus assembling defect free layers is fundamental to produce flawless composites.

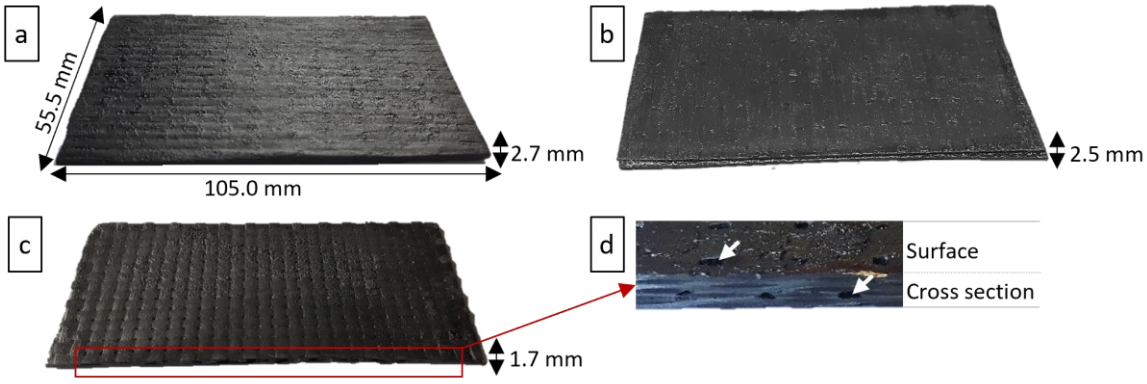

Figure 4.2. Optical images of the as-processed samples: (a) sample 0/0°, (b) sample 0/90° and (c) sample 2D. (d) Optical detail image of the sample 2D in (c) cut perpendicular to the plain weaves, highlighting the presence of voids on the surface and in the cross section (white arrows) in correspondence to intersections of the carbon bundles.

4.3 Microstructural characterization

Compositions, densities and residual porosities of the composites after 6 PIP cycles are reported in Table 4.1.

Table 4.1. Composition, open porosity and Archimedes' density of the fabricated composites.

Sample label	C_f (vol%)	UHTC (vol%)	SiC (vol%)	Open porosity (%)	Bulk density (g/cm^3)
0/0°	30 ± 1	29 ± 1	35 ± 1	~6	3.2 ± 0.2
0/90°	31 ± 1	27 ±1	36 ± 1	~6	3.2 ± 0.2
2D	30 ± 1	19 ± 1	42 ± 1	~9	2.7 ± 0.3

The porosity of the impregnated preforms was initially around 40–50 vol% and gradually decreased with the infiltration cycles. The increment of bulk density as function

of N° of PIP cycles followed a logarithmic trend (Figure 4.3), reaching final bulk densities of ~3.2 g/cm^3 for 0/0° and 0/90° and ~2.7 g/cm^3 for 2D, respectively.

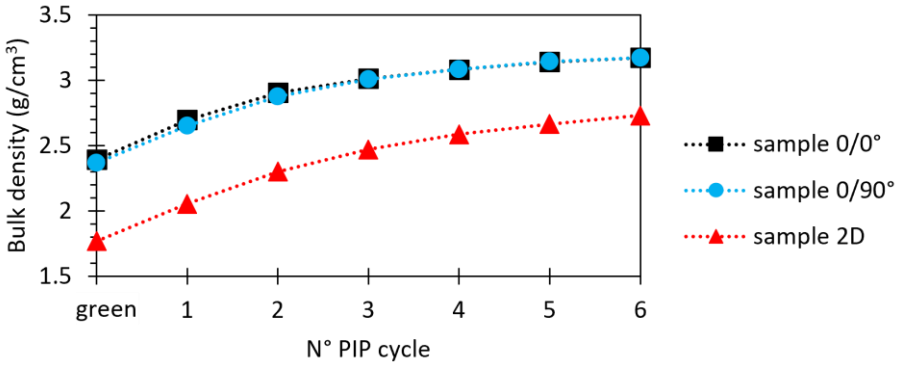

Figure 4.3. Variation of the bulk densities, which are measured by geometric method after each manufacturing step, for sample 0/0° (black line), sample 0/90° (blue line) and sample 2D (red line).

The porosity measured by mercury intrusion porosimetry was 6 vol% for 0/0° and 0/90° and 9 vol% for 2D. Concerning the pore size distribution, see the graphs in Figure 4.4 (example in Figure 4.4a refers to 0/0° sample which was very similar to 0/90°), the sample 2D contains a larger volume fraction of pores in the range 30–100 µm; this evidence is in agreement with optical analysis in Figure 4.2d.

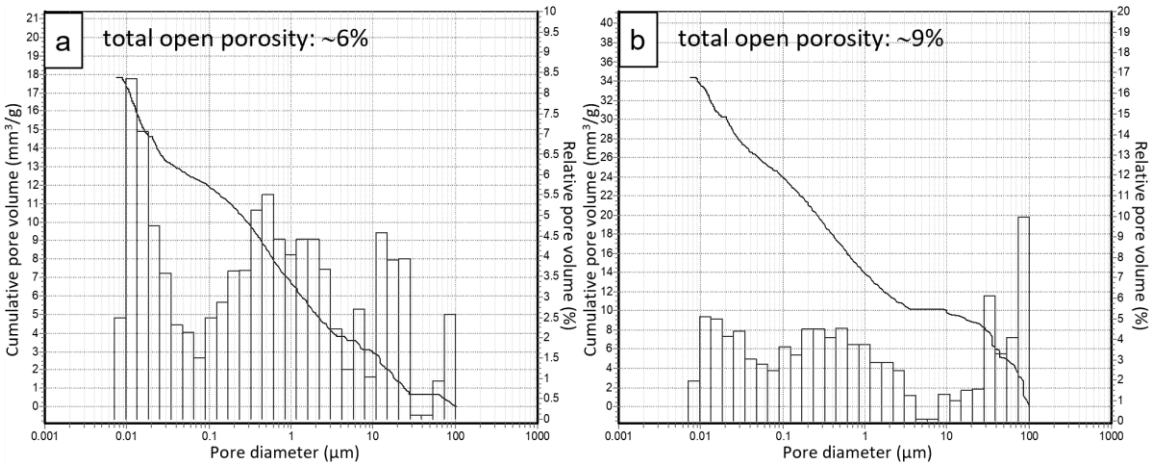

Figure 4.4. Pore size distribution by Mercury Intrusion Porosimetry (MIP) of the samples obtained after 6 PIP cycles: (a) sample 0/0° and (b) sample 2D.

Starting from the fibre mass content (which was calculated considering the fibre areal weight given by the supplier, number of layers and sample area), the matrix amount added through powder slurry infiltration (determined as the difference between the infiltrated material weight and fibre weight) and the total amount of the added polymer-derived SiC, fibre volumetric content (FVC) and volume fractions of matrix phases were

determined. All the composites contained similar fractions of Carbon fibres. UHTC (27–29%) and SiC (35–36%) phase contents were similar for 0/0° and 0/90° composites, whilst 2D samples contained a larger fraction of SiC, with consequent reduction of the bulk density.

X-Ray diffraction patterns collected on the surface of the three composites after the 6 PIP cycles were very similar (example in Figure 4.5 refers to 2D sample) and confirmed the presence of ZrB_2 (PDF 65-3389) and graphite (PDF 26-1079), while the amorphous SiC(O) obtained by pyrolysis of polycarbosilane generated only a broad X-Ray scattering profile. No reflections from the α-SiC powder (introduced by slurry infiltration) were observed, due to the content below the minimum detectable.

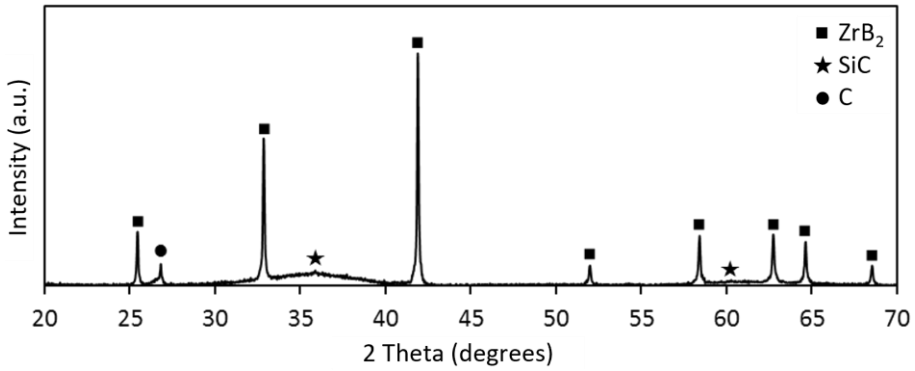

Figure 4.5. X-Ray diffraction patterns of the surface of 2D sample.

The differences in composition were ascribed to the higher complexity of the 2D fibre architectures compared to the UD ones, which hindered the powder slurry infiltration. The lower powder fraction in the infiltrated fabrics explained the lower UHTC content in the consolidated material, which was offset by a higher content of polymer-derived ceramic (PDC). The higher number of voids in the powder/fibre compact of 2D sample was easily reduced by repetitive cycles of PIP due to the use of a higher amount of low viscous SMP-10 [9]. The resulting 2D sample presented a higher roughness compared to UD samples. In Figure 4.6a,b, the optical picture and the roughness profile mapping of the 2D sample were reported. The Figure 4.6b shows the shape and depth of four cavities formed at the intersection of the bundles on the external layer, and the 3D surface topography of two cavities were reported in Figure 4.6c. Finally, the SEM analysis of the sample cross section highlighted the presence of PDC spots showing shape and size

similar to the cavities visible on the sample surface (Figure 4.6d). Detailed description of each composite typology is reported below.

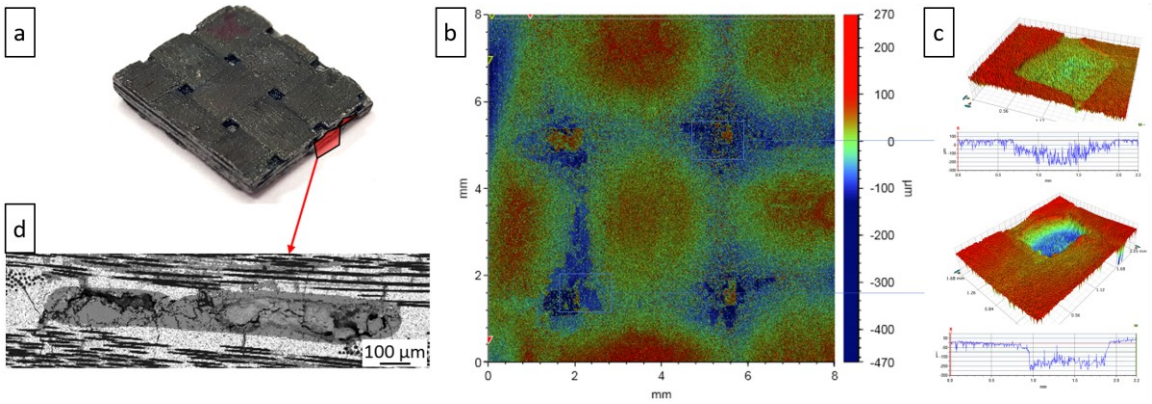

Figure 4.6. Sample 2D: (a) optical picture, (b) 2D image obtained by laser profilometer, (c) 3D detail of two areas of (b) showing surface topography, (d) back-scattering micrograph of cross section showing a PDC spot (grey colour) in the cross of fibre bundles.

0/0° composite: this sample achieved a bulk density of 3.2 g/cm^3 and a porosity around 6% (Figure 4.7a-c). Polished cross sections (Figure 4.7a) of the 0° side showed a homogeneous microstructure with regions infiltrated by the slurry alternated with polymer-derived ceramic (PDC) and occasionally unfilled areas of 100–300 µm in size, probably due to air trapped during the stage of powder slurry infiltration. The 90° view (inset in Figure 4.7a) revealed the presence of periodic cracks, formed during the drying stage after slurry infiltration. An enlarged view of the 90° section confirmed the homogenous distribution of carbon fibre, dark grey phase, in the matrix and evidenced the SiC(O) regions obtained by the precursor (Figure 4.7b). The white contrasting phase is ZrB_2, the grey phases are SiC and SiC(O). SiC powder and SiC(O) are hardly distinguishable due to the low contrast between them. The good homogeneity of powder distribution in the material and the low level of defectiveness obtained with infiltration process are comparable (or even better) than other composites obtained with the PIP process [3,10,11]. A typical fibre/matrix interface is shown in Figure 4.7c; the fibre was surrounded by a film of SiC(O) (a part is indicated as a yellow area in Figure 4.7c), in which ZrB_2 particles are embedded. In any case the interface was quite smooth.

0/90° composite: this composite, illustrated in Figure 4.7e,f,g, showed microstructural features similar to 0/0° sample in terms of density, homogenous dispersion of fibre in the matrix as well as powder mixture in SiC(O) matrix (see blue

rectangle highlighting Figure 4.7b,c,f,g). It can be noticed that the number of cracks increased due to additional stresses introduced by the 0/90° stacking configuration.

2D composite: this sample had a bulk density of 2.7 g/cm^3 and a porosity around 10%. The higher porosity was a consequence of voids in the weaving structure of 2D fabrics. The resulting microstructure was less homogeneous than the previous cases, showing typical flaws of these composites (Figure 4.7i): non-infiltrated intra-bundle regions and cracks in UHTC matrix-rich inter-bundles area. The powder slurry infiltration of 2D fabrics was less effective than in the case of UD fabrics, particularly in the central area of bundles. Accordingly, an inhomogeneous distribution of SiC(O) was achieved, with a higher content in the central part of bundles (see arrow Figure 4.7i). Two different fibre/matrix interfaces were hence created for those composites: a ZrB_2-rich interface and a SiC(O)-rich interface, see Figure 4.7g and Figure 4.7m respectively. Both interfaces were relatively smooth, however SiC(O)-rich interface showed radial cracks and partial detachment of the SiC(O) phase from the C_f (see arrows in Figure 4.7m). Two different contrasting SiC(O) phases, light grey and grey showed in Figure 4.7m (see yellow lines), revealed a layered structure around the C_f, created by the repetitive infiltration and pyrolysis cycles. As already reported in previous works these defects were caused by shrinkage of preceramic polymers during pyrolysis (up to 50 vol%) [2,12]. On the contrary, where SiC(O) was homogeneously mixed with ZrB_2 and SiC particles no cracks were found, see Figure 4.7c,g. Detail of the UHTC-rich interface shows at least 200–300 nm film of SiC(O) between ZrB_2 particles and the fibre, see yellow lines in Figure 4.7c.

As expected, the size and shape of ZrB_2 and SiC particles, analysed by image analysis, were found similar to the starting raw powders due the relative mild conditions of pyrolysis (1000 °C). EDS analysis (Figure 4.7n) on the SiC(O) confirm the presence of oxygen in the polymer-derived ceramic structure [13]. An oxygen content of approximately 15 at.% was estimated, in agreement with data given by SMP-10 supplier and as Kaur et al. revealed in [14]; moreover, further oxygen could derive from spurious oxides present on the surface of ZrB_2 and SiC particles. EDS analysis of ZrB_2 and SiC particles are reported in Figure 4.7d,h. Image analysis showed a mean fibre diameter of consolidated composites perfectly in agreement with that of pristine fibre (Figure 4.7o). Hence the fibre was not strongly degraded by SiC(O) and its bimodal distribution, centred at 9.7 and 11.3 μm, can be seen in Figure 4.7b,f,l.

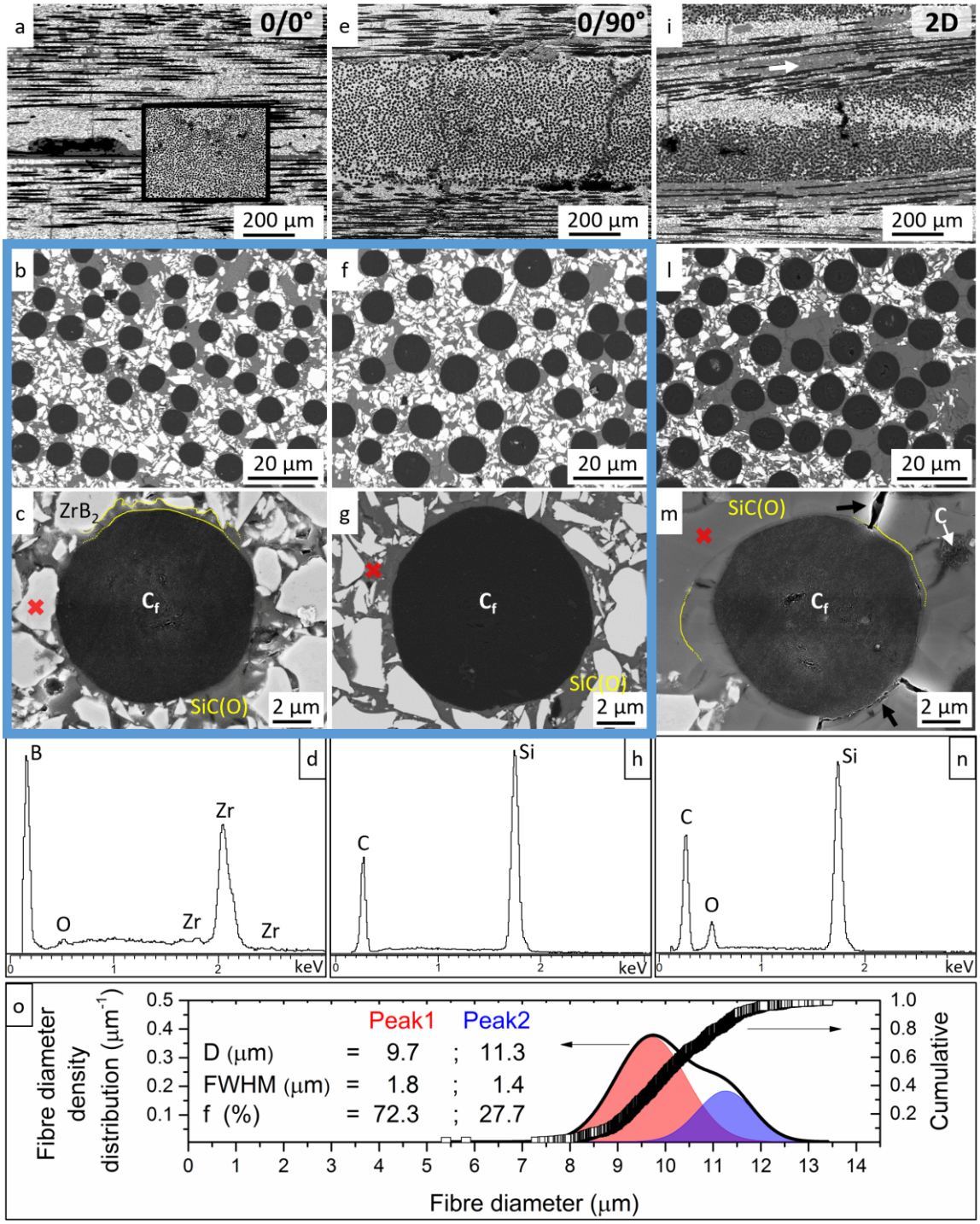

Figure 4.7. Polished sections of C_f/ZrB_2-SiC composites obtained after 6 cycles of PIP. Low magnification micrographs of (a) 0/0° sample, (e) 0/90° sample and (i) 2D sample; white arrow points a higher content of SiC(O) in intra-bundle regions. Details of microstructure of (b) 0/0° sample, (f) 0/90° sample, (l) 2D sample. A single fibre surrounded by the matrix: (c) ZrB_2-rich area in 0/0° sample, where a SiC(O) film around the C_f is shown (a part is indicated as a yellow area), (g) ZrB_2-rich area in 0/90°, (m) SiC(O)-rich area in 2D sample; yellow lines show the layered structure of SiC(O) due to repetitive PIP cycles, black arrows point cracks in SiC(O) and detachment between fibre and SiC(O) due to the shrinkage of preceramic polymer during pyrolysis. (d, h, n) EDS spectra (EDS spots were marked with red crosses in Figure 3c,g,m). (o) Density distribution and cumulative curves of fibre diameter after PIP process.

From the microstructure features just presented, a general densification mechanism can be drawn. A schematic of the microstructure evolution occurring during the main stages of the process is sketched in Figure 4.8, also showing a possible rationale for the formation of pores. The first stage, i.e. slurry infiltration, allows to homogenously distribute ZrB_2-SiC powders among the carbon fibres, thanks to the low slurry viscosity due to the aqueous solvent. However, air bubbles can be trapped in the slurry or incorporated during the infiltration and the stacking of the layers, causing the formation of big pores in the green sample. Before polymer infiltration, the green sample is kept in vacuum to remove air and, thus, to facilitate the flowability of SMP-10 in the small interstices among particles. At each PIP cycle, the voids are progressively filled with PDC SiC(O), which forms an amorphous phase in which ZrB_2-SiC particles are embedded. After 6 PIP cycles, a dense matrix is obtained with an open porosity less than 10%, constituted by small pores, which are typical of PIP process since they are due to the escape of gaseous by-products and volumetric shrinkage from precursor to ceramic, and big pores (> 50 µm) attributable to the shaping stage. These latter show SiC(O) along their edges. Therefore, we can hypothesize the presence of remaining air trapped in the larger voids that hinders the SMP-10 penetration during the first polymer infiltration, which acts as a system "freezing" and makes next infiltrations impossible.

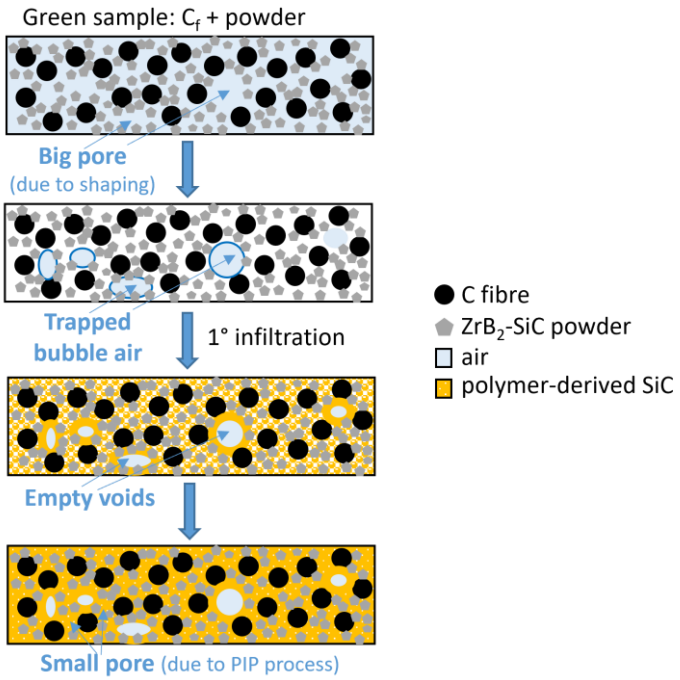

Figure 4.8. Schematic sketch of the microstructure evolution occurring during the main steps of manufacturing, showing a rationale of pore formation.

Figure 4.9a,b shows the typical fracture surfaces of 0/0° and 2D samples after 6 PIP cycles. The high homogeneity of the infiltration obtained for 0/0° is visible in the fracture surface shown in Figure4.9a, the extent of fibre pull-out of tens of microns is reduced compared to the fracture of 2D sample reported in Figure 4.9b. A more complex fracture is pointed out in Figure 4.9b due to the presence of patchwork of SiC(O)-rich and powder-rich areas where fibre/matrix weak and strong interfaces are formed, respectively.

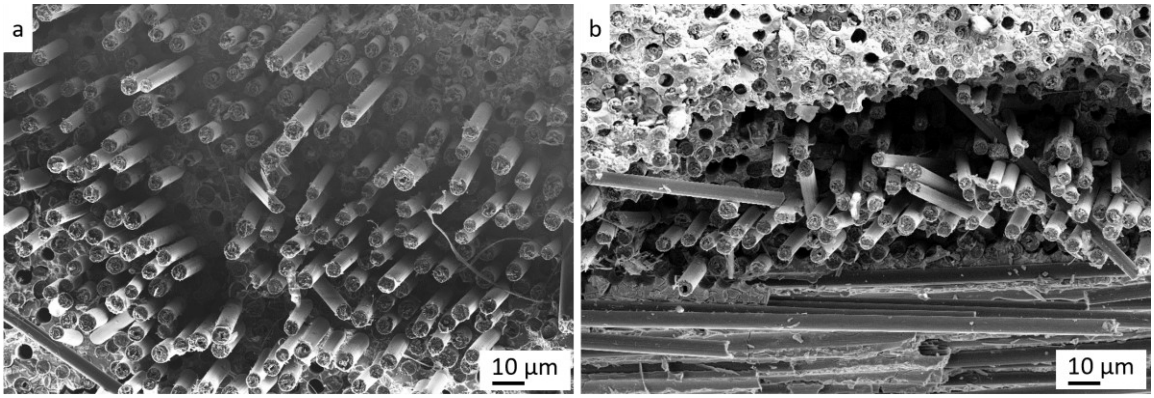

Figure 4.9. Fracture surface micrographs of samples, a) 0/0°, and b) 2D, where an extensive and limited pull-out is shown at SiC(O)-rich and powder-rich interfaces respectively.

4.4 Mechanical properties

Bending strength, Young's modulus, shear modulus and fracture toughness of 0/0°, 0/90° and 2D samples were measured according to procedures described in Section 3.3.2. The results of mechanical tests are summarized in Table 4.2.

Table 4.2. Microstructural and mechanical properties, i.e. bending strength, Young's modulus, shear modulus and fracture toughness measured at room temperature (see light blue area), of C_f/ZrB_2-SiC composites produced by PIP, and comparison with similar CMCs produced by PIP in literature.

Ref.	PIP cycles	Heat treatment	Carbon Fibre		C_f Preform architecture	UHTC powder	Porosity	Density	Bending strength, σ_f	Young's modulus, E	Shear modulus, G	Fracture toughness, K_{Ic}
	n°	°C	type	vol%		vol%	vol%	g/cm^3	MPa	GPa	GPa	MPa · m$^{0.5}$
This work	6	1000	pitch	30	0/0°	29	6	3.2	491 ± 44	220 ± 9	25 ± 1	17.9 ± 0.3
This work	6	1000	pitch	31	0/90°	27	6	3.2	364 ± 27	101 ± 19	17 ± 4	13.5 ± 2.4
This work	6	1000	pitch	30	2D	19	9	2.7	188 ± 19	78 ± 13	11 ± 1	9.2 ± 0.7
[3]	1	1900	pitch	55	0/90°	27	5	3.3	152 ± 12	-	-	10.6 ± 1.6
[3]	0	1900	pitch	55	0/90°	40	12	3.3	125 ± 35	-	-	7.3 ± 0.9
[11]	n.a.	1200	PAN	18.9	2D	25	23	2.6	163	24	-	8.1 ± 2.2

Stress-displacement curves of the bars tested at room temperature are reported in Figure 4.10; mean values of maximum stress are reported in Table 4.2.

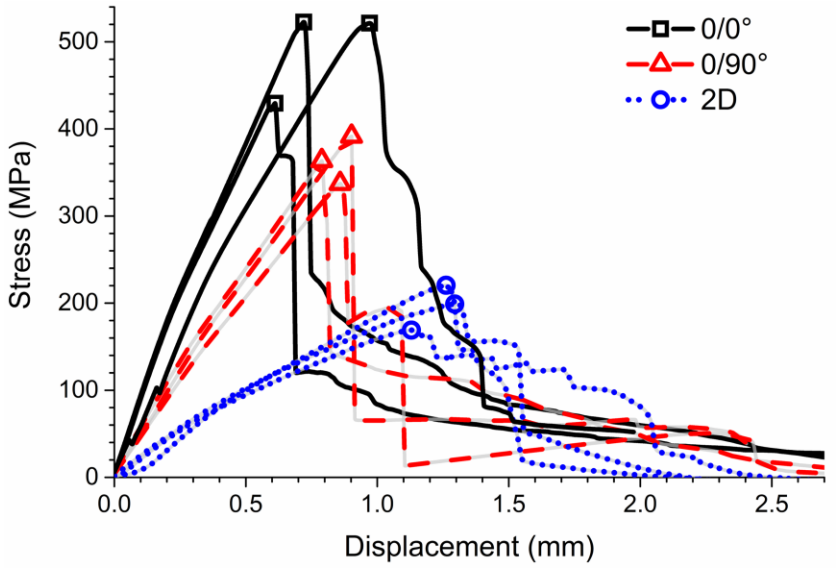

Figure 4.10. Stress/displacement curves of 0/0° and 0/90° samples tested by 3-point bending, and 2D samples tested by 4-point bending. The point at the maximum stress was highlighted with a symbol.

As expected, the highest stress value was showed by 0/0° samples and it ranged from 429 to 523 MPa. The range of flexural strength values decreased down to 364–392 MPa in case of 0/90° composites. The lower flexural strength of 0/90° composites, as well as the lower slope of their curve, was due to the lower mechanical properties of C_f/ZrB_2-SiC along the transverse direction. Both kind of composites may have failed by a sequential combination of interlaminar shear and tensile modes. This was suggested by the sharp decrease of stress after its maximum value and the following gradual decrease or slightly increase [15]. The interlaminar shear contribution to the failure was more pronounced in case of 0/90° composites. The reason is the higher number of cracks and the higher residual stress between the stacked 0° and 90° layers that resulted in low-strength planes. On the other side, a 0/0° composite showed a graceful failure, suggesting that the span-to-thickness ratio of 20 is close to the minimum value to guarantee a valid flexural test. However, the curve characterized by a graceful failure showed two pop-ins at the early stage of the loading. Hence, the failure may have been influenced by a pop-in crack, which propagated from a critical flaw in the tensile surface and crossed the neutral axis without being deflected. According to the theory, the interlaminar shear stress achieved at the maximum load for 0/0° and 0/90° composites was 13.7 ±0.9 MPa and 9.1 ±0.5 MPa,

respectively. For 2D composites, no sign of interlaminar shear failure was observed neither in the fractured specimens nor in the stress-displacement curves. Furthermore, all the fracture surfaces passed through the inter-bundle voids present on the tensile surface. The flexural strength values ranged from 170 to 221 MPa, and were possibly affected by these critical flaws, in addition to the lower amount of longitudinal fibre and their waviness. Also, the elastic moduli showed the tendency to decrease with decreasing the longitudinal fibre volumetric amount and increasing of the preforms complexity (Table 4.2).

The flexural strengths of the tested composites are comparable or even better than those of similar CMCs produced by PIP (Table 4.2). Although there are remarkable similarities between present materials and those reported in literature, the direct comparison among flexural strengths was not possible due to the different testing conditions, e.g. span/thickness ratio (s/t) and crosshead speed. For instance, 0/90° pitch-based fibre-reinforced ZrB_2-SiC produced by slurry infiltration (with SMP-10) and hot pressing at 1900 °C, although was characterized by a microstructure similar to that of the present 0/90° sample, showed less than half resistance (Table 4.2). This lower flexural strength may be ascribed to the lower span/thickness ratio (s/t = 5) that increased the interlaminar shear stress rate under loading with respect to the tensile stress rate in the outermost fibres [3]. As for 2D architecture of similar materials, only 3-point bending tests were reported in literature [11,16–18]. Since inter-bundle voids are generally not under the load pin, the failure may occur beyond the cross section under the maximum bending moment, hence the flexural strength may be overestimated. However, the reported values range from 120 to 270 MPa. Hu et al. [11] developed C/SiC material enriched with about 25 vol% ZrB_2 particles, and reported a flexural strength of 163 MPa. Wang et al. [17] obtained a strength of 237 ±30 MPa for 2D C_f/ZrB_2-SiC. L. Li et al. [18] reported a value of 255 ±15 MPa for 2D woven C_f/SiC enriched with a ZrB_2-TaC mixture. Q. Li et al. [16] developed a C_f/ZrC-SiC characterized by 34 vol% of UTHC and 34 vol% of carbon fibres and reported 143 ±21 MPa of flexural strength.

The fracture toughness (K_{Ic}) measured by Chevron Notch Beam (CNB) in 4-point flexure are reported in Table 4.2, whilst a comparison of typical load/displacement curves recorded for the three samples is shown in Figure 4.11.

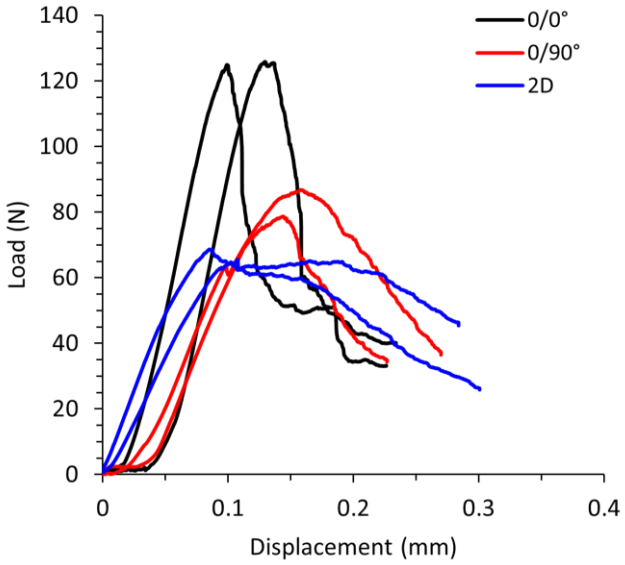

Figure 4.11. Load-displacement curves of 4-point Chevron notch bending tests (CNB) of samples 0/0°, 0/90° and 2D.

As expected, the toughness values for the three samples followed the same trend as flexural strength. The 0/0° sample showed the highest value, reporting a K_{Ic} value of 17.9 MPa·m$^{0.5}$. K_{Ic} values decreased down to 13.5 MPa·m$^{0.5}$ and 9.2 MPa·m$^{0.5}$ for 0/90° and 2D samples, respectively. The fracture toughness of the materials of this work were found to be higher than those of UHTCMCs prepared by hot pressing. For instance, ZrB_2-SiC ceramics with the introduction of 30% of carbon fibre revealed a toughness of 6.2 MPa·m$^{0.5}$ in ref. [19]. In agreement with it, Vinci et al. [20] reported K_{Ic} values ranging from 4.7 to 8.3 MPa·m$^{0.5}$ for ZrB_2-SiC composites with pitch-based carbon fibre (in 0/90° configuration) content varying between 36.6 and 49.3 vol%. Similarly, Zoli et al. [3] reported a value of 7.3 MPa·m$^{0.5}$ for C_f/ZrB_2-SiC with 55 vol% of carbon fibre produced by slurry infiltration and sintering process. Zoli et al. [3] also reported a composite characterized by the same content of fibre showing a fracture toughness of 10.6 MPa·m$^{0.5}$, thanks to the addition of SiC through SMP-10 which generated a weaker C/SiC interface increasing the mechanical properties (Table 4.2). Therefore, the higher performances found for the 0/0°, 0/90° and 2D samples, despite the lower amount of fibres, could be due to the features of fibre/matrix interface: low processing temperature led to slight reaction between carbon fibres and SiC(O) surrounding the fibres, which results in tailored interfaces and played a crucial role in the damage tolerance of these materials.

By presenting the strength and toughness values obtained in a Ashby chart (Figure 4.12), it is clear that these values are in agreement with those obtained for other UHTCMCs made by a combination of PIP and CVI. The flexural strengths of C_f/ZrB_2-SiC produced by RMI are often less than 200 MPa, lower strengths and toughness has been also observed for composites made by HP [21,22]. Finally, it is interesting to compare the properties of the samples obtained in this work with the other classes of engineering materials. All engineering structural materials require both high strength and high toughness, however such properties are mutually exclusive. For instance, the engineering ceramics have low toughness and small damage tolerance. The value of fracture toughness of the prepared composites is significantly higher than that of conventional ceramics and ZrB_2-based ceramics (considering typical values of strength ~800 MPa and toughness 3.5 $MPam^{0.5}$ [23]). This suggests that the proposed process allows to develop strong fibre-reinforced ceramic composites with a high resistance catastrophic failure.

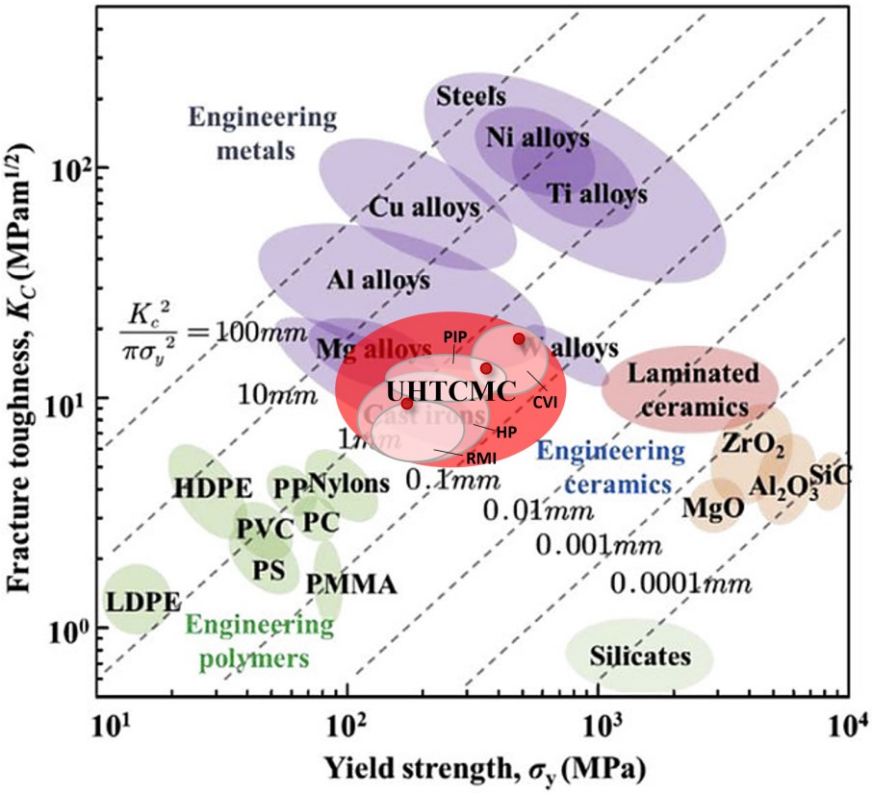

Figure 4.12. Data of fracture toughness vs. flexural strength (Table 4.2) plotted as red spheres on Ashby map for engineering materials redrawn from ref. [24]. The different levels of damage tolerance are marked with the dotted lines.

In addition, mechanical tests at elevated temperature were carried out. 4-point flexural strength at 1000 °C of 0/0° samples reached 603 ±32 MPa, and it was maintained

up to 554 ±16 MPa at 1400 °C. The higher value was related to the release of thermal residual stresses that can be developed during the cooling step of the pyrolysis process owing to the coefficient of thermal expansion mismatch between carbon fibre and ceramic matrix [25]. At 1500 °C, 0/0° composites deformed plastically during 4-point bending test due to softening of glassy phases (e.g. B_2O_3, SiO_2 and borosilicate) present at grain boundaries of ZrB_2 and within SiC(O). 1500 °C is higher than T_g (glass transition temperature) of pure silica, ~1200 °C [26], and borosilicate glass, ~820 °C [27].

4.5 Oxidation behaviour

4.5.1 Thermogravimetric analysis

A preliminary investigation via TGA was carried out to identify the critical oxidation temperatures for these UHTCMCs obtained at mild conditions. The test was conducted in in synthetic air (composition: 80 vol% N_2 + 20 vol% O_2, with 30 mL/min gas flow) up to 1350 °C with a heating rate of 10 °C/min, following the procedures described in Paragraph 3.3.11. Figure 4.13 shows the non-isothermal TG curve, the critical oxidation temperatures, and the microstructure and chemical composition of the glassy phase.

Above 700 °C and up to 950 °C a rapid weight loss occurred (Figure 4.13a). This was attributed to the rapid oxidation of the exposed carbon fibres due to the evolution of carbon oxides according to the following reactions:

$$C + 1/2\ O_2 \rightarrow CO \quad (1)$$

$$C + O_2 \rightarrow CO_2 \quad (2)$$

In this range of temperature, the rate of oxidation of ZrB_2, see reaction (3), was not sufficient to balance the weight loss due to fibre oxidation. The passivation mechanism promoted by liquid B_2O_3 was not sufficient to limit O_2-diffusion into the bulk [28].

$$ZrB_2 + 1/2\ O_2 \rightarrow ZrO_2 + B_2O_3 \quad (3)$$

At 950 °C, mass loss came to a halt. This change in the curve was probably due to an increase in oxidation rate of ZrB_2 and formation of a partially effective, self-protective liquid glass layer percolating in the holes left by fibre removal. Beyond 950 °C and up to 1050 °C, mass gain became predominant. In this range of temperatures, the oxidation of polymer-derived silicon carbide (pyrolysed at 1000 °C) started to be relevant [29], see reaction (4):

$$SiC + 3/2\ O_2 \longrightarrow SiO_2 + CO \quad (4)$$

The slope reduction from 1050 to 1250 °C was attributed to the formation of borosilicate glass, see reaction (5), which is more effective to hinder oxygen diffusion. Above 1250 °C a slight increase in the slope pointed out an increase in the rate of oxidation which was attributed to faster ZrO_2 formation.

$$SiO_2 + B_2O_3 \longrightarrow SiO_2 \cdot B_2O_3 \quad (5)$$

The sample surface after TGA was characterized by a uniform glassy phase covering the majority of the composite, with the presence of partially filled fibre hollows (Figure 4.13b). The glassy phase mainly consisted of silicon and boron oxides with small zirconia nanoparticles embedded in the glass (Figure 4.13c).

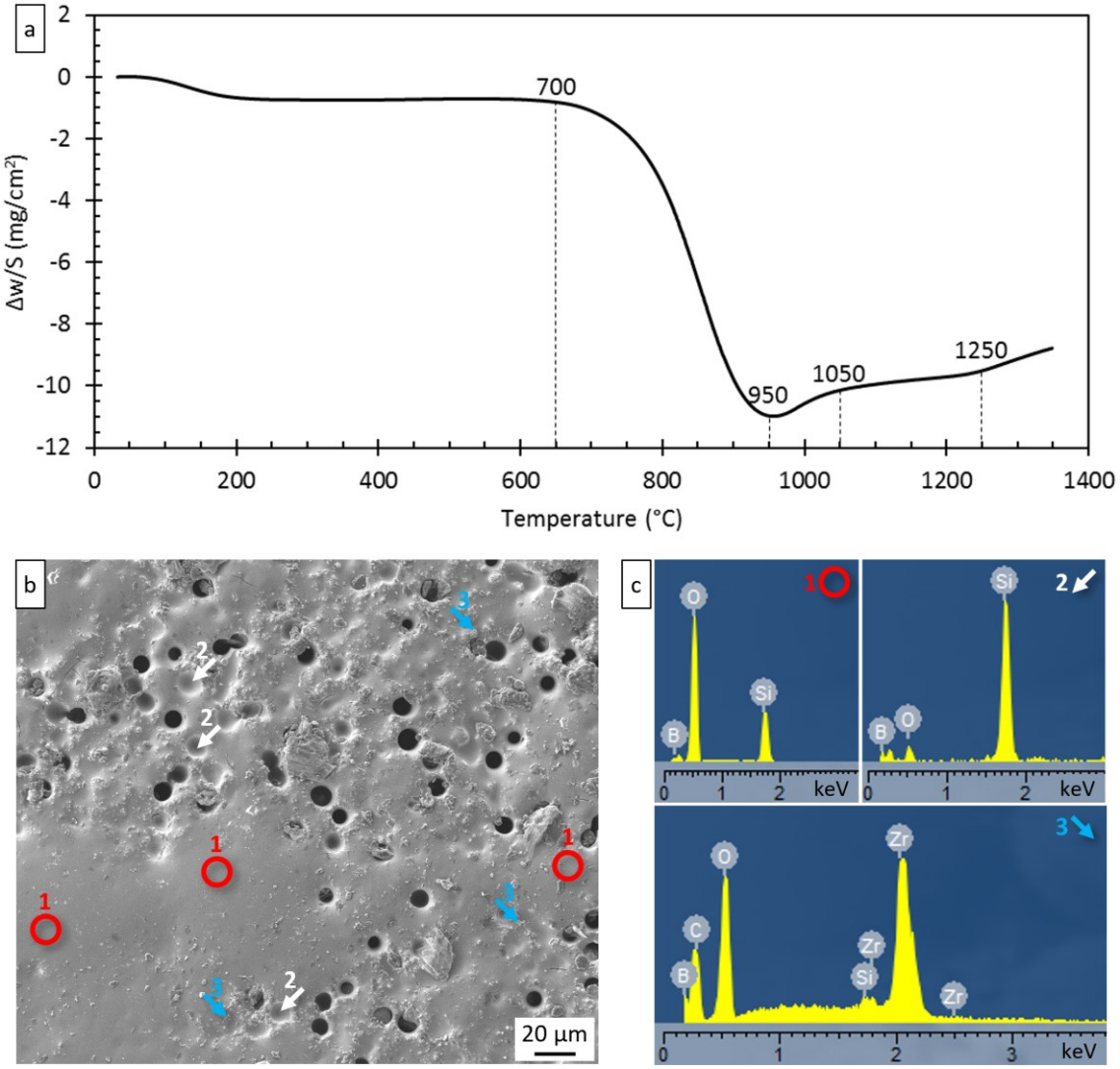

Figure 4.13. (a) Specific weight change (Δw/S) vs temperature (°C) of the tested material and (b) SEM micrograph of the oxidized surfaces after TGA. (c) EDS spectra (EDS spots were marked in Figure 4.13b) of the glassy phase, mainly consisting of boron and silicon oxides with embedded ZrO_2 particles.

4.5.2 Short term oxidation tests

Optical pictures of 0/0°, 0/90° and 2D samples after 1 min and 5 min oxidation tests at 1500 °C and 1650 °C are shown in Figure 4.14. After 1 min exposure in air at 1500 °C, the grey colour typical of the as-processed materials acquired a dark blueish tint, sign of borosilicate glass formation, and after 5 min, white spots were visible on the surface, indicating the presence of ZrO_2. The oxidized samples at 1650 °C for 1 min appeared the most damaged of the series, showing flakes of silica; nevertheless the original shape was preserved, while after 5 min exposure, a soft bubble of iridescent glass was formed on the surface of the samples (Figure 4.14d).

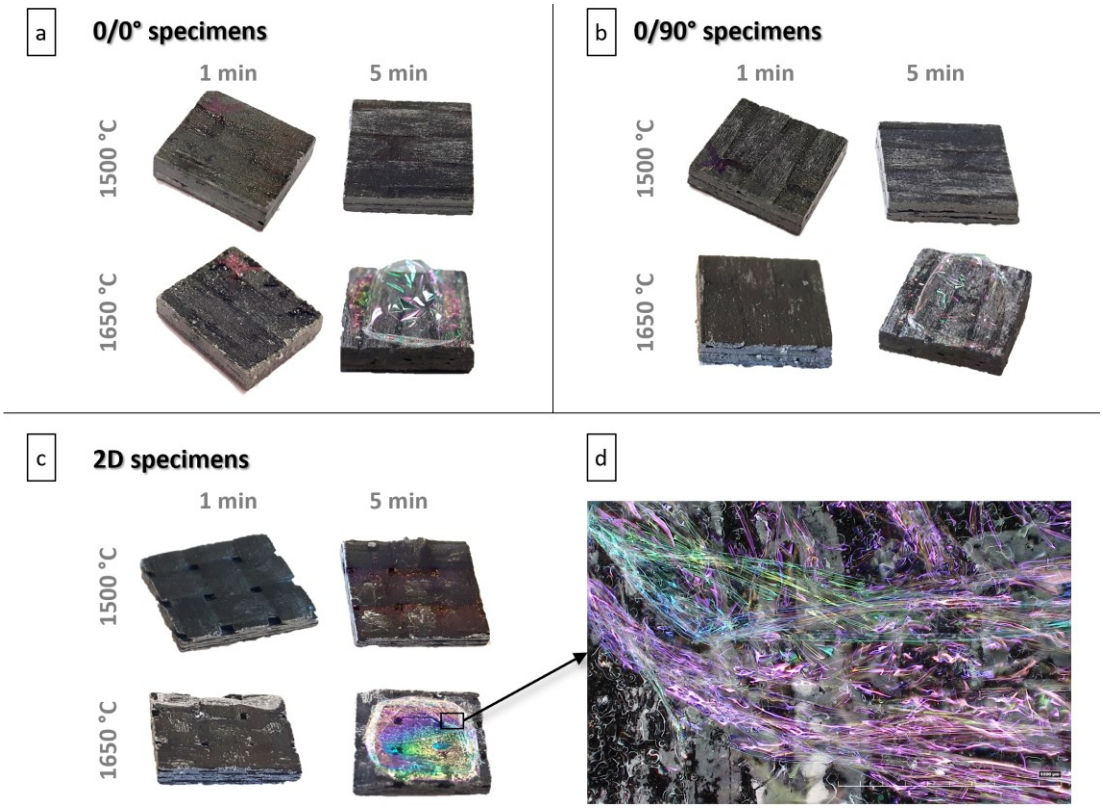

Figure 4.14. Appearance of the oxidized specimens after bottom loading furnace tests at 1500 °C and 1650 °C for 1 min and 5 min in air: (a) sample 0/0°, (b) sample 0/90° and (c) sample 2D. (d) Optical image detail of a soft iridescent glass bubble grown on the surface of the specimen shown in (c).

A way to evaluate the oxidation extent is the weight change. However, it is important to point out that mass changes are the result of negative terms (carbon fibres oxidation and matrix decomposition in volatile species) and positive terms (formation of solid oxide scale). Among sample 0/0°, 0/90° and 2D, the main differences were caused by the greater number of defects and rougher surface of 2D samples compared to the others.

Weight loss was notably higher at 1650 °C than at 1500 °C. However, after an initial weight loss, the protective film acted as a barrier and the weight was nearly unchanged after 5 min exposure in air for all of the samples both at 1500 °C and 1650 °C (Table 4.3).

Table 4.3. Mass variations normalized to the surface area and average thickness of the oxidized layer after short oxidation tests at 1500 °C and 1650 °C for 1 min and 5 min of samples 0/0°, 0/90° and 2D.

	Exposure time (min)	Sample label 0/0°	0/90°	2D
Δm/S 1500 °C (mg/cm^2)	1	-2.9	-3.1	-5.1
	5	-1.6	-2.9	-4.9
Δm/S 1650 °C (mg/cm^2)	1	-11.6	-10.7	-7.6
	5	-12.3	-10.1	-8.3
Oxide thickness 1500 °C (µm)	1	~20	~21	~27
	5	~26	~26	~40
Oxide thickness 1650 °C (µm)	1	~30	~30	~43
	5	~32	~33	~46

Several manufacturing methods have been used to produce CMCs able to withstand atomic oxygen-rich environments (see some examples in Table 4.4). Some authors applied an environmental barrier coating (EBC), made of UHTCs, on conventional C/C composites [30–32] and tested the material from 1500 to 2600 °C. The adhesion between the composite and the coating could be compromised due to the different chemistry of the materials and the thermal expansion mismatch under severe thermal stresses. Other authors introduced ZrB_2 powders into fibre preforms via slurry impregnation and consolidated the material using non-sintering routes: chemical vapour infiltration (CVI) with methane gas [33], polymer infiltration and pyrolysis (PIP) with polycarbosilane [11,34–36] and sintering approaches: pack cementation (PC) [31] and hot pressing (HP) [3,28,37].

Unfortunately, although there are remarkable similarities between the materials of this study and those reported in literature (Table 4.4), the comparison among mass variations after oxidation tests is not often reliable due to testing conditions (e.g. time and temperature exposure, oxidizing environment, specimen dimensions). In literature, we can often find oxidation tests carried out under static air using a muffle furnace or thermo-gravimetric analysis (TGA). The bottom loading furnace used to test the oxidation resistance of the composites in this study has the advantage to introduce the specimens when the target temperature is reached, avoiding further oxidation during heating ramp.

However, during the introduction of the samples in the furnace, cold air enters the lower part of the chamber, heats up and causes a turbulent flow, leading to harsher conditions than those of a thermo-gravimetric analyser: Vinci et al. [37] reported that the exposure to air at 1500 °C for 1 min in the bottom loading furnace induced almost the same degree of oxidation of the equivalent TGA test carried out at 1550 °C for 2.5 h.

Table 4.4. Main results that have been done in this field of ceramic matrix composites and tests at high temperature to evaluate oxidation resistance.

Techniques	**Materials**	**Fibre (vol%)**	**UHTC (vol%)**	**SiC (vol%)**	**Testing**	**Authors**
PIP, VSI	C/C+ZrB_2-SiC coating	n/a	n/a	n/a	Furnace, 1500 °C, 40 min	Zhou et al. [26]
CVI, PC	C/C+ZrB_2-SiO_2 coating	n/a	n/a	n/a	Furnace, 1500 °C, 330 h	Haibo et al. [27]
CVI	C/C+ZrB_2-SiC coating	n/a	n/a	n/a	Solar furnace, 1700–2600 °C	Corral et al. [28]
CVI	C/SiC-ZrB_2	25	4	71	Electric furnace, 1000–1400 °C, 5 min	Tang et al. [29]
PIP, SI, CVD	C/ZrB_2-SiC	54	n/a	n/a	Blow torch, 3000 °C, 20 s	Liu et al. [31]
PIP	C/ZrB_2-SiC	26	19	35	Furnace, 1200 °C, 20-40 min	Hu et al. [11]
SI, HP	C/ZrB_2-SiC	42	52	6	TGA	Vinci et al. [24]
SI, HP	C/ZrB_2-SiC	37	46	12	Furnace, 1500–1650 °C, 1 min	Vinci et al. [33]
SI, HP	C/ZrB_2-SiC	53	26	17	Furnace, 1650 °C, 1 min	Zoli et al. [3]
SI, PIP	C/ZrB_2-SiC	30-31	29-19	35-42	TGA, furnace, 1500–1650 °C, 1-5 min	Present work

PIP: Polymer Infiltration and Pyrolysis.

VSI: Vapour Silicon Infiltration.

CVI: Chemical Vapour Infiltration.

PC: Pack Cementation.

SI: Slurry Infiltration.

CVD: Chemical Vapour Deposition.

HP: Hot Pressing.

In addition, the results are often not available or are expressed differently (e.g. weight loss percentage or mass variation normalized over to initial surface). For instance, H. Hu et al. [11] developed C/SiC material enriched with about 25 vol% ZrB_2 particles by PIP and studied the oxidation properties at 1200 °C in a muffle furnace; they reported a mass loss of 4.5% and 11.4% after oxidation for 20 min and 40 min, respectively. D. Huang et al. [38] evaluated the oxidation resistance of C/C-ZrB_2-ZrC-SiC composite under static air in a muffle furnace at 1100 °C up to 60 min; after 20 min the mass loss was no more than 1%, while after 60 min a mass loss of 10.96 % was reported.

Given the large scattering of experiments and conditions reported in literature, it is worthy to compare the results achieved in this study only with those reported in our last work [37] adopting the same testing conditions and weight loss measurements. Vinci et al. [37] reported a range of weight loss from -1.9 to -3.6 mg/cm^2 testing similar materials in the same furnace at 1500 °C for 1 min. It is interesting to note that despite the content of ZrB_2 was higher than 46 vol%, it was not effective to reduce weight loss.

In the following, the crystalline phases of tested samples were discussed. X-ray diffraction patterns collected on the surface of the 0/0° specimens, after oxidation in air at 1500 °C and 1650 °C for 1 min and 5 min, were reported in Figure 4.15. The main crystalline phase was monoclinic ZrO_2 (PDF 65-1025) as product of ZrB_2 oxidation, whose reflections obviously increased with the increase of time and oxidation temperature; trace amounts of tetragonal zirconia (PDF 88-1007) were detected only in XRD patterns after oxidation at 1500 °C. B_2O_3 was not detected in the surface layer; this could be attributed to its relatively low melting temperature (445 °C) [39] which leads to the formation of a glass. SiC(O) evolution was more difficult to track because of its surficial oxidation into glassy and crystalline SiO_2 (PDF 47-1144) [40], which is labelled as quartz. Indeed, α quartz is expected at room temperature, however rapid air quenching does not allow crystallization led mainly to the formation of vitreous silica. The underlying SiC(O), not exposed to air, was subjected to crystallization into β-SiC (PDF 65-0360). After 5 min at 1650°C, XRD reflections of β-SiC are sharper than the pattern after 1 min at the same temperature. A similar trend, less marked, was detected at 1500°C. No reflections relative to carbon or carbides were observed for all the oxidized specimens. For all the oxidized composites peaks relative to ZrB_2 were still well visible. On the contrary, Vinci et al. [37] did

not observe ZrB_2 reflections after oxidation of C/ZrB_2-SiC at 1500 °C and 1650 °C despite the initial higher content of ZrB_2 in the matrix, see Table 4.1. XRD patterns of samples 0/90° and 2D were mostly identical, with no relevant differences across the samples, and therefore they were not shown.

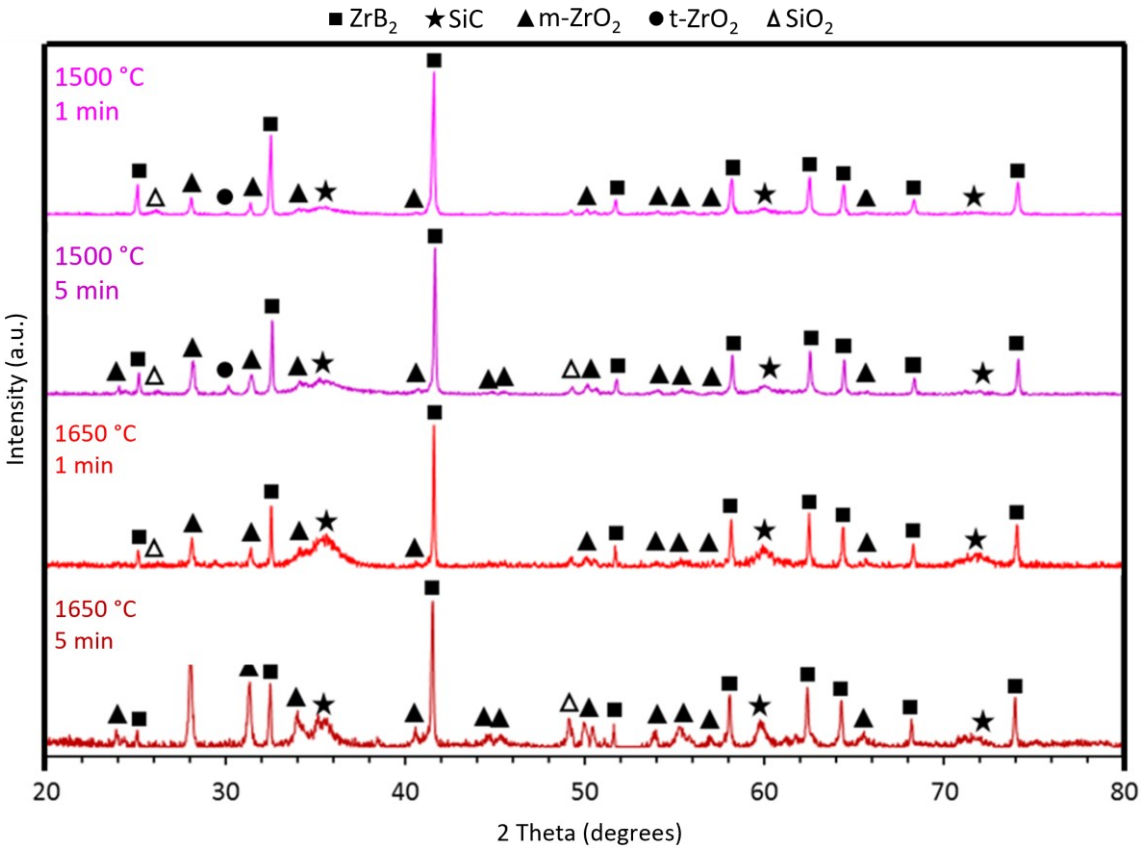

Figure 4.15. X-ray diffraction patterns collected on the surface of 0/0° specimens after oxidation at 1500 °C and 1650 °C in air for 1 min and 5 min.

Following the XRD investigation, SEM-EDS characterization was carried out on the surface and cross section of the oxidized samples. A typical top view of the surface of the specimens oxidized at 1500 °C and 1650 °C for 1 min and 5 min is shown in Figure 4.16a-d, insets in Figures highlight the evolution of morphology of ZrO_2 grains with increasing time and temperature of the oxidation test.

As can be seen in Figure 4.16a, after oxidation at 1500 °C for 1 min fibres onto or close to the surface were consumed and grooves are visible in their place. Tiny precipitated ZrO_2 crystals (bright phase) were found immersed into a borosilicate (BS) glass layer formed on the top. Oxidation at 1500 °C for 5 min induced the formation of a continuous BS glass scale which homogeneously covered the surface, flowing in the

grooves left by oxidized fibres, thus preventing further oxygen penetration inside the material (Figure 4.16b). After oxidation at 1650 °C for 1 min, a thin layer of liquid phase almost entirely covered the surface and embedded the scattered residues of SiC(O) phase from the polycarbosilane found on the specimen surface after pyrolysis (Figure 4.16c). Also, the surface appeared more damaged, a higher amount of blisters was observed and the whole surface became rougher (Figure 4.16c,d). The great amount of liquid phase which spread from the subsurface towards the surface and the evolution of volatile oxides formed during oxidation led to bubble formation and rupturing. This in turn exposed the underlying bulk layer to oxygen again [37,41]. Further inspection on the ruptured bubbles showed islands of tiny ZrO_2 crystals in coral-like shape, in agreement with [37] (inset in Figure 4.16c), due to the evolution of small nuclei in branches of a dendrite. Previously Karlsdottir et al. [42] called this type of dendritic zirconia as "secondary zirconia" and reported that it is dissolved in the boria–silica–zirconia liquid, thus crystals precipitated when the B_2O_3 evaporates. The number of blisters in the borosilicate glass scale increased with the exposure time at 1650 °C (Figure 4.16d), precipitated ZrO_2 crystals underneath the ruptured bubbles increased in size and took on a rounded shape (inset in Figure 4.16d).

The surface of samples 0/90° and 2D was very similar to that reported in Figure 4.16, so only the surface of the 0/0° sample was reported.

A SEM image of an exploded bubble on the surface of the specimen 0/0° after 1 min exposure at 1650 °C and details of the growth of the secondary zirconia found underneath it are shown in Figure 4.17a-c. Columns of fine ZrO_2 particles grew on ZrO_2 islands due to the precipitation from the boria-silica-zirconia glass, surrounded by a glassy matrix constituted of a silicate-rich liquid oxide [42] (Figure 4.17b). At higher magnification, it is possible to observe the growth of small nuclei on the side and on the tips of the ZrO_2 islands at the very beginning (Figure 4.17c).

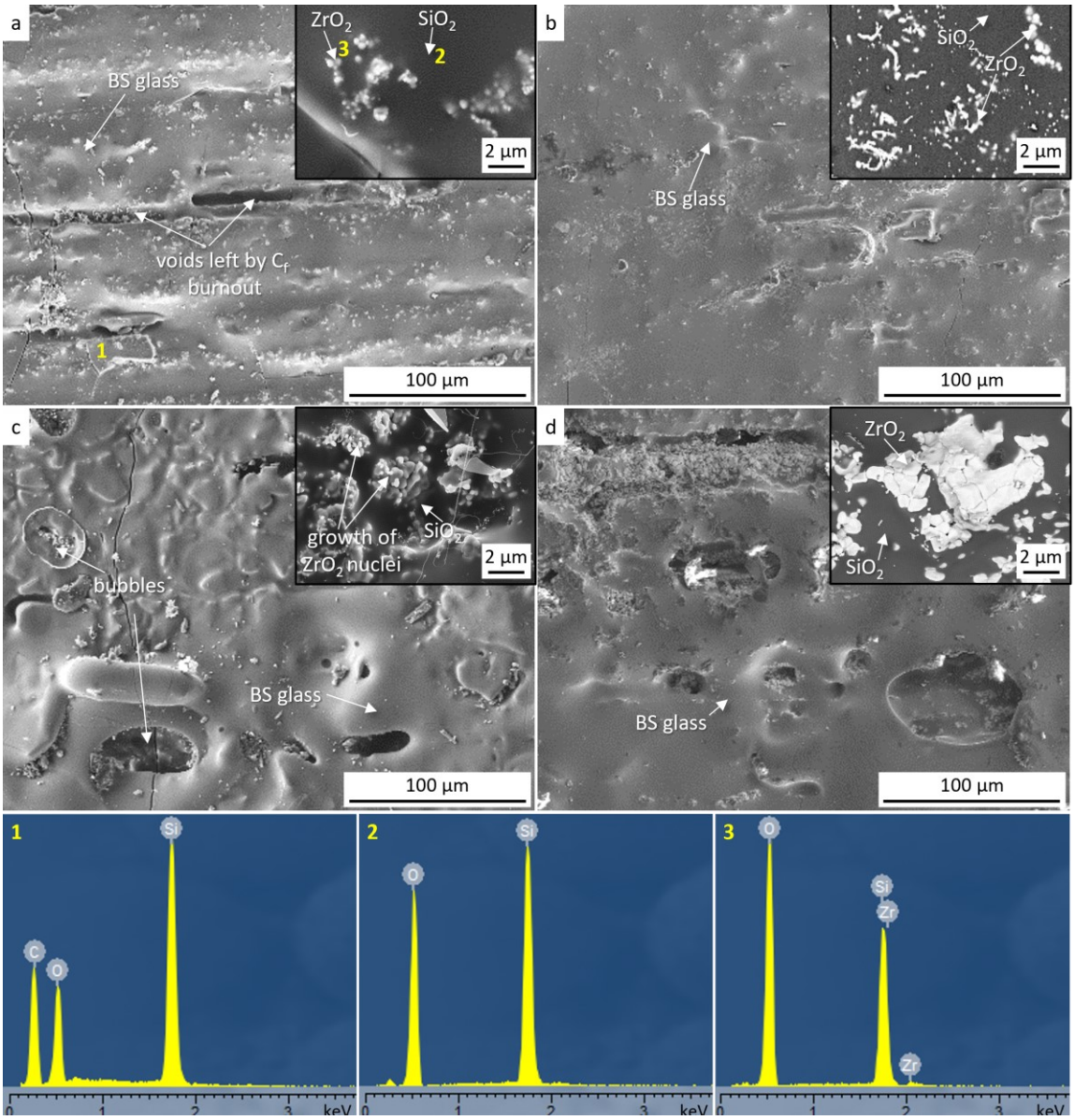

Figure 4.16. Top view of specimens (0-0° sample) oxidized in air in a bottom load furnace: at 1500 °C for (a) 1 min and (b) 5 min; at 1650 °C for (c) 1 min and (d) 5 min. Insets of the figures highlight the morphology of ZrO_2 grains embedded in the glass. At the bottom, EDS spectra of the phases as indicated.

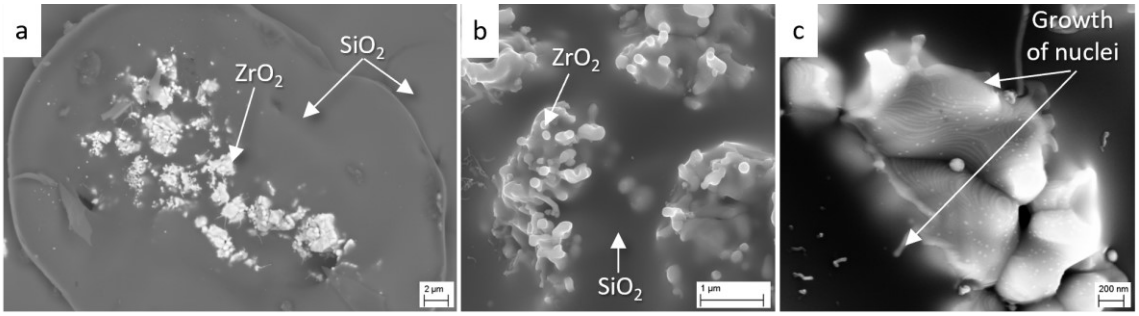

Figure 4.17. (a) Ruptured bubble with tiny zirconia crystals on the surface of specimen 0/0° oxidized at 1650 °C for 1 min, highlighting (b) column of fine ZrO_2 that remind the branches of a dendrite and (c) growth of small nuclei at initial stage.

The low magnification micrographs of the cross section of samples 0/0°, 0/90° and 2D after the four oxidation tests are reported in Figure 4.18. The specimens underwent oxidation both on the surface and on the sides, thus fibres were exposed to air both circumvented by the ZrB_2-SiC matrix and facing outwards directly exposed to the oxidizing atmosphere respectively. In the latter case, the oxidation of carbon fibres results in the formation of channels that promote diffusion of oxygen inside the material [37]. It is worthy to note that these materials are meant for the application as thermal protection systems (TPSs) for the leading edges of aerospace vehicles, in which only the outer surface of the tile would be exposed to the corrosive atmosphere and usually fibres do not face outwards [43]. For that reason, micrographs of the cross section of sample 0/0° after the four oxidation tests were chosen as an example and presented below.

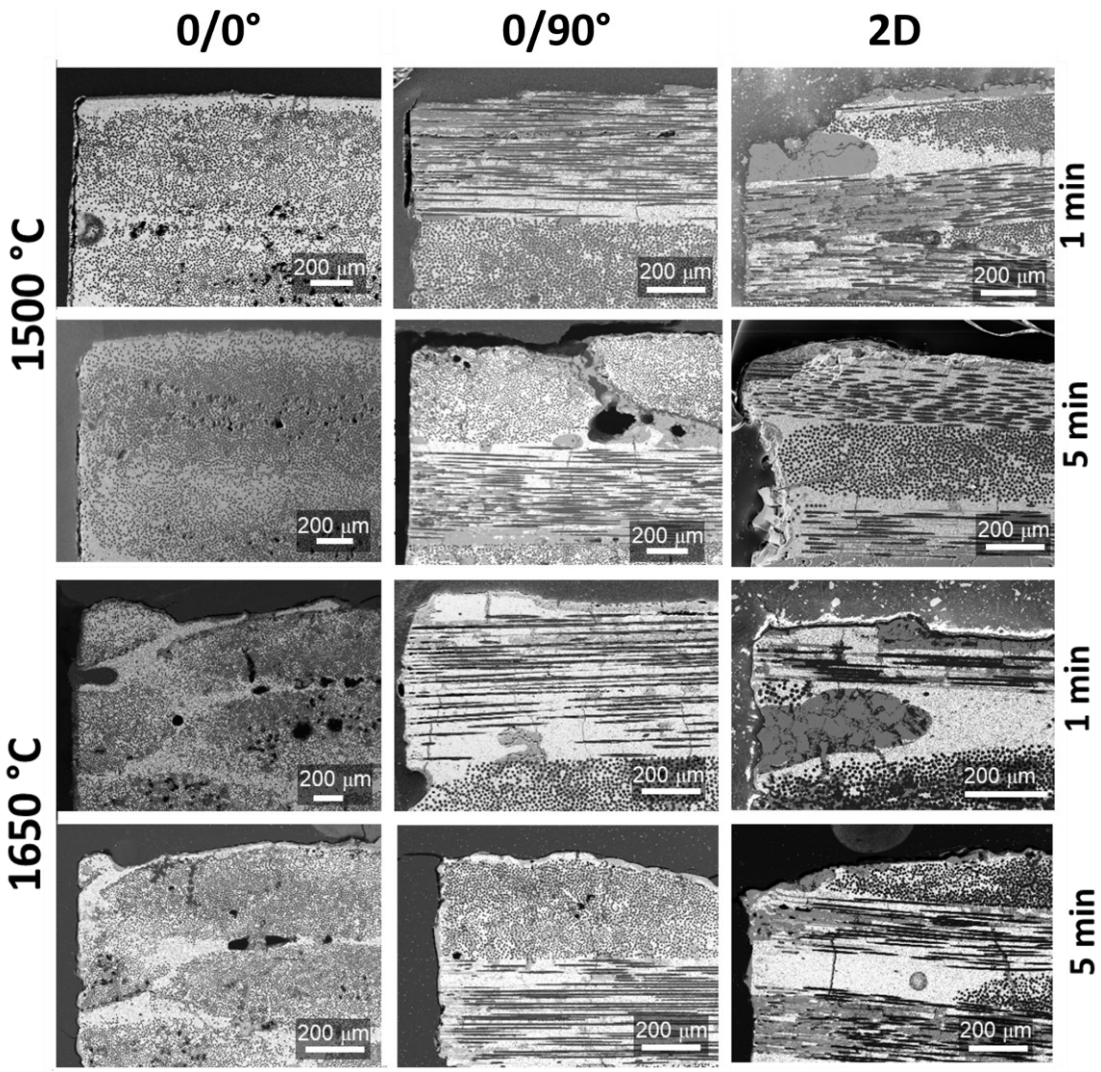

Figure 4.18. SEM images of cross section of samples 0/0°, 0/90° and 2D after short term oxidation tests at 1500 °C and 1650 °C for 1 min and 5 min.

Micrographs of the cross section of samples 0/0° oxidised at 1500 °C for 1 min are reported in Figure 4.19a-e with the corresponding EDS spectra acquired in different spots, even though it was difficult to detect B_2O_3 by EDS, as boron is a light element [44].

Figure 4.19a,b shows the cross section of the sample close to the top surface, which was not grinded after manufacturing to avoid interruption of fibres, while Figure 4.19c shows the cross section of the specimen close to a machined side. As can be seen in Figure 4.19a, the matrix underneath the top (orange dashed lines) was enriched of SiC(O) and SiO_2 (see EDS spectrum in Figure 4.19).

A detail of partially filled holes left by carbon fibres oxidation is reported in Figure 4.19b. It is worthy to note that ZrB_2 close to the surface appeared only partially oxidized, showing nano-crystals of ZrO_2 on the particle surface (Figure 4.19c). In the cross section of a machined side (Figure 4.19d), it is easier to evaluate the thickness of the oxide scale. Hence, the modified layer thickness of the specimen was found in the range of 5–25 µm. Moving inwards in the oxidized scale, it was also possible to see a carbon fibre partially surrounded by BS glass film containing inclusions of ZrO_2, that could be considered a further mechanism of fibre protection toward oxidation (Figure 4.19e).

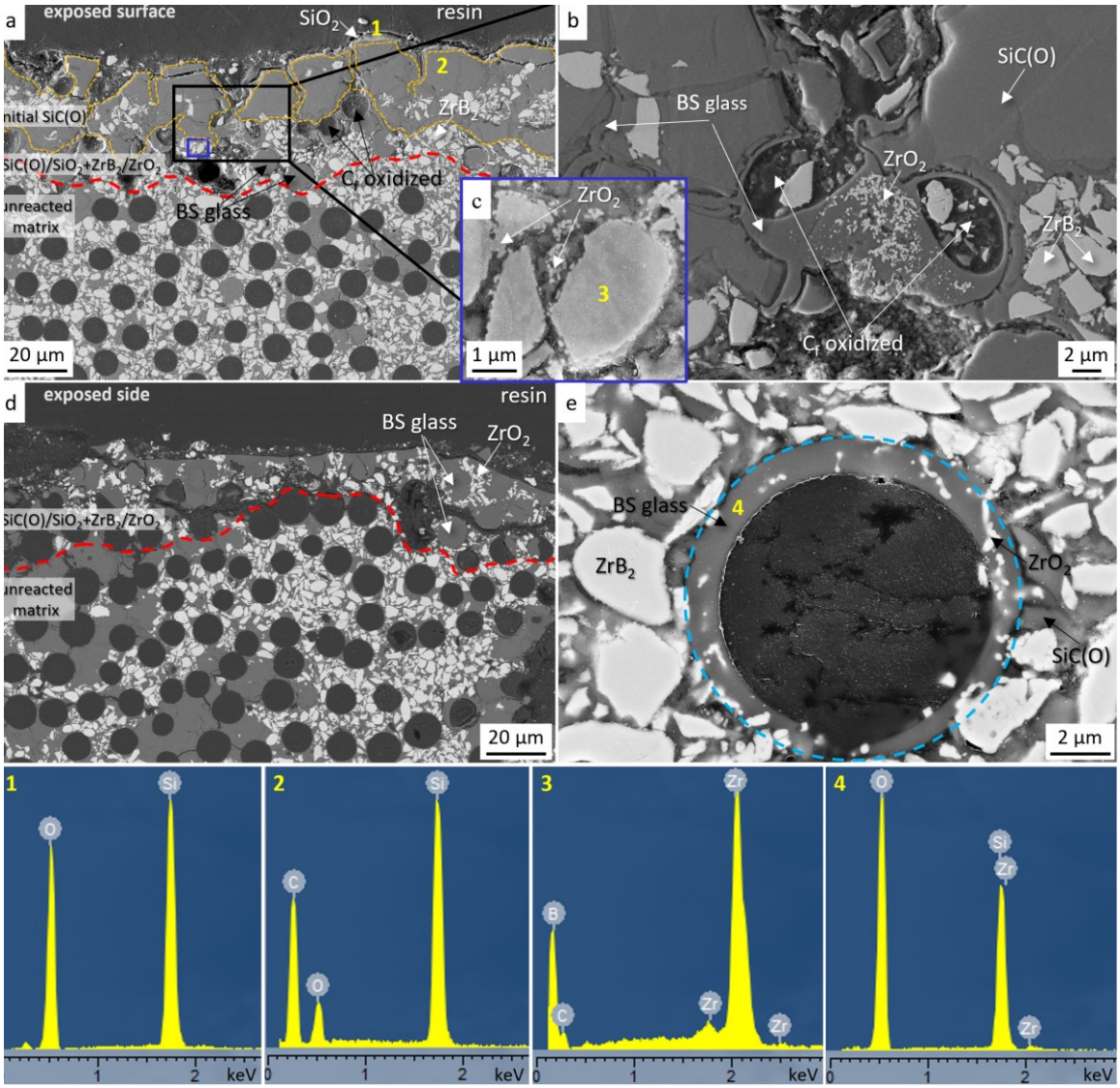

Figure 4.19. Polished cross section of the specimen (sample 0/0°) after short term oxidation test at 1500 °C for 1 min in air. (a) Micrograph of the exposed surface, SiC(O)-rich area, (b) magnification of the BS glass in the voids left by the C_f oxidation and (c) magnification of the partially oxidized ZrB_2 particles; (d) micrograph of the exposed side. (e) High magnification micrograph of a fibre where the oxidation stopped thanks to the BS glass (marked with blue circle) that surrounded it. In the bottom EDS spectra of the phases as numbered.

The morphology of the cross section after 5 min exposure at 1500 °C is shown in Figure 4.20a-c. The outer part was composed by a compact scale of BS glass and solid inclusions (ZrO_2) with a thickness of ~26 µm (Figure 4.20a). Despite the thickness of the oxide scale was found similar to the shorter oxidation test, the prolonged time of exposure to oxygen caused the almost complete conversion of surficial SiC(O) into SiO_2 and later into BS glass due to reaction with B_2O_3. High magnification micrographs showed many ridges consisting of a core of fine secondary ZrO_2 surrounded by glass [42] (Figure

4.20b) and the progressive oxidation of ZrB_2 particles from the external surface towards the unreacted matrix (Figure 4.20c).

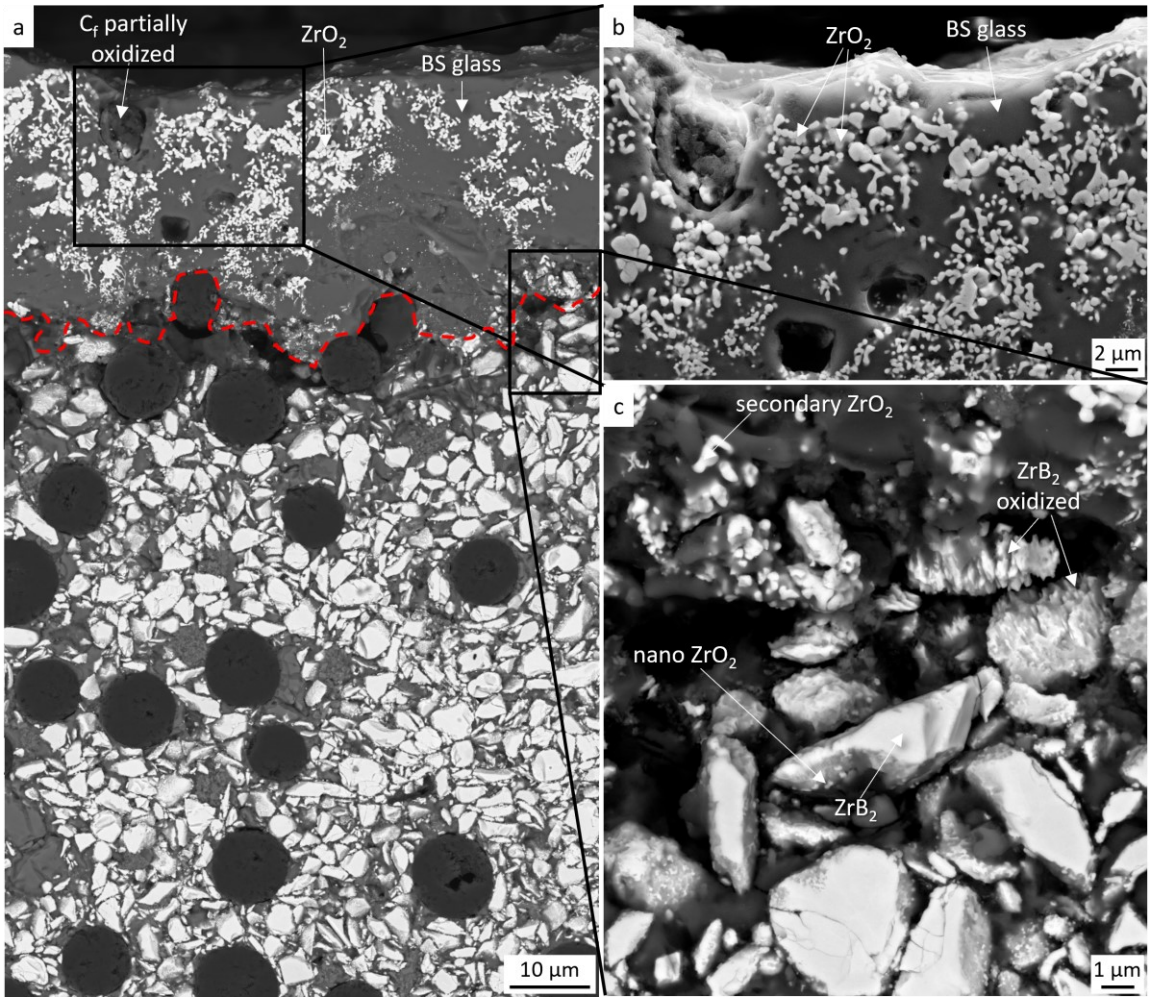

Figure 4.20. Polished cross section of specimen (sample 0/0°) after short term oxidation test at 1500 °C for 5 min in air: (a) overview of the microstructure, (b) magnification of the BS glass in which secondary ZrO_2 precipitates are embedded and (c) detail of ZrB_2 particles and progressive oxidation to ZrO_2 moving towards the top.

The microstructure of the cross section after oxidation at 1650 °C for 1 min is visible in Figure 4.21a-d. In Figure 4.21a, a layered structure is visible: an external borosilicate glass scale, an intermediate layer of ZrO_2/SiO_2 and an unreacted matrix layer. The coarsening of ZrO_2 grains is visible in Figure 4.21b. A SiC-depleted layer between the ZrO_2/SiO_2 scale and the unreacted matrix was not detected. That region is commonly found in oxidized ZrB_2-SiC bulk ceramics, because of the active oxidation of SiC to volatile SiO [23,41]. Rezaie et al. [45] studied that graphite addition in ZrB_2/SiC ceramic may affect the

formation of this layer, as it promotes the preferential formation of $CO_{(g)}$. Hence, the lack of SiC-depleted region very likely depends on the high carbon fibre content.

Figure 4.21c shows a SiC(O)-rich area, where the matrix damage was higher and oxygen could penetrate the sample to a depth of 55 µm. This observation is in agreement with ref. [46], where the cracked surficial SiC(O) acted as a preferential channel for oxygen diffusion trough the composite. Such SiC(O)-rich areas were found more prevalently in the sample 2D (Figure 4.6d), compared to samples 0/0° and 0/90°.

For the sake of comparison, in Figure 4.21d, a cross section highlighting the lateral view of the fibres is shown. The micrograph captured the dynamics of two opposite mechanisms: the inward diffusion of the glassy phase through the channels and the evolution of volatile species that bubble through the molten glass. The oxidized thickness was calculated to be about 90–150 µm.

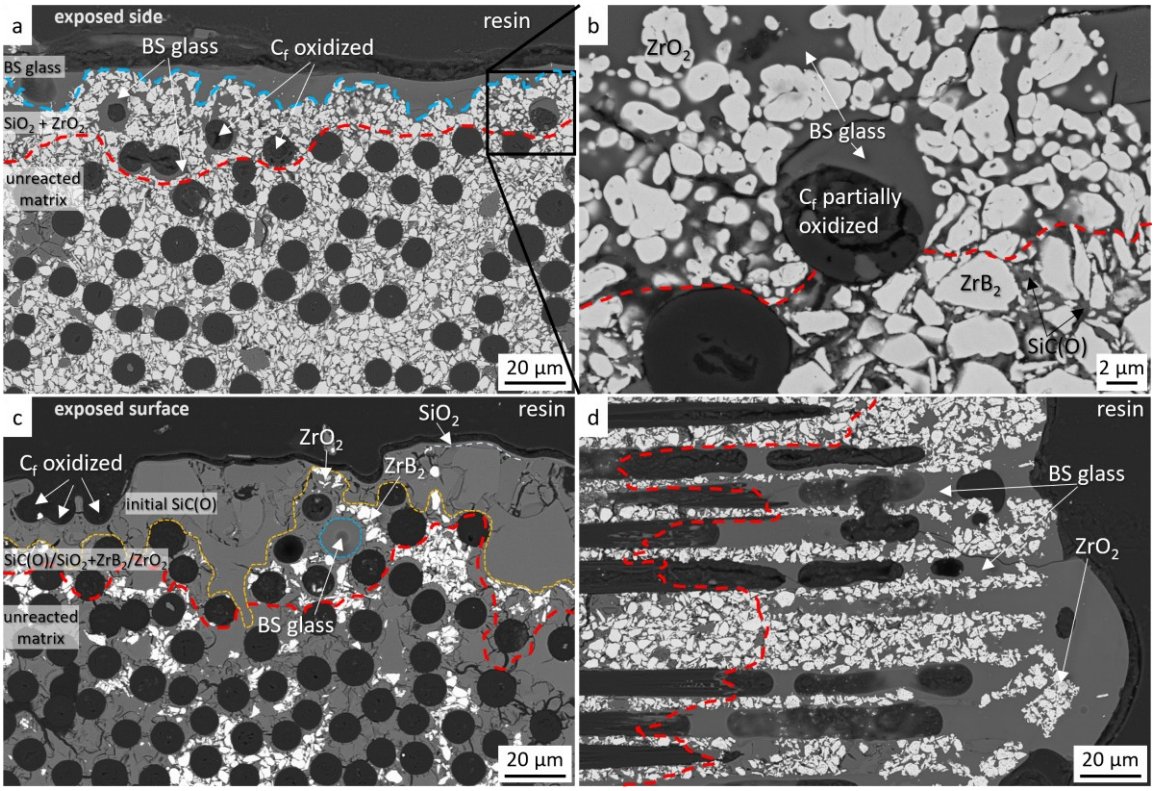

Figure 4.21. Polished cross section of specimen (sample 0/0°) after short term oxidation test at 1650 °C for 1 min in air: (a) micrograph of the exposed surface in a ZrB_2-rich area and (b) magnification of a partially oxidized fibre beneath the surface and the void filled by the BS glassy phase, (c) micrograph of the exposed surface in a SiC(O)-rich area, (d) lateral view of fibres.

The same microstructural features were observed after oxidation at 1650 °C for 5 min in air (Figure 4.22a-e). A low magnification micrograph (Figure 4.22a) shows that the

specimens were not erode severely after 5 min exposure to air. The function of the borosilicate glass was evident in oxidized sections of the air exposed side (Figure 4.22b), where the oxide thickness was around 25–35 µm (Table 4.3). Similarly to what was seen above (Figure 4.21a,c), in regions with a higher amount of SiC(O), e.g. top of the specimens, the modified layer was thicker, up to 75 µm. In addition, the formation of a large BS glass bubble owing to the vigorous gas escape was reported in Figure 4.22c. Partially attacked matrix and fibres were found underneath the oxide scale (Figure 4.22d) and non-oxidized bulk matrix and C_f (Figure 4.22e) were reported to highlight the difference in microstructure.

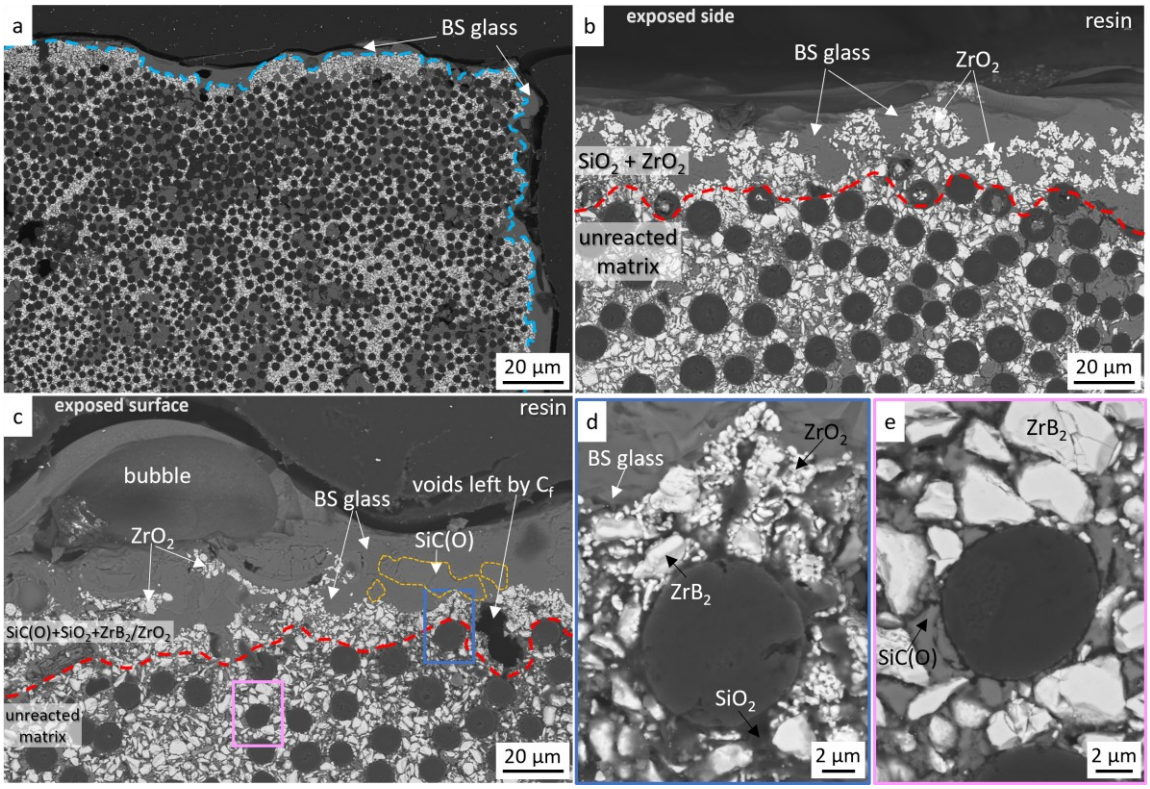

Figure 4.22. Polished cross section of specimen (sample 0/0°) after short term oxidation test at 1650 °C for 5 min in air: (a) low magnification micrograph of an edge exposed to air flow, (b) micrograph of the exposed surface in a ZrB_2-rich area and (c) micrograph of the exposed surface in a SiC(O)-rich area, showing oxidized thicknesses; high magnification micrographs of a fibre underneath the exposed surface surrounded by: a partially oxidized matrix (d), unreacted matrix (e).

Finally, the cross sections of specimens are reported (sample 0/0°) after the four oxidation tests at the same magnification to have a comparison of the different oxide scale thickness in a glance (Figure 4.23).

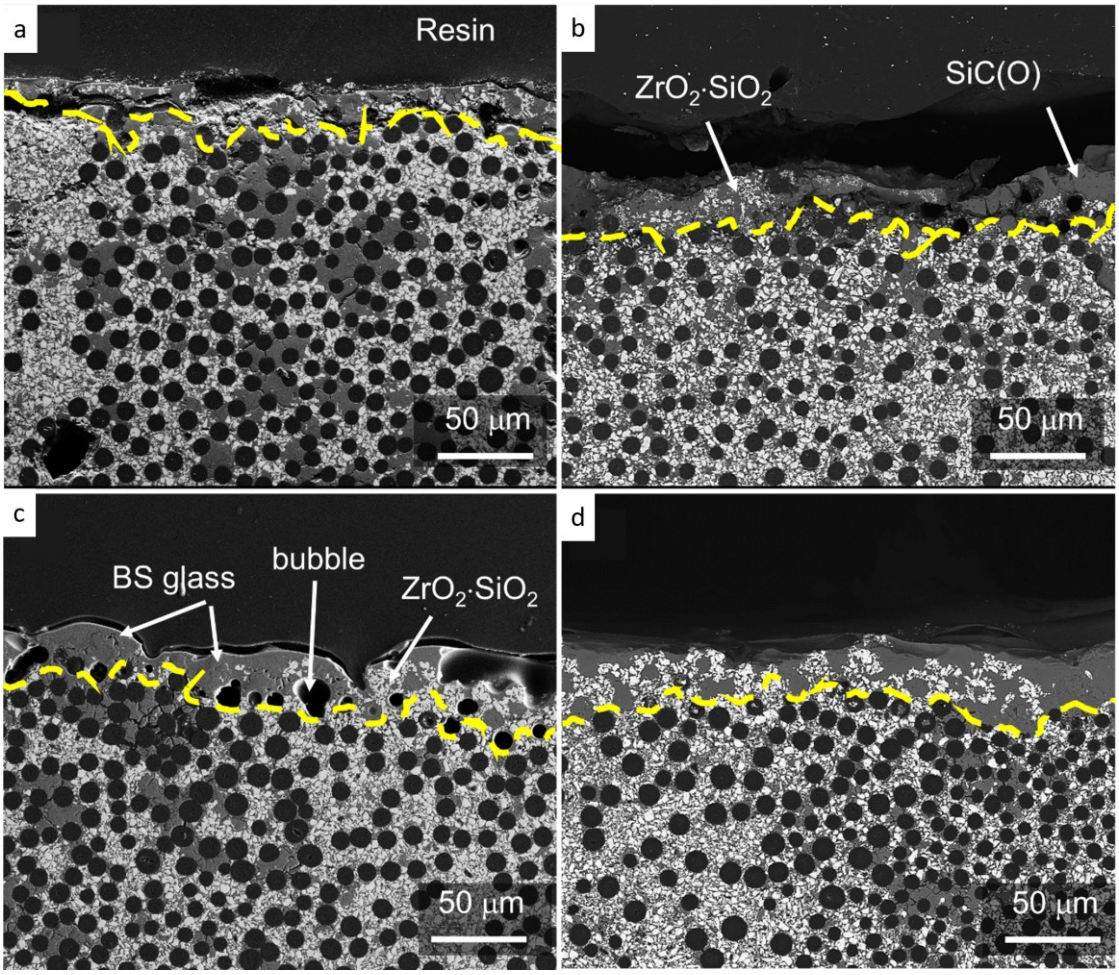

Figure 4.23. SEM images of cross section of sample 0/0° after short term oxidation tests at: a) 1500 °C for 1 min, b) 1500 °C for 5 min and c) 1650 °C for 1 min, d) 1650 °C for 5 min.

Based on the above analysis, the main phenomena occurring during exposition of C/ZrB_2-SiC were: oxidation of carbon fibres on or close to the surface, oxidation of ZrB_2 to zirconia and boron oxide, oxidation of SiC to silica, formation of a borosilicate glass [28,36,37]. As described before, samples were introduced inside the hot chamber when the target temperature was reached, i.e. 1500 °C and 1650 °C. Opening the furnace the temperature slightly decreased, but in a few tens of seconds, the temperature was re-stabilized. Thus, all oxidation phenomena occurred almost simultaneously. Although the permanence in the critical temperature range (700–1200 °C) [28] was rather short, near-surface fibres were still oxidized rapidly, and this contributed to an initial weight loss. However, the weight losses observed were much higher than expected and could be hardly attributed solely to that phenomenon or to the thin layer of oxide scale observed. The explanation could lie in the conversion of SiC(O) matrix into crystalline SiC, as it was obtained at the relatively mild condition of 1000 °C. Indeed, polymer-derived SiC(O) often contains free

turbostratic carbon and terminal Si-CH_3 and Si-OH groups in case of incomplete pyrolysis [47]. Moreover, oxygen in polymer-derived SiC(O) reacts with carbon causing mass loss decomposing into SiO and CO gases via reaction 6 [48].

$$SiO_2 + C \longrightarrow SiO + CO \quad (6)$$

According to the microstructural features of the specimens, the main mechanisms occurring in the UHTCMCs containing ZrB_2 particles embedded in amorphous SiC(O) are sketched in Figure 4.24.

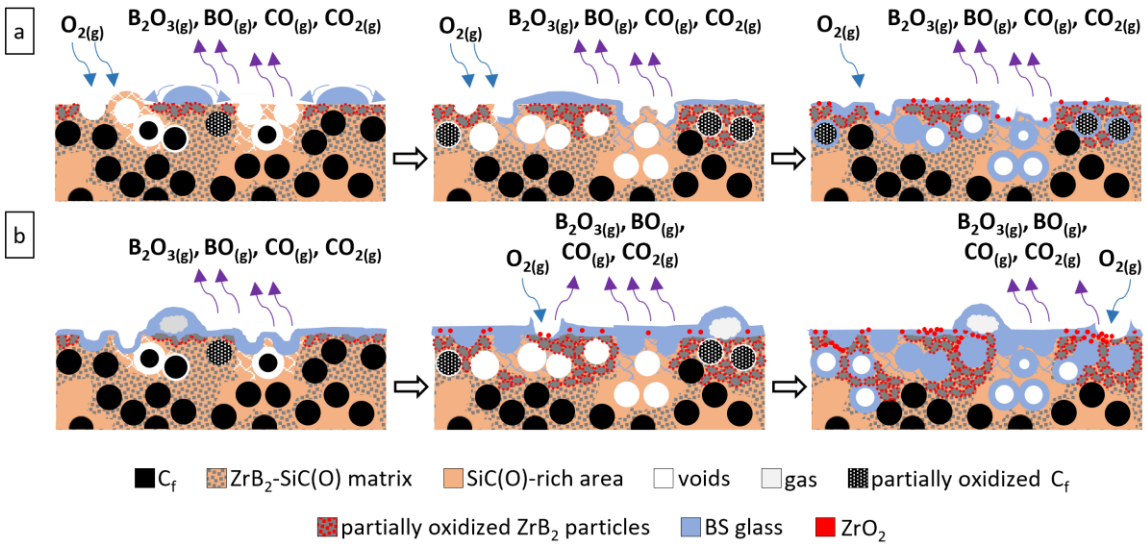

Figure 4.24. Sketch of oxidation mechanism of C_f/ZrB_2-SiC fabricated by water-based ZrB_2 powder slurry infiltration followed by 6 PIP cycles at (a) 1500 °C and (b) 1650 °C.

Yang et al. studied and comprehensively discussed the evolution of microstructure and properties of C/SiC composites prepared by PIP process after high-temperature oxidation. After oxidation in air at 1500 °C, the C/SiC composites were severely damaged, carbon fibres oxidation and many microcracks were evident [49]. The same author tested PIP-C/SiC at 1600 °C, and the carbon fibres were completely consumed and SiC matrix became loose due to the escape of the gas phases produced beneath the surface [50]. The results obtained here indicate that the addition of ZrB_2 particles through a first cycle of slurry infiltration was essential for the formation of a borosilicate glassy layer, which played an important role in closing the holes left by carbon fibres oxidation and the cracks in the surface and subsurface layer. In a previous work [3], we tried to define the most important factors that may enhance the matrix efficacy in protecting the most vulnerable phase, e.g. C fibres. These factors were:

I) C fibres must be circumvented by the protective ZrB_2-SiC matrix;

II) the matrix should have a low open porosity (<10%) to hinder oxygen penetration;

III) fibre content does not exceed the matrix content.

The results obtained here indicate that these criteria hold true also for samples processed by PIP, the only difference being the different SiC/ZrB_2 phase volumetric ratio.

On this basis, the oxidation behaviour of C/SiC and C/ZrB_2-SiC at temperatures in the range 1500–1650 °C can be compared emphasizing the self-protection effect in these latter, as depicted in the simplified sketch in Figure 4.25.

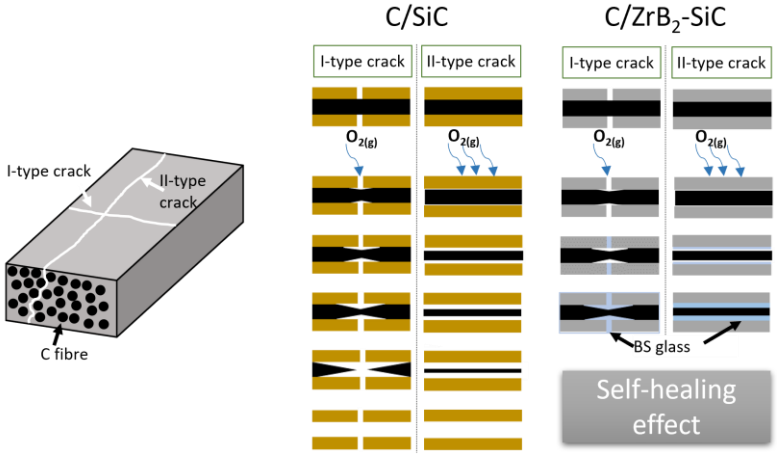

Figure 4.25. Sketch of oxidation behaviour of C/SiC and C/ZrB_2-SiC at elevated temperature (1500–1650 °C) in comparison. Two types of matrix cracks were considered in this simulation: I-type crack and II-type crack, perpendicular and parallel to the fibres respectively.

Several works concerning oxidation and ablation resistance of UHTCMCs have been done [21]. However, to the best of our knowledge, it is the first time that the capability of protecting carbon fibres of a ZrB_2-SiC matrix consolidated at mild conditions (i.e. 1000 °C) was investigated under oxidizing atmosphere. It is interesting to compare the performance of the three samples analysed in this work with samples reported in ref [37] and [3], prepared trough different manufacturing methods at higher temperature. To this aim, the plot of Figure 4.26a shows the oxide scale thickness after oxidation tests and carbon fibre content of samples while the plot of Figure 4.26b shows density and the relative amounts of ZrB_2, SiC, C_f and porosity (normalized values) of samples. It can be clearly seen that from sample 0/0° to ZS10-55F the oxidation resistance is not strictly correlated to the increase of fibre content. However, in the case of sample Z40S-55F the amount of fibres (55 vol%) was too high to have a uniform coating by the matrix, resulting

in poor resistance to oxidation, moreover the sample presents large ZrB_2-free matrix intra-bundle zones. The overall amount of SiC in the composite is also important to passivate the material surface. In sample Z10S-40F the presence of 6 vol% SiC promoted the formation of a borosilicate glass that diffused across the scale but efficacy is lower than in case of sample ZS20 and all of the samples of this work.

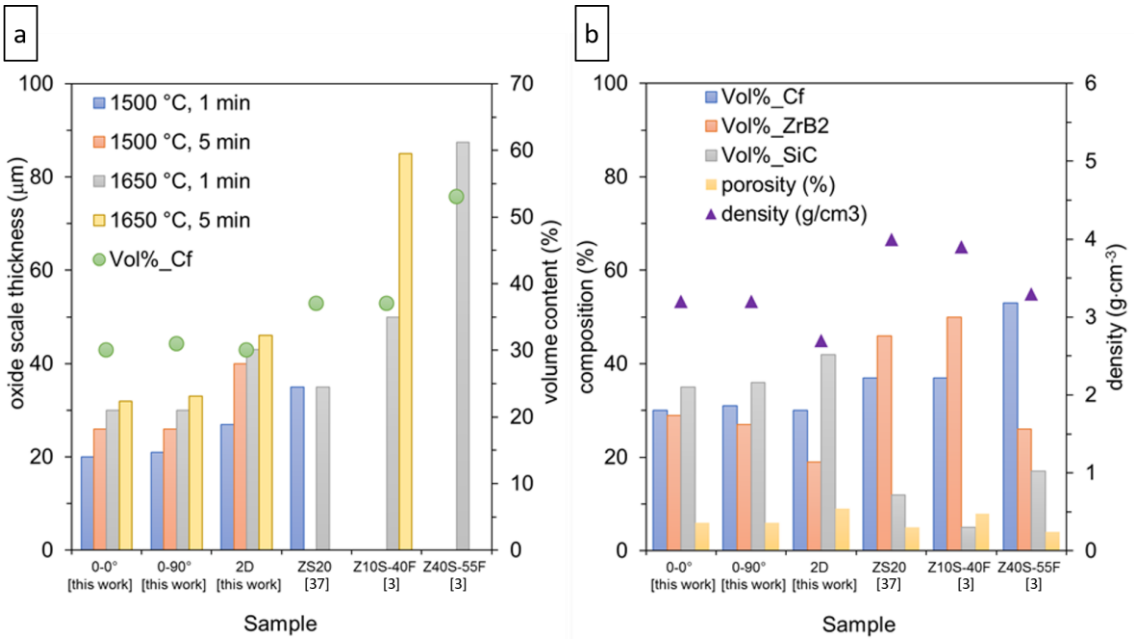

Figure 4.26. Plots show (a) the volumetric content of fibre (Vol%_Cf) of samples and the thickness of the oxide scale after tests, (b) density and relative amounts of ZrB_2, SiC, C_f and porosity (normalized values) of the three samples of this work and three samples of ref. [37] and [3]. Unpublished data of the oxide scale thickness after tests at 1650 °C were reported for samples ZS10-40F and ZS40S-55F.

The composition of the oxide layer depends on the oxidation temperature as well as the composition of the ZrB_2-SiC composite. In the binary phase diagram of SiO_2-B_2O_3 shown in Figure 4.27, it can be seen that there is a significant solubility of boron in liquid silica due to the absence of a defined compound above 450 °C [51]. However, the content of B_2O_3 affects the viscosity of the initial liquid [52,53]. Luke Sky Walker and Corral [53] studied that SiC filled C-C composite during oxidation testing at 1600 °C formed a glass of such high viscosity that it did not spread, resulting in complete oxidation of composite. Glass from C-C composites containing 5–9 vol% of ZrB_2 fillers had lower viscosity and could spread more easily, but it was unable to generate a continuous layer leaving regions unprotected. A higher B_2O_3 content reduced viscosity allowing the glass to spread quickly

across the sample; on the other hand, an excessive B_2O_3 caused more oxidation until a stable oxide scale was developed thanks to B_2O_3 evaporation.

A calculation was made to predict the composition of oxide layer for the compared samples, which have different SiC/ZrB_2 phase volumetric ratio. In ZrB_2-SiC composites, chemical reactions (3) and (4) represent the oxidation reaction, thus the amount of condensed oxides formed due to oxidation is as follows:

1 mol of ZrB_2 ⇒ 1 mol of ZrO_2 + 1 mol of B_2O_3

1 mol of SiC ⇒ 1 mol of SiO_2.

By considering the only binary interaction between SiO_2 and B_2O_3, the hypothetical compositions of the initial liquid oxide formed on each sample due to the oxidation tests were reported on the phase diagram (Figure 4.27).

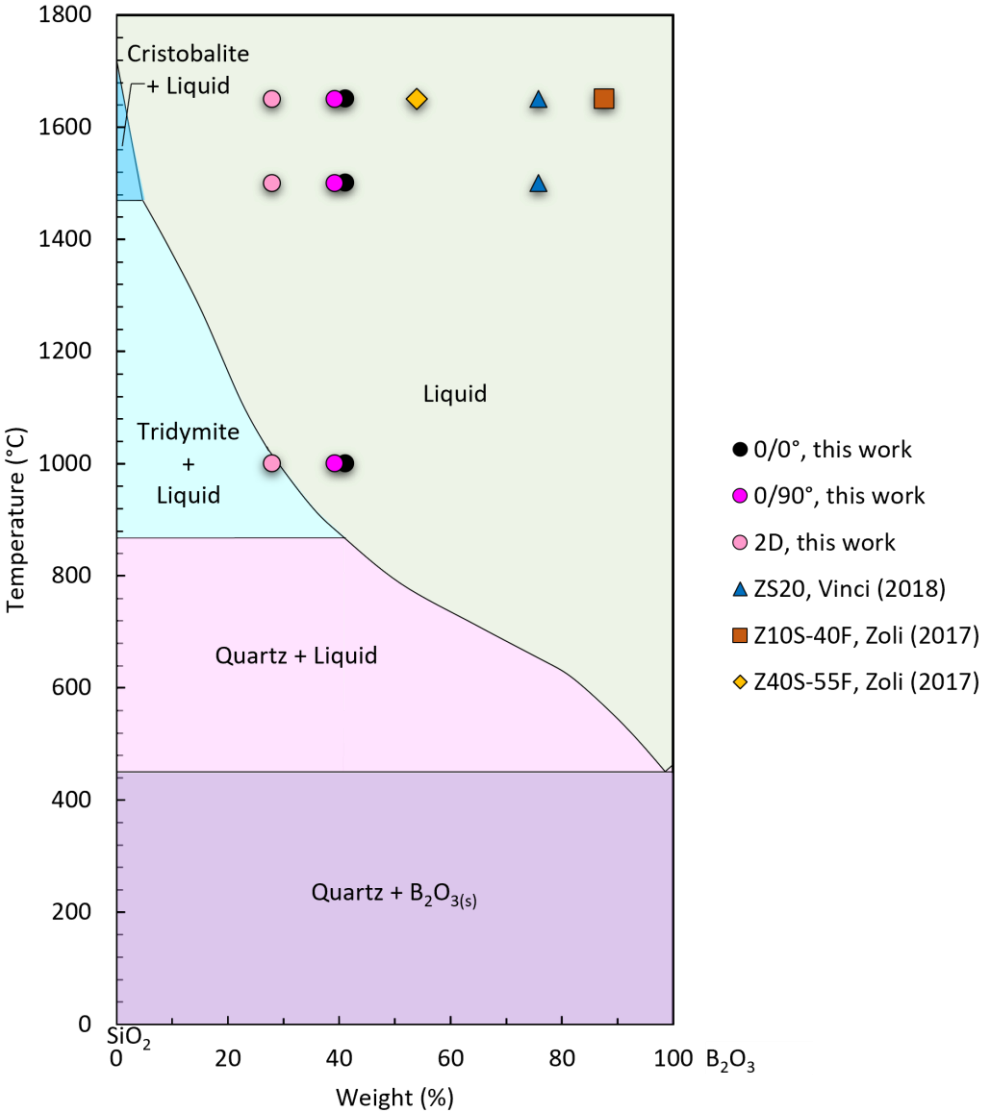

Figure 4.27. Binary phase diagram of SiO_2-B_2O_3 system, showing hypothetical compositions of the initial liquid oxide for the three samples of this work and samples of ref. [37] and [3].

4.6 Conclusions

In this work, pitch-based carbon fibres reinforced 20–30 vol% ZrB_2-enriched composites were fabricated via slurry infiltration (water based) coupled with polymer infiltration and pyrolysis at relatively low temperatures. Composites obtained using unidirectional fabrics (0/0° and 0/90°) had a bulk density of 3.2 g/cm^3 and a residual open porosity of ~6%. Good homogeneity of ZrB_2 distribution and low defectiveness were achieved. As expected, the composite obtained using plain woven fabrics made with very stiff fibres led to a less homogeneous microstructure, higher porosity (~10%) and consequently lower bulk density of 2.7 g/cm^3.

The mechanical properties, including bending strength, elastic and shear modulus, were critically evaluated. The performance showed the tendency to decrease with increase of the C_f preform complexity. For instance, the flexural strength was approaching 500 MPa for 0/0°, 370 MPa for 0/90° and 190 MPa for 2D. Moreover, preliminary mechanical tests at elevated temperature indicated that oxide impurities have a strong impact on material performance at extremely hot environments, consequently further optimizations are necessary.

Nevertheless, self-healing functionality, typical of sintered ZrB_2-SiC systems, was achieved also for these materials obtained at mild conditions. The oxidation behaviour was investigated via TGA up to 1350 °C. The capability of the material to withstand the extreme harsh conditions was evaluated via short term oxidation tests in air at 1500 °C and 1650 °C in a bottom loading furnace for 1 min and 5 min. The exposure to high temperature in air activated the formation of a borosilicate glass, typical of ZrB_2-SiC binary systems, and it was found that a ZrB_2 content of 20–30 vol% of the matrix is able to impart a fast passivation. As expected, the oxidation resistance was affected by the distribution of ZrB_2 into the SiC matrix, highlighting the direct correlation between the oxide scale thickness and the quality of the slurry infiltration process. Independently of fibre architecture and complexity, the material hindered oxygen penetration within 5 min of exposure to air at high temperature.

Lastly, a qualitative analysis of the environmental impact has been done taking into account the temperature and time of the proposed process compared to State of the Art. From a cost-effectiveness point of view, Polymer Impregnation Pyrolysis (PIP) technique

is in-between CVI and LSI. The first needs up to six months to realize a dense block of material requiring large energy input due to extended processing times, while the second usually takes just few days. However, properties of resulting materials and maximum temperature of application follow an inverse trend. Among the State of the Art of PIP processes described in literature, proposed process in this thesis has the common aim to reduce the time of manufacturing and reduce the waste of chemicals keeping high performance of the final material. The main advantages are described below:

(i) avoid the use of solvents to realize the slurry for powder impregnation,

(ii) avoid the use of solvents to dilute polycarbosilane to decrease viscosity during polymer infiltration,

(iii) use of mild temperature of pyrolysis,

(iv) high content of UHTC phase in the matrix,

(v) homogeneity of UHTC phase distribution around carbon fibres.

4.7 References

1. Reimer, T., Petkov, I., Koch, D., Fließ, M. & Dellin, C. Fabrication and characterization of C/C-SiC material made with pitch-based carbon fibers. *Ceram. Trans.* **252**, 277–293 (2015).

2. Mainzer, B. *et al.* Characterization and application of a novel low viscosity polysilazane for the manufacture of C- and SiC-fiber reinforced SiCN ceramic matrix composites by PIP process. *J. Eur. Ceram. Soc.* **39**, 212–221 (2019).

3. Zoli, L. & Sciti, D. Efficacy of a ZrB_2–SiC matrix in protecting C fibres from oxidation in novel UHTCMC materials. *Mater. Des.* **113**, 207–213 (2017).

4. Huang, Y. & Young, R. J. Effect of fibre microstructure upon the modulus of PAN- and pitch-based carbon fibres. *Carbon N. Y.* (1995) doi:10.1016/0008-6223(94)00109-D.

5. Chung, D. D. L. Ceramic-Matrix Composites. in *Carbon Composites* (ed. Chung, D.) 467–531 (Elsevier Inc., 2017). doi:10.1016/B978-0-12-804459-9/00008-7.

6. Zhang, D., Hu, P., Dong, S., Qu, Q. & Zhang, X. Effect of pyrolytic carbon coating on the microstructure and fracture behavior of the C_f/ZrB_2-SiC composite. *Ceram. Int.* **44**, 19612–19618 (2018).

7. Fellah, C., Braun, J., Sauder, C., Sirotti, F. & Berger, M. H. Influence of the carbon interface on the mechanical behavior of SiC/SiC composites. *Compos. Part A Appl. Sci. Manuf.* **133**, 105867 (2020).

8. Zhou, Y., Zhou, W. C., Luo, F. & Zhu, D. M. Effects of dip-coated BN interphase on mechanical properties of SiC_f/SiC composites prepared by CVI process. *Trans.*

Nonferrous Met. Soc. China (English Ed. **24**, 1400–1406 (2014).

9. Starfire® Systems Inc. StarPCS SMP-10. (2018).

10. Justin, J. F., Julian-Jankowiak, A., Guérineau, V., Mathivet, V. & Debarre, A. Ultra-high temperature ceramics developments for hypersonic applications. *CEAS Aeronaut. J.* **11**, 651–664 (2020).

11. Hu, H. *et al.* Preparation and characterization of C/SiC-ZrB_2 composites by precursor infiltration and pyrolysis process. *Ceram. Int.* **36**, 1011–1016 (2010).

12. Zoli, L. *et al.* Additive Manufacturing of Ceramics Enabled by Flash Pyrolysis of Polymer Precursors with Nanoscale Layers. *J. Am. Ceram. Soc.* **99**, 57–63 (2016).

13. Colombo, P., Mera, G., Riedel, R. & Sorarù, G. D. Polymer-derived ceramics: 40 Years of research and innovation in advanced ceramics. *J. Am. Ceram. Soc.* **93**, 1805–1837 (2010).

14. Kaur, S., Riedel, R. & Ionescu, E. Pressureless fabrication of dense monolithic SiC ceramics from a polycarbosilane. *J. Eur. Ceram. Soc.* **34**, 3571–3578 (2014).

15. Lin, Y., Liu, C., Li, H., Jin, K. & Tao, J. Interlaminar failure behavior of GLARE laminates under double beam five-point-bending load. *Compos. Struct.* **201**, 79–85 (2018).

16. Li, Q. *et al.* Mechanical properties and microstructures of 2D C_f/ZrC-SiC composites using ZrC precursor and polycarbosilane. *Ceram. Int.* **38**, 6041–6045 (2012).

17. Wang, Y., Liu, W., Cheng, L. & Zhang, L. Preparation and properties of 2D C/ZrB_2-SiC ultra high temperature ceramic composites. *Mater. Sci. Eng. A* **524**, 129–133 (2009).

18. Li, L., Wang, Y., Cheng, L. & Zhang, L. Preparation and properties of 2D C/SiC-ZrB_2-TaC composites. *Ceram. Int.* **37**, 891–896 (2011).

19. Gui, K., Liu, F., Wang, G., Huang, Z. & Hu, P. Microstructural evolution and performance of carbon fiber-toughened ZrB_2 ceramics with SiC or $ZrSi_2$ additive. *J. Adv. Ceram.* **7**, 343–351 (2018).

20. Vinci, A., Zoli, L., Sciti, D., Melandri, C. & Guicciardi, S. Understanding the mechanical properties of novel UHTCMCs through random forest and regression tree analysis. *Mater. Des.* **145**, 97–107 (2018).

21. Binner, J. *et al.* Selection, processing, properties and applications of ultra-high temperature ceramic matrix composites, UHTCMCs–a review. *Int. Mater. Rev.* **65**, 389–444 (2020).

22. Arai, Y. Pitch-based carbon fibers. in *High-Performance and Specialty Fibers: Concepts, Technology and Modern Applications of Man-Made Fibers for the Future* (ed. Japan The Society of Fiber Science and Techno) 343–354 (Springer Japan, 2016). doi:10.1007/978-4-431-55203-1_21.

23. Fahrenholtz, W. G., Hilmas, G. E., Talmy, I. G. & Zaykoski, J. A. Refractory

diborides of zirconium and hafnium. *J. Am. Ceram. Soc.* **90**, 1347–1364 (2007).

24. Demetriou, M. D. *et al.* A damage-tolerant glass. *Nat. Mater. 2011 102* **10**, 123–128 (2011).

25. Galizia, P., Zoli, L. & Sciti, D. Impact of residual stress on thermal damage accumulation, and Young's modulus of fiber-reinforced ultra-high temperature ceramics. *Mater. Des.* **160**, 803–809 (2018).

26. Ojovan, M. I. Glass formation in amorphous SiO_2 as a percolation phase transition in a system of network defects. *JETP Lett.* **79**, 632–634 (2004).

27. Altemose, V. O. 7. Glass vacuum systems. in *Methods in Experimental Physics* (eds. Weissler, G. L. & Carlson, R. W.) vol. 14 313–343 (Academic Press, 1980).

28. Vinci, A., Zoli, L., Landi, E. & Sciti, D. Oxidation behaviour of a continuous carbon fibre reinforced ZrB_2–SiC composite. *Corros. Sci.* **123**, 129–138 (2017).

29. Chollon, G. Oxidation Behavior of Ceramic Fibers from the Si-C-N-O System and Sub-Systems. *Key Eng. Mater.* **164**–**165**, 395–398 (1999).

30. Zhou, H., Gao, L., Wang, Z. & Dong, S. ZrB_2 -SiC Oxidation Protective Coating on C/C Composites Prepared by Vapor Silicon Infiltration Process. *J. Am. Ceram. Soc.* **93**, 915–919 (2010).

31. Haibo, O. *et al.* Self-healing ZrB_2–SiO_2 oxidation resistance coating for SiC coated carbon/carbon composites. *Corros. Sci.* **110**, 265–272 (2016).

32. Corral, E. L. & Loehman, R. E. Ultra-high-temperature ceramic coatings for oxidation protection of carbon-carbon composites. *J. Am. Ceram. Soc.* **91**, 1495–1502 (2008).

33. Tang, S., Deng, J., Wang, S. & Liu, W. Fabrication and Characterization of an Ultra-High-Temperature Carbon Fiber-Reinforced ZrB_2-SiC Matrix Composite. *J. Am. Ceram. Soc.* **90**, 3320–3322 (2007).

34. Liu, L. *et al.* Ablation in different heat fluxes of C/C composites modified by ZrB_2-ZrC and ZrB2-ZrC-SiC particles. *Corros. Sci.* **74**, 159–167 (2013).

35. Li, Q., Dong, S., Wang, Z. & Shi, G. Fabrication and properties of 3-D C_f/ZrB_2-ZrC-SiC composites via polymer infiltration and pyrolysis. *Ceram. Int.* **39**, 5937–5941 (2013).

36. Servadei, F., Zoli, L., Galizia, P., Vinci, A. & Sciti, D. Development of UHTCMCs via water based ZrB_2 powder slurry infiltration and polymer infiltration and pyrolysis. *J. Eur. Ceram. Soc.* **40**, 5076–5084 (2020).

37. Vinci, A., Zoli, L. & Sciti, D. Influence of SiC content on the oxidation of carbon fibre reinforced ZrB_2/SiC composites at 1500 and 1650 °C in air. *J. Eur. Ceram. Soc.* **38**, 3767–3776 (2018).

38. Huang, D., Zhang, M., Huang, Q., Wang, L. & Tong, K. Mechanical Property, Oxidation and Ablation Resistance of C/C–ZrB_2–ZrC–SiC Composite Fabricated by Polymer Infiltration and Pyrolysis with Preform of C_f/ZrB_2. *J. Mater. Sci. Technol.*

33, 481–486 (2017).

39. Seong, Y. H. & Kim, D. K. Oxidation behavior of ZrB_2-xSiC composites at 1500 °C under different oxygen partial pressures. *Ceram. Int.* **40**, 15303–15311 (2014).

40. Gao, D. *et al.* Oxidation of zirconium diboride-silicon carbide ceramics under an oxygen partial pressure of 200Pa: Formation of zircon. *Corros. Sci.* **52**, 3297–3303 (2010).

41. Opila, E., Levine, S. & Lorincz, J. Oxidation of ZrB_2- And HfB_2-based ultra-high temperature ceramics: Effect of Ta additions. *J. Mater. Sci.* **39**, 5969–5977 (2004).

42. Karlsdottir, S. N., Halloran, J. W. & Grundy, A. N. Zirconia transport by liquid convection during oxidation of zirconium diboride-silicon carbide. *J. Am. Ceram. Soc.* **91**, 272–277 (2008).

43. Glass, D. E. Ceramic matrix composite (CMC) thermal protection systems (TPS) and hot structures for hypersonic vehicles. *15th AIAA Int. Sp. Planes Hypersonic Syst. Technol. Conf.* (2008) doi:10.2514/6.2008-2682.

44. Williams, P. A., Sakidja, R., Perepezko, J. H. & Ritt, P. Oxidation of ZrB_2-SiC ultra-high temperature composites over a wide range of SiC content. *J. Eur. Ceram. Soc.* **32**, 3875–3883 (2012).

45. Rezaie, A., Fahrenholtz, W. G. & Hilmas, G. E. The effect of a graphite addition on oxidation of ZrB_2-SiC in air at 1500°C. *J. Eur. Ceram. Soc.* **33**, 413–421 (2013).

46. Uhlmann, F. *et al.* Preparation and characterization of ZrB_2 and TaC containing C_f/SiC composites via Polymer-Infiltration-Pyrolysis process. *J. Eur. Ceram. Soc.* **37**, 1955–1960 (2017).

47. Chollon, G. Oxidation behaviour of polymer-derived ceramics. *Polym. Deriv. Ceram. From Nano-structure to Appl.* 292–308 (2010).

48. Hasegawa, Y. & Okamura, K. Synthesis of continuous silicon carbide fibre - Part 3 Pyrolysis process of polycarbosilane and structure of the products. *J. Mater. Sci.* **18**, 3633–3648 (1983).

49. Xiang, Y., Li, W., Wang, S. & Chen, Z. H. Oxidation behavior of oxidation protective coatings for PIP-C/SiC composites at 1500 °C. *Ceram. Int.* **38**, 9–13 (2012).

50. Yang, X., Feng, C., Peng, Z. hang, Yi, W. & Li, G. de. Evolution of microstructure and mechanical properties of PIP-C/SiC composites after high-temperature oxidation. *J. Asian Ceram. Soc.* **5**, 370–376 (2017).

51. Vadon, M. Extraction de bore par oxydation du silicium liquide pour applications photovoltaïques Boron extraction from liquid silicon by oxidation for photovoltaic applications. (Université Grenoble Alpes, 2017).

52. Karlsdottir, S. N. & Halloran, J. W. Oxidation of ZrB_2-SiC: Influence of SiC content on solid and liquid oxide phase formation. *J. Am. Ceram. Soc.* **92**, 481–486 (2009).

53. Walker, L. S. & Corral, E. L. Self-Generating High-Temperature Oxidation-Resistant Glass-Ceramic Coatings for C-C Composites Using UHTCs. *J. Am. Ceram. Soc.* **97**,

3004–3011 (2014).

5. PAN-based carbon fibre-reinforced UHTCMCs via water-based slurry infiltration and polymer infiltration and pyrolysis

5.1 Introduction

In Chapter 4, pitch-based C_f/ZrB_2-SiC composites containing about 20–30 vol% of ZrB_2 (depending on fibre architecture) were presented. Overall, good homogeneity of ZrB_2 distribution and low defectiveness were obtained. The use of mild conditions was found to limit the reactivity of fibres with boride and silicide phases. Hence, pitch-based carbon fibres, even without a coating, provided intra-bundle pull-out during fracture.

Polyacrylonitrile (PAN)-based carbon fibres are the favourite option for the manufacturing of C/C or C/SiC composites. The main reasons are lower price, wider availability on the market, as well as the high tenacity and strength, and lower stiffness which makes weaving easier, in turn enabling more complex preform architectures. Similar to steel wires in reinforced concrete, fibre is the structural backbone of a composite. Starting with linear assemblies of fibres in continuous form, these fibres with diameter of few micrometres can be organized into two- and three-dimensional structures to impart properties in different directions. Different layers of the ceramic matrix structure may be arranged differently to achieve different objectives in different regions of the ceramic matrix structure. The fibre tow spacing, fibre count and/or other characteristics may be varied within individual layers and/or among different layers of the ceramic matrix structure.

This chapter discusses the challenge to realize Ultra-High Temperature Ceramic Matrix Composites (UHTCMCs) by water-based slurry infiltration followed by six Polymer Infiltration and Pyrolysis (PIP) cycles at relatively low temperature, using uncoated PAN-based carbon fibres. Four cloths at increased level of fibre architecture complexity were selected to ensure toughening of the material at different angles: unidirectional, twill, plain, and 2.5D. The scope was to investigate the microstructural features and mechanical properties to understand advantages and drawbacks of PAN-based carbon fibres as reinforcement in UHTCMCs manufactured under mild conditions.

5.2 Manufactured C_f/ZrB_2-SiC composites

Four C_f/ZrB_2-SiC samples with different fibre architectures were fabricated by a cycle of water-based slurry infiltration of fibre fabrics, using a mixture of ZrB_2-10 vol% SiC powders, followed by repetitive cycles of PIP, according to the procedure reported in Chapter 3. Infiltration with SMP-10 (containing 1 wt% of catalyst DCP) and pyrolysis cycles at 1000 °C under argon flux were carried out six times, as for pitch-based C_f/ZrB_2-SiC composites previously studied (Chapter 4).

The architecture of the preforms and the resulting UHTCMCs, obtained by infiltration of those cloths, are shown in Figure 5.1.

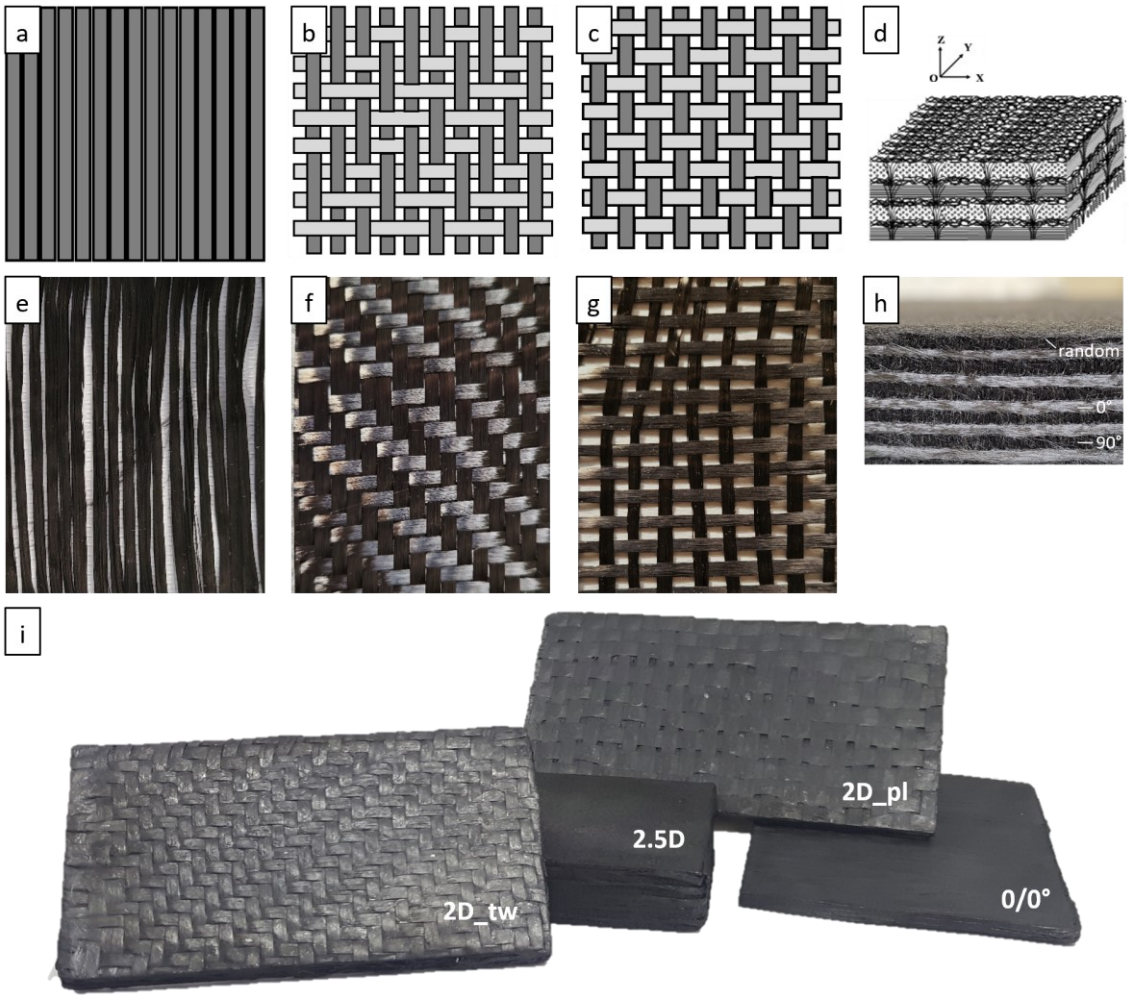

Figure 5.1. Schematic representation and optical images of used carbon fibres: (a,e) unidirectional (UD) fabrics, (b,f) 2D twill weave fabrics, (c,g) 2D plain weave fabrics and (d,h) 2.5D needle-punched preform. (i) C_f/ZrB_2-SiC samples with different C_f architectures: sample 0/0°, prepared by stacking infiltrated UD fabrics with the same orientation, samples 2D_tw and 2D_pl, realized with infiltrated and subsequently piled up twill and plain-woven fabrics respectively, sample 2.5D prepared by infiltrating 2.5D preform.

Sketches of weaving and optical pictures of the used fibre cloths, with increasing complexity of the architecture, are reported in Figure 5.1a-d and Figure 5.1e-h, respectively. Unidirectional one (Figure 5.1a,e) is the most anisotropic while 2D cloths supply a balanced reinforcement on *xy* plan. Unidirectional fabrics (Figure 5.1d) were prepared homemade starting from 2D twill-woven fabrics. 2D twill (Figure 5.1b,f) and 2D plain (Figure 5.1c,g) woven cloths differs for the number of crimps. Both 2D cloths were selected to see the stress induced by weaving on carbon fibres. Finally, the needle-punched 2.5D one (Figure 5.1d,h) offers the most isotropic reinforcement among selected ones due to the presence of carbon fibres oriented in *z* axis. Indeed, the structure of this C_f preform consisted of layers of fabric stacked in an arrangement of random/0°/random/90°/random orientation fibres, where 0° and 90° are unidirectional layers and the random layers were formed as a result of Surface Transform's needling process [1,2].

A sample, with an asymmetric orientation of fibres, was realized by stacking infiltrated unidirectional fabrics with the same orientation (sample labelled as **0/0°**). A second sample was realized by stacking infiltrated twill-woven fabrics (sample labelled as **2D_tw**), while a third sample was prepared by stacking infiltrated plain-woven fabrics alternating PAN/pitch orientation between the layers (sample labelled as **2D_pl**). A fourth sample was obtained by using a squeeze impregnation technique where the 17 mm- thick preform was fully immersed in a container containing the slurry and squeezed manually repeatedly to achieve maximum slurry intake [3] (sample labelled as **2.5D**) (Figure 5.1i).

5.3 Microstructural characterization

Compositions, densities and residual porosities of the final composites reinforced with different architectures after 6 PIP cycles are reported in Table 5.1.

Table 5.1. Composition, open porosity (measured by MIP) and bulk density (measured via geometric method) of the fabricated composites with different carbon fibre architectures.

Sample label	C_f (vol%)	UHTC (vol%)	SiC (vol%)	Open porosity (%)	Bulk density (g/cm^3)
0/0°	24	48	17	~11	3.42
2D_tw	28	34	33	~5	2.85
2D_pl	21	38	36	~5	2.86
2.5D	26	22	24	~28	2.20

After slurry infiltration step, the porosity was in the range 30–50 vol% depending on the fibre architecture. As a consequence, green samples showed different levels of bulk densities: ~3.0 g/cm^3 for sample 0/0°, 2.2 g/cm^3 for samples prepared using 2D woven fabrics, and ~1.7 g/cm^3 for sample 2.5D. Then, bulk densities gradually decreased step-by-step carrying out repetitive PIP cycles, see Figure 5.2.

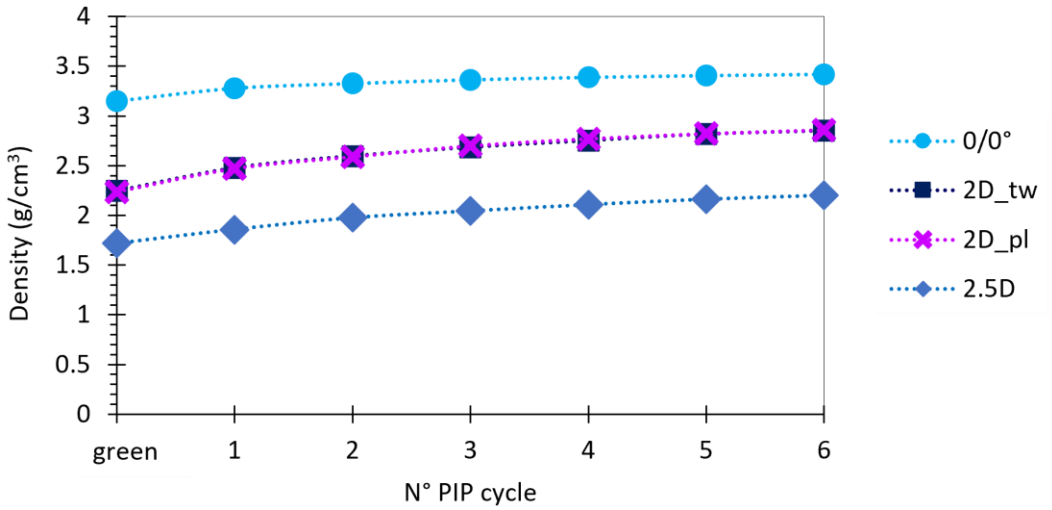

Figure 5.2. Variation of the bulk densities, which are measured by geometric method after slurry infiltration step (green) and each PIP cycle for samples 0/0°, 2D_tw, 2D_pl and 2.5D.

After six PIP cycles, sample 0/0° reinforced with the UD cloth had the highest density (3.42 g/cm^3); samples reinforced with 2D-woven cloths, irrespectively of the different weaving, achieved similar porosity (2.85 g/cm^3 for 2D_tw and 2.86 g/cm^3 for 2D_pl), lower than that of 0/0° sample; sample 2.5D had the lowest density (2.20 g/cm^3).

Starting from the fibre mass content (which was calculated considering the fibre areal weight given by the supplier, number of layers and sample area), the matrix amount added through powder slurry infiltration (determined as the difference between the infiltrated material weight and fibre weight) and the total amount of the added polymer-derived SiC, fibre volumetric content (FVC) and volume fractions of matrix phases were determined. All the composites contained fraction of carbon fibres below 30 vol%. As expected, a trend similar to bulk density was observed for the ZrB_2 volume content which was higher in the sample with the less crimped fibre architecture, explaining the higher density. Likely, the tight bonding of the carbon fibre fabrics due to the twill and plain textures as well as complex 2.5D preform did not allow an equally penetration of the slurry [4]. Due to the lower extent of ZrB_2 infiltration, samples with more complex

architecture had a larger fraction of amorphous SiC(O) obtained by low-temperature pyrolysis of polycarbosilane, in particular 2D_tw (33 vol%) and 2D_pl (36 vol%).

The porosity measured by mercury intrusion porosimetry was ~11% for 0/0° sample and ~5% for 2D_tw and 2D_pl, while sample 2.5D revealed a significantly higher porosity ~28%. The pore size distribution of all samples is reported in Figure 5.3. The samples 0/0°, 2D_tw and 2D_pl contained a larger volume fraction of pores with diameter less than 20 µm, due to incomplete densification via PIP. For sample 2.5D a monomodal distribution centred at diameters around 60–70 µm was observed, suggesting non-optimized infiltration of the fibre preform with slurry [5]. A single slurry infiltration of a thick 2.5 D preform is less effective than previous cloths but overlapping of infiltrated UD and 2D cloths; however, overlapping of infiltrated UD and 2D fabrics probably caused the formation of macro-pores which were missing in 2.5D sample out of revelation range of porosimeter.

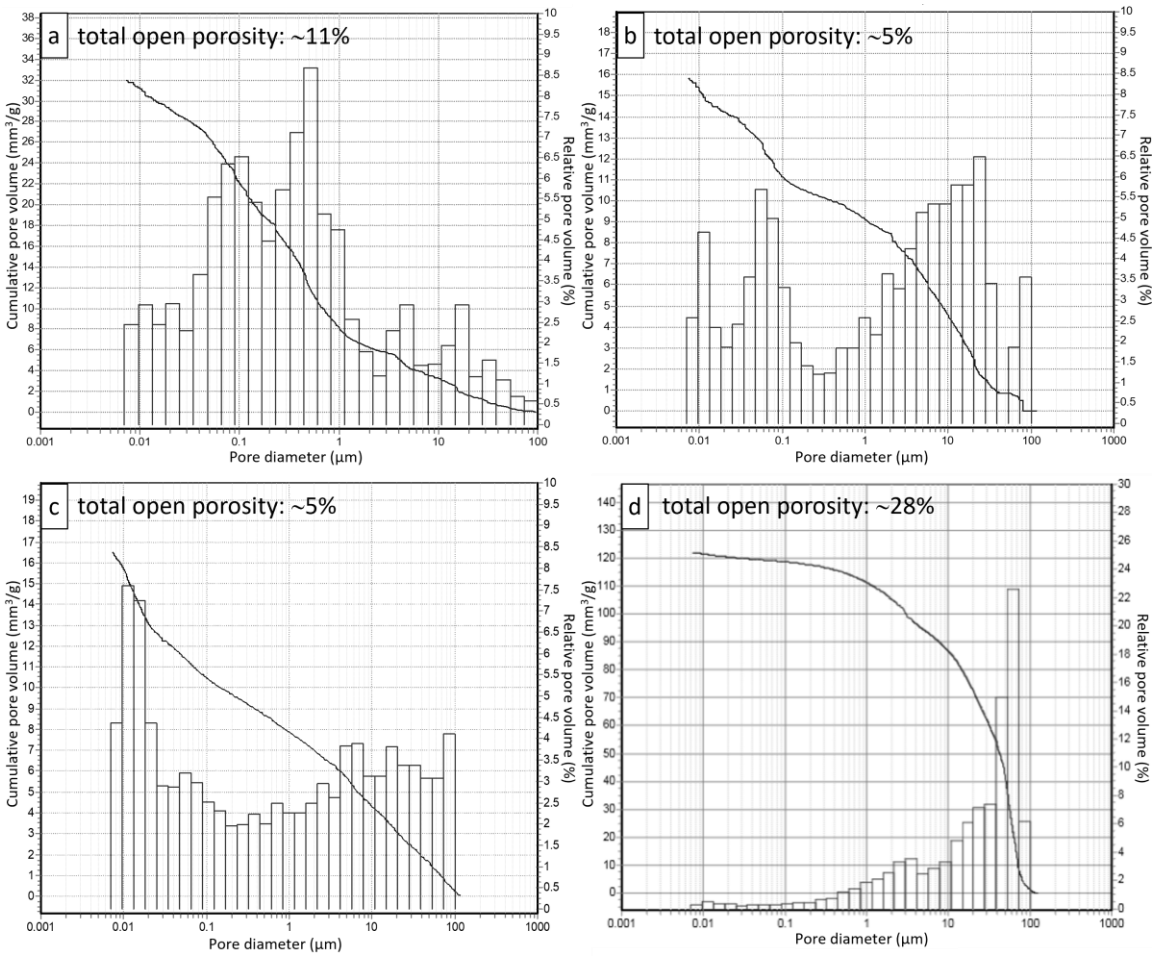

Figure 5.3. Pore size distribution by Mercury Intrusion Porosimetry (MIP) of the samples obtained after 6 PIP cycles: (a) sample 0/0°, (b) sample 2D_tw, (c) sample 2D_pl and (d) sample 2.5D.

Description of microstructural features of each sample is reported below, while micrographs are shown from Figure 5.4 to Figure 5.8.

0/0° Sample: Polished surface (Figure 5.4a) showed a homogeneous distribution of the matrix among fibres (fibre dark lines while the matrix is grey contrasting area). It can be noted that through the adopted manual procedure it was difficult to control the fibre density all over the linear array and the bundles alignment. At higher magnification (Figure 5.4b), pores are visible, that were probably caused by bubbles of air entrapped during slurry infiltration. Polymer-derived amorphous SiC(O) (grey phase) was found well distributed at grain boundary of ZrB_2 particles (light phase). Some large SiC(O)-rich area were probably due to the capability of the liquid precursor to fill small voids formed during slurry infiltration. No cracks were found in the samples.

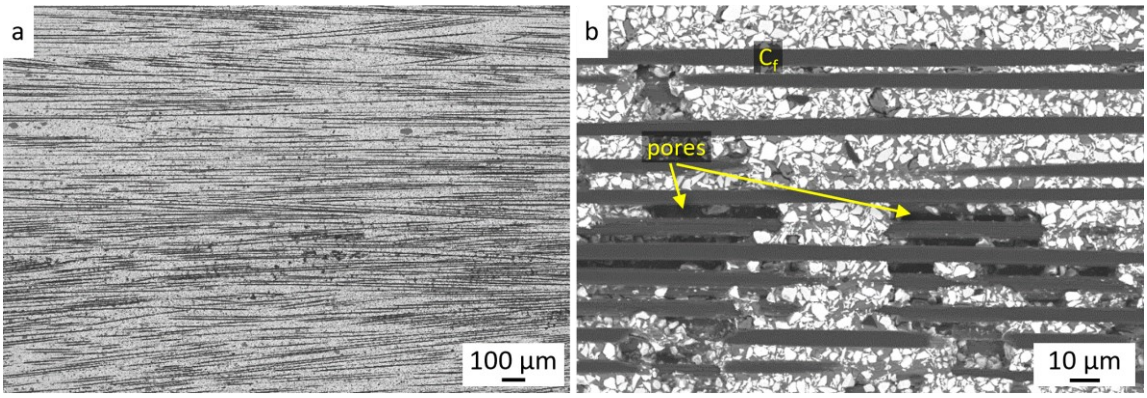

Figure 5.4. Polished surface of sample 0/0°. (a) Overview highlighting fibre distribution (fibres are black lines) and (b) enlarged view on residual porosity.

The cross section images at 90° view with increasing magnification are reported in Figure 5.5a-d. Figure 5.5a revealed the presence of large voids among the fibre layers out of the range of MIP (> 100 µm). These defects in the interplay zones formed during the overlapping of infiltrated cloths before drying stage as a result of imperfections in the shaping process. They were likely favoured by the defectiveness of home-made UD fabrics starting from 2D twill texture. In that case, the low viscous polycarbosilane was unable to fill the macro-voids. An enlarged view (Figure 5.5b) evidenced the homogenous distribution of carbon fibre in the matrix into single cloth, highlighting a high content of ZrB_2 particles. In Figure 5.5c, fibres, ZrB_2 and SiC are well distinguishable: dark contrasting bean-like dots are cross-sectional view of C fibres, ZrB_2 is the light contrasting phase, SiC is the grey areas, SiC from powder in form of particles aggregates while SiC(O) among

fibres and ceramic particles as glassy phase. The morphology of ZrB_2 grains and fibres are similar to starting raw materials, coarsening of ZrB_2 was not revealed and mean fibre diameter is in agreement with that of pristine ones. Fibre/matrix interface is shown in Figure 5.5d. A thin amorphous film of SiC(O) was found along the fibre interface, but it is not clear its reactivity with the rugged surface of turbostratic carbon fibre.

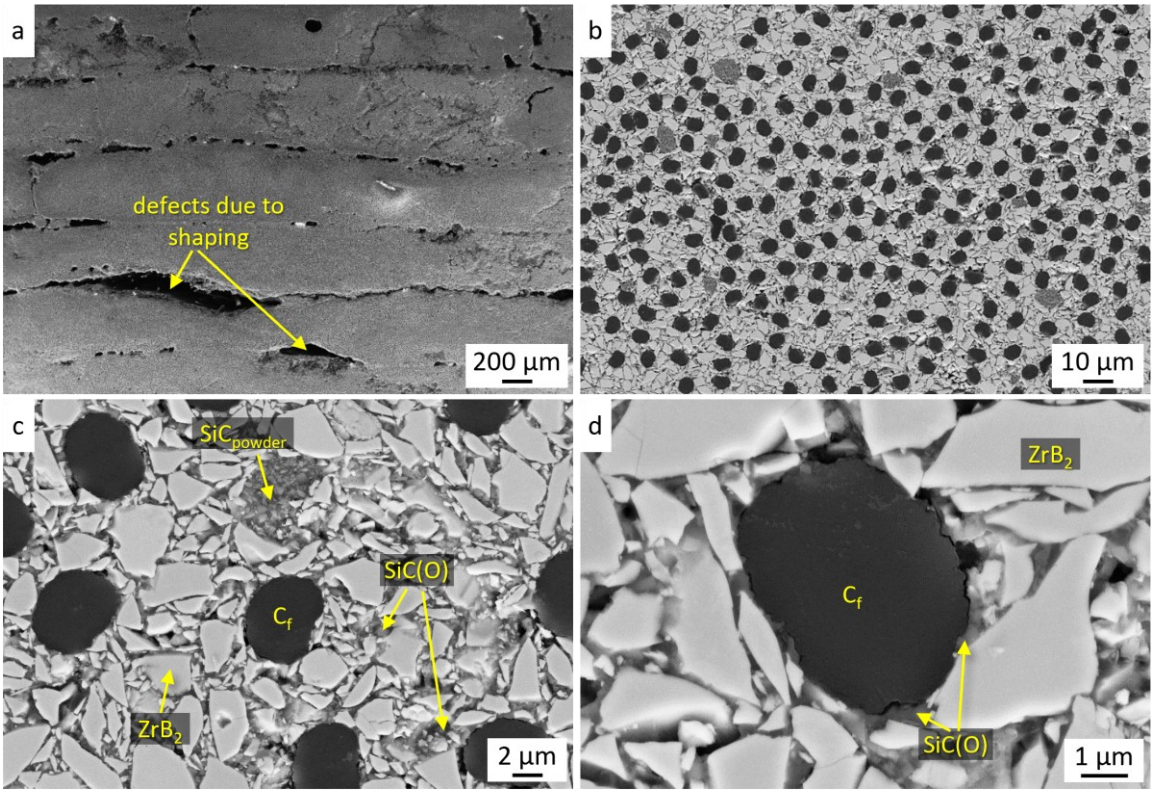

Figure 5.5. Polished cross section of sample 0/0°. (a) General overview showing macro-voids between the layers due to imperfect shaping step. (b) Low magnification micrograph, (c) microstructure inside bundle (fibres are black dots, ZrB_2 is bright phase, SiC from powder and polymer is the grey phase as indicated), (d) detail of a single fibre.

2D_tw Sample: Polished surface (Figure 5.6a) showed a dense matrix, in which voids due to the geometry of fibre bundles in the warp and weft directions of twill pattern were filled with ZrB_2-rich matrix. An enlarged view (Figure 5.6b,c) confirmed the homogeneous distribution of carbon fibre in the matrix and evidenced a high degree of slurry infiltration also inside the bundle. However, cross section was characterised by well consolidated regions, where a small residual porosity due to PIP process was observed, interspersed with periodically (8–10 mm) distributed macro-voids with size ranging from 1.5 to 2.5 mm. SEM images are reported in Figure 5.7a-g.

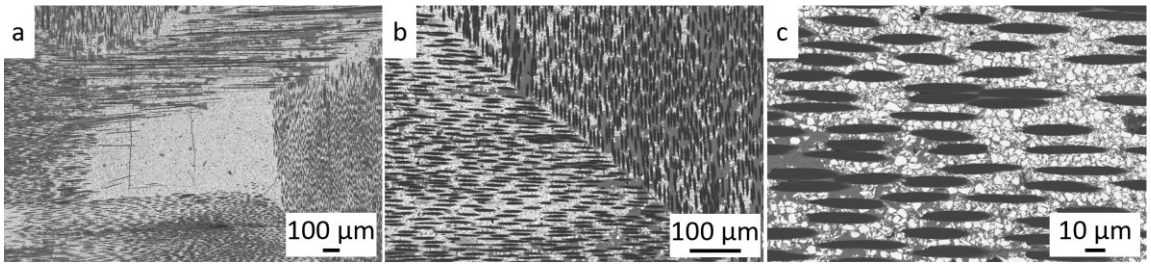

Figure 5.6. Polished surface of sample 2D_tw. (a) Overview highlighting matrix-rich areas in the cross of fibre bundles and (b,c) enlarged views.

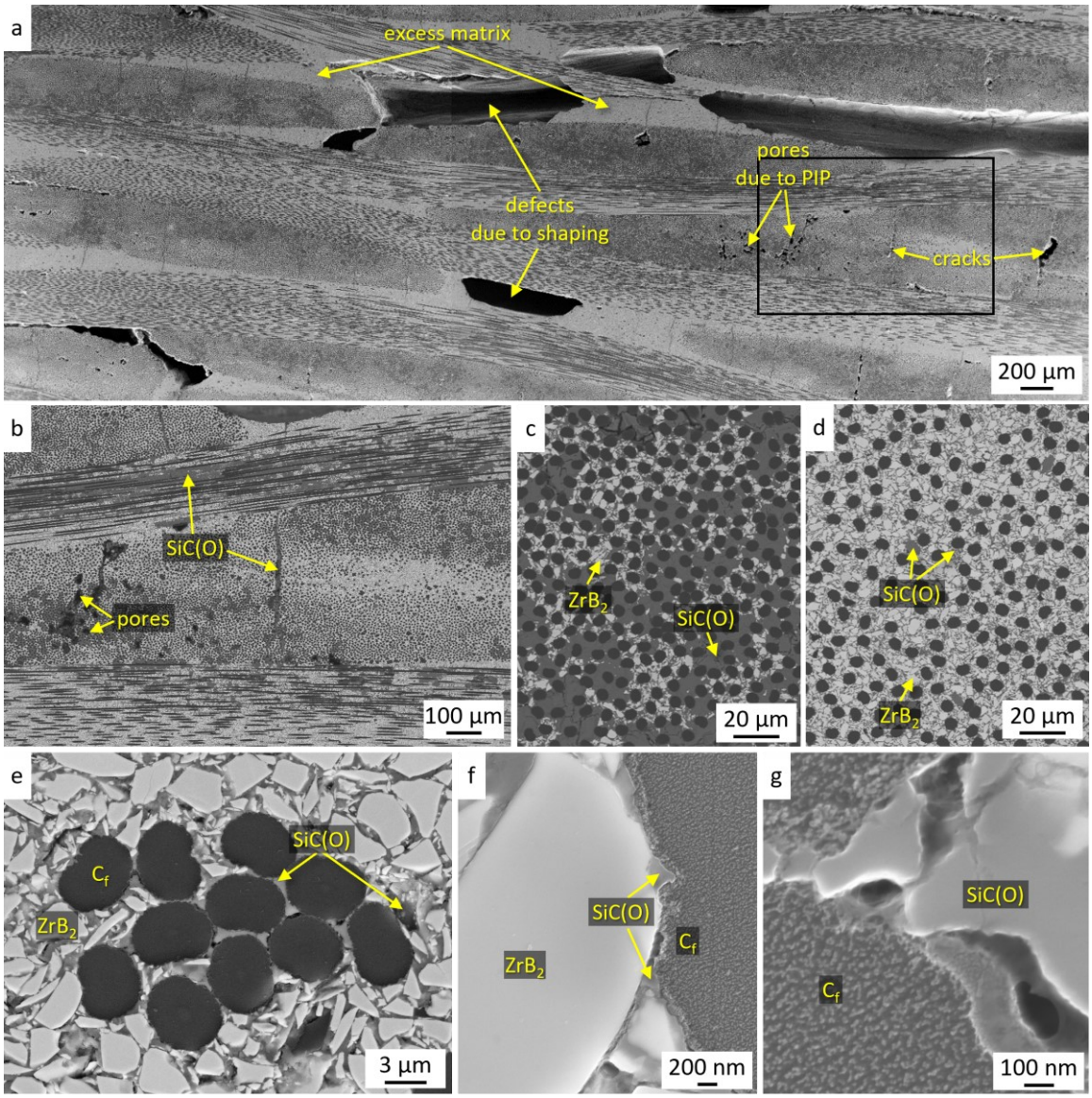

Figure 5.7. Polished cross section of sample 2D_tw. (a) General overview showing macro-voids due to 2D weaving and (b) its enlarged view (by BSE detector) as marked in (a). Details of microstructure (c) in the inner part and (d) in the outer part of bundle, where fibres are black dots, ZrB_2 is bright phase, SiC is grey phase. (e) Fibre agglomeration in ZrB_2-rich area. (f,g) Detail of fibre/matrix interface.

A panoramic view of the cross section (Figure 5.7a) showed typical defects of these composites: non-infiltrated areas due to shaping step [6,7], excess matrix in inter-bundle regions, and cracks in UHTC-rich matrix regions [4,5]. Cracks, that are usually originated during drying stage after slurry infiltration, were partially replenished by SMP-10 infiltrations (Figure 5.7b). The resulting microstructure was less homogeneous than the previous case, since powder slurry infiltration of 2D fabrics is less effective than UD fabrics [4]. A higher content of polymer-derived SiC(O) was often found in the central part of bundles (Figure 5.7c) compared to ZrB_2-rich areas in the outer part (Figure 5.7d). The low viscous polymer precursor allowed a very high degree of infiltration in the entire sample, both inside the bundles and in narrow gaps between sticked fibres, among which the powder slurry did not penetrate (Figure 5.7e). Detail of the fibre/matrix interface revealed a quite strong interaction between the thin SiC(O) film and uncoated carbon fibres, which appeared anchored to the matrix having several tens of microns of the surface impregnated with SiC(O) (Figure 5.7f,g). No spurious phases were detected.

2D_tw Sample: This sample had a bulk density of 2.86 g/cm^3 and an open porosity of ~5%, similarly to the 2D_tw sample. Cross section likewise showed densified regions with low residual porosity as well as large defects between fibre tows at the intersection of bundles due to the spaces in plain weave cloth. The most of macro-voids were evaluated by image analysis 1–2.5 mm sized spaced every 5–10 mm, but a fraction with size ranging 4.5–6.5 mm was revealed too. As can be seen in Figure 5.8a, polymer-derived SiC(O) was found in macro-voids with dimensions comparable with tow width but was not able to close them, due to the typically low PIP efficiency in filling such large pores [8].

The degree of infiltration was quite good, the water-based powder slurry penetrated the bundles to the middle part. However, powder-rich areas formed between in intra-bundle regions (Figure 5.8a), that very likely were favoured by loosely woven fabrics, thus explaining the low fibre volumetric content. PAN-based C_f and pitch-based C_f bundles showed a similar fibre/matrix ratio regardless the type of carbon fibre, in both cases a C_f content around 30 vol% was estimated by image analysis (Figure 5.8a,b). Also, the distribution of ZrB_2 and SiC(O) phases were ultimately similar (Figure 5.8c,d). As for the fibre/matrix interface, PAN-based carbon fibres made of turbostratic carbon exhibited rough surfaces (Figure 5.8e,f) suggesting a higher reactivity with the matrix phases compared to graphitic pitch-based ones showing smooth surfaces (Figure 5.8g).

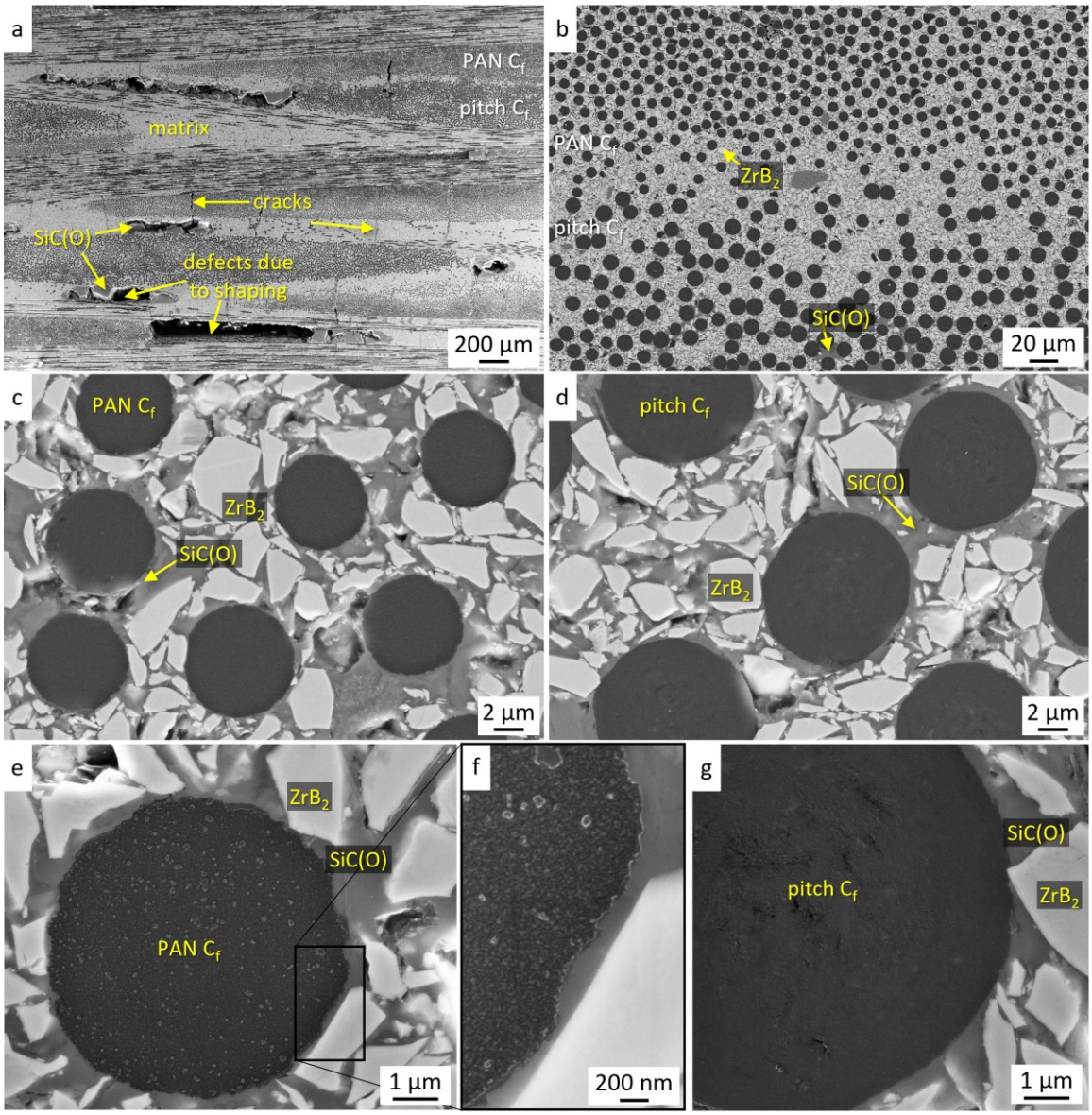

Figure 5.8. Polished cross section of sample 2D_pl. (a) General overview showing macro-voids due to 2D weaving. (b) Microstructure in intra-bundle PAN-based/pitch-based carbon fibre region; the light and the grey phases represent ZrB_2 and SiC respectively, carbon fibres are black. Detail of microstructure in microstructure inside (c) PAN-based carbon fibre bundle and (d) pitch-based carbon fibre bundle. Detail of fibre/matrix interface: (e,f) PAN-based carbon fibre, (g) pitch-based carbon fibre.

2.5D Sample: Figure 5.9a-c displays optical images of the cross section of the composite reinforced with 2.5D preform shown in its full height after six PIP cycles. 11 carbon fibre layers with alternating fibre orientation 0°/90° can be distinguishable. As expected, the outermost layers appeared denser as they were richer in UHTC powder (indicated as bright grey phase in Figure 5.9a-c). Powder slurry containing ZrB_2 infiltrated from one side of the preform to the opposite. Indeed, it seems that the ZrB_2 powder has penetrated into the preform with the impregnation depth being around 8 mm. The level

of powder uptake achieved with the pressureless impregnation technique was good, it seems even better than that achieved by Tang et al. [9] and Paul et al. [3].

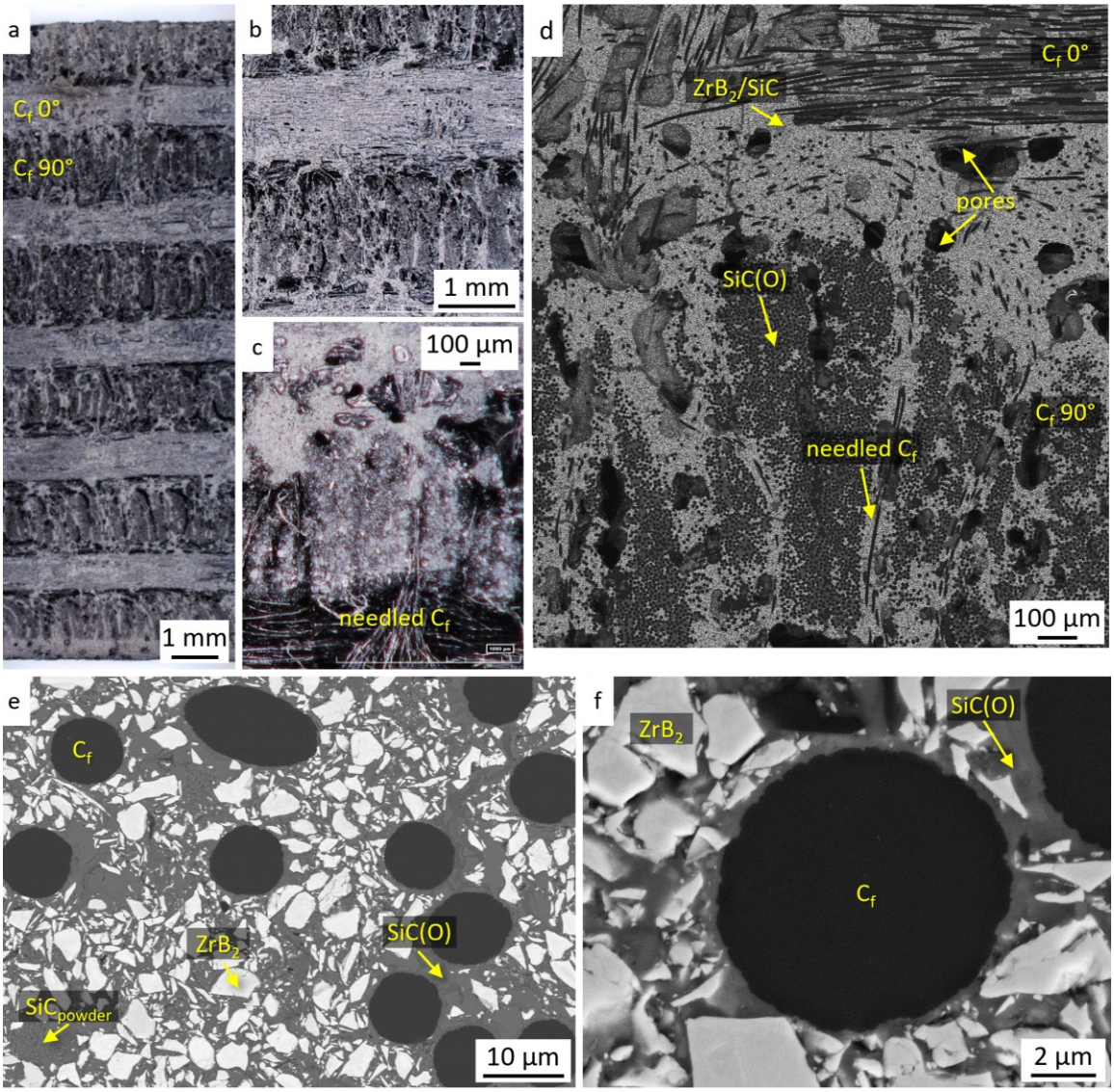

Figure 5.9. Polished cross section of sample 2.5D. (a,b,c) Optical images of 2.5D preform infiltrated with ZrB_2/SiC. (d) SEM image at low magnification of microstructure in the inner part of sample; carbon fibres are black, the light and dark grey phases represent ZrB_2/SiC from slurry and SiC(O) respectively. (e) Detail of microstructure. (f) A single fibre surrounded by the matrix.

A SEM image of the innermost part of the sample is reported in Figure 5.9d. it can be clearly seen that then UHTC powder was mainly distributed in random orientated areas (Figure 5.9d,e), as voids around needle-punched fibres were larger and provided channel for slurry permeation [10]. The non-woven layers had small gaps between fibres, thus ZrB_2 was mainly accumulated around carbon fibre bundles. Due to the subsequent PIP process with low viscous SMP-10 that flowed efficiently in narrow gaps among the fibres closed

to particles, SiC(O) was found prevalently in the central region of the bundles. The densification was not complete, thus contributing to the total amount of porosity, in agreement with MIP analysis. The used 2.5D preform was made of PANOX fibres [1], that exhibited a limited reactivity with matrix phases (Figure 5.9f).

Figure 5.10a,b illustrates the typical fracture surface of obtained samples 0/0° and 2D_tw. A high degree of fibre pull-out was favoured in points of sample 0/0° in which the presence of a higher residual porosity led to weaker interfaces (Figure 5.10a). Conversely, in the regions with reduced porosity as well as in the sample 2D_tw showing a less porous matrix a flatter surface was exhibited, the extent of fibre pull-out was much more limited, resulting in a few of microns (Figure 5.10b). A limited interface debonding between SiC(O) matrix and pulled-out fibres is visible in Figure 5.10b,c, thus leading to quite rough fibre surface with matrix fragments stuck on it.

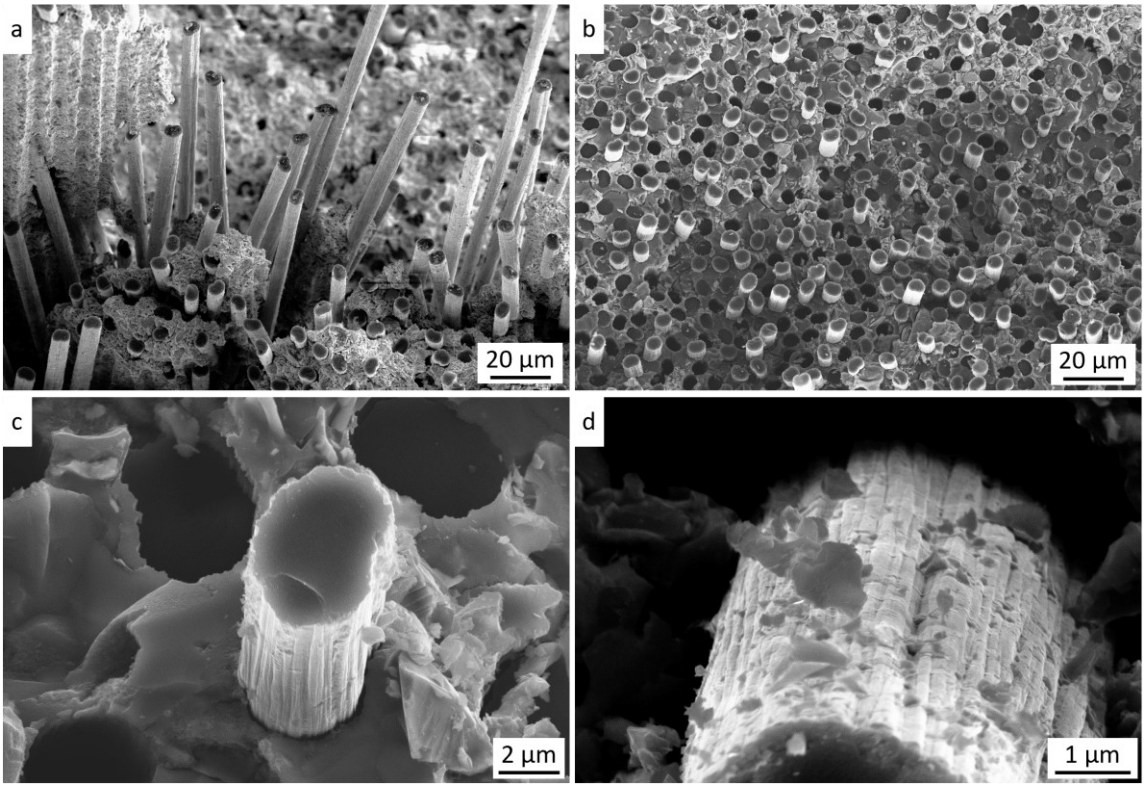

Figure 5.10. Fracture surface micrographs of (a) sample 0/0° in point with high residual porosity, where an extensive pull-out is shown, and (b) sample 2D_tw. (c) Individual fibre pull-out, (d) detail of a pulled-out fibre surface.

5.4 Mechanical properties

Mechanical properties, i.e. bending strength, Young's modulus, shear modulus and fracture toughness, were measured according to procedures described in Section 3.3.2 and the results are summarized in Table 5.2. The flexural strength for 2.5D sample owing to the complexity of the preform was determined on bars tested placing reinforcement along the vertical direction. For comparison, samples 2D_tw and 2D_pl were tested with skins plies both along the horizontal and vertical direction; the obtained results are reported as a single average (Table 5.2) because values were in the same range.

Table 5.2. Mechanical properties, i.e. bending strength, Young's modulus, shear modulus and fracture toughness measured at room temperature PAN-based C_f/ZrB_2-SiC composites produced by PIP.

Sample	Bending strength, σ_f	Young's modulus, E	Shear modulus, G	Fracture toughness, K_{Ic}
	MPa	GPa	GPa	MPa · $m^{0.5}$
0/0°	324 ± 128	95 ± 3	25 ± 1	9.68 ± 1.99
2D_tw	123 ± 19	81 ± 8	22 ± 13	6.42 ± 1.29
2D_pl	197 ± 64	105 ± 15	17 ± 6	7.13 ± 3.76
2.5D	116 ± 26	269 ± 82	25 ± 14	-

The highest stress value was exhibited by 0/0° sample and it ranged from 181 to 430 MPa. It can be seen that the composite suffered from interlaminar shear. The load-displacement curves (Figure 5.11), show sharp decrease of stress after its maximum value and subsequent re-loading. Hence, the low adhesion between the layers caused by shaping defects made the 0/0° composite prone to delamination (Figure 5.12a). As expected, the range of flexural strength values decreased down to 91–145 MPa and 125–281 MPa in case of the composites 2D_tw and 2D_pl, respectively. The lower flexural strength of 2D composites was due to the to the lower amount of longitudinal fibre and their waviness. In addition, the mechanical properties were likely affected by the critical flaws. In response of typical stress-displacement curves (Figure 5.11), no sign of interlaminar shear failure was observed in 2D composites neither in the fractured specimens nor in the stress-displacement curves. Specifically, sample 2D_twill showed quasi-brittle failure mode, whereas sample 2D_pl displayed a more graceful fracture. An example of fractured bar for sample 2D_tw is shown in Figure 5.12b, which reveals both fibre bundle and individual fibre pull-out. For 2.5D composite, flexural strength ranging

from 94 to 145 MPa were achieved; this was possibly affected by the high amount of porosity, beside the lower fraction of fibre in longitudinal orientation (Figure 5.12c).

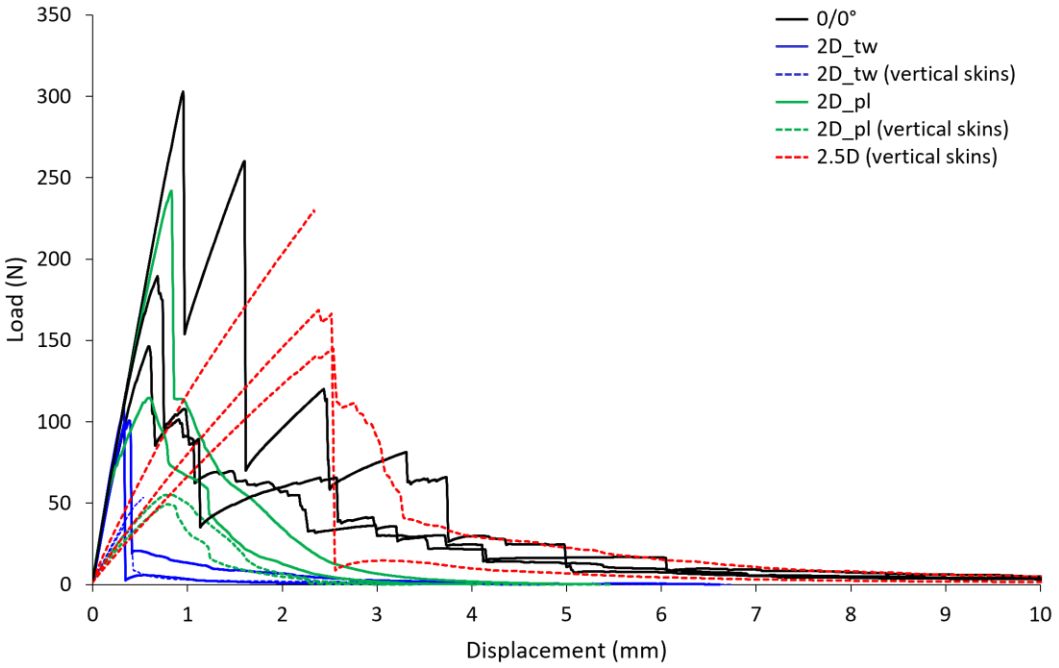

Figure 5.11. Stress/displacement curves of samples 0/0°, 2D_tw, 2D_pl and 2.5D tested by 3-point bending.

Figure 5.12. Optical images of a fractured bar reported as examples of fractures of (a) sample 0/0°, (b) sample 2D_tw and (c) sample 2.5D.

In addition, the fracture toughness (K_{Ic}) measured by Chevron Notch Beam (CNB) in 4-point flexure are reported in Table 5.2. The toughness values for the three tested samples (i.e. 0/0°, 2D_tw and 2D_pl) followed the same trend as flexural strength. The 0/0° sample exhibited the highest value, reporting a K_{Ic} of 9.68 MPa·m$^{0.5}$. K_{Ic} values decreased for samples reinforced with 2D woven fabrics, specifically down to 6.42 MPa·m$^{0.5}$ for sample 2D_tw and 7.13 MPa·m$^{0.5}$ for 2D_pl.

Although there are remarkable similarities between these PAN-based C_f/ZrB_2-SiC and those reported in literature, the direct comparison among values was not possible due to the different testing conditions. Approximately, the mechanical properties of the tested

composites are comparable with those of similar CMCs produced by PIP. Hu et al. [11] developed PAN-based 2D C_f/SiC material enriched with about 25 vol% ZrB_2 particles, and reported a flexural strength of 163 MPa and a fracture toughness of 8.1 MPa·$m^{0.5}$. Q. Li et al. [12] developed a 3D needled C_f/ZrB_2-ZrC-SiC characterized by 30 vol% of UTHC, 34 vol% of carbon fibres and a porosity of 12% and reported a flexural strength of 136 MPa; however, he noted that bending stress could increase up to 248 MPa with PyC/SiC interphases between fibre and matrix since it prevented UHTC phases from going through the wrapped bundles during the infiltration process. In agreement with this, Ran et al. [10] prepared C/C–ZrB_2–SiC composites reinforced with a PyC-coated needle-punched preform enriched with 23 vol% ZrB_2 and a porosity of about 7%, that reached a flexural strength of 309 MPa. By comparing these PAN-based C_f/ZrB_2-SiC composites with the previously studied pitch-based C_f/ZrB_2-SiC (Chapter 4), it is evident that the present materials gave lower mechanical properties, although the higher strength of the constituent PAN-based carbon fibres. For instance, the flexural strength was approaching 500 MPa for 0/0° and 190 MPa for 2D pitch-based C_f/ZrB_2-SiC. For ceramic matrix composites, fibre, matrix and fibre/matrix interface are the key factors to determine the mechanical performance of the material. Despite the mild processing conditions, uncoated PAN-based carbon fibres resulted in a strong interface, that implied a little pull-out. Thus, properties predominantly affected by weak interface, such as strength and toughness, were better when pitch-based carbon fibres were utilised as reinforcement. This was also suggested by the better performance of sample reinforced with 2D PAN/pitch-based C_f plain-woven fabric compared to 2D twill-woven cloth made of only PAN-based C fibres.

5.5 Conclusions

PAN-based carbon fibre-reinforced 20–50 vol% ZrB_2-enriched composites were fabricated via slurry infiltration (water based) coupled with polymer infiltration and pyrolysis at relatively low temperatures. ZrB_2 and submicrometric SiC powder slurry was found effective for a good homogeneity of the fibre distribution into the matrix. As expected, the composite prepared using needle-punched 2.5D preform contained a lower content of UHTC phase, nevertheless ZrB_2 were penetrated in the inner part of the felt. The subsequent PIP cycles with allyl-hydrido polycarbosilane under mild conditions

allowed to produce materials with a residual open porosity in the range 5–11% using UD and 2D fabrics, while a higher porosity (~28%) were obtained with 2.5D preform.

The mechanical properties, including bending strength, elastic and shear modulus and fracture toughness, were evaluated. They resulted in the same range of CMCs obtained by more complex or more time-consuming processes. However, the use of naked PAN-based carbon fibres was found to lead to a strong interface with little pull-out. Further improvement could be achieved using a fibre coating for interfacing with polymer-derived SiC and boride phases, in order to have a weaker bond.

5.6 References

1. Galizia, P. *et al.* Retained strength of UHTCMCs after oxidation at 2278 K. *Compos. Part A Appl. Sci. Manuf.* **149**, 106523 (2021).
2. Rubio, V. *et al.* Materials characterisation and mechanical properties of C_f-UHTC powder composites. *J. Eur. Ceram. Soc.* **39**, 813–824 (2019).
3. Paul, A. *et al.* UHTC-carbon fibre composites: Preparation, oxyacetylene torch testing and characterisation. *J. Eur. Ceram. Soc.* **33**, 423–432 (2013).
4. Zoli, L., Medri, V., Melandri, C. & Sciti, D. Continuous SiC fibers-ZrB_2 composites. *J. Eur. Ceram. Soc.* **35**, 4371–4376 (2015).
5. Sciti, D., Natali Murri, A., Medri, V. & Zoli, L. Continuous C fibre composites with a porous ZrB_2 Matrix. *Mater. Des.* **85**, 127–134 (2015).
6. Mehdikhani, M., Gorbatikh, L., Verpoest, I. & Lomov, S. V. Voids in fiber-reinforced polymer composites: A review on their formation, characteristics, and effects on mechanical performance: *J. Compos. Mater.* **53**, 1579–1669 (2018).
7. Marshall, D. B. & Cox, B. N. Integral Textile Ceramic Structures. *Annu. Rev. Mater. Res.* **38**, 425–443 (2008).
8. Zhu, Y., Huang, Z., Dong, S., Yuan, M. & Jiang, D. Manufacturing 2D carbon-fiber-reinforced SiC matrix composites by slurry infiltration and PIP process. *Ceram. Int.* **34**, 1201–1205 (2008).
9. Tang, S., Deng, J., Wang, S., Liu, W. & Yang, K. Ablation behaviors of ultra-high temperature ceramic composites. *Mater. Sci. Eng. A* **465**, 1–7 (2007).
10. RAN, L. ping, RAO, F., PENG, K., YIN, H. & YI, M. zhong. Preparation and properties of C/C–ZrB_2–SiC composites by high-solid-loading slurry impregnation and polymer infiltration and pyrolysis (PIP). *Trans. Nonferrous Met. Soc. China* **29**, 2141–2150 (2019).
11. Hu, H. *et al.* Preparation and characterization of C/SiC-ZrB_2 composites by

precursor infiltration and pyrolysis process. *Ceram. Int.* **36**, 1011–1016 (2010).

12. Li, Q., Dong, S., Wang, Z. & Shi, G. Fabrication and properties of 3-D Cf/ZrB_2-ZrC-SiC composites via polymer infiltration and pyrolysis. *Ceram. Int.* **39**, 5937–5941 (2013).

6. Thermal stabilization of UHTCMCs containing polymer-derived SiC

6.1 Introduction

In the previous chapters (Chapters 4 and 5), carbon fibre-reinforced ZrB_2-enriched composites were manufactured via aqueous slurry impregnation coupled with polymer infiltration, using an allyl-hydrido polycarbosilane precursor, and pyrolysis is at relatively low temperature (i.e. 1000 °C). These materials showed excellent mechanical properties at room temperature, for instance 0/0° pitch-based C_f/ZrB_2-SiC composite reached flexural strength approaching 500 MPa. Preliminary mechanical tests at elevated temperature indicated that such high values of flexural strength were kept up to 1400 °C. However, a loss of performance was found at 1500 °C. This is likely due to the mild processing conditions, that hindered the conversion of the polymer-derived amorphous SiC(O) into crystalline SiC, thus compromising the material performance at elevated temperature.

Although ceramic matrix composites containing polymer-derived SiC from polycarbosilane have been widely investigated in literature [1–10], it is hard to find a thread linking processing steps and reported material properties. In most of the studies the starting polycarbosilane is different, often in-house synthesized, hence parameters such as physic state, softening point or boiling point, molecular weight, functional groups and ceramic yield differ. As a result, also composite processing conditions, such as use of solvents as well as heating rate, curing/pyrolysis temperature and holding time may vary, besides the fact that these have frequently not been spelled out in detail. In such scenario it was unviable to adopt any previously reported processing methodology for the production via Polymer Infiltration and Pyrolysis (PIP) of C_f/ZrB_2-SiC composites with desired properties. For this reason, a first study (Chapter 3 – Section 3.1.2 and Chapter 4) was planned to carry out initial experiments to establish the basic steps and processing parameters for the development of a novel route manufacturing. The pyrolysis step was performed at relatively low temperature to obtain a complete conversion of the allyl-hydrido polycarbosilane in its early ceramic form, amorphous SiC.

Part of the data included in this chapter will be used to prepare a paper with tentative title "Servadei F., Zoli L., Galizia P., Piancastelli A., Melandri C., Sciti D., *Effect of pyrolysis temperature on the microstructure, thermal stability and mechanical behaviour of UHTCMCs prepared by Polymer Infiltration and Pyrolysis*".

In this chapter the work was aimed at enhancing the mechanical properties at elevated temperature of UHTCMCs consolidated under mild conditions, by adding a further cycle of pyrolysis at higher temperature that enabled conversion of amorphous SiC(O) into crystalline SiC. The optimal pyrolysis temperature for the stabilization of polymer-derived SiC matrix in order to achieve mechanical resistance over a broad temperature range was sought by performing systematic post-consolidation heat treatments at every 100 °C in the temperature range 1100–1900 °C.

The investigation was conducted on the composite reinforced with pitch-based carbon fibre due to the involved high temperature, in a 0/0° orientation, since it was taken as reference sample among the PIP-ed UHTCMCs at 1000 °C. The material properties were discussed in the light of microstructure evolution due to the post-consolidation heat treatment. The overarching aim was to study the effect of pyrolysis temperature on the flexural strength at elevated temperature up to 1500 °C.

6.2 Microstructural features

6.2.1 Microstructure of as-obtained material

C_f/ZrB_2-SiC composite reinforced with pitch-based carbon fibre in a 0/0° configuration was prepared following the procedures reported in Sections 3.1.2.1 – 3.1.2.3. The sample was fabricated by a cycle of slurry infiltration using a water-based ZrB_2 powder slurry on unidirectional fibre fabrics then stacked in the same orientation, followed by six cycles of polymer infiltration with allyl-hydrido polycarbosilane precursor and pyrolysis at 1000 °C. Final composition and open porosity of the as-obtained sample (here labelled as 6PIP-10) are shown in Table 6.1.

Table 6.1. Resulting composition (volumetric amounts of carbon fibres (C_f), zirconium diboride (ZrB_2), powder derived silicon carbide (SiC_p) and polymer-derived silicon carbide (SiC_{PDC})) and open porosity of the sample obtained after 6 PIP cycles at 1000 °C.

Sample	C_f (vol%)	ZrB_2 (vol%)	SiC_p (vol%)	SiC_{PDC} (vol%)	Open porosity (%)
6PIP-10	30	29	3	32	6

After the sixth PIP cycle, the composite contained a fraction of carbon fibres around 30 vol%, contents of UHTC phase and SiC (SiC_p) introduced through slurry of 29 and 3

vol% respectively, and a larger fraction of polymer-derived SiC (SiC_{PDC}). The latter represented 32% of the total sample volume and resulted in an amorphous phase due to the low temperature processing (see Section 4.3). According to mercury intrusion measurements, the amount of open porosity was around 6%.

Microstructural features of the sample 6PIP-10 are shown in Figure 6.1a-e. Black dots are carbon fibres, the white contrasting phase is ZrB_2, while the grey regions are silicon carbide. SiC_{PDC} was hardly distinguishable from SiC_p particles due to the low contrast difference (Figure 6.1a,b). In general, SiC_p was mainly found homogeneously mixed with ZrB_2 particles and distributed around the fibres, whereas SiC_{PDC} was found either finely dispersed in the ZrB_2 matrix or in large spots filling the cavities and in thin films surrounding the fibres (Figure 6.1c). Figure 6.1d highlights the amorphicity of SiC(O) (see EDS signal Si-C-O in Figure 6.1e) and the unreacted ZrB_2 grain boundaries.

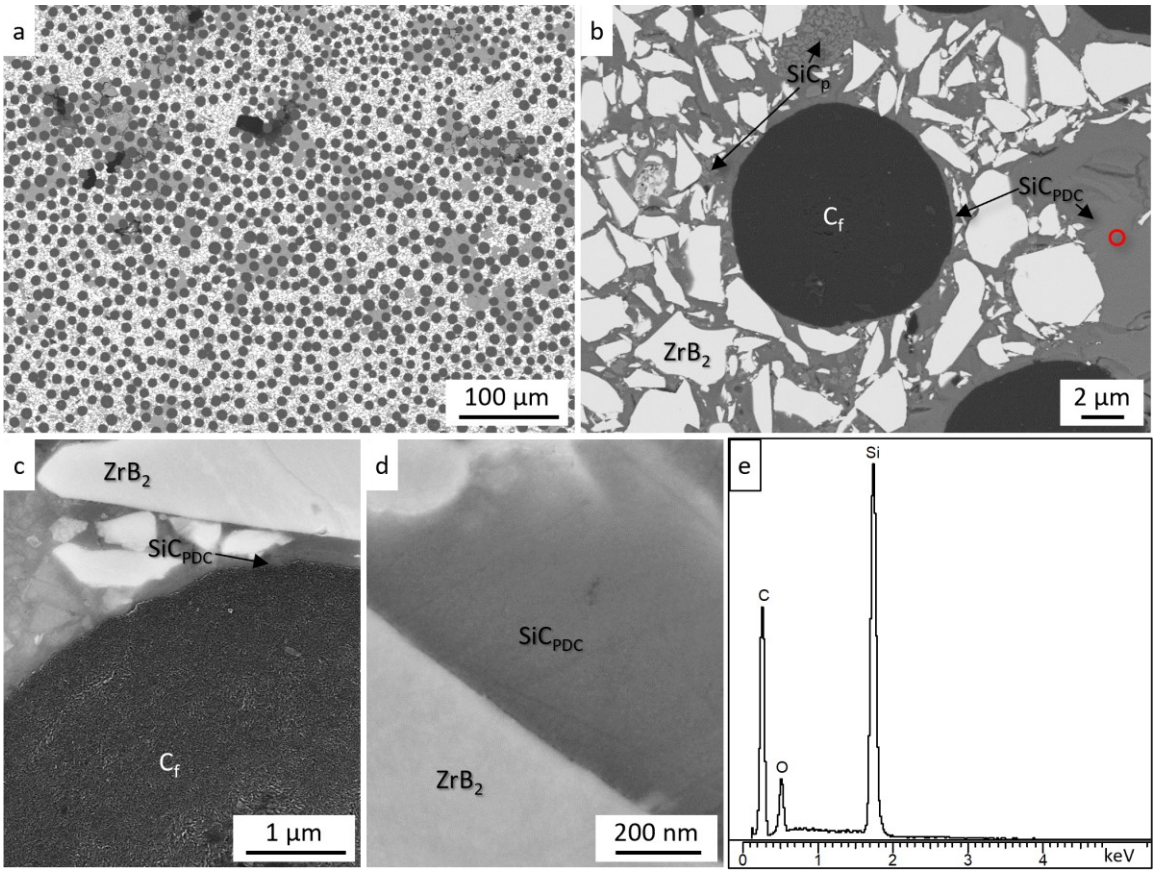

Figure 6.1. Polished section of C_f/ZrB_2-SiC obtained by 6 PIP cycles at mild conditions, i.e. 1000 °C (sample 6PIP-10). (a) Low magnification micrograph; C_f is the dark phase, ZrB_2 is the bright phase, SiC is the grey phase, while black areas are pores. (b) A single fibre surrounded by the matrix. Detail of (c) fibre/matrix interface and (d) ZrB_2 grain boundaries embedded in amorphous SiC_{PDC}. (e) EDS spectrum (EDS spot is marked in (b)) of SiC_{PDC} resulted in SiC(O).

6.2.2 Microstructure of treated materials

Bulk and skeletal densities, open porosities, weight loss and volume variations measured after the heat treatments at temperature from 1100 to 1900 °C are reported in Table 6.2, in comparison with the starting material 6PIP-10, and represented in the plot in Figure 6.2.

Table 6.2. Bulk density (via geometric and Archimedes' method), skeletal density, open porosity, weight loss and volume variations of the reference sample 6PIP-10 and treated samples at higher temperature.

Sample	T pyrolysis (°C)	Bulk $d_{geom.}$ (g/cm^3)	Bulk $d_{Arch.}$ (g/cm^3) *	Skeletal d (g/cm^3) *	Open poros. (%) *	wt. loss (%)	ΔV (%)
6PIP-10	-	3.01 ± 0.06	3.17	3.36	5.7	-	-
P-11	1100	3.01 ± 0.01	3.13	3.39	7.8	-0.41 ± 0.03	0.0
P-12	1200	2.99 ± 0.01	3.15	3.36	6.3	-0.60 ± 0.09	0.0
P-13	1300	3.00 ± 0.06	3.15	3.40	8.0	-0.71 ± 0.02	0.0
P-14	1400	2.97 ± 0.03	3.13	3.41	8.2	-2.28 ± 0.58	0.5 ± 0.2
P-15	1500	2.72 ± 0.10	2.78	3.45	19.3	-6.47 ± 1.67	1.9 ± 0.7
P-16	1600	2.59 ± 0.04	2.62	3.77	30.5	-9.75 ± 0.18	4.5 ± 0.4
P-17	1700	2.58 ± 0.07	2.68	3.87	30.7	-9.73 ± 0.15	6.1 ± 1.4
P-18	1800	2.54 ± 0.02	2.66	3.87	31.2	-9.75 ± 0.14	7.3 ± 2.9
P-19	1900	2.44 ± 0.25	2.60	3.94	31.5	-10.04 ± 0.18	11.2 ± 10.8

. * measurement by Mercury Intrusion Porosimetry (MIP)

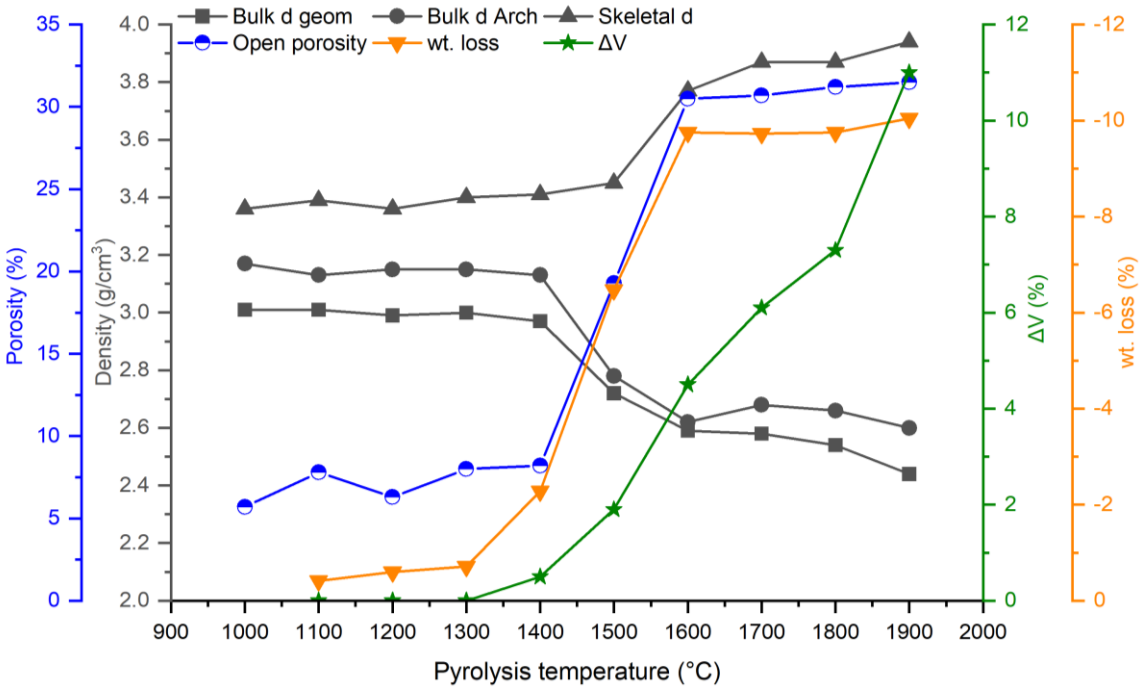

Figure 6.2. Plot representing bulk densities measured via geometric method and via Archimedes' method through MIP, skeletal density, open porosity, weight loss and volume variation as a function of temperature of the heat treatment carried out on specimens.

The geometrical bulk density decreased by increasing the pyrolysis temperature [11]. Specifically, the sample 6PIP-10 had a geometrical bulk density of ~3 g/cm^3 and this value was found almost constant after pyrolysis at low temperature until 1300 °C; then, a gradual decrease was observed measuring values in the range 2.6–2.7 g/cm^3 for the samples P-15, P-16 and P-17, and down to ~2.4 g/cm^3 in P-19. Bulk density values determined by MIP analysis were generally higher for all specimens, but the trend is similar, also considering the data variability because of intrinsic inhomogeneity of the analysed small specimens. On the contrary, skeletal density increased with the increase of pyrolysis temperature (Table 6.2) due to the crystallization of SiC_{PDC} [12,13]. Indeed, the density of SMP-10-derived products changes as it is processed to higher temperatures. Amorphous SiC obtained by pyrolysis at 1000 °C has a bulk density of about 2.5 g/cm^3(measured by helium pycnometer, not shown here, in agreement with supplier's datasheet); the density increases to about 3.1 g/cm^3 when pyrolysis is executed at temperature near 1600 °C. As predictable from the measurements of bulk and skeletal densities, an increase of the pyrolysis temperature caused an increase of the porosity. Open porosity from an initial value of ~6% slightly increased up to ~8% after heat treatments until 1400 °C, while was notably higher (~19%) in the sample P-15. A distinct change can be seen from pyrolysis temperature of 1600 °C, open porosity increased over 30%, until reaching a value of 31.5% with the treatment at the highest temperature (Table 6.2).

Pore size distribution graphs of the reference sample 6PIP-10 and specimens treated at temperature above 1500 °C are reported in Figure 6.3. MIP analysis of samples treated at temperature <1500 °C was not considered reliable due to the low fraction of porosity, <10%.

For sample 6PIP-10 a continuous multimodal pore size distribution in the range 0.058–100 µm was observed. The fraction of macropores with diameter >50 µm were attributable to non-optimized slurry infiltration and stacking of fibre layers. Sample P-15 (open porosity 19.3%) showed a narrower pore size distribution characterized by most of the pore diameter in the range 0.01–0.2 µm. Samples pyrolysed at temperature above 1600 °C showed a prevalently monomodal distribution, with the most frequent pore size located at higher dimensional ranges than that of P-15 because of increasing SiC_{PDC}

shrinkage as temperature increases. For instance, it can be notice that pyrolysis at 1900 °C led to bigger pores distributed in a wider range of pore diameters and peaked at 1 µm (see P-19 in Figure 6.3).

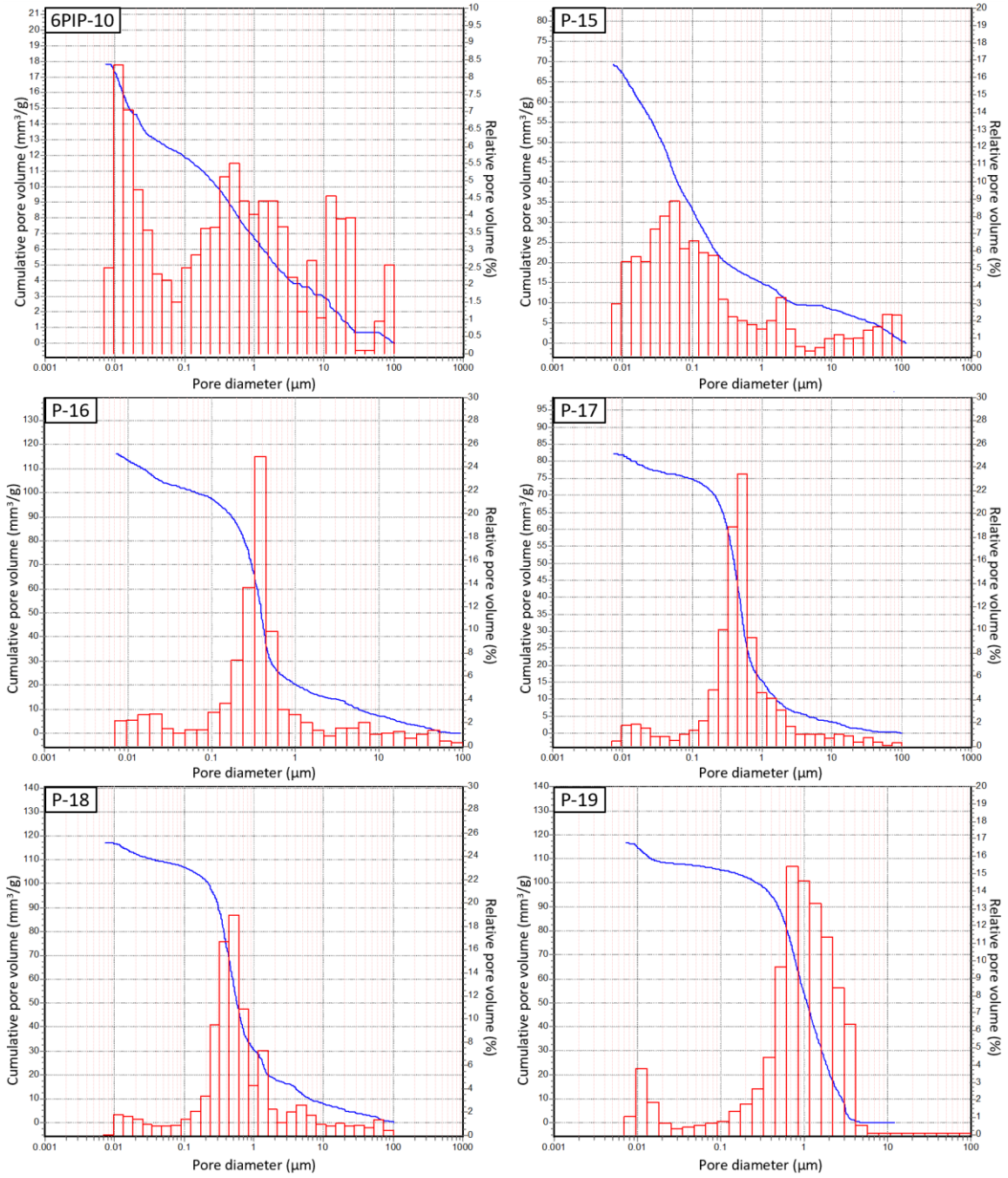

Figure 6.3. Pore size distribution by Hg intrusion porosimetry (MIP) of reference sample 6PIP-10 and samples treated in the temperature range 1500–1900 °C (P-15, P-16, P-17, P-18 and P-19).

Weight losses likewise were almost negligible (less than 1%) until 1300 °C (Table 6.2). A weight loss of few percentage points (-2.28%) was measured after pyrolysis at 1400 °C, then jumped to -6% in the sample P-15 and over -9% in samples treated at 1600 °C, reaching a maximum of -10% in the sample P-19. The marginal mass loss until 1400 °C is in agreement with TGA studies on SMP-10 reported in ref. [5,11,14], where no significant mass change takes place beyond 800–850 °C until 1400 °C. In the range 1400–1600 °C, Zunjarrao et al. [15] measured a slight increase in mass loss which amounted about to -4%, whereas Yin et al. [16] who prepared CMCs using a different type of polycarbosilane reported a strong mass loss amounting to -17% only in this temperature range. The weight loss above the ceramization temperature (800 °C for SMP-10) can be attributed to the loss of oxygen, whose amounts in the PDCs generally ranges from 3 to 6.8 wt% [11]. Indeed, oxygen reacts at 1200–1400 °C due to the reaction (1) [17], and at higher temperature also the crystallization of β-SiC starts via carbothermal reaction between the Si-O bonds and excess carbon of the silicon oxycarbide (see reaction 2) [11,18].

$$SiO_{2\,(s)} + C_{(s)} \longrightarrow SiO_{(g)} + CO_{(g)} \quad (1)$$

$$SiO_{2\,(s)} + 3C_{(s)} \longrightarrow SiC_{(s)} + 2CO_{(g)} \quad (2)$$

As demonstrated by Kaur et al. [11], heat treatments at high temperature (i.e. 1700 °C) lead to stoichiometric SiC composition, but at the same time the release of oxygen and excess carbon in form of CO causes mass loss and porosity. Furthermore, Kaur et al. [11] reported that as the temperature goes up an increasingly shrinkage occurred in bulk ceramics. On the contrary, we measured a slight increase in volume, mainly due to the elongation of specimen width and thickness sizes in materials pyrolysed at 1500 °C and above. It is worthy to note that the change in volume, even if it was overall little, was practically negligible up to 1400 °C, then increased exponentially.

X-Ray Diffraction analysis was carried out on the surface of all treated specimens and compared with the reference 6PIP-10 to follow SiC phase transformation (Figure 6.4).

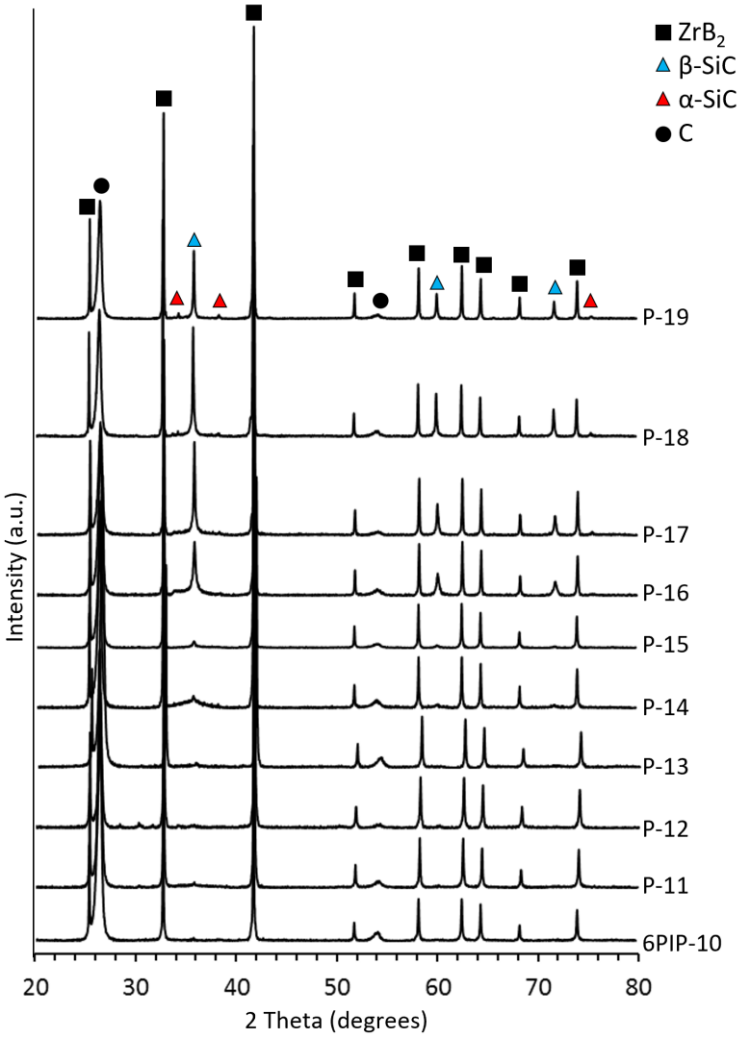

Figure 6.4. X-ray diffraction patterns collected on the surface of the reference sample 6PIP-10 and samples after pyrolysis at temperature between 1100 and 1900 °C.

XRD patterns confirmed the presence of graphite (PDF #41-1487), ZrB_2 (PDF #34-0423) and SiC species in all the samples. Peaks corresponding to graphite and ZrB_2 showed very similar shape and intensity due to the similar content of these phases among the samples. SiC(O) obtained as product of pyrolysis of the polycarbosilane at temperature below 1300 °C resulted amorphous and generated only poorly defined humps in the X-ray scattering profiles. Broad diffractions peaks at 2θ = 36°, 60° and 72° corresponding to β-SiC polymorph (PDF #65-0360) started to appear in the sample P-14 and became sharper by increasing the temperature. This indicates that a partial conversion of SiC(O) occurred with pyrolysis at 1400 °C and 1500 °C, leading to the formation of nano-sized crystals considering the broad shape of the peaks. Pyrolysis cycles at temperatures in the range 1600–1800 °C led to a gradually increasing conversion

to β-SiC with grown crystallites. The crystallite sizes of β-SiC produced by pyrolysis of SMP-10 were estimated to be 4 and 41 nm at 1500 °C and 1800 °C, respectively [19]. XRD pattern of sample P-19 revealed the presence of peaks at 2θ = 34° and 60° which are attributable to α-SiC polymorph (PDF #49-1428). Small traces might be also seen in the XRD pattern of sample P-18; this could be both due to an initial formation of α-SiC, in agreement with ref. [11,20,21], and low reflections derived from particles introduced by slurry infiltration whose content was close to the minimum detectable.

The cross sections of all the samples subjected to heat treatment at higher temperature were observed by SEM to analyse microstructural modifications (Figure 6.5). Specimens P-11, P-12, P-13 and P-14 presented morphologies similar to sample 6PIP-10 (see Figure 6.1). Homogeneous microstructures with regions infiltrated by the ZrB_2 slurry alternated with regions of amorphous polymer-derived SiC(O) were observed. Occasionally pores of few μm as well as radial cracks around fibres in SiC(O) areas were found as after pyrolysis at 1000 °C. The shrinkage that typically accompanies the formation of crystalline SiC led to the increase of porosity and the widening of microcracks and interstices between the fibres and SiC_{PDC}-based matrix. In the composite P-15, thin cracks can be observed mainly in the larger regions of SiC(O) in the layered structure around C_f that formed due to the repetitive PIP cycles, whereas the matrix was still anchored to the fibre. Since the fairly high temperature, reaction between Si from PDC and C from fibre might be occurred, nevertheless the fibre/matrix interface was quite smooth. Specimens pyrolysed treated at 1600 °C and above showed drastic changes in their microstructure. In agreement with XRD patterns, at 1600 °C the conversion of SiC(O) into crystalline SiC became stronger, which ultimately ended in a higher volumetric ceramic shrinkage. It can be clearly seen the formation of a highly porous matrix in samples P-16, P-17, P-18 and P-19, endorsing the observation made from the MIP measurements (Table 6.2). This caused the detachment of SiC_{PDC} phase from the carbon fibres, which remained partially anchored to the matrix through ZrB_2 particles and submicrometric SiC particles. Interfaces appeared rougher than those in low-temperature treated samples, highlighting a quite strong interaction leading to, albeit limited, fibre degradation.

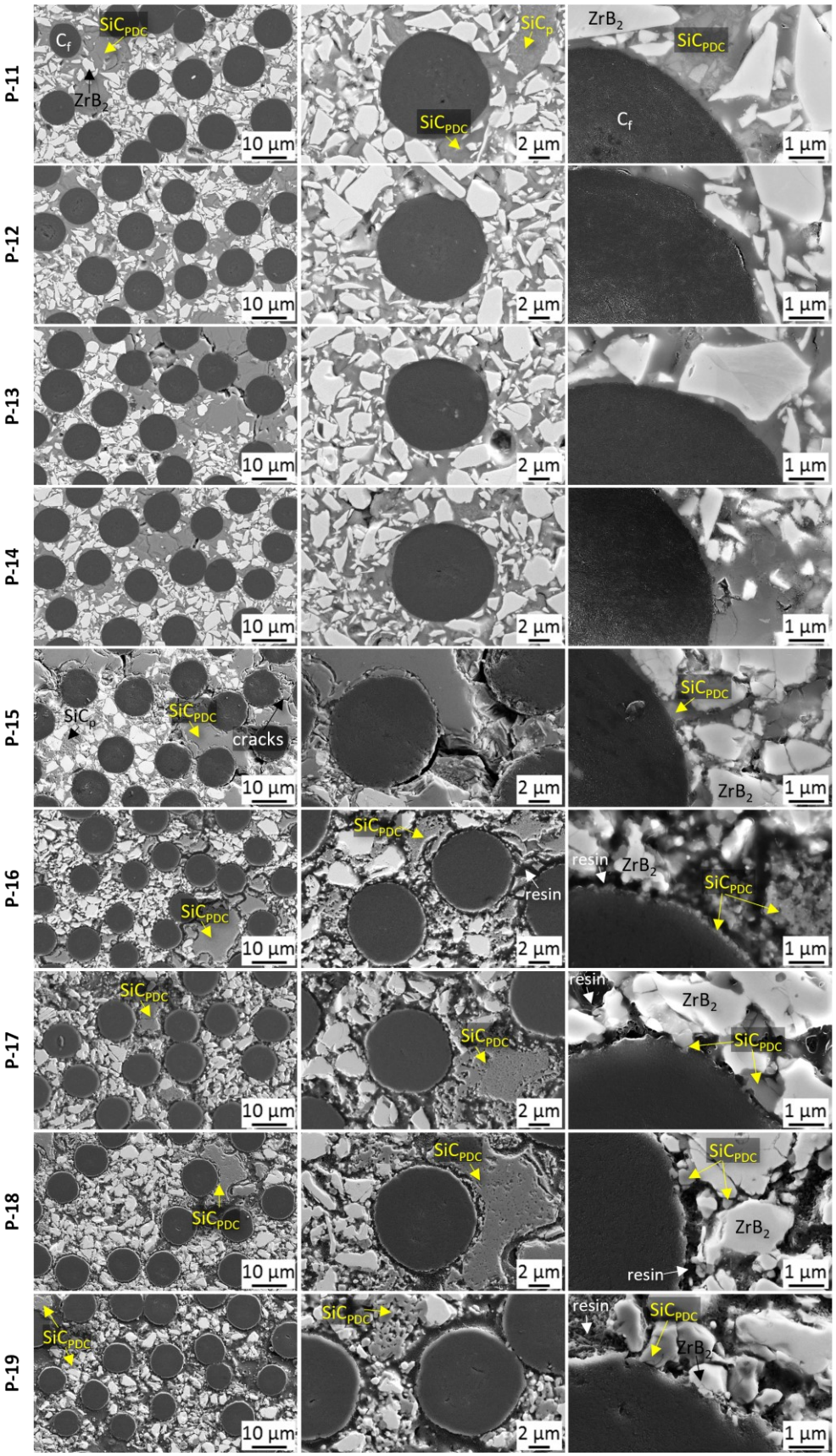

Figure 6.5. Polished cross section of samples treated at temperature in the range 1100–1900 °C, showing for each sample: intra-bundle region, a fibre surrounded by the matrix, a detail of the fibre/matrix interface.

Figure 6.6 shows a detail of the matrix in all samples in order to get information on the morphological changes of polymer-derived SiC during crystallization. Up to 1300 °C SiC(O) appeared glassy, uniform, with a dense and pore-free microstructure. ZrB_2 grains which are embedded in the amorphous SiC(O) did not show signs of reaction. In specimen P-14 a change in SiC(O) nature was found, as SiC generated nanocrystalline domains in amorphous SiC(O), in which intermittent pores and some microcracks formed because of a low extent of shrinkage. Pyrolysis at 1500 °C induced a rather diffused porosity, while ZrB_2 particles appeared partially altered likely due to the reaction at grain boundaries with oxygen impurities contained in the glassy matrix. In specimens P-16, P-17, P-18 and P-19 the matrix consisted of fine crystallized SiC networks and ZrB_2 particles. The former slightly coarsened up to submicrometric sizes, while the latter lost its original shape getting less sharp and rounded as temperature increased, thus proving that high temperature treatments are sufficient to initiate ZrB_2 sintering.

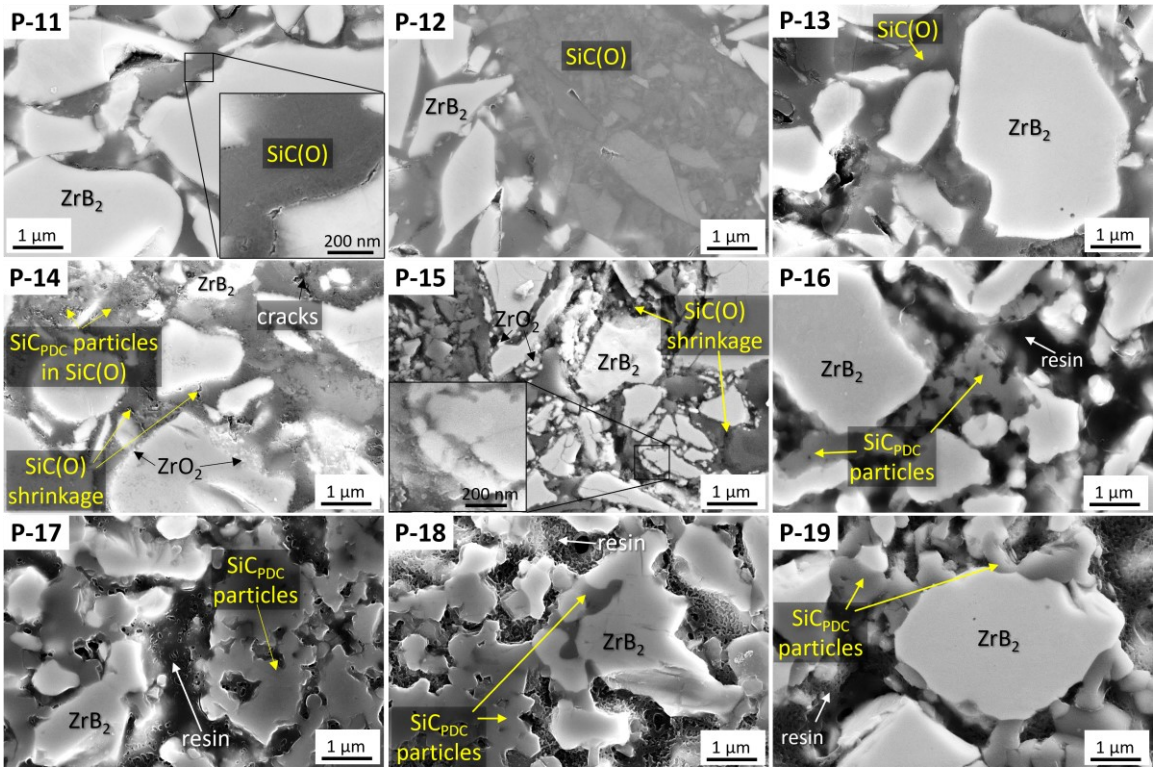

Figure 6.6. Polished cross section of samples treated at temperature in the range 1100–1900 °C, showing for each sample a detail of the matrix and highlighting evolution of SiC_{PDC} and grain boundaries of ZrB_2 particles.

6.3 Mechanical properties

Mechanical properties of reference sample and treated samples, both at room temperature and at high temperature up to 1500 °C, are summarized in Table 6.3.

Table 6.3. Flexural strength by 4-pt bending test of reference sample 6PIP-10 tested at room temperature, and at high temperature (1000, 1400 and 1500 °C in Argon flow) until performance loss, and samples treated at temperatures 1400-1900 °C at room temperature and 1500 °C.

Sample	σ 4-pt RT	σ 4-pt 1000 °C	σ 4-pt 1400 °C	σ 4-pt 1500 °C
	(MPa)			
6PIP-10	474 ± 14	603 ± 32	554 ± 16	invalid
P-14	297 ± 6			212 ± 105
P-15	173 ± 21	-	-	62 ± 9
P-16	184 ± 23	-	-	92 ± 1
P-17	200 ± 6	-	-	168 ± 54
P-18	161 ± 6	-	-	105 ± 45
P-19	213 ± 8	-	-	100 ± 85

6.3.1 Mechanical properties of as-obtained material

The average value of flexural strength at room temperature was 474 ± 14 MPa for reference sample 6PIP-10. For the sake of clarity, all bending tests at room temperature were conducted on small bars (size 25 mm x 2.5 mm x 2 mm) for comparison purposes with high temperature bending strength tests. Load displacement curves are reported in Figure 6.7a.

Preliminary bending tests at 1200 and 1300 °C exhibited flexural strength over 500 MPa (values not reported here), that was confirmed also at 1400 °C reaching an average value of 554 MPa (Table 6.3). These values were slightly lower than the strength registered at 1000 °C but still higher than that at room temperature (Table 6.3), as found in other works on UHTCMCs [22–24]. This behaviour was attributed to the relaxation of the residual thermal stresses generated during the cooling step of the pyrolysis process owing to the CTE mismatch between carbon fibre and ceramic matrix [25] and to the increase of the fibre strength at high temperature [26,27]. Load-displacement curves (Figure 6.7b) and optical figures of the bars after bending test (Figure 6.7c) showed that up to 1300 °C failure likely occurred with the same mechanism observed at RT, highlighting cracks crossing the bar and fibre pull-out from the matrix (Figure 6.7c,d). At 1400 °C, some

shrinkage of the bar was observed at points where it was in contact with the support pins and a most extended interlaminar failure mode seems to be occurred leading to the higher delamination among the layers (Figure 6.7c). Also, in such conditions composite exhibited no fibre pull-out during the fracture process (Figure 6.7e).

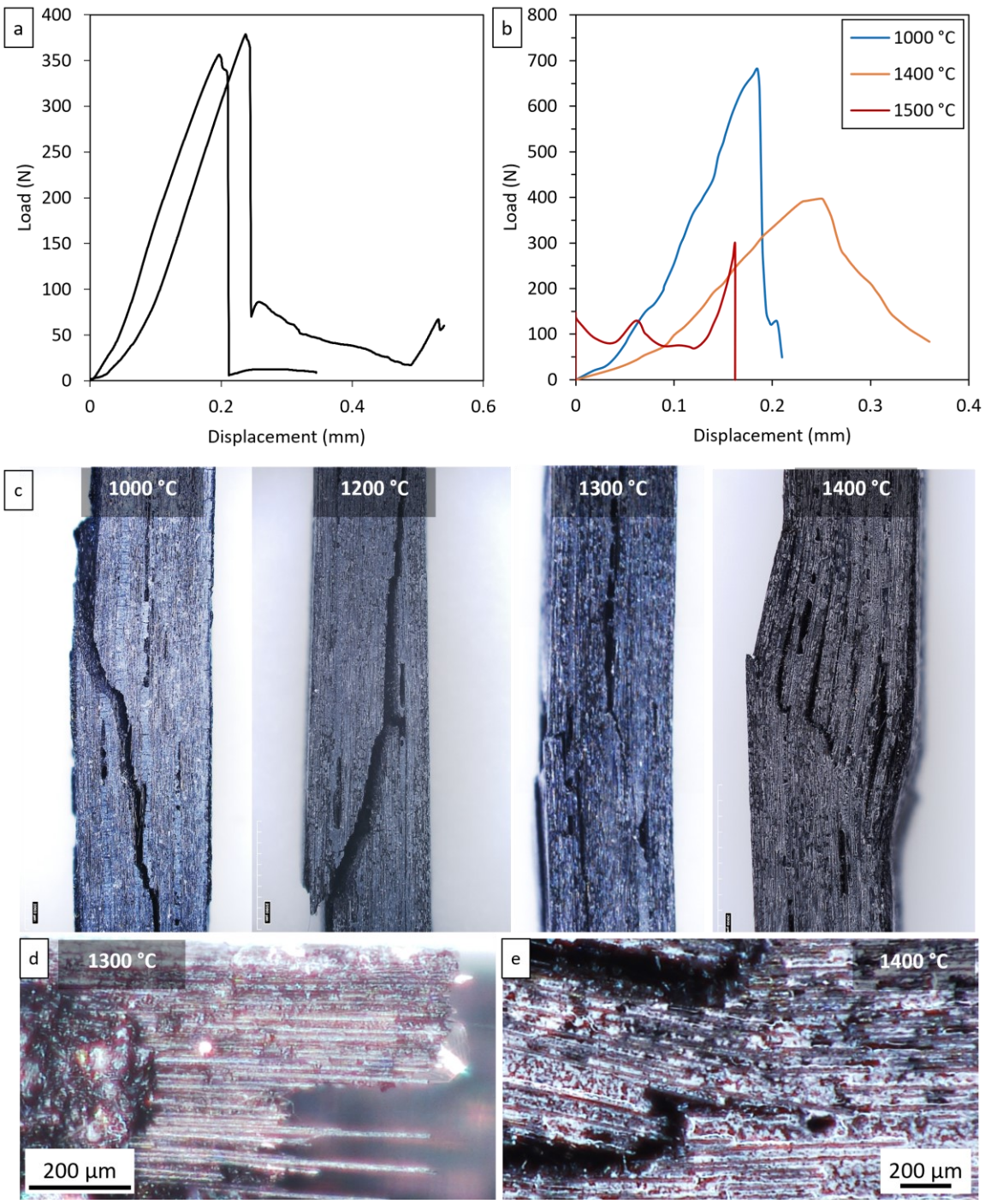

Figure 6.7. 4-pt bending tests on sample 6PIP-10 at room and high temperature (under Ar flow). Load-displacement curves at (a) RT and (b) 1000, 1400 and 1500 °C. Optical images (lateral view) of (c) fractured bars at 1000, 1200, 1300 and 1400 °C, and detail of fracture at (d) 1300 °C and (e) 1400 °C.

Conversely, as visible in load-displacement curve reported in Figure 6.7b, at 1500 °C the specimens never fractured, and the test was stopped when the bar touched the limit of the support fixture. Indeed, bars plastically deformed under applied load during bending test, resulting in a material that offered no mechanical (Figure 6.8a). It must be recalled that the bars before rupture were kept inside the furnace for about two hours, and despite the tests were carried out in Ar environment, the oxidation phenomena were not completely hindered. As confirmed by SEM/EDS analysis, borosilicate glass formed due to oxidation of ZrB_2 and SiC, covering the entire bar surface (Figure 6.8b-e). Nevertheless, this provided a fast passivation, thus protecting pristine carbon fibres within a few tens of microns underneath the surface (Figure 6.8e and Figure 6.9a,b).

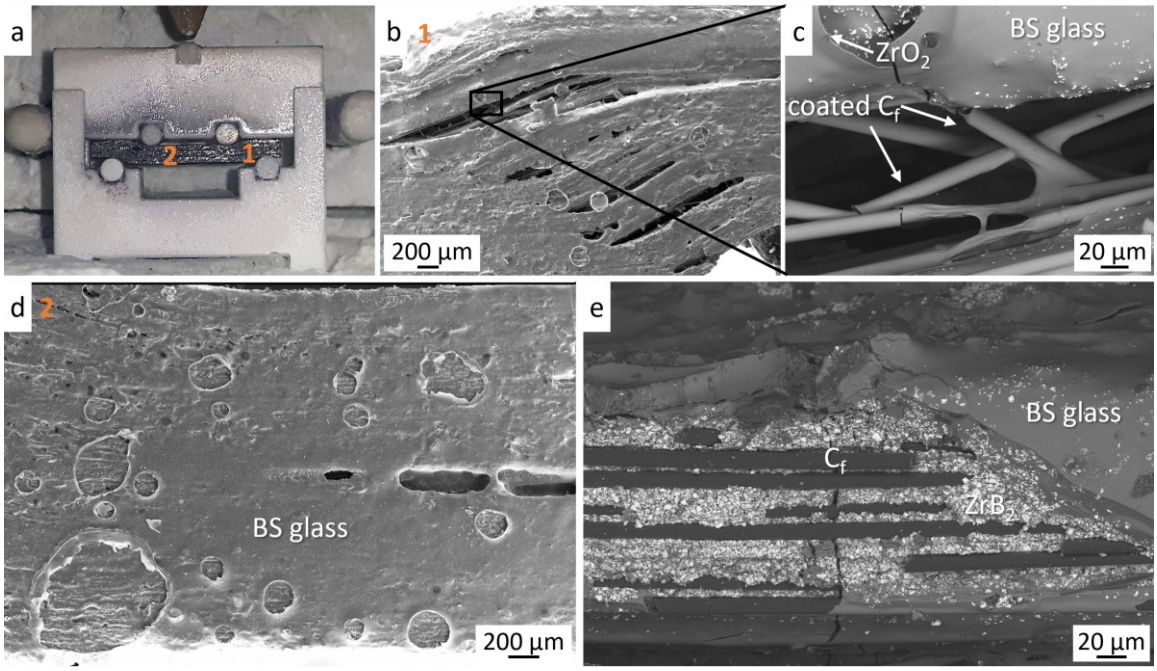

Figure 6.8. (a) Optical image of bar of sample 6PIP-10 tested by bending test at 1500 °C under Ar flow, deformed plastically on alumina fixture. (b) SEM image (lateral view) in deformed point under load pin (indicated as 1 in (a)) highlighting opening among layers and (c) magnification of carbon fibres coated by borosilicate glass. (d) SEM image (lateral view) in the middle part (indicated as 2 in (a)). (e) SEM image (BSE signal) of undamaged fibres underneath BS glass.

However, despite the fast self-passivation of the material, the matrix appeared partially reacted in the inner part of the bar (Figure 6.9c-e). Carbon fibres were preserved (Figure 6.9d), whereas ZrB_2 grain boundaries resulted oxidized showing ZrO_2 nano-crystals all around particles embedded in SiC(O) (Figure 6.9e,f,h). For that reason, we can speculate that the permeation of oxygen contained in testing environment inward the

bar was blocked by BS glass, but it came from polymer-derived SiC(O) converting into SiC at 1500 °C. Hence, the deterioration in mechanical properties was attributed to the presence at grain boundaries of diffused porosity due to the partial conversion of SiC(O) into SiC and glassy phases, such as B_2O_3 and SiO_2, softening at 1500 °C. Indeed, 1500 °C is a temperature well above the glass transition temperature, T_g, of borosilicate glass (~820 °C [28]) and pure silica (~1200 °C [29]).

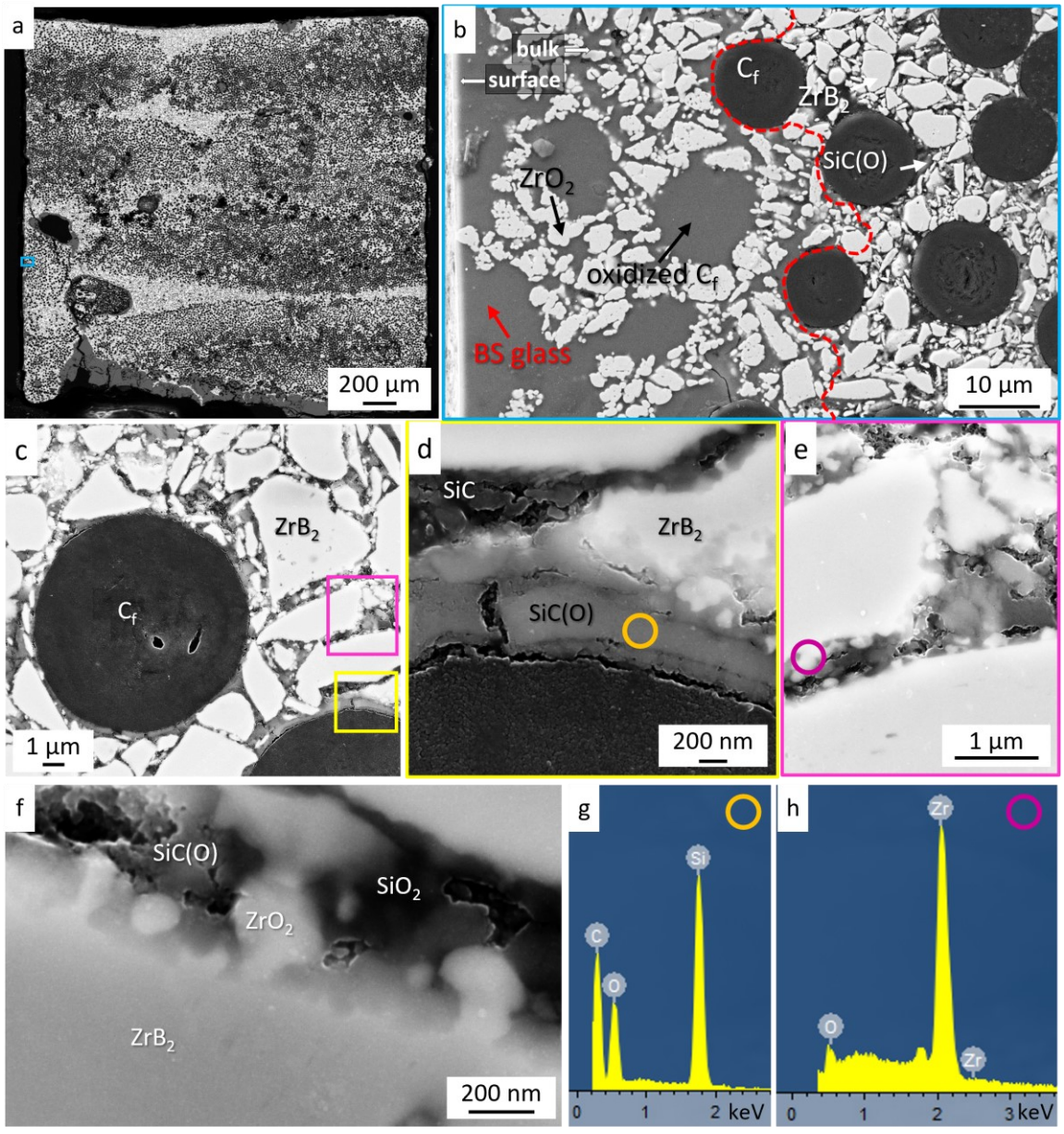

Figure 6.9. Polished section of sample 6PIP-10 tested by bending test at 1500 °C under Ar flow, cut in a deformed point under load pin. (a) Low magnification micrograph, (b) exposed bar surface (magnification of the point indicated with red arrow in (a)). (c) A single fibre surrounded by the matrix in the inner part and details of (d) fibre/matrix interface and (e) ZrB_2 grains embedded in SiC_{PDC} matrix. (f) High magnification micrograph of reacted ZrB_2 grain boundaries. (g, h) EDS spectra (EDS spots marked in (d,e)).

6.3.2 Mechanical properties of treated materials

On the basis of the microstructure observations on the treated samples, SiC_{PDC} crystallization started at around 1400 °C. Therefore, the effect of post-consolidation treatments on mechanical properties were evaluated on the bars treated at temperatures in the range 1400–1900 °C. The strength values obtained by bending tests at room temperature and 1500 °C in Argon were reported in Table 6.3.

Generally, the crystallization of the amorphous SiC(O) worsened performance at RT because of the porosity and crack formation caused by the volume shrinkage [30–32]. Bending strength fell by more than 150 MPa, decreasing from 474 ± 14 MPa to values in the range 152–303 MPa (Table 6.3). Specifically, strength values approaching 300 MPa were achieved for specimens P-14, whereas they dropped down to ~200 MPa for the other samples. No appreciable variation in the strength was noticed amongst the latter, despite the different pyrolysis conditions and levels of matrix porosity (i.e. 19–32%). This is mirrored in the work of Kimura et al. [33–36], who demonstrated that porosity above a threshold of ~15% affects dramatically the strength as it lowers the fraction of fibre strength manifested in CMCs.

Examples of load-displacement curves of a bar for each sample fractured at RT are reported in Figure 6.10.

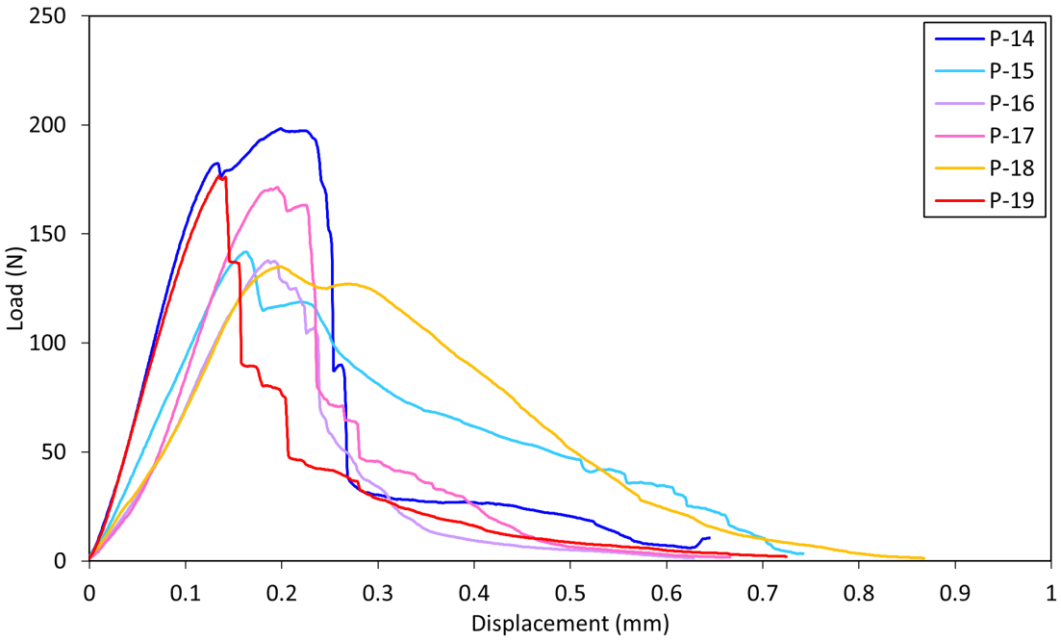

Figure 6.10. An example of load displacement curves for samples treated at temperature in the range 1400–1900 °C fractured by 4-pt bending tests at room temperature.

The jagged stress-strain curves in the failure stage revealed a non-brittle behaviour of all the specimens. Similarly, in our previous study [37], continuous carbon fibre-reinforced ZrB_2 matrix with porosity around 20–30% exhibited a pseudo-plasticity failure promoted from the weak fibre/matrix interface and the high porous weak matrix. According to Seyrek et al. [38], the decrease of the strength with increasing of the pyrolysis temperature could be the attributed to the weakening of the fibre/matrix interfaces and strengthening of the matrix. In fact, the post-consolidation heat treatments, proportionally to the temperature of pyrolysis, on one side affected the fibre/matrix interface leading to increasingly detached interfaces, on the other side, made the matrix increasingly stronger as evidenced by the enhanced SiC crystallization and skeletal density.

The fracture surfaces were studied to understand the interaction of fibres with the matrix and the extent of fibre pull-out (Figure 6.11). Due to the low preparation temperature, the micrograph of the reference sample 6PIP-10 displayed a dense matrix with no visible cracks, from which fibres tend to pull-out remaining intact and with rather smooth surfaces. The specimens P-14 fractured at RT showed a crack propagating from tensile surface in a tortuous path due to the involvement of delamination phenomena. The fracture surface did not differ significantly from the sample 6PIP-10 due to the low extent of SiC crystallization. However, detachment of the SiC_{PDC} matrix from the pulled-out carbon fibres suggests weakening of the fibre/matrix interface.

After 1500 °C pyrolysis, a high amount of amorphous phase is still visible in the matrix, but the occurred shrinkage led to microcracks perpendicular to the fibre axis and promote fibre/matrix debonding. As for P-14, stress generated cracks were deflected along the fibre periphery until the failure of the composite. In the specimens processed at 1600 °C and above, microstructure of the fracture upon fracture revealed in situ generated nano-pins [39] which were absent in samples pyrolysed at lower temperature. As the temperature increases, the matrix shows the tendency to become denser due to sintering effects while the interface with fibres resulted more degraded. This resulted in a higher pull-out. Failure occurred by multiple microcrackings, that proceeded highlighting phenomena of crack arresting, deflection or fibre bridging until total failure of the composite took place, as demonstrated by zig-zag bending curves and tortuous cracks paths.

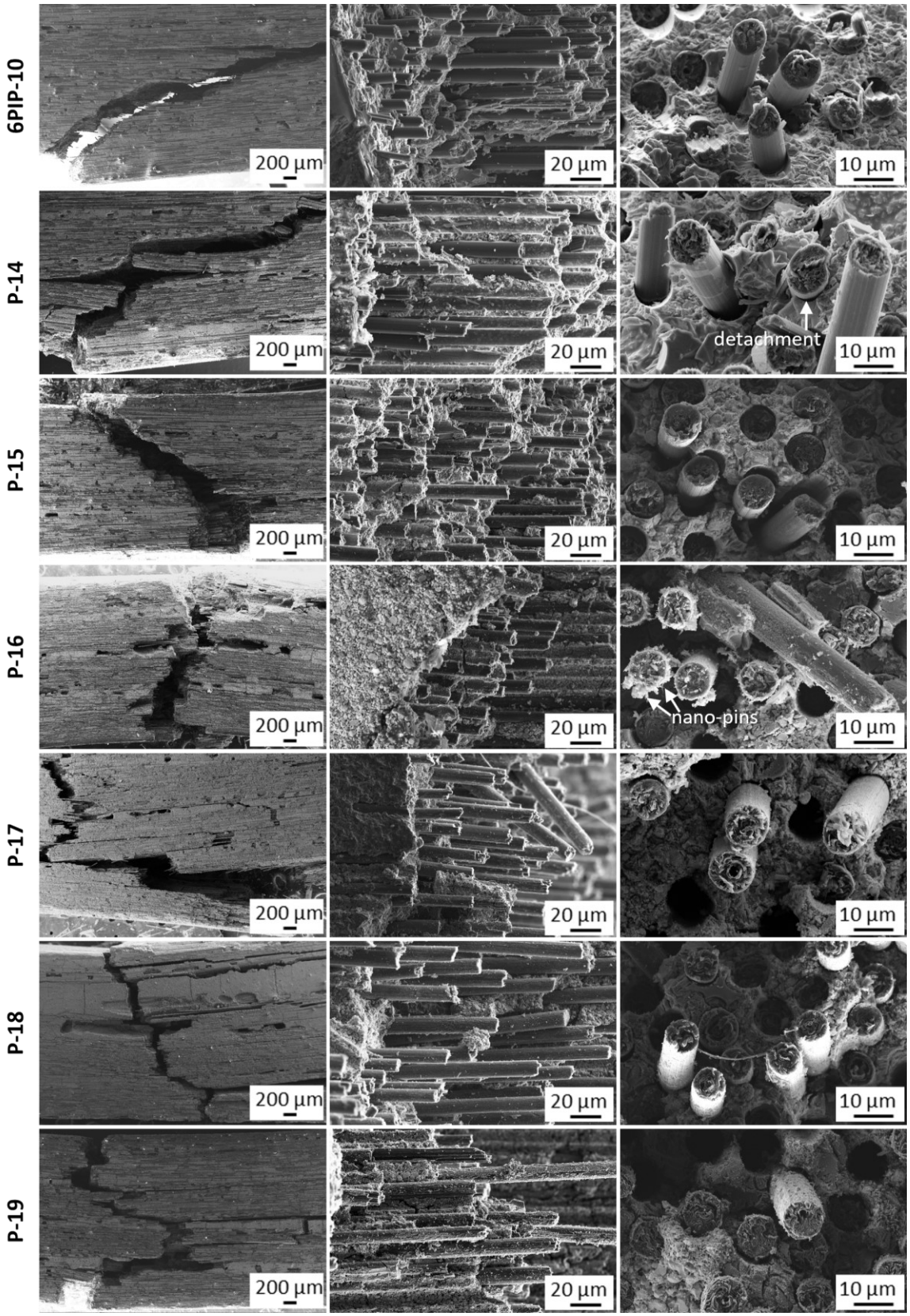

Figure 6.11. Micrographs of bars of samples treated at temperature in the range 1400–1900 °C fractured by 4-pt bending test at room temperature, showing for each sample: lateral view showing crack path, tensile surface, fracture surface.

Samples P-14, P-15, P-16, P-17, P-18 and P-19 were further tested at elevated temperature (i.e. 1500 °C under Ar flow). Typical load-displacement curves are shown in Figure 6.12, while optical pictures of some bars are in Figure 6.13a-f to show the appearance after 4-pt bending test.

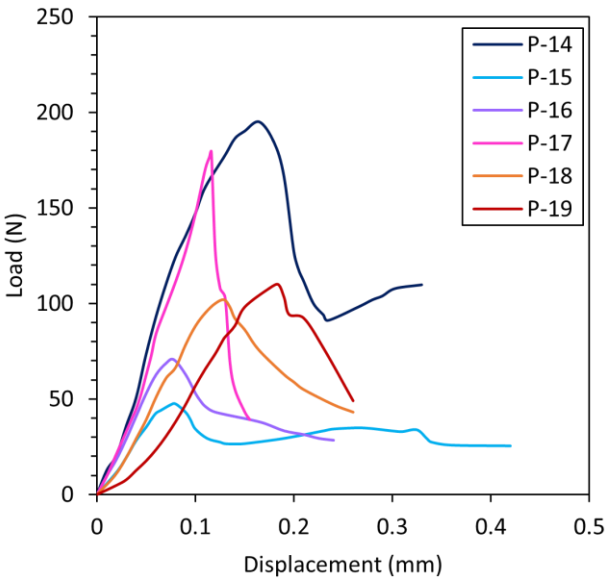

Figure 6.12. An example of load displacement curves for samples treated at temperature in the range 1400–1900 °C fractured by 4-pt bending tests at 1500 °C under Ar flow.

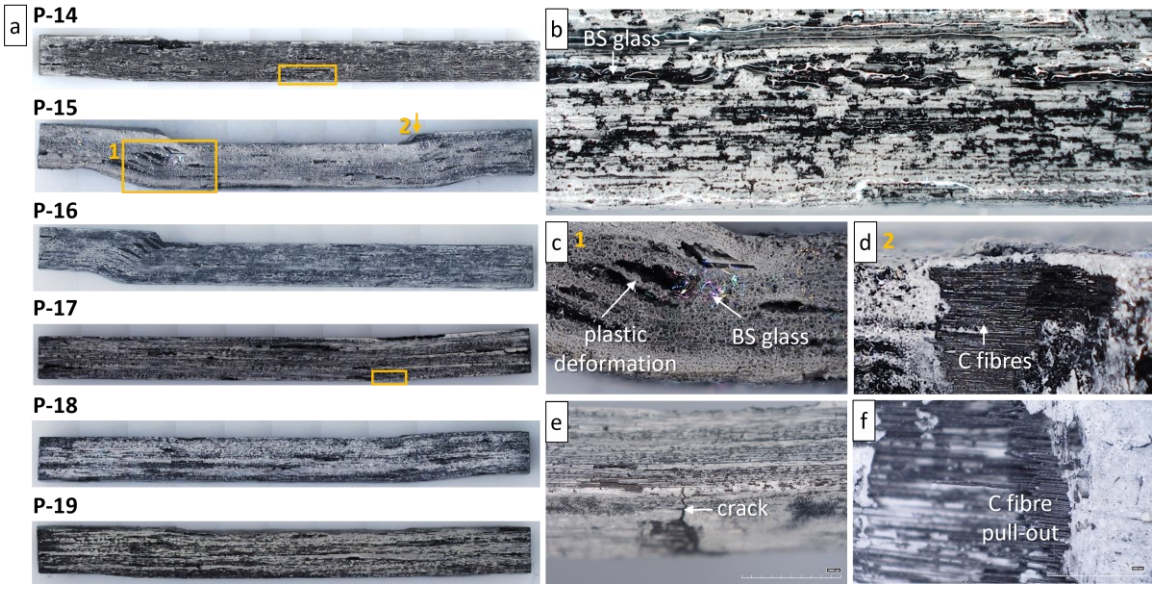

Figure 6.13. Optical images of bars reported as example for samples treated at 1400–1900 °C and tested by 4-pt bending test at 1500 °C under Ar flow. (a) Lateral view. (b) Detail of P-14 (lateral view, as indicated in (a)) highlighting formation of borosilicate glass. (c,d) Details of P-15 (lateral view and top view, indicated as 1 and 2 in (a)) that show the plastic deformation of material, and the formation of borosilicated glass protecting carbon fibres. (e,f) Details of P-17 (point indicated in (a)), showing the crack on the tensile surface and carbon fibre pull-out from the matrix.

Bars of P-14, P-15 and P-16 plastically deformed during bending moment and large cracks opened in correspondence of point load application (Figure 6.13a-d). Bar surfaces were covered by a dark silica glassy layer with a good adhesion to the bulk, only where the bar is bent it shows the tendency to spell-off baring undamaged C fibres. The failures were likely caused by a combination of bending and plastic deformation. Indeed, differently from sample 6PIP-10 that tested at 1500 °C resulted in invalid test, in this case tests worked for all material types making it possible to determine a flexural strength value. An average value of 212, 62 and 92 MPa were measured for P-14, P-15 and P-16 respectively (Table 6.3), however the strength at the elastic limit could be even lower.

The tested bars of treated materials at 1700 °C and above appeared outwardly oxidized with a limited amount of glassy phases softening at 1500 °C and no notable signs of plastic deformation (Figure 6.13a,e,f). The average flexural strength for P-17 was 168 MPa, resulting from values ranging from 108 up to 212 MPa. Samples P-18 and P-19 bumped into failure at quite scattering values, recording both average values approaching 100 MPa (Table 6.3).

The overarching purpose of this work was to obtain indications on the optimal temperature of pyrolysis for the consolidation of UHTCMCs through PIP process using a polycarbosilane, in order to reach a compromise between performance at room and elevated temperature. In the plot in Figure 6.14, the obtained values of open porosity, bulk density, flexural strength at room temperature and at 1500 °C and range of values of ratio of the bending strength at RT to bending strength at 1500 °C are reported as a function of the pyrolysis temperature in order to see main findings in one glance.

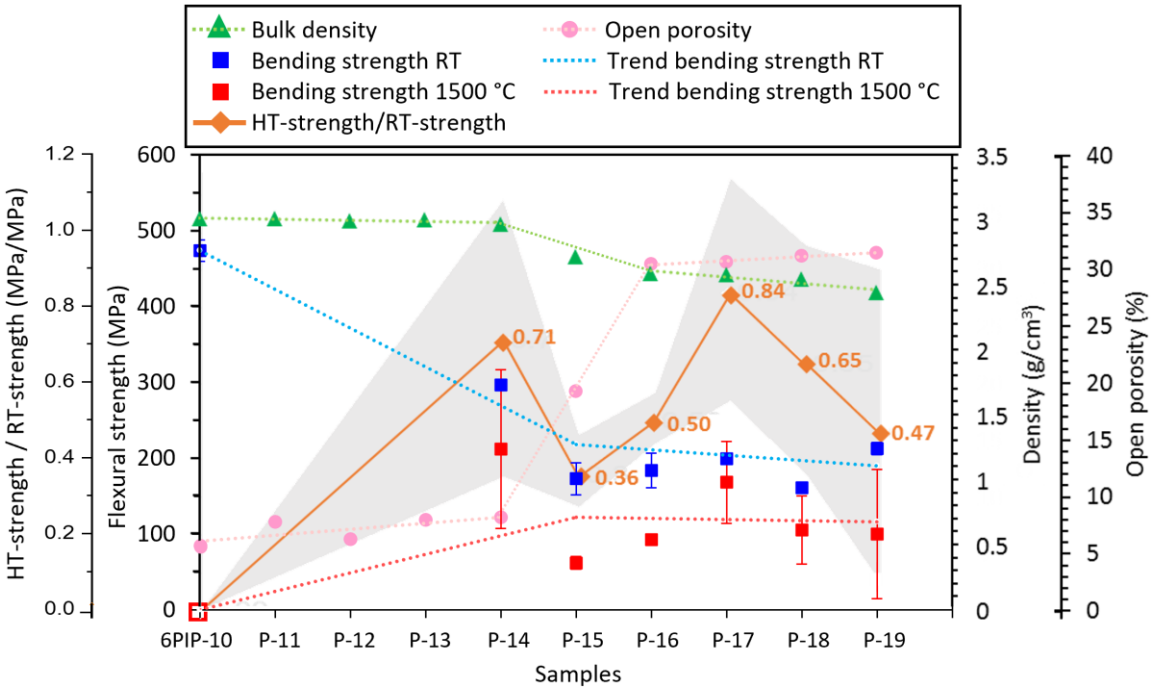

Figure 6.14. Plot shows the bulk density and open porosity of sample 6PIP-10 and all treated samples (temperature range 1100–1900 °C), flexural strength at room temperature and 1500 °C and HT-strength/Rt-strength ratio of sample 6PIP-10 and samples treated in temperature range 1400–1900 °C tested by 4-pt bending test as a function of pyrolysis temperature.

Bulk density decreases meanwhile open porosity increases with the pyrolysis temperature rise, recording substantial changes with treatments at 1500 °C and 1600 °C. The transformation from amorphous to crystalline phase of the SiC introduced by polymer infiltration led to an overall worsening of the RT strengths and to an improvement of the HT strengths compared to the reference material 6PIP-10. As we can see, all samples exhibited 1500 °C strength values lower than those at RT, in contrast to what observed for sample 6PIP-10 tested up to 1400 °C. However, a general correlation between pyrolysis temperature and mechanical properties cannot be found. Although, the best performances were exhibited from sample P-14 both at RT and HT, the conversion of SiC(O) not yet completed is undesired for applications in extreme conditions. The drop of the properties after pyrolysis at higher temperatures (i.e. 1500–1900 °C) could be due to processing conditions but also to the significantly higher void fraction, or a combination of them.

We will just consider post-consolidation treatments in the temperature range 1500–1900 °C. RT strength tests gave similar values for all samples. Even if higher average values were achieved for composites pyrolysed at 1700 °C and 1900 °C, the interpolation of the

data may suggest a slight decrease whereas a clearer beneficial effect of pyrolysis cycle at 1700 °C was achieved on HT strength, although the quite scattered values. Moreover, in this case decline in performances at elevated temperature was limited, in particular average strength was estimated only 16% lower than that at RT. Conversely, post-consolidation treatments at 1500 and 1600 °C were demonstrated ineffective in completing SiC(O) conversion and as a consequence improving mechanical properties. HT resistance of samples P-18 and P-19 could be likely affected by the higher amount of pores and transverse microcracks induced in the matrix by high temperature pyrolysis, that coupled with oxidation phenomena jeopardized the native strength. The above discussion can find confirmation in the ratio between the HT bending strength at 1500 °C to the bending strength at RT. Looking at this ratio, it seems that the pyrolysis at 1700 °C, with a ratio of 0.84, was the best compromise between the microstructure consolidation and the tested mechanical properties.

The above discussed findings are in line with some studies concerning C_f/SiC or SiC_f/SiC composites prepared using polycarbosilane. Yin et al. [16] consolidated SiC_f/SiC composites at 1400 °C and then tested them both at RT and 1500 °C in Argon, revealing a strong strength deterioration (from 305 to only 39 MPa) attributable to the mass loss and crystallization of the precursor derived ceramic matrix at elevated temperature. Kumar et al. [39] studied that C_f/SiC pyrolysed at 1600 °C achieved better mechanical properties than the same composites pyrolysed at 1400 °C, thanks to in-situ growth of SiC nano-pins which strengthened the matrix, leading to about 20% higher values. Similarly, Jian et al. [40] showed that increasing the pyrolysis temperature up to 1600 °C weakened the interfacial bonding between carbon fibre and SiC matrix, leading to the desirable interfacial structure and superior flexural strength. Wang et al. [41] prepared SiC_f/SiC composites under 1000, 1300 and 1500 °C and confirmed that SiC crystallite size and crystallinity increased with increasing temperature while flexural strength decreased. Moreover, they found higher mechanical degradation after heat-treatment, whose degree decreased as increase the pyrolysis temperature.

Unfortunately, to the best of our knowledge, no efforts have been devoted to study the correlation between pyrolysis temperature and mechanical properties on UHTCMCs fabricated by PIP. However, in view of the above, a pyrolysis temperature of 1700 °C is

reasonable to obtain a right combination of resistance in a broad temperature range, due to the combination of matrix porosity and fibre/matrix interaction.

6.4 Conclusions

A unidirectional C_f/ZrB_2-SiC composite was fabricated through a cycle of powder slurry infiltration followed by six repetitive PIP cycles using a commercial allyl-hydrido polycarbosilane precursor. The adopted mild conditions (i.e. 1000 °C) led to a final matrix containing 32 vol% of polymer-derived amorphous SiC(O). This composite exhibited flexural strength over 550 MPa up to 1400 °C. However, at 1500 °C a loss of performance was observed because of the presence of oxide impurities in the low-temperature pyrolysed SiC(O). The effect of adding a further pyrolysis cycle at higher temperature (i.e. 1100–1900 °C) on the microstructure and mechanical properties was investigated.

Pyrolysis at temperature beyond 1500 °C led to conversion of amorphous SiC(O) into crystalline β-SiC and, as a consequence, to an increase of open porosity up to 30%. Flexural strength of post-treated composites resulted in performance deterioration at room temperature, reaching values not higher than of 220 MPa. Bending tests at 1500 °C revealed an improvement of the strength compared to material consolidated at mild conditions, however heat treatments until 1600 °C were not effective to avoid plastic deformation of the material. The best candidate pyrolysis temperature to find a right compromise between strength at room et elevated temperature resulted 1700 °C (RT strength ~200 MPa and 1500 °C strength ~170 MPa).

The investigation methodology adopted in this study had the advantage to save time because it allowed to explore nine different testing conditions starting from a single material. In future studies, some efforts should be made to optimize the process in order to limit porosity and microcracks in the matrix and fibre/matrix detachment and thus, to further enhance mechanical properties.

6.5 References

1. Kumar, S. *et al.* Factorial design, processing, characterization and microstructure analysis of PIP-based C/SiC composites. *Bull. Mater. Sci.* **41**, 1–13 (2018).

2. Ding, Y., Dong, S., Zhou, Q., Huang, Z. & Jiang, D. Preparation of C/SiC composites by hot pressing, using different C fiber content as reinforcement. *J. Am. Ceram.*

Soc. **89**, 1447–1449 (2006).

3. Hurwitz, F. I. Filler/Polycarbosilane Systems as CMC Matrix Precursors. in *22nd Annual Conference on Composites, Advanced Ceramics, Materials, and Structures: A: Ceramic Engineering and Science Proceedings, Volume 19* (ed. Bray, D. E.) 267–274 (The American Ceramic Society, 1988). doi:10.1002/9780470294482.CH30.

4. Gupta, R. K. *et al.* Development of Polycarbosilane (PCS) Polymer and PCS-Derived SiC Fibers and Their Composites. in *Handbook of Advanced Ceramics and Composites* (eds. Mahajan, Y. R. & Johnson, R.) 913–928 (Springer, Cham, 2020). doi:10.1007/978-3-030-16347-1_29.

5. King, D., Apostolov, Z., Key, T., Carney, C. & Cinibulk, M. Novel processing approach to polymer-derived ceramic matrix composites. *Int. J. Appl. Ceram. Technol.* **15**, 399–408 (2018).

6. Swaminathan, B., Painuly, A., Prabhakaran, P. V. & Packirisamy, S. Liquid polycarbosilane-derived C/C–SiC composites with improved mechanical strength for high temperature applications. *Ceram. Int.* **41**, 3574–3577 (2015).

7. Hu, H. *et al.* Preparation and characterization of C/SiC-ZrB_2 composites by precursor infiltration and pyrolysis process. *Ceram. Int.* **36**, 1011–1016 (2010).

8. Li, Q. *et al.* Fabrication and properties of 3-D C_f/SiC-ZrC composites, using ZrC precursor and polycarbosilane. *J. Am. Ceram. Soc.* **95**, 1216–1219 (2012).

9. Li, L., Wang, Y., Cheng, L. & Zhang, L. Preparation and properties of 2D C/SiC-ZrB_2-TaC composites. *Ceram. Int.* **37**, 891–896 (2011).

10. Wang, Y., Liu, W., Cheng, L. & Zhang, L. Preparation and properties of 2D C/ZrB_2-SiC ultra high temperature ceramic composites. *Mater. Sci. Eng. A* **524**, 129–133 (2009).

11. Kaur, S., Riedel, R. & Ionescu, E. Pressureless fabrication of dense monolithic SiC ceramics from a polycarbosilane. *J. Eur. Ceram. Soc.* **34**, 3571–3578 (2014).

12. Starfire® Systems Inc. StarPCS SMP-10. (2018).

13. Süß, F. *et al.* Combination of PIP and LSI processes for SiC/SiC ceramic matrix composites. *Open Ceram.* **5**, (2021).

14. Key, T. S., Patel, D. K., Wilks, G. B. & Cinibulk, M. K. Modeling the pyrolysis of preceramic polymers: A kinetic study of the polycarbosilane SMP-10. *J. Eur. Ceram. Soc.* **41**, 6356–6365 (2021).

15. Zunjarrao, S. C., Rahman, A. & Singh, R. P. Characterization of the evolution and properties of silicon carbide derived from a preceramic polymer precursor. *J. Am. Ceram. Soc.* **96**, 1869–1876 (2013).

16. Yin, J. *et al.* The effects of SiC precursors on the microstructures and mechanical properties of SiC_f/SiC composites prepared via polymer impregnation and pyrolysis process. *Ceram. Int.* **41**, 4145–4153 (2015).

17. Hasegawa, Y. & Okamura, K. Synthesis of continuous silicon carbide fibre. *J. Mater. Sci. 1983 1812* **18**, 3633–3648 (1983).

18. Hasegawa, Y. Synthesis of continuous silicon carbide fibre. *J. Mater. Sci. 1989 244* **24**, 1177–1190 (1989).

19. Sreeja, R., Swaminathan, B., Painuly, A., Sebastian, T. V. & Packirisamy, S. Allylhydridopolycarbosilane (AHPCS) as matrix resin for C/SiC ceramic matrix composites. *Mater. Sci. Eng. B Solid-State Mater. Adv. Technol.* **168**, 204–207 (2010).

20. Kaur, S., Mera, G., Riedel, R. & Ionescu, E. Effect of boron incorporation on the phase composition and high-temperature behavior of polymer-derived silicon carbide. *J. Eur. Ceram. Soc.* **36**, 967–977 (2016).

21. Soraru, G. D., Babonneau, F. & Mackenzie, J. D. Structural evolutions from polycarbosilane to SiC ceramic. *J. Mater. Sci. 1990 259* **25**, 3886–3893 (1990).

22. Sciti, D. *et al.* Properties of large scale ultra-high temperature ceramic matrix composites made by filament winding and spark plasma sintering. *Compos. Part B Eng.* **216**, 108839 (2021).

23. Vinci, A. *et al.* Mechanical behaviour of carbon fibre reinforced TaC/SiC and ZrC/SiC composites up to 2100°C. *J. Eur. Ceram. Soc.* **39**, 780–787 (2019).

24. Vinci, A. *et al.* Influence of fibre content on the strength of carbon fibre reinforced HfC/SiC composites up to 2100 °C. *J. Eur. Ceram. Soc.* **39**, 3594–3603 (2019).

25. Galizia, P., Zoli, L. & Sciti, D. Impact of residual stress on thermal damage accumulation, and Young's modulus of fiber-reinforced ultra-high temperature ceramics. *Mater. Des.* **160**, 803–809 (2018).

26. Sauder, C., Lamon, J. & Pailler, R. The tensile behavior of carbon fibers at high temperatures up to 2400°C. *Carbon N. Y.* **42**, 715–725 (2004).

27. Sciti, D. *et al.* Effect of PAN-based and pitch-based carbon fibres on microstructure and properties of continuous C_f/ZrB_2-SiC UHTCMCs. *J. Eur. Ceram. Soc.* **41**, 3045–3050 (2021).

28. Altemose, V. O. 7. Glass vacuum systems. in *Methods in Experimental Physics* (eds. Weissler, G. L. & Carlson, R. W.) vol. 14 313–343 (Academic Press, 1980).

29. Ojovan, M. I. Glass formation in amorphous SiO_2 as a percolation phase transition in a system of network defects. *JETP Lett.* **79**, 632–634 (2004).

30. Colombo, P., Mera, G., Riedel, R. & Sorarù, G. D. Polymer-derived ceramics: 40 Years of research and innovation in advanced ceramics. *J. Am. Ceram. Soc.* **93**, 1805–1837 (2010).

31. Lee, S. H., Weinmann, M. & Aldinger, F. Particulate-Reinforced Precursor-Derived Si–C–N Ceramics: Optimization of Pyrolysis Atmosphere and Schedules. *J. Am.*

Ceram. Soc. **88**, 3024–3031 (2005).

32. Gu, J. *et al.* Fast fabrication of SiC particulate-reinforced SiC composites by modified PIP process using spark plasma sintering – effects of green density and heating rate. *J. Eur. Ceram. Soc.* **41**, 4037–4047 (2021).

33. Kimura, S., Yasuda, E., Tanaka, H. & Yamada, S. Graphitization and microstructure of carbon fiber/glassy carbon composite. *Yogyo-kyokai-shi* **83**, 122–127 (1975).

34. Kimura, S. Fracture behaviour of carbon-fiber/CVD carbon composites. (1981).

35. Kimura, S., Tanabe, Y., Takase, N. & Yasuda, E. Pressure graphitization of matrix in carbon-fiber glass-like carbon composite. *Nippon Kagaku Kaishi* 1474–1480 (1981).

36. Savage, G. *Carbon-Carbon Composites*. (Springer Netherlands, 1993).

37. Sciti, D., Natali Murri, A., Medri, V. & Zoli, L. Continuous C fibre composites with a porous ZrB2 Matrix. *Mater. Des.* **85**, 127–134 (2015).

38. Seyrek, Y. & Felekoğlu, K. T. Selection of proper matrix with plasma-treated HTPP fiber reinforced cementitious composites in terms of flexural toughness. *J. Build. Eng.* **45**, 103632 (2022).

39. Kumar, S. *et al.* Polycarbosilane based UD C/SiC composites: Effect of in-situ grown SiC nano-pins on mechanical properties. *Ceram. Int.* **41**, 12849–12860 (2015).

40. Jian, K., Chen, Z. H., Ma, Q. S., Hu, H. feng & Zheng, W. W. Effects of pyrolysis temperatures on the microstructure and mechanical properties of 2D-C_f/SiC composites using polycarbosilane. *Ceram. Int.* **33**, 73–76 (2007).

41. Wang, L. Y., Luo, R. Y. & Cui, G. Y. Effect of pyrolysis temperature on the mechanical evolution of SiC_f/SiC composites fabricated by PIP. *Ceram. Int.* **46**, 1297–1306 (2020).

7. Preparation of UHTCMCs by hybrid processes coupling Polymer Infiltration and Pyrolysis with Hot Pressing and vice versa

7.1 Introduction

In order to obtain a dense matrix in a fast and cost-effective manner, the combination of the PIP process with other techniques has been recently investigated [1–5]. One of the most effective routes may involve the hot pressing (HP) method thanks to its remarkably short manufacturing time (e.g hours). Moreover, sintered UHTC matrix can contribute to the structural properties in extremely hot environments but the applied pressure combined with the elevated temperature may lead to fibre damage. Previous works concerning the combination of PIP and sintering of CMCs are mainly focused on SiC fibre-reinforced SiC matrix composites [6–9], since these fibres are less reactive than carbon ones. Nevertheless, sintering process have been rethought for UHTCMC manufacturing [10]. Justin et al. [11] prepared C_f/HfC-SiC trough a single-step slurry infiltration (HfC powders/SMP-10-based slurry) and two-step infiltration (powders first and SMP-10 after) and densification by HP. Zhang et al. [12] developed a hybrid technique involving slurry impregnation, PIP and HP for the preparation of 3D C_f/ZrB_2-SiC. Furthermore, some published works report the development of hybrid processes combining the same techniques (i.e. PIP and HP) in reverse order. Wang et al. [13] fabricated C_f/ZrC-SiC by hot-pressing of infiltrated preforms followed by densification via four PIP cycles. Kannan et al. [14,15] studied a process based on reactive hot pressing (RHP) coupled by several PIP cycles (up to 10) to obtain C_f/SiC-ZrB_2 and C_f/SiC-ZrB_2-Ta_xC_y composites. However, evaluation of the complex relationships among processing steps, microstructure and mechanical properties caused by the opposite application sequence of consolidation techniques was not discussed. Moreover, while ablation resistance was widely reported to demonstrate the superior resistance of UHTCMCs vs CMCs, the elevated temperature strength of hybrid PIP plus HP made UHTCMCs has not been discussed yet.

Part of the content of this chapter has been published in Journal of the European Ceramic Society 42 (2022) 2118–2126 as "*F. Servadei, L. Zoli, P. Galizia, A. Vinci, D. Sciti, Development of UHTCMCs via water based ZrB_2 powder slurry infiltration and polymer infiltration and pyrolysis*".

In this work, we evaluated (i) the efficacy of HP sintering step on the densification of the composites, either applying it as a pre-treatment (e.g. before polymer infiltration and pyrolysis cycles) or as a post-treatment (e.g. after PIP cycles) and (ii) the ability of the PIP process to tailor the UHTC-matrix/fibre interface or to heal the cracks always present in the matrix [16] by performing the PIP process before or after HP, respectively. The number of PIP cycles was set to be the same in the two cases as well as the final porosity adjusting HP cycles. Microstructural features and the thermo-mechanical properties of the composites were compared to explore the potential of the two hybrid processes for a faster and cheaper manufacturing of UHTCMCs possessing improved thermo-mechanical properties at elevated temperature (i.e. 1500 °C). This study will reveal interesting findings but also some critical issues due to the opposite application sequence of consolidation techniques.

7.2 Microstructural features

Process cycles, volumetric amounts of the phases, residual and open porosities, and densities for the composites are reported in Table 7.1.

Table 7.1. Sintering and pyrolysis parameters (T: maximum temperature, t: dwell at T, P: applied pressure), resulting composition (volumetric amounts of carbon fibre (C_f), zirconium diboride (ZrB_2), powder derived silicon carbide (SiC_p) and polymer-derived silicon carbide (SiC_{PDC})), residual porosity, open porosity, Thermo-mechanical properties.

Label	Techniques sequence	T,t,P	Composition				Residual porosity	Open porosity	Bulk density	σ R.T.	σ 1500 °C	K_{Ic} RT	K_{Ic} 1500 °C
			C_f	ZrB_2	SiC_p	SiC_{PDC}							
		(°C,min,MPa)	(vol%)					(%)	(g/cm³)	(MPa)		(MPa·m$^{0.5}$)	
HPP	1) HP	1850,0,40.											
	2) PIP	1000,120,0.1	39.9 ± 0.8	34.0 ± 0.3	3.8 ± 0.1	7.9 ± 0.1	~14	~12	3.2 ± 0.1	72 ± 23	230 ± 52	6.9 ± 1.1	7.2 ± 2.5
PHP	1) PIP	1000,120,0.1											
	2) HP	1900,15,40	33.5 ± 1.0	31.8 ± 0.3	3.5 ± 0.1	18.2 ± 0.1	~13	~13	3.3 ± 0.1	167 ± 13	592 ± 83	6.7 ± 0.7	7.4 ± 0.6

Samples labelled HPP and PHP had similar volumetric fractions of carbon fibres (39.9% vs. 33.5%), ZrB_2 (34.0% vs. 31.8%) and SiC introduced with the powder slurry (SiC_p) (3.8% vs. 3.5%), whilst a larger fraction of polymer-derived ceramic SiC (SiC_{PDC}) was contained in sample PHP (18.2% vs. 7.9%). Regardless of the consolidation route used (route A vs. route B), both final porosities were found to be about ¼ of the starting porosity (green samples). This represents a good result in term of shortening of process time and less consumption of SiC precursor compared to PIP process. A final porosity of

22–27 % was reported after three PIP cycles to realize SICARBON and UHTCMCs [17]. Moreover, in our experience, at least four PIP cycles are necessary to achieve a porosity of about 13% (not published data).

The variation of the bulk and relative densities after each manufacturing step are reported in Table 7.2 while a visual presentation of the variation of bulk density is shown in Figure 7.1. The relative density of a green pellet was ~51%. In the case of HPP, the preliminary hot pressing treatment caused a remarkable increase of relative density to ~77%, while a slight relative density variation was recorded after the first and second PIP cycles (83% and 86% respectively). In case of PHP, the density increased gradually after each PIP cycle (62% and 69% respectively) and leaped to a final value of 87% after the HP cycle.

Table 7.2. Bulk density and relative density of samples HPP and PHP measured after each manufacturing step.

Sample label		N° step			
		0	1	2	3
HPP	Bulk density (g/cm^3)	2.05	2.95	3.09	3.15
	Relative density (%)	51	77	83	86
PHP	Bulk density (g/cm^3)	2.05	2.33	2.51	3.27
	Relative density (%)	51	62	69	87

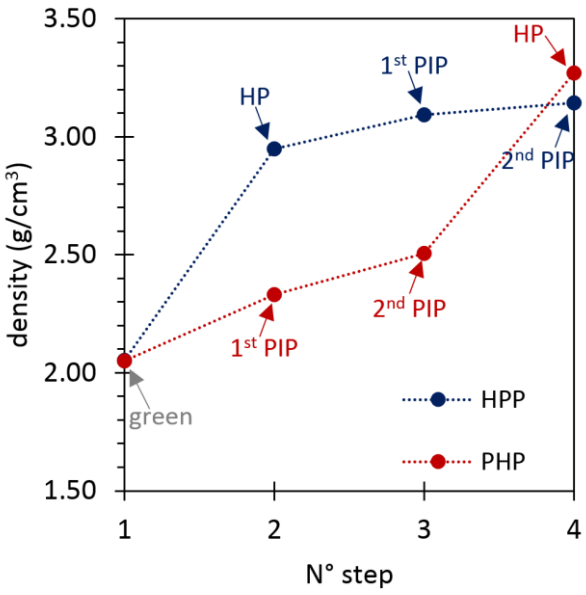

Figure 7.1. Variation of the bulk densities, which are measured by geometric method after each manufacturing step, for PIP/HP (red line) and HP/PIP (blue line) samples.

X-ray diffraction patterns (Figure 7.2) collected on the cross sections of the two composites confirmed the presence of the following crystalline phases: graphite (PDF #75-1621), ZrB_2 (PDF #34-0423) and SiC. In the HPP sample, low reflections belong to α-SiC (PDF #29-1131) were detected for the small amount of SiC powder (introduced by slurry), while, in agreement with supplier datasheet [18], only a broad scattering profile was associated to the amorphous SiC(O) [19,20] obtained by pyrolysis of polycarbosilane at 1000 °C. In PHP sample, peaks belong to β-SiC (PDF #65-0360) and α-SiC (PDF #29-1131) were observed. Based on supplier datasheet [18], only α-SiC should be observed after a heat treatment of SMP-10 above 1800 °C; however, as reported by Delobel et al. [21], the application of mechanical pressure during a heat treatment may delay the phase transformation of beta (β) polytype into alpha (α) polytype at higher temperature.

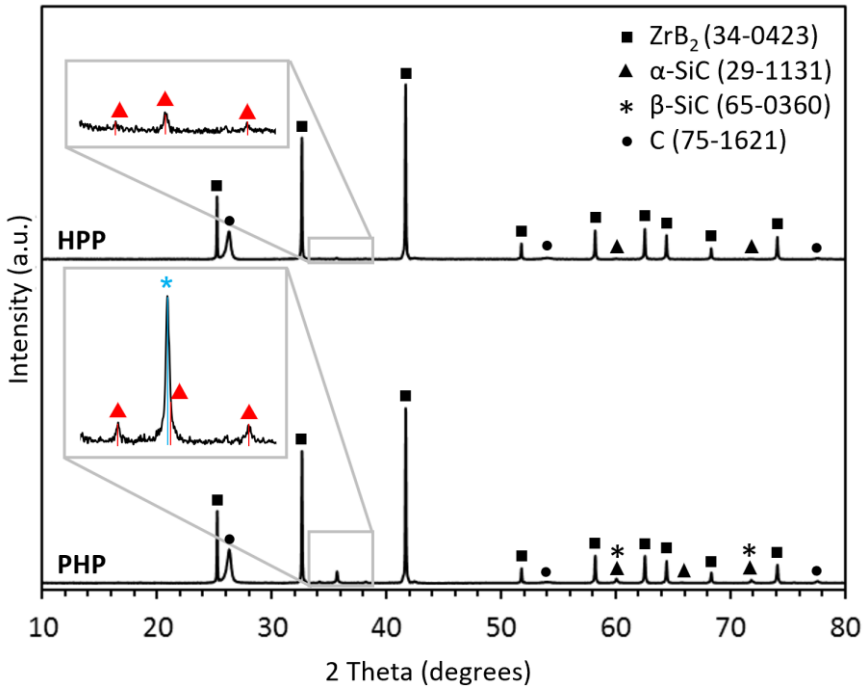

Figure 7.2. X-ray diffraction patterns of samples HPP and PHP.

Polished sections of the samples are shown in Figure 7.3a-c and Figure 7.4a-c. Black dots and lines are carbon fibres stacked in 0/90° orientation, the white contrasting phase is ZrB_2, the grey phase is SiC. SiC powder (SiC_p) and polymer-derived SiC or SiC(O) (SiC_{PDC}) are hardly distinguishable due to the low contrast between them, however the PDC generated larger spots in the matrix and took up tight gaps inaccessible for the powder. Detailed description of each sample is reported below.

HPP Sample: In Figure 7.3a, the overview of the cross section shows a layered structure with a thickness of 405 ± 30 µm for each layer, highlighting a good compaction of the green pellet. Defects such as voids and cracks are well visible in the polished sections and they were generated at different stages of the process (slurry impregnation, drying stage, matrix shrinkage during sintering). Parallel cracks, spaced in the range 100–600 µm, were observed, and likely formed during the drying of impregnated preforms. Reasonably, these cracks were not closed during the sintering owing to the lower sintering temperature with respect to that typically used for UHTCMCs developed in ISTEC [16]. The cracks formed due to the difference in CTE of the matrix and fibres are visible only in the plane of the fibre axis (for this reason they are also called transverse cracks, where "transverse" is respect to the fibre axis) and are narrower and typically spaced in the range of 15–40 µm [16,22]. Interestingly, between some bundles voids with size in the range 10–100 µm were found, in agreement with MIP analysis (not shown). The distribution of SiC_{PDC} in the matrix among fibres was found to be quite homogenous along the cross section of the sample, however, none of the defects, including parallel cracks, inter-layer and inter-bundle voids were filled with SiC_{PDC}. Indeed, SiC_{PDC} prevalently seeped into intra-bundle regions with a scarce powder content (e.g. not infiltrated fibre agglomerations, see Figure 7.3b). The coarsening of ZrB_2 was minimal, which displayed sharp edges, only formation of necks among grains and a mean grain size around 1.5 µm (Figure 7.3c).

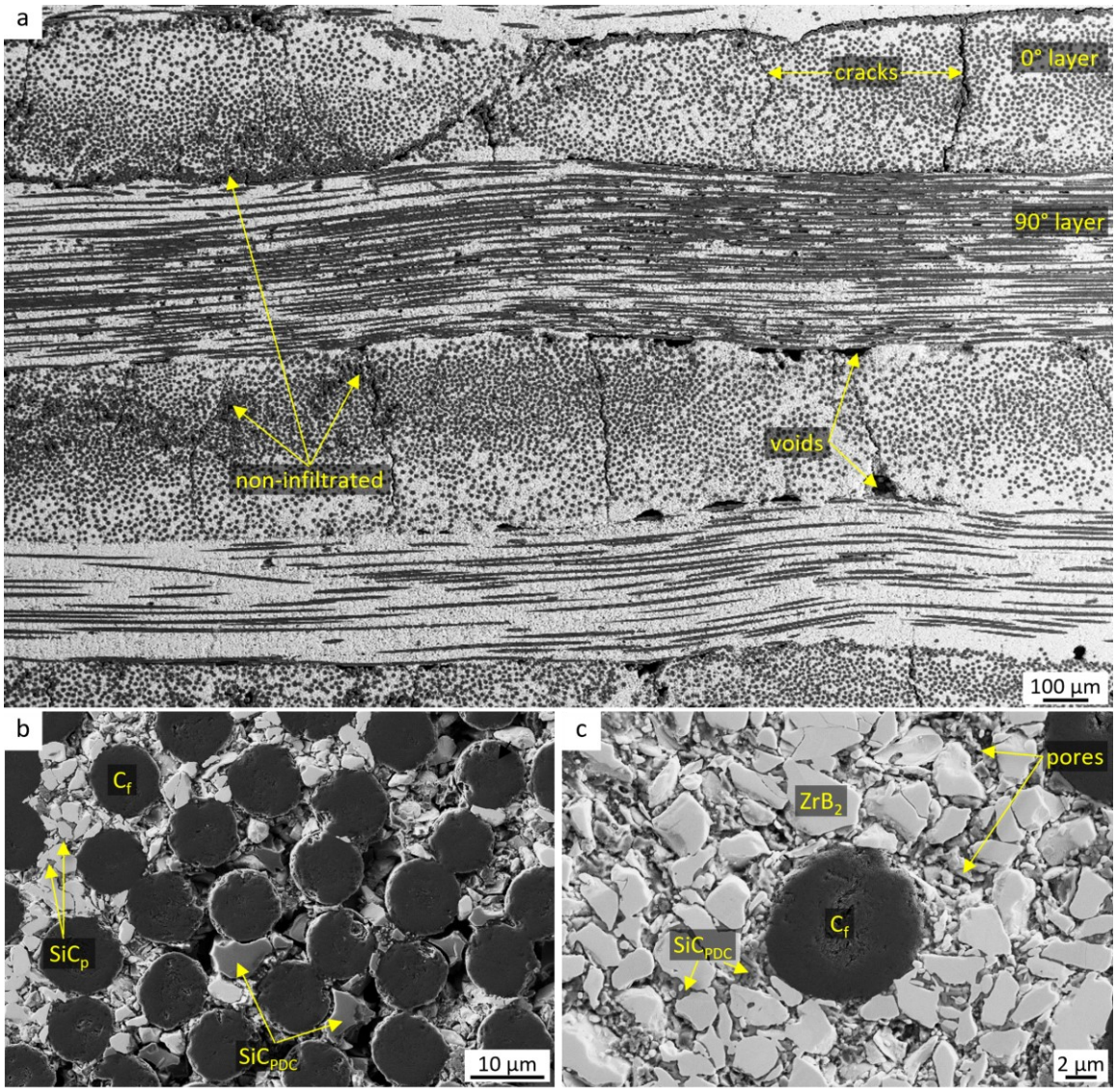

Figure 7.3. Polished sections of HPP sample. (a) General overview at low magnification, (b) microstructure inside bundles; the light and the grey phases represent ZrB_2 and SiC respectively, while carbon fibres are black, (c) detail of a single fibre.

PHP Sample: A low magnification micrograph (Figure 7.4a) shows the 0/90° configuration of the layers that have an average thickness of 420 ± 20 µm. Defects created in the stages before sintering were partially replenished by percolation of the SMP-10 and stronger sintering conditions. MIP analysis indicates an absence of open porosity in the range 10–100 µm indeed (not shown). In Figure 7.4b, a detail of the microstructure inside bundles is reported. Fibres are well distributed in the UHTC matrix and the interface was quite smooth. The low viscous preceramic polymer allowed a very good degree of infiltration inside the bundles and in narrow gaps between adjacent fibres. The sintered ZrB_2 grains underwent coarsening until an average grain size of 2.1 ± 1.2 µm, as

ascertained by image analysis, see Figure 7.4c; the simultaneous presence of ZrB_2, SiC_p, SiC_{PDC}, and pores around a single fibre is highlighted in the same figure.

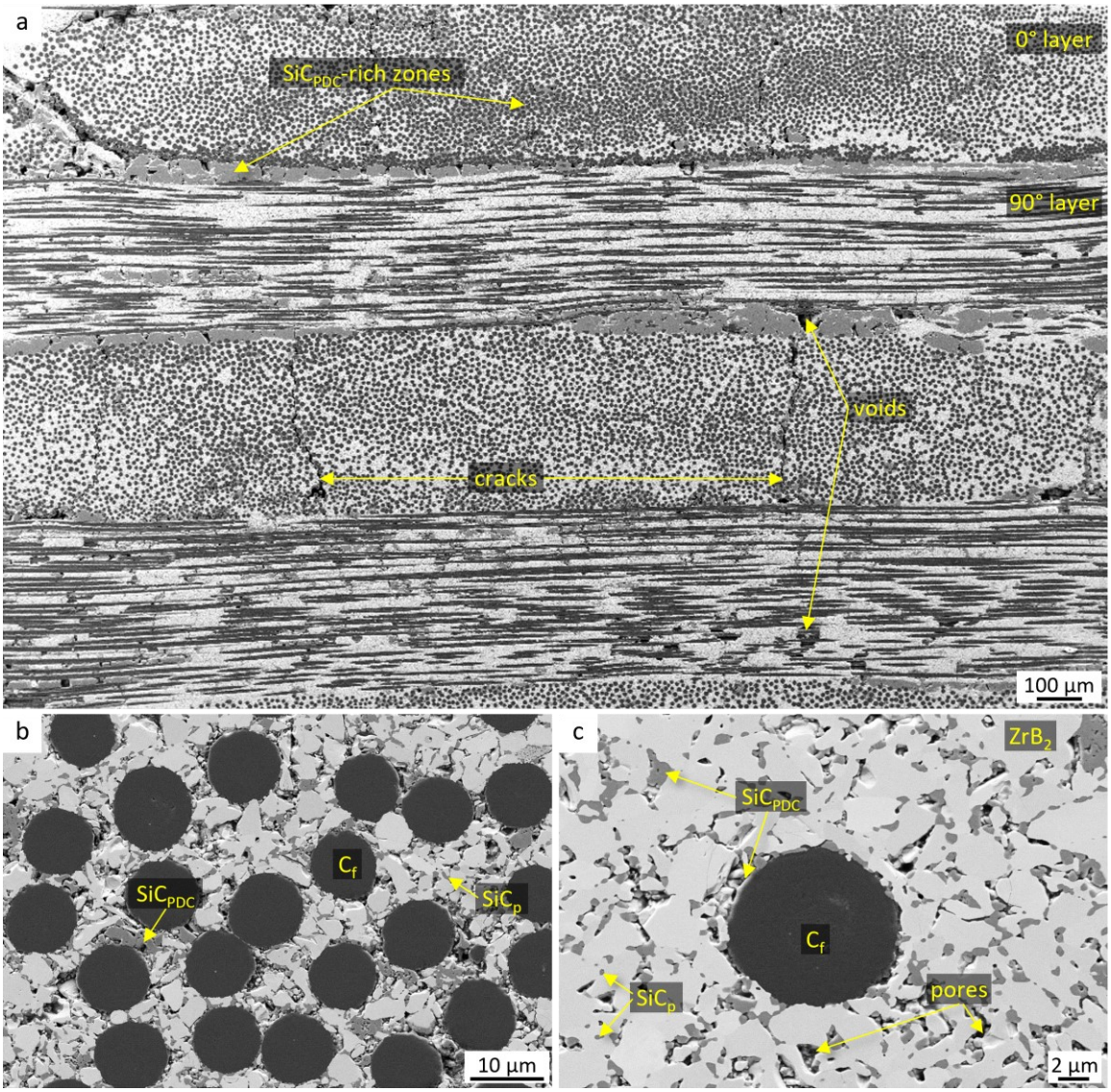

Figure 7.4. Polished sections of PHP sample. (a) General overview at low magnification, (b) microstructure inside bundles; carbon fibres are the dark phase while the light and grey contrasting phases represent ZrB_2 and SiC respectively, (c) detail of a single fibre.

7.3 Mechanical properties vs route A and B

Mechanical properties, i.e. bending strength and fracture toughness at RT and at 1500 °C, are summarized in Table 7.1. Despite the very similar porosities and lower fibre volumetric content, sample PHP showed a better resistance to bending stress.

The RT flexural strength of PHP ranged from 151 to 176 MPa. These values match those of UHTCMCs consolidated by HP. As for HPP, the range of values decreased by over

a half, in the range 53–98 MPa, and matches that of porous UHTCMCs sintered by HP but under milder conditions, 1600–1800 °C [23]. Typical load-displacement curves of each sample tested at RT are reported in Figure 7.5a. The failures were likely caused by a combination opening mode (mode I) and shearing mode (mode II). Indeed, in most of the curves, a drop of the applied load after the maximum value and a subsequent re-loading were shown, suggesting the interlaminar shear involvement to the failure [17,24]. However, at this state of study, it is not clear if (first case) the failure occurred by pure mode I: the fracture propagated from a critical flaw in the tensile surface and then it subjected to delamination phenomena that produced a tortuous path or (second case) damages by mode II occurred before, or together with, the fracture propagation from tensile surfaces. However, it is clear that the lower strength of HPP is due to the lower adhesion of layers.

At 1500 °C, the average values of sample HPP was 230 MPa, ranging from 178 MPa to 282 MPa (Table 7.1). The flexural strength at 1500 °C was again higher for sample PHP (average value of 592 MPa), although it can be noticed that measurements on sample PHP yielded quite a broad range of values, varying it ranged from 503 MPa to 682 MPa. Load-displacement curves of two tested bars at 1500 °C are reported in Figure 7.5b. It confirmed the improvement of mechanical properties with increasing temperature reported in other works on UHTCMCs [25]. This phenomenon is related to the increase of mechanical properties of carbon fibres with increasing temperature [26] and the release of thermal residual stresses caused by rapid cooling step of the manufacturing owing to the thermal expansion coefficient mismatch between fibre and matrix [22].

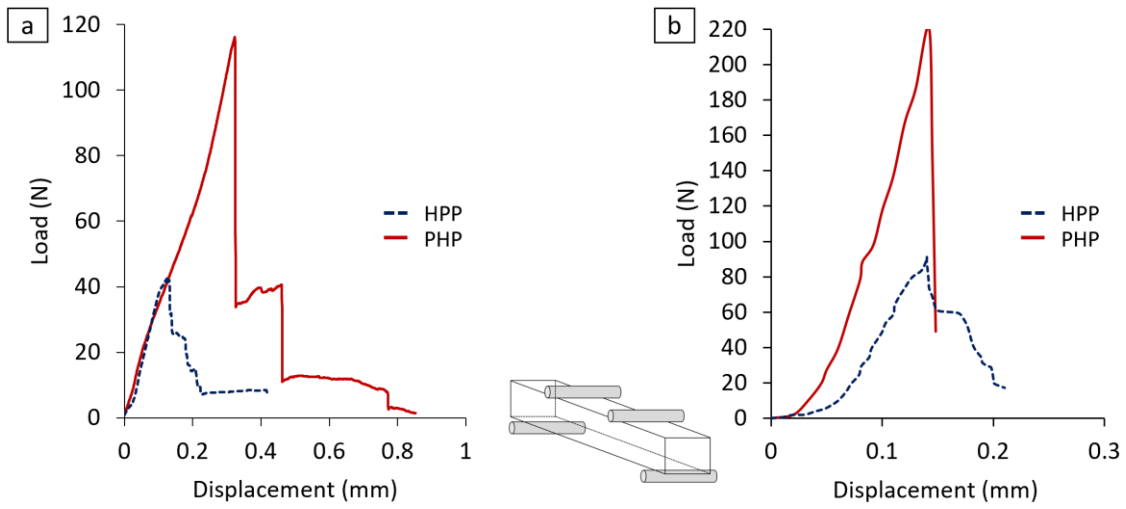

Figure 7.5. An example of 4-point bending strength tests for HPP and PHP samples. Load-displacement curves of bending tests (a) at room temperature and (b) at 1500 °C under Ar flow.

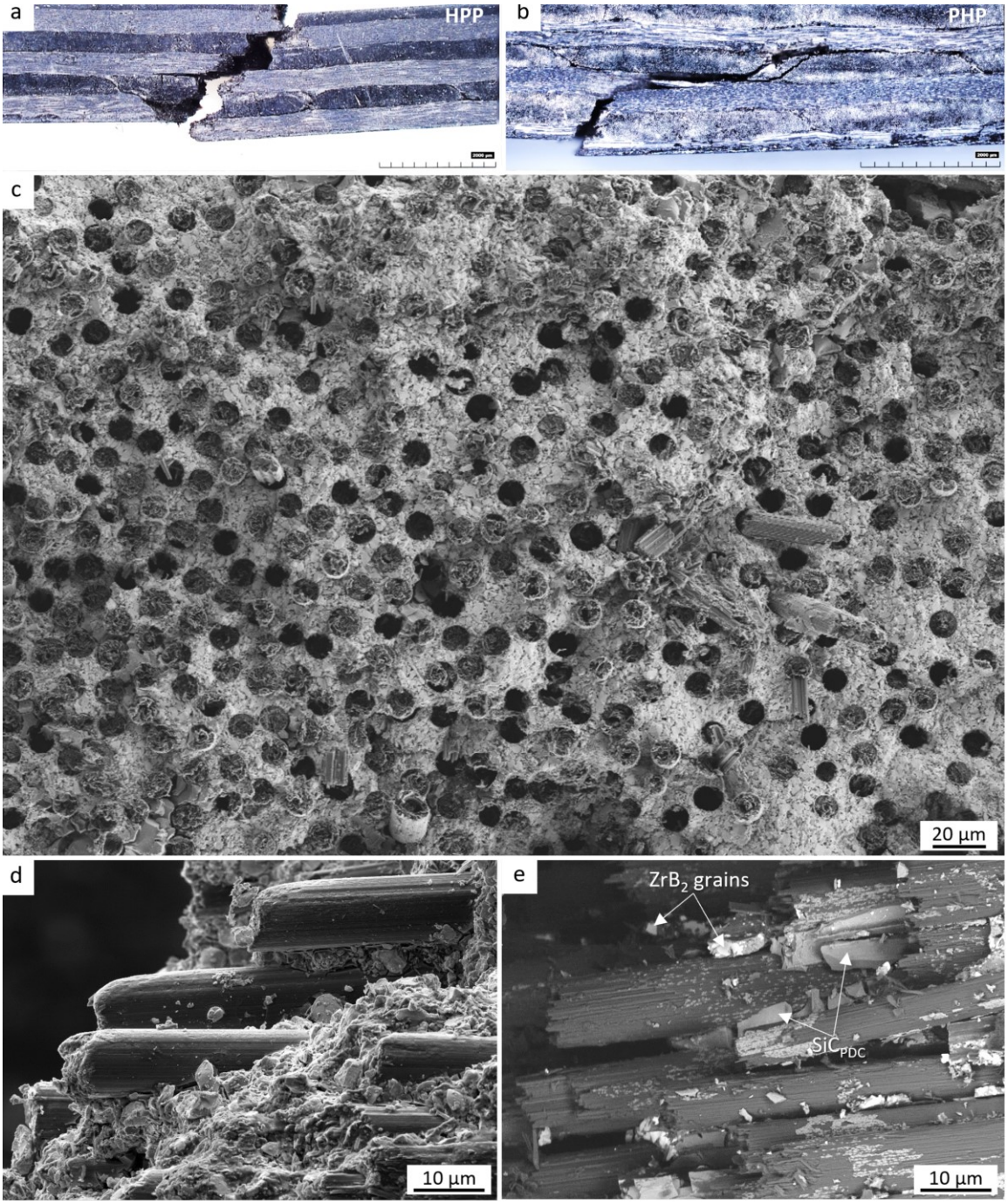

Figure 7.6. (a, b) Optical image of a fractured bars (lateral view) reported as examples of fractures of samples HPP and PHP, respectively. (c, d, e) Examples of fracture surfaces after 4-pt bending strength test at RT of samples HPP and PHP. Fracture surface shown in (d) is predominant in sample HPP, while fracture surface shown in (e) is predominant in PHP.

Figure 7.6 illustrates examples of fracture surfaces of samples HPP and PHP. In Figure 7.6a and Figure 7.6b, the observable cracks in bars (HPP and PHP respectively) tested are shown. Flexural strength of HPP sample was affected by severe delamination due to scarce adhesion between the layers (Figure 7.6a). On the one hand, it should be noted

that both samples did not suffer from the creep as it did for the only PIPed composites in Chapter 4. On the other hand, looking at the fracture surface (Figure 7.6c), a limited fibre pull-out was observed for both samples, if compared to previous only PIPed composites (see Chapter 4). Some examples of fibre/matrix interfaces, after flexural tests, are shown in Figure 7.6d and Figure 7.6e. Surface of fibres of HPP samples was smooth with only some ZrB_2 particles glued on them (Figure 7.6d). Conversely, fibres of PHP had a rough surface and a thin film of SiC_{PDC} surrounding the fibre was detected (Figure 7.6e). The same remarks are valid for surface fractures after bending strength test at 1500 °C.

The average values of fracture toughness evaluated with CNB method are reported in Table 7.1, whilst a comparison of load-displacement curves recorded at RT and 1500 °C is shown in Figure 7.7a and Figure 7.7b. The toughness values of two composites were similar, both at room and at elevated temperature. Differently, the load-displacement curves of CNB tests for sample HPP recorded during test at RT increased sharply to the maximum value, whilst for sample PHP a less steep slope was followed by a gradual descent in a zig-zag pattern, which was attributed to a more stable crack propagation.

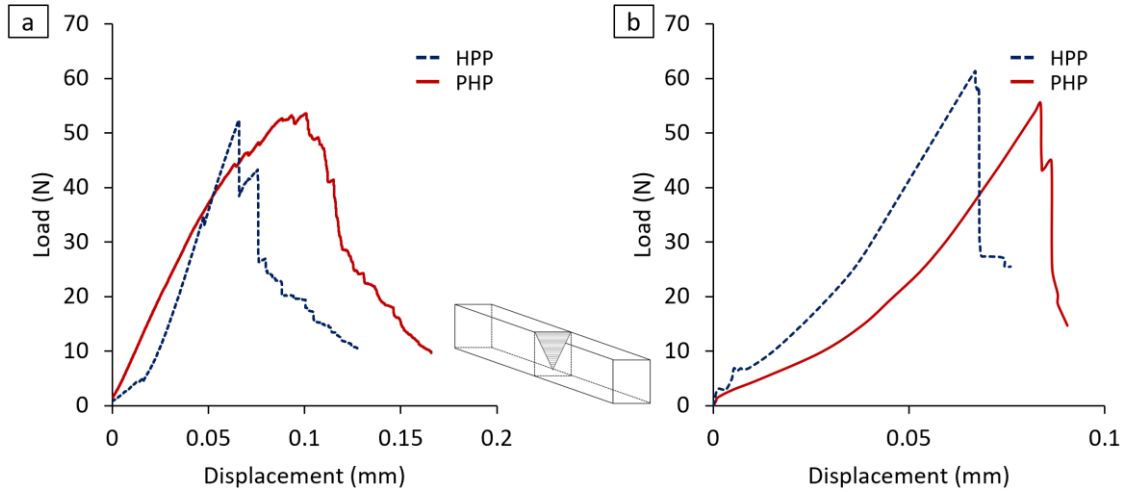

Figure 7.7. An example 4-point bending strength tests of Chevron Notched Beams (CNB) bars of HPP and PHP samples. Load-displacement curves of bending tests (a) at room temperature and (b) at 1500 °C under Ar flow.

The purpose of this work was to obtain indications on the possibility to exploit a hot pressing (HP) cycle as an intermediate or final consolidation step combined with PIP. Sample HPP, where HP precedes the PIP cycles resulted to be more demanding. Indeed, a sintering conducted at too low temperature, e.g. below 1700 °C, would result in no consolidation at all of the preforms, making it impossible to handle pre-sintered samples

for the subsequent PIP cycles. Sintering conducted at a temperature as high as 1850 °C resulted in a rigid skeleton, with defects that were very difficult to infiltrate, as evidenced by the lower amount of SiC in the final composites. Large defects, scarce adhesion between the layers led to delamination and poor mechanical properties. Possible remedies include a better setting of the pre-sintering temperature but finding out the best range seems to be quite challenging.

On the contrary, the post treatment of PIPed samples with hot pressing is a viable solution, because consecutive PIP cycles in a highly porous structure allow to repair the defects created in the green state, during impregnation and pile-up. As a result, the adhesion between the layers and the consolidation were better, which led to a higher mechanical performance.

For both types of composites, the bending strength at room temperature was remarkably lower than for the previous produced PIP composites (6 PIP cycles) (in Chapter 4), which is due to the presence of porosity. However, for PHP sample there is still a good margin for improvement, for instance, increasing the number of PIP cycles or optimizing the final hot pressing cycle, which is not possible for the reverse case. Another interesting benefit of the hot pressing treatment as a final consolidation step is the complete conversion of SiC_{PDC} in crystalline SiC ceramic, which could explain the high value of strength at 1500 °C. A counter effect of hot pressing could be generation of new defects or residual stresses, a feature that needs further investigation. All these issues suggest that this version of the process deserves additional studies and that hot pressing as a post treatment could lead to very interesting results.

7.4 Conclusions

In this paper, carbon fibre-reinforced ZrB_2-based composites were fabricated by powder slurry infiltration and a hybrid process coupling Polymer Infiltration and Pyrolysis (PIP) with Hot Pressing (HP) techniques. Two different routes for the consolidation of the materials were carried out: (a), a pre-sintering cycle by HP at 1850 °C followed by two cycles of PIP at 1000 °C, and vice versa, (b), two cycles of PIP at mild conditions (1000 °C) followed by HP at 1900 °C for 15 min.

This study led to the conclusions that sample PHP obtained by route (b) is the best viable solution between the two ways studied.

C_f/ZrB_2-SiC with C_f content ~34% (0/90° architecture), ZrB_2 content ~32% and SiC content ~22% were achieved. Moreover, improved mechanical properties at elevated temperature of 1500 °C (strength up to 590 MPa and fracture toughness of 7.4 $MPa \cdot m^{0.5}$) and lower number of treatments needed compared to the conventional time-consuming PIP process were found.

7.5 References

1. Zhao, Z., Li, K., Kou, G., Liu, T. & Li, W. Mechanical properties and ablation behavior of C/C-ZrC and C/C-ZrC-SiC composites prepared by precursor infiltration and pyrolysis combined with chemical vapor infiltration. *Ceram. Int.* **44**, 23191–23201 (2018).

2. Zhang, L. *et al.* 3D C_f/ZrC-SiC composites fabricated with ZrC nanoparticles and $ZrSi_2$ alloy. *Ceram. Int.* **40**, 11795–11801 (2014).

3. Maillé, L. *et al.* Manufacturing of ceramic matrix composite using a hybrid process combining $TiSi_2$ active filler infiltration and preceramic impregnation and pyrolysis. *J. Eur. Ceram. Soc.* **34**, 189–195 (2014).

4. Stalin, M., Rajaguru, K. & Rangaraj, L. Processing of C_f/SiC composites by hot pressing using polymer binders followed by polymer impregnation and pyrolysis. *J. Eur. Ceram. Soc.* **40**, 290–297 (2020).

5. Zhang, D. *et al.* Characterization and mechanical properties of C_f/ZrB_2-SiC composites fabricated by a hybrid technique based on slurry impregnation, polymer infiltration and pyrolysis and low-temperature hot pressing. *Ceram. Int.* **45**, 5467–5474 (2019).

6. Lim, K. Y., Kim, Y. W. & Park, J. Y. Fabrication of SiC fiber-SiC matrix composites by reaction sintering. *J. Korean Ceram. Soc.* **45**, 204–207 (2008).

7. Yonathan, P., Lee, J.-H., Kim, H.-T. & Yoon, D.-H. Properties of SiC_f/SiC composites fabricated by slurry infiltration and hot pressing. *Mater. Sci. Technol.* **27**, 257–263 (2014).

8. Dong, S., Katoh, Y. & Kohyama, A. Preparation of SiC/SiC Composites by Hot Pressing, Using Tyranno-SA Fiber as Reinforcement. *J. Am. Ceram. Soc.* **86**, 26–32 (2003).

9. Gu, J. *et al.* Fast fabrication of SiC particulate-reinforced SiC composites by modified PIP process using spark plasma sintering – effects of green density and heating rate. *J. Eur. Ceram. Soc.* **41**, 4037–4047 (2021).

10. Zoli, L. *et al.* Ultra-High Temperature Ceramic Matrix Composites. *Encyclopedia of Materials: Technical Ceramics and Glasses* 340–352 (2021) doi:10.1016/b978-0-12-818542-1.00023-0.

11. Justin, J. F., Julian-Jankowiak, A., Guérineau, V., Mathivet, V. & Debarre, A. Ultra-high temperature ceramics developments for hypersonic applications. *CEAS Aeronaut. J.* **11**, 651–664 (2020).

12. Zhang, D. *et al.* Characterization and mechanical properties of C_f/ZrB_2 -SiC composites fabricated by a hybrid technique based on slurry impregnation, polymer infiltration and pyrolysis and low-temperature hot pressing. *Ceram. Int.* **45**, 5467–5474 (2019).

13. Wang, Z. *et al.* Fabrication and Properties of C_f/SiC-ZrC Composites. *J. Am. Ceram. Soc.* **91**, 3434–3436 (2008).

14. Kannan, R. & Rangaraj, L. Processing and characterization of C_f/ZrB_2-SiC-ZrC composites produced at moderate pressure and temperature. *Ceram. Int.* **43**, 2625–2631 (2017).

15. Kannan, R. & Rangaraj, L. Properties of C_f/SiC-ZrB_2-Ta_xC_y composite produced by reactive hot pressing and polymer impregnation pyrolysis (RHP/PIP). *J. Eur. Ceram. Soc.* **39**, 2257–2265 (2019).

16. Galizia, P., Sciti, D., Saraga, F. & Zoli, L. Off-axis damage tolerance of fiber-reinforced composites for aerospace systems. *J. Eur. Ceram. Soc.* **40**, 2691–2698 (2020).

17. Galizia, P., Sciti, D. & Jain, N. Insight into microstructure and flexural strength of ultra-high temperature ceramics enriched SICARBON™ composite. *Mater. Des.* **208**, 109888 (2021).

18. Starfire® Systems Inc. StarPCS SMP-10. (2018).

19. Kaur, S., Riedel, R. & Ionescu, E. Pressureless fabrication of dense monolithic SiC ceramics from a polycarbosilane. *J. Eur. Ceram. Soc.* **34**, 3571–3578 (2014).

20. Süß, F. *et al.* Combination of PIP and LSI processes for SiC/SiC ceramic matrix composites. *Open Ceram.* **5**, (2021).

21. Delobel, F., Lemonnier, S., Barraud, É. & Cambedouzou, J. Influence of sintering temperature and pressure on the 3C-6H transition of silicon carbide. *J. Eur. Ceram. Soc.* **39**, 150–156 (2019).

22. Galizia, P., Zoli, L. & Sciti, D. Impact of residual stress on thermal damage accumulation, and Young's modulus of fiber-reinforced ultra-high temperature ceramics. *Mater. Des.* **160**, 803–809 (2018).

23. Sciti, D., Natali Murri, A., Medri, V. & Zoli, L. Continuous C fibre composites with a porous ZrB_2 Matrix. *Mater. Des.* **85**, 127–134 (2015).

24. Lin, Y., Liu, C., Li, H., Jin, K. & Tao, J. Interlaminar failure behavior of GLARE laminates under double beam five-point-bending load. *Compos. Struct.* **201**, 79–85 (2018).

25. Sciti, D. *et al.* Properties of large scale ultra-high temperature ceramic matrix

composites made by filament winding and spark plasma sintering. *Compos. Part B Eng.* **216**, 108839 (2021).

26. Sauder, C., Lamon, J. & Pailler, R. The tensile behavior of carbon fibers at high temperatures up to 2400°C. *Carbon N. Y.* **42**, 715–725 (2004).

8. Polymer-derived Si-C-X and ZrC ceramics

8.1 Introduction

This chapter deals with preceramic polymers and organometallic compounds as precursors for the fabrication of advanced ceramics, commonly denoted as polymer-derived ceramics (PDCs). Herein the results of experiments aimed at the improvement of the ceramic yield of PDCs and the development of simple ways to prepare polymer-derived ceramics with higher thermal stability than SiC are collected.

Specifically, the first basic study investigated the effect of catalysts, (such as dicumyl peroxide and trimethyl(methylcyclopentadienyl)platinum(IV), and pre-curing heat treatment on the ceramic yield of commercial allyl-hydrido polycarbosilane (SMP-10, Startfire) to understand its curing and pyrolysis behaviour. Methods and procedures were mostly inspired by previous studies available in the literature [1–3]. SMP-10 was heat-treated below the onset of curing (> 90 °C) and/or mixed with small amounts of the two additives. Final sample masses were recorded to determine yield of ceramic conversion.

The second study was focused on silicoboron carbonitride, due to its superior thermal stability and excellent oxidation resistance, that provide high-temperature self-healing capability exceeding even that of silicon carbide [4,5]. In detail, a tentative of synthesising SiBCN(O) ceramic was carried out by coupling SMP-10 with ammonia borane (BH_3NH_3). Our idea is to exploit the hydroboration reaction between ammonia borane and terminal alkenes. Unlike conventional hydroboration, ammonia (the Lewis base) is not dissociated from the boron centre. Other alkenes selectively provided ammonia-trialkylborane complexes, see ref.[6]. The as-prepared precursor and obtained ceramic were analysed to identify chemical composition and microstructural features.

Zirconium carbide (ZrC) has been of great interest for many high-temperature applications, including rocket nozzles and thrust chambers in space propulsion systems [7,8]. Thus, finally, a simple route was proposed for the synthesis of polymer precursors for ZrC, using zirconium tetrachloride ($ZrCl_4$) as zirconium source and three different carbon sources: two phenolic resins and a type of bitumen. As obtained organometallic compounds were heat treated up to 1800 °C to achieve ZrC. The pyrolysis behaviour and structural evolution of the carbon sources and the prepared precursors were analysed.

8.2 Effect of catalysts and pre-curing heat treatment on the ceramic yield of allyl-hydrido polycarbosilane

The different catalysts tested, pre-curing treatment on the commercially available allyl-hydrido polycarbosilane (SMP-10), here labelled as SMP, and resulting yield of conversion of precursor-to-ceramic are summarised in Table 8.1. The detailed description of the mixing of catalysts and SMP, their manipulation and pre-curing treatments are reported in Chapter 3 – Section 3.2.2.

Table 8.1. Yield of SiC ceramics prepared using allyl-hydrido polycarbosilane, as-received or additivated with catalysts and/or heat-treated before curing.
DCP: dicumyl peroxide, $MePtCpMe_3$: trimethyl(methylcyclopentadienyl)platinum(IV).

Sample code	Heat treatment	Catalyst		Ceramic yield
	T (°C), time (h), Pressure (mbar)	type	wt%	%
SMP	-	-	-	63
SMP_1DCP	-	DCP	1	83
SMP_1Pt	-	$MePtCpMe_3$	1	82
SMP_HT	90 °C x 5 h, vacuum	-	-	74
SMP_HT_1Pt	90 °C x 5 h, vacuum	$MePtCpMe_3$	1	79

As-received SMP (Table 8.1) experienced a ceramic yield of about 63%, which was lower than the yield range stated in supplier datasheet [9] (i.e. 72–78%). In agreement with it, several TGA studies [10–15] reported for SMP-10 pyrolysed at temperature above 900 °C yield values comprised in the range 72–77%. However, King et al. [2] found that different lots of as-received SMP-10 showed variability as much as several percentage points in SiC mass yield.

- Addition of catalysts. The added catalysts were DCP and $MePtCpMe_3$, which were selected because two distinct mechanisms of polymerization are involved: radicals and hydrosilylation, respectively. As expected, with the addition of catalysts SMP-10 achieved higher ceramic yields, over 80% both with 1 wt% DCP and $MePtCpMe_3$ (Table 8.1), in line with the valued reported in the literature [1,11]. Indeed, it is well known that DCP and $MePtCpMe_3$ induce cross-linking in polycarbosilane and polysilazane systems [16–24], resulting in an increase of ceramic yield.

DCP acts as a radical initiator, releasing cumyloxy free radicals, which react with vinyl double bonds thus forming macromolecular free radicals (Figure 8.1a), that will continue

to react with other vinyl double bonds and form $-CH_2-$ bridges [23]. According to the literature [18], this reaction takes place at a temperature between 105 and 250 °C for SMP-10 with addition of a peroxide cure initiator.

Pt-based compounds catalyses the self-hydrosilylation reaction among SiH_x and C=C groups [25–27] (Figure 8.1b). Hydrosilanes are inert concerning unsaturated functional groups. The reaction is possible only under UV exposure, high temperature, or the presence of a catalyst, for instance Pt organometallics are particularly effective in promoting this reaction. The classical mechanism, proposed by Chalk and Harrod [28] in the 1960s, includes the formation reaction of the active form of the catalyst. It represents a complex of platinum with an alkenyl functional group, which undergoes several transformations in the catalytic cycle described in Figure 8.1c.

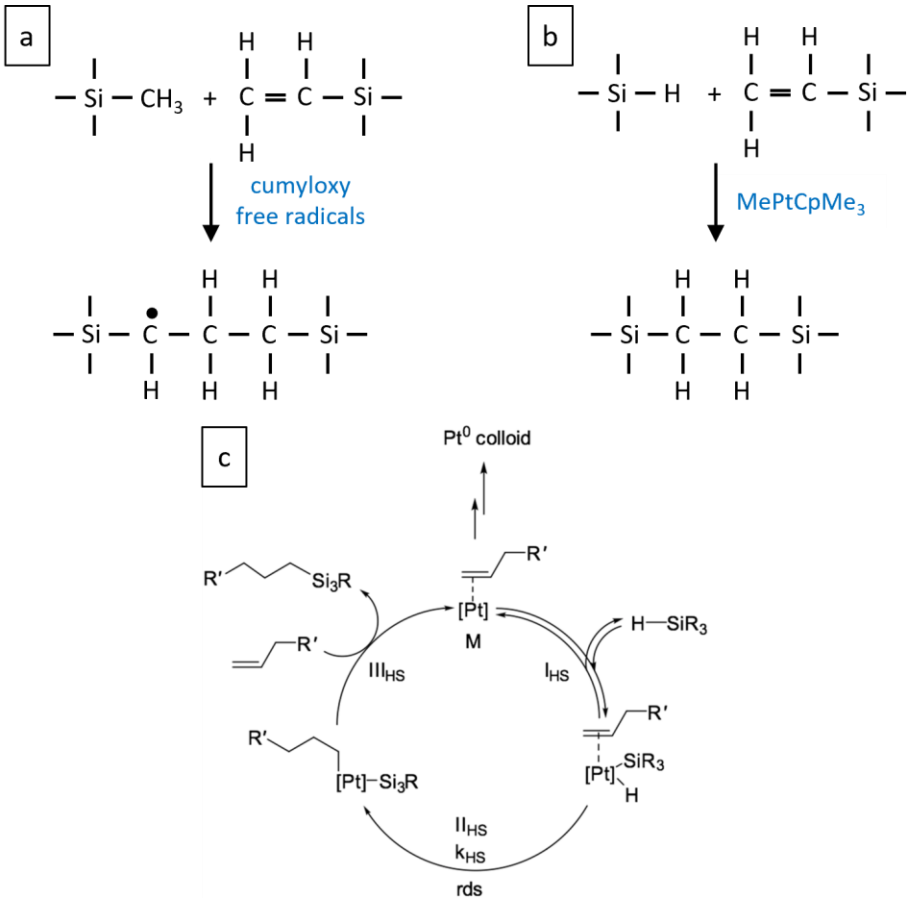

Figure 8.1. Reactions induced by cross-linking agents: a) free-radical polymerization induced by DCP initiator, b) hydrosilylation induced by $MePtCpMe_3$ catalyst. (c) The Chalk-Harrod mechanism of hydrosilylation reaction of alkenes [28].

The Figure 8.2 shows ATR-FTIR spectra of as-received liquid SMP-10 and SMP-10 with 1 wt% additive after curing at 300 °C for 4 h (SMP_1DCP reported as example).

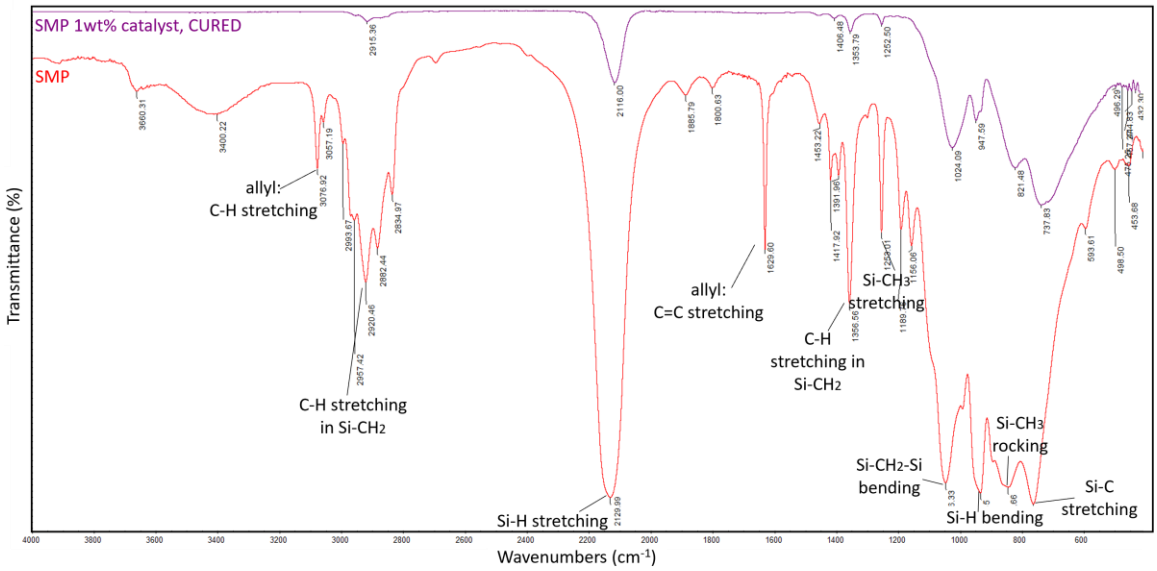

Figure 8.2. ATR-FTIR spectra of as received liquid SMP-10 (sample SMP) and cross-linked SMP-10 with 1 wt% catalyst (SMP_1DCP reported as an example) by curing at 300 °C.

FTIR spectrum of the liquid SMP displays strong bands at about 2130 and 933 cm^{-1} which were attributed to Si–H bond stretching and Si–H bond bending respectively, while the bands at 3077 and 1630 cm^{-1} were assigned to the allyl groups [10,29–31]. As obvious, there is a large excess of Si–H groups respect to the amount of allyl groups. As the polycarbosilane was thermally treated at the curing temperature, the cured sample showed the decrease of the peaks corresponding to Si–H. Moreover, the allyl bands disappeared because vinyl polyaddition is promoted with regard to dehydrogenation [10]. This indicates that hydrosilylation reaction was involved in the curing process because DCP avoided the formation of Si–Si bonds through uncontrolled reactions , thus leading to a high cross-linking degree of the preceramic polymer [10].

- Pre-curing heat treatment. Thermal treatments were carried out holding SMP-10 at 90 °C for 5 h under vacuum. The vacuum atmosphere was applied to assist with removal of low molecular weight oligomers, prior to curing which was determined to be as low as 100 °C [2]. The heat-treated SMP-10, SMP_HT sample, appeared as a darker amber-coloured inviscid liquid in comparison with as-received SMP-10 (Figure 8.3).

Figure 8.3. Polycarbosilane SMP-10 after heat treatment at 90 °C.

During heat treatment, a change in mass of about -0.6% was measured. Of the 0.6%, ~0.2% was lost from the start until 50 °C, and the remaining mass loss was observed to occur mostly at 90 °C within 1 h, then slowed over time but continued throughout the entire dwell. Such mass loss was attributed to the volatilization of low molecular weight (MW) oligomers, since it was demonstrated that they can be driven off thermally while the polycarbosilane is in a liquid state. However, King et al. [2] measured higher mass losses during hold of SMP-10 at 90 °C; this may depend on variability of MW oligomer distribution in the polycarbosilane as well as experimental settings, storage conditions and ageing. The release of volatile corresponds to higher cured mass yield, which enhances SiC mass yields [2,3,32]. The ceramic yield of the heat treated SMP-10 without any addition of cross-linking agent or further modifications was 74% (sample SMP_HT in Table 8.1), resulting in an increase of about 11% compared to as-received SMP-10.

The as-received SMP-10 and pre-treated SMP_HT sample were investigated by means of ATR-FTIR spectroscopy (Figure 8.4).

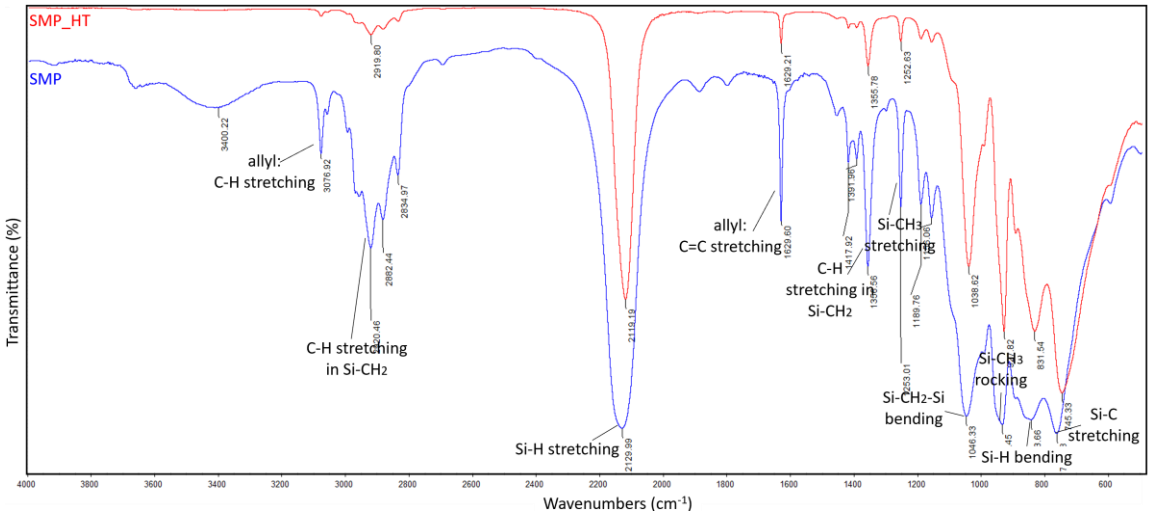

Figure 8.4. ATR-FTIR spectra of liquid SMP-10, as received (SMP) and upon pre-treatment at 90 °C (SMP_HT).

The sample SMP_HT upon heat treatment up to 90 °C with a total dwell of 5 h contained weaker bands associated to Si–CH_2 and Si–CH_3 bonds, which corroborates the release of low MW macromolecules [2,3,32]. A decrease of the peak intensity for allyl groups was observed at 3077 and 1630 cm^{-1}. Hence, despite the intrinsic nonuniform low MW distribution of SMP-10, we can speculate why the ceramic yield of SMP_HT_1Pt was lower than that of SMP_1DCP and SMP_1Pt.

It is worth to note that low MW species are in significant amounts in commercial preceramic polymers to improve the low viscosity for the purpose of composite infiltration [33–35]. Rheologic measurements revealed a dynamic viscosity at room temperature of 125 MPa·s for SMP_HT, which was higher than that of as-received SMP-10 (i.e. 77 MPa·s corresponding to a kinematic viscosity of about 77 cSt, in agreement with supplier datasheet [9]). Despite the higher viscosity, SMP-10 subjected to pre-treatment at 90 °C was demonstrated suitable for PIP processing on fibre-reinforced UHTCMCs (not shown).

By combining pre-treatment at 90° C for 5 h under vacuum and the subsequently addition of 1wt% $MePtCpMe_3$, SMP-10 exhibited a further increase in ceramic yield up to 79% (sample SMP_HT_1Pt in Table 8.1), but still lower than that of samples SMP_1DCP and SMP_1Pt, in which catalysts were added to as-received SMP-10. Hence, thermal treatments can represent a potential payoff for the improved yield of polymer ceramic precursors whether the use of cross-linking agents wants to be avoided. However, these seem detrimental on SiC yield in the case of polymer catalyst are added.

8.3 Boron and nitrogen incorporation on the phase composition of polymer-derived SiC

8.3.1 Summary of the process

A tentative synthesis of a siliconboron carbonitride polymer-derived ceramic was carried out coupling the commercially available allyl-hydrido polycarbosilane SMP-10 and ammonia borane (AB) via hydroboration reaction, see the resulting products obtained by the main processing steps (Figure 8.5).

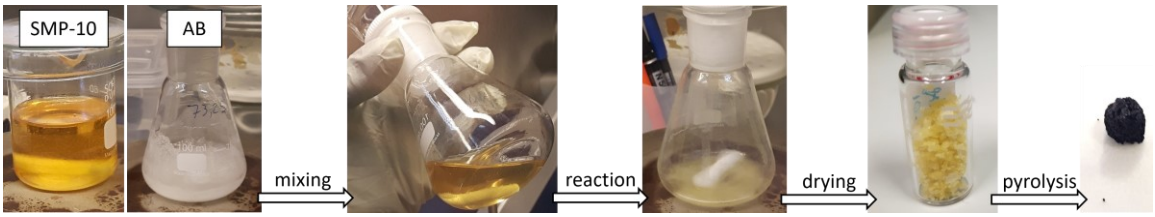

Figure 8.5. Scheme of the processing and resulting synthesis products until SiBCN(O) ceramic formed: 1) starting materials: pure SMP-10 and solution in THF containing ammonia borane (AB), 2) SMP-10 and AB solution after mixing (evolution of gases), 3) solution after heating under THF reflux for 30 min, 4) solid single-source precursor upon drying, 5) SiBCN(O) ceramic after pyrolysis at 800 °C for 12 h.

8.3.2 Synthesis of single source precursor of SiBCN(O)

AB and SMP were mixed following the procedure described in in the experimental part (Chapter 3 – Section 3.2.3). The Si:C:B:N atomic ratio and different time and temperature of the hydroboration, and resulting yield of conversion of precursor-to-ceramic are summarised in Table 8.2.

Table 8.2. Samples obtained via reaction between SMP-10 and AB solution. Si:C:B:N Atomic ratio, different conditions of hydroboration reaction and pyrolysis, resulting yield of ceramics.

Label	Si:C:B:N atomic ratio	Hydroboration		Pyrolysis	Yield
		T (h)	T (°C)	T (°C), t (h)	(%)
SMP_AB, 0.25h	1:1:1:1	0.25	RT	*	-
SMP_AB, 2h	1:1:1:1	2	RT	*	-
SMP_AB, 4h	1:1:1:1	4	RT	*	-
SMP_AB, R0.5h-P0.5	1:1:1:1	0.5	66 °C	800, 0.5	89
SMP_AB, R0.5h-P12	1:1:1:1	0.5	66 °C	800, 12	88

* not pyrolysed

Unlike pure SMP-10 that should remain in a liquid state if treated at 100 °C even for long time [2], boron- nitrogen- modified polycarbosilane upon heat treatment for few minutes (about 30 min) underwent rapid solidification and converted in a rubbery solid with light yellow appearance (Figure 8.5). As reported by Kaur et al. [11] that prepared SiBC via hydroboration of SMP-10 with borane dimethyl sulfide complex, the incorporation of boron in polycarbosilane strongly affected the cross-linking behaviour. Indeed, the hydrocoupling reactions of Si–H units in the boron-modified precursor were shown to be activated already at temperatures as low as 100 °C, resulting in a high cross-linking degree [11]. Consequently, the ceramic yield of SiBCN(O) ceramic upon pyrolysis at 800 °C for 12h

was found significantly higher (~88%) compared to the SiC mass yield typically reached from the boron-free SMP-10 (72–78% [9]) and was similar to the result obtained by Weinmann et al. [36] via pyrolysis of boron-modified polysilazanes.

Hydroboration, hydrosilylation and dehydrocoupling are the three main mechanisms (see reactions schematized in Figure 8.6a) that likely contributed to the formation and subsequent thermal cross-linking of boron- nitrogen- modified polycarbosilane precursor.

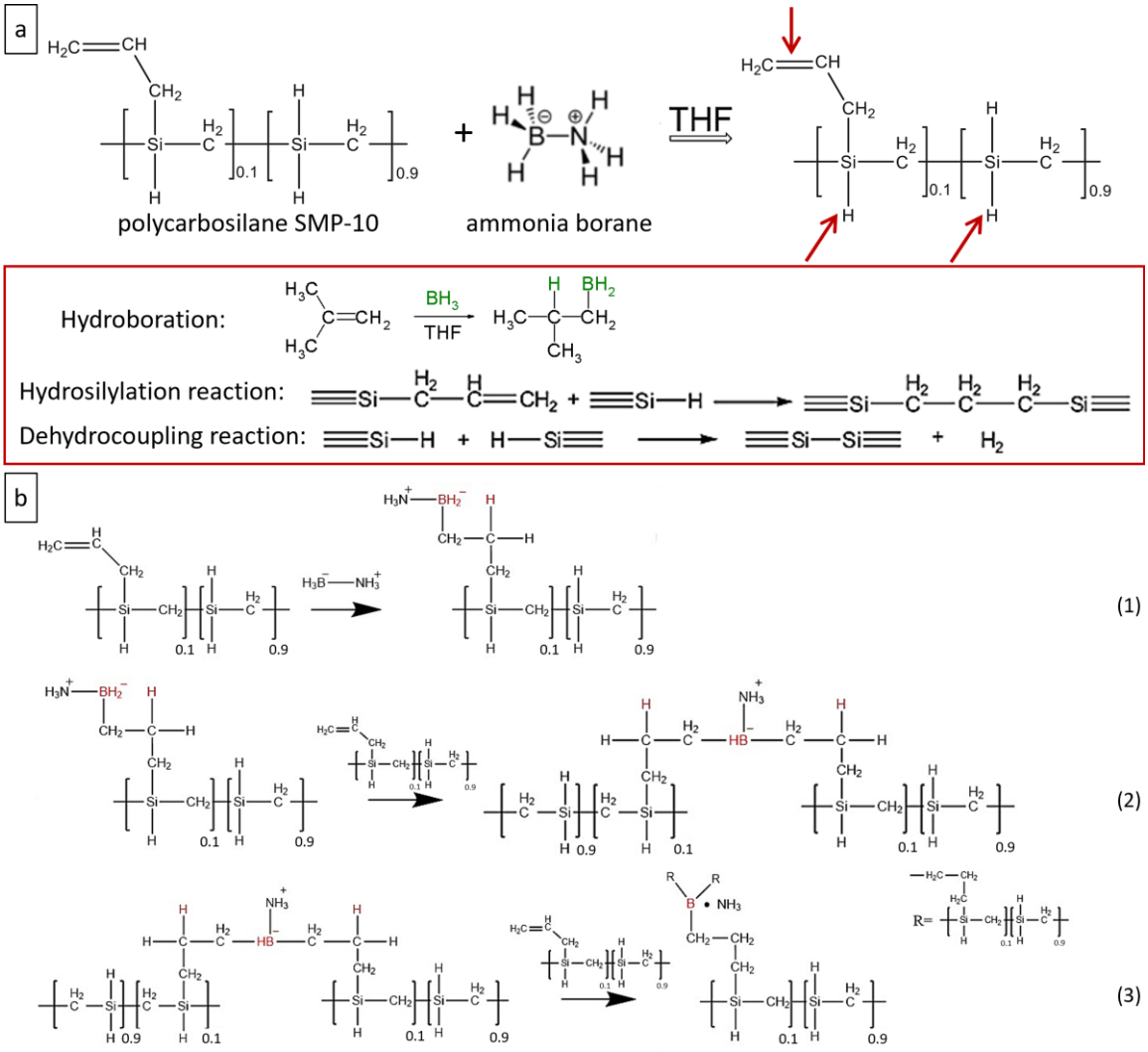

Figure 8.6. (a) Possible reaction pathways for the synthesis and thermal cross-linking of boron- nitrogen-modified polycarbosilane: hydroboration reaction between BH_3 group of AB and allyl groups of SMP-10, hydrosilylation and dehydrocoupling reactions involving Si–H/C=C and Si–H/ Si–H respectively that contributed to cross-linking of SMP-10 chains. (b) Hypothesized hydroboration sequence (reactions (1), (2) and (3)) that leads to ammonia-trialkylborane complexes.

In literature [11,30,31,37], it is well known that the incorporation of boron within the network of allyl-hydrido polycarbosilane is achieved upon hydroboration reactions of the allyl groups. In this study, ammonia borane was used for hydroboration purpose, that is expected to occur through the reaction (1) due to the reaction between a B–H bond and C=C group. When ammonia borane hydroborates allyl group, unlike conventional hydroboration, ammonia (the Lewis base) is not dissociated from the boron centre and is retained in the product. This leads to the formation of ammonia-trialkylborane complexes from terminal alkenes [6]. Hence, it could be speculated that hydroboration reaction between SMP-10 and AB proceeds following the sequence of reactions (2) and (3).

The structural evolution of the prepared single-source polymer precursor for SiBCN(O) was investigated by ATR-FTIR (Figure 8.7) before and after curing and pyrolysis. The resulting FTIR spectra of samples SMP_AB,0.25h, SMP_AB,4h, and SMP_AB,R0.5h (before pyrolysis) were compared with those of the two starting materials (Figure 8.7a).

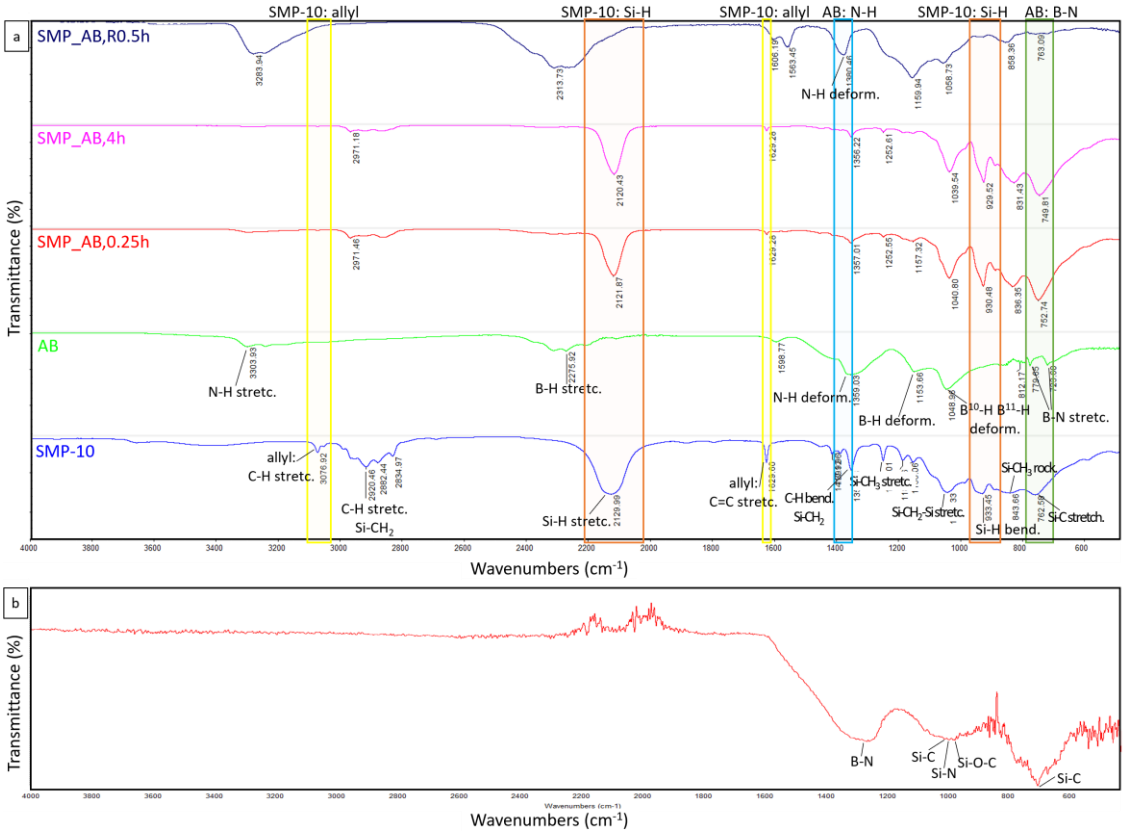

Figure 8.7. ATR-FTIR spectra of (a) starting materials: liquid SMP-10 and solution of ammonia borane (AB), and precursor synthesised after 0.25 and 4 h, and heat-treated at 66 °C for 30 min. The areas in yellow and orange highlight absorption peaks of SMP-10 due to allyl and silane groups, respectively, while blue and green areas highlight N-H and B-N bond of AB; (b) SiBCN(O) ceramic upon pyrolysis at 800 °C for 12h.

The ATR-FTIR spectrum of the liquid SMP-10 shows an absorption band at about 2130 cm^{-1} that was assigned to silane (Si–H) groups, and bands at 3077 and 1630 cm^{-1} attributed to C–H stretching and C=C stretching in allyls groups, respectively. These latter have lower intensity due to the low amount of allyl moieties (ranging from 5 to 10 vol% [10,11]), see SMP-10 formula in Figure 8.6. Absorption bands associated with Si–CH_2, Si–CH_3, Si–CH_2–Si, Si–C vibrations [31,38–43] are observable at around 2920 cm^{-1} and at low-wavenumber region ranging from 1500 to 600 cm^{-1}.

ATR-FTIR spectrum of the pristine AB displays typical peaks in the range 3400–3100 cm^{-1} assigned to N–H stretching vibrations (see three large peaks around 3300, 3250 and 3180 cm^{-1} in Figure 8.7a) and peaks near to 2276 cm^{-1} assigned to B–H stretching modes. At low wavenumbers, peaks at 1600 and 1360 cm^{-1} are associated to N–H bond deformation, while the pair of partially resolved peaks at 1154 and 1049 cm^{-1} were attributed to B–H deformations; peaks around 780 and 723 cm^{-1} are likely due to B–N stretching and N–B–H rocking modes, respectively [44–47].

In the ATR-FTIR spectrum collected on the product after 15 min of stirring at room temperature SMP-10 and AB (see sample SMP-10_AB,0.25h in Figure 8.7a), absorption peaks with low intensity for allyl groups are visible, indicating that hydroboration reaction occurred [11] under these conditions, but not to completion. Some changes are also observable in the absorption bands in the region 1400–800 cm^{-1} due to overlapping of signals associated to C–H, Si–CH_3, Si–CH_2–Si bonds of the polycarbosilane and those for B–H and N–H bonds of the AB. High intensity peaks corresponding to Si–H are still present, implying that hydrosilylation and dehydrocoupling did not occur or occurred very limitedly.

The spectrum registered after 4 h, sample SMP_AB,4h remains unchanged (Figure 8.7a). Hence, it could be possible to incorporate more boron in the structure of SMP-10. An accurate titration of allyl groups into SMP-10 could be necessary to add the sufficient amount of AB to have a complete reaction.

The rubbery solid obtained by heat treatment under THF reflux at 66 °C exhibited a different spectrum, in which absorption bands derived to AB became more obvious. The disappearance of the bands associated to the allyl groups (3077 and 1630 cm^{-1}) suggests that hydroboration reaction between them and BH_3 groups went to completion. The

absorption peak corresponding to Si–H stretching (2130 cm^{-1}) almost vanished, showing a markedly lower intensity broad signal. This fact demonstrates that dehydrocoupling reaction happened by heating at temperature as low as 66 °C although it generally starts at higher temperature (e.g. 300 °C) [10,11], thus leading to a rapid cross-linking. Also, the N–H and B–H stretching mode peak position shifted decreasing slightly compared to the pristine AB case. this can be explained by the loss of the high symmetry stretching modes in ammonia borane toward a $-[HN=BH]_n-$ type chemical structure [46]. The presence of N–H peaks is in accordance with the finding from Frueh et al. [46] that the activation of the dehydrocoupling reaction between Si–H and N–H proceeds at temperature above 120 °C.

Spectra of SiBCN(O) ceramic obtained by pyrolysis of the precursor at the temperature of 800 °C for 30 min and 12h were very similar, Figure 8.7b reports that of the sample pyrolysed for 12h as example (SMP_AB,R0.5-P12 sample label). No peaks corresponding to Si–H, B–H and N–H bands, meaning that the hydrocoupling reactions (Si–H/ Si–H, Si–H/ N–H, N–H/B–H) were completed. Moreover, the disappearance of the bands due to C–H highlights the decomposition of organic groups during ceramic conversion. Resulting absorption peaks are assigned to B–N (1300 cm^{-1}), Si–C (1095 and 760 cm^{-1}), Si–O–C (1000 cm^{-1}) and likely to Si–N (1050 cm^{-1}) [44–49].

SiBCN(O) prepared through pyrolysis at 800 °C (both for 30 min and 12 h) was also studied by XRD. Both samples were amorphous and generated only broad scattering profiles (Figure 8.8). The hump detected between 60 and 70° was typically attributed to β-SiC obtained by pyrolysis of SMP-10, while the signal at around 26° could be due to hexagonal boron nitride (h-BN) [50].

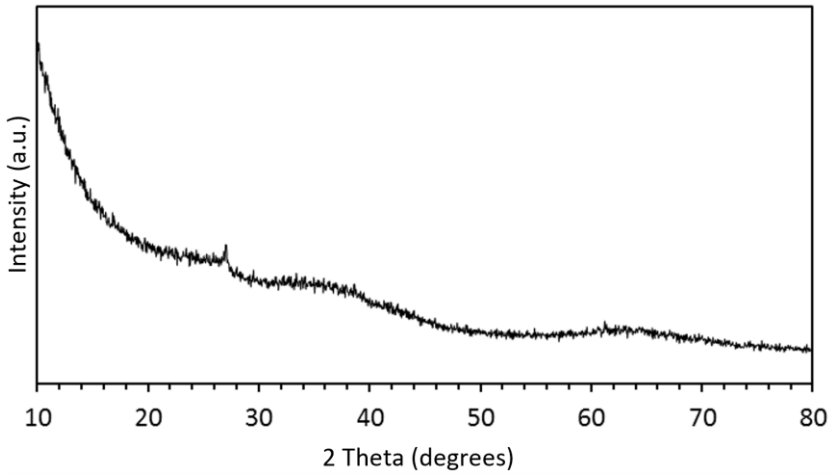

Figure 8.8. XRD pattern of amorphous SiBCN(O) obtained by pyrolysis at 800 °C for 12 h.

8.3.3 Microstructure

Regardless of the difference in pyrolysis time, the microstructure of as obtained samples are very similar to each other, indicating that the obtained ceramics are stable at 800 °C. An example of microstructure is shown in Figure 8.9. As expected, the material is amorphous and EDS analysis confirmed the incorporation of boron and nitrogen in SiC(O) ceramic (EDS signals: B, C, N, O, Si, see inset in Figure 8.9a).

However, back scattered electron (BSE) detector revealed compositional inhomogeneity. Figure 8.9b shows a region of sample mainly constituted of BN(O) (dark phase) comprising isolated SiC(O) areas (bright phase), which are clearly distinguishable due to the contrasting shades. Conversely, on the same sample it could also be observed regions almost entirely composed of glassy SiC(O) containing small BN(O)-rich areas (Figure 8.9c-e).

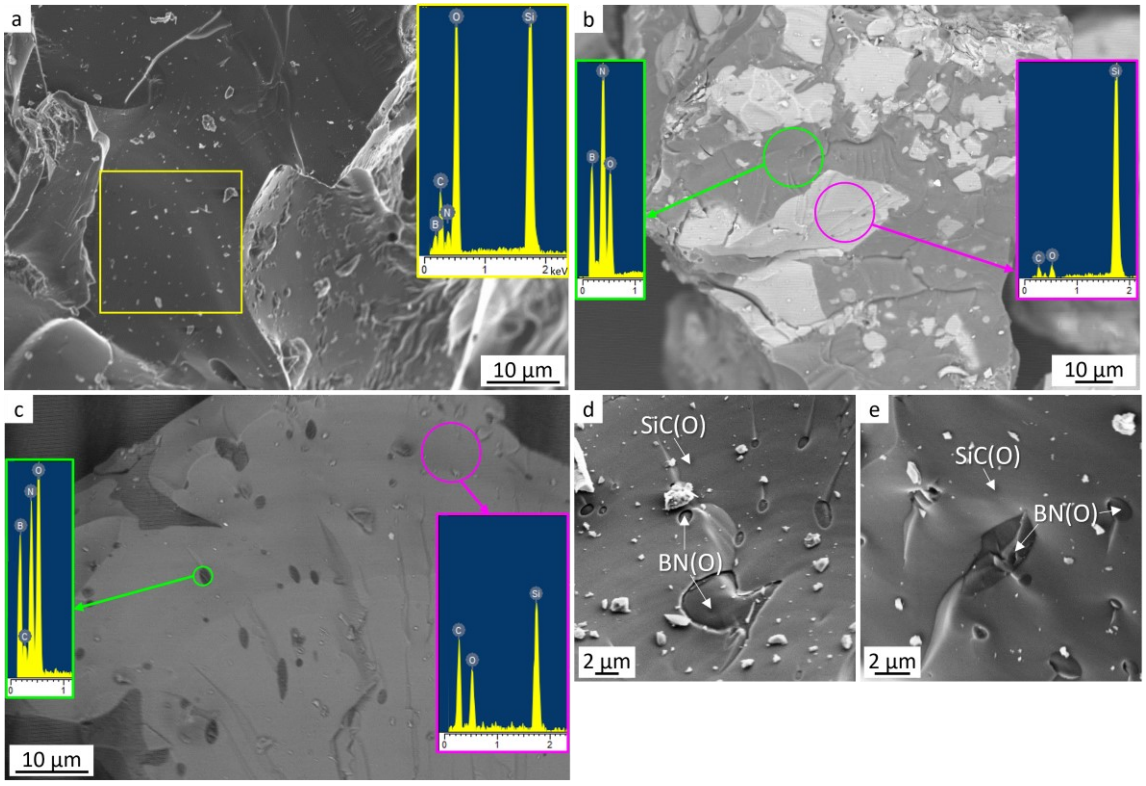

Figure 8.9. SEM micrographs of the surface of pieces of SiBCN(O) after pyrolysis at 800 °C for 12 h. (a) Overview at low magnification; EDS spectrum (collected in yellow squared area) revealing the incorporation of boron and nitrogen in SiC(O). (b) BSE image of a minor sample region constituted mainly by BN(O) and SiC(O) areas. (c) BSE image of a sample region constituted mainly by SiC(O) and BNO-rich areas. Insets in (b) and (c) are respective EDS of the marked spots. (d,e) SE images highlighting BNO-rich inclusions in glassy SiC(O).

Further investigations are needed to explain such inhomogeneities, however several hypotheses may be advanced:

a) As the borane only reacts with the allyl groups, the approximate boron contents in borane-modified SMP-10 with 5–30 wt% borane complexes was estimated 0.98–1.27 wt% respectively [11]. Hence in this work, an ammonia borane excess very likely was still present in the mixture.
b) During the pyrolysis step, excess ammonia borane could begin to decompose releasing H_2, thus leading to polymeric $-[HN=BH]_n-$ species at 130 °C and boron nitride at high temperature [46] (see reaction in Figure 8.10).

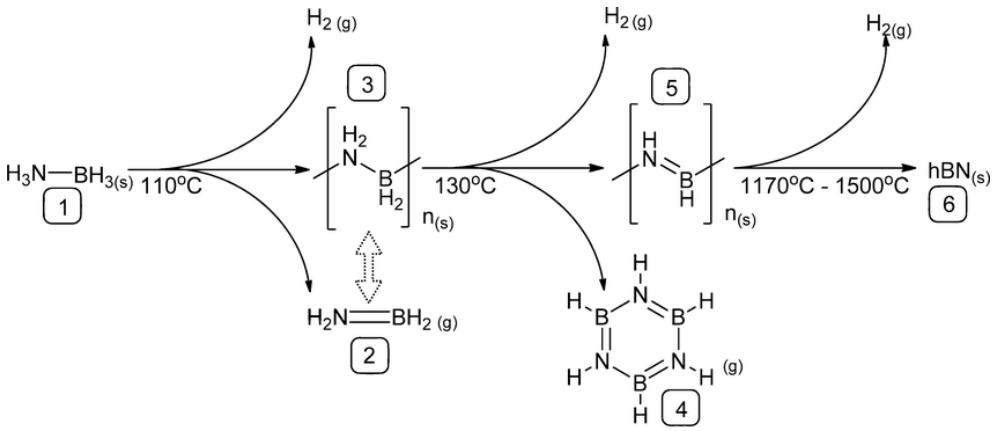

Figure 8.10. Pyrolytic decomposition of ammonia borane to boron nitride [46].

c) In literature, these morphologies are typically reported in case of polymer blends where coalescence of freshly formed droplets gains importance as the probability of collision increases [51].

However, further investigations are needed to understand these phenomena, because compositional inhomogeneities play a critical role in the application or not application of polycarbosilane-ammonia borane adducts as single-source precursors for SiCBN(O).

8.4 Carbothermal synthesis and pyrolysis behaviour of polymer precursors for ZrC powders

8.4.1 Summary of the process

In this work, a series of ZrC precursors were prepared using zirconium tetrachloride ($ZrCl_4$) as zirconium source and three different carbon sources: two phenolic resins and a type of bitumen. The carbon sources were pyrolysed at 1000 °C to determine the yield of

conversion into carbon and analysed by SEM/EDS. Considering the conversion yields, the phenolic resins and bitumen were mixed with $ZrCl_4$ via a THF-based solution. For comparison, Zr and C precursors were also mixed via dry-method. The pyrolysis behaviour and structural and compositional evolution at 1000, 1400, 1600 and 1800 °C were investigated by means FTIR, TG-DSC and XRD. Details of the carried-out syntheses and characterization are reported in experimental part (Chapter 3 – Section 3.2.4).

8.4.2 Carbon precursors

Optical pictures of the used carbon sources are shown in Figure 8.11a. The curing of novolac-type liquid phenolic resin BAKELITE® PF 8978 FL 01 formed a brownish rubbery solid, which was ground into small pieces (< 1 mm). A glass-like orange powder and a black powder were prepared by grinding raw phenolic resin GP® 2074 and bitumen pellets, respectively (Figure 8.11b) with an agate mortar. From this point forward, carbon sources will always be intended as ground powders and they will be labelled as resin PF, resin GP and bitumen for convenience.

Solubility tests on resin PF confirmed the nature of the thermoset solid, which was insoluble in the most common solvents (e.g. water, ethanol, acetone, THF, cyclohexane, petroleum ether) and infusible. Conversely, resin GP was easily solved in THF at room temperature. For the liquefaction of bitumen, a THF/cyclohexane mixture (solvent ratio 1:1) was effective in dissolving most of the fractions. This finding was in agreement with studies in the literature, which report that the bitumen recovery increases with the solvent aromaticity [52] and with the use of a composite solvent compared to a single solvent [53].

The pyrolysis reaction led to the conversion into amorphous carbon of both resins and bitumen. Resin PF generated a dark porous pellet (Figure 8.11c), which may have been obtained by shrinkage and adhesion of starting granules. Resin GP and bitumen produced highly porous silver-grey samples (Figure 8.11c), likely due to the melting at low temperature of novolac and bituminous products.

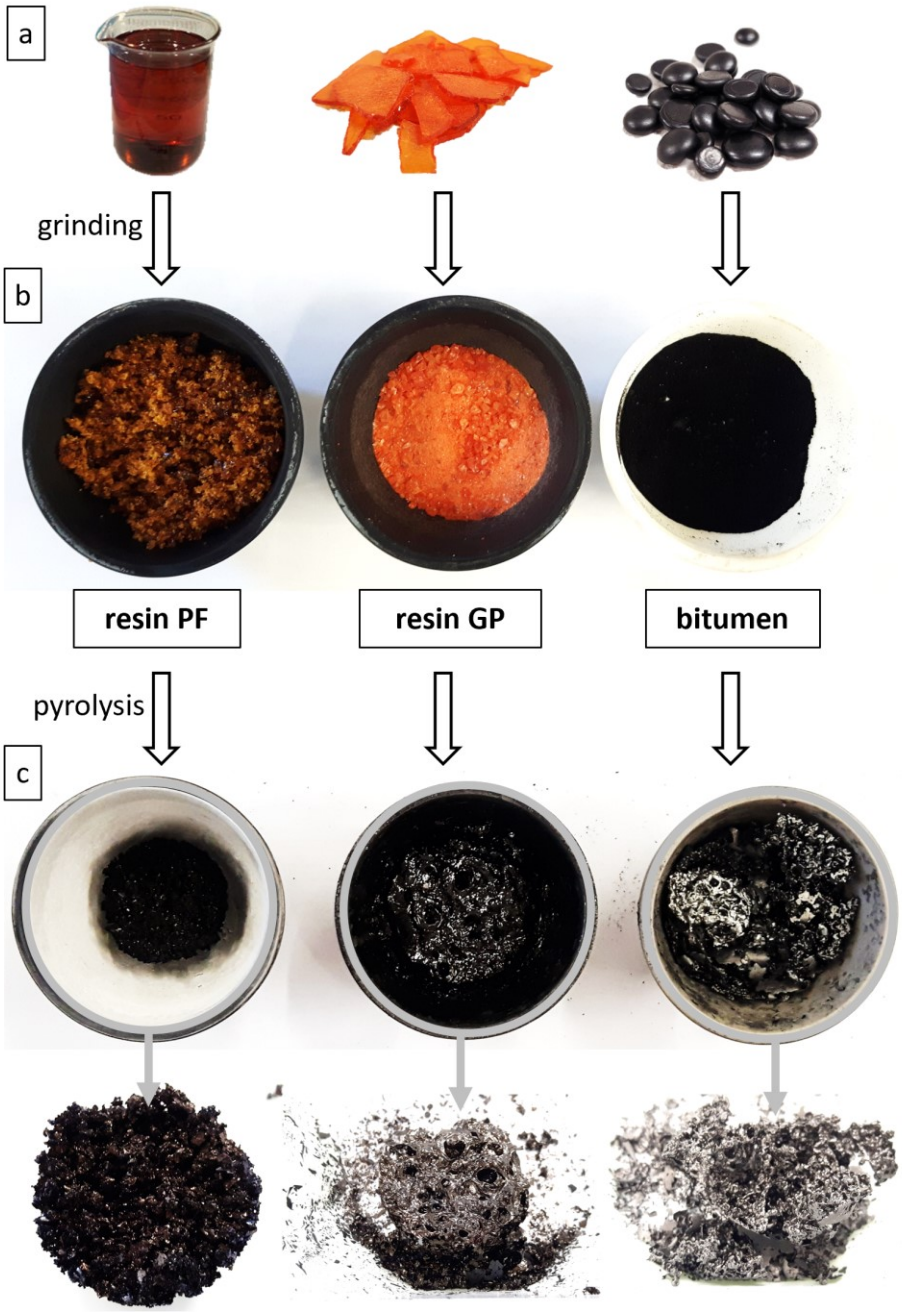

Figure 8.11. Carbon precursors used for the synthesis of ZrC, from the left: BAKELITE PF 8978 FL 01, phenolic resin GP 2074, and bitumen, as (a) raw materials, (b) after grinding, (c) after pyrolysis at 1000 °C.

Their morphology was investigated by SEM/EDS (Figure 8.12). Both novolac-type resins PF and GP displayed relatively rough surfaces, in which contrasting areas were highlighted using BSE (i.e. back scattered electrons) detector because of different C:O:Na ratios (see EDS spectra as insets in Figure 8.12). Bitumen showed a smooth surface of the particles, which is characterised by a uniform elemental distribution (C and low extent of O, see EDS spectrum inset in Figure 8.12).

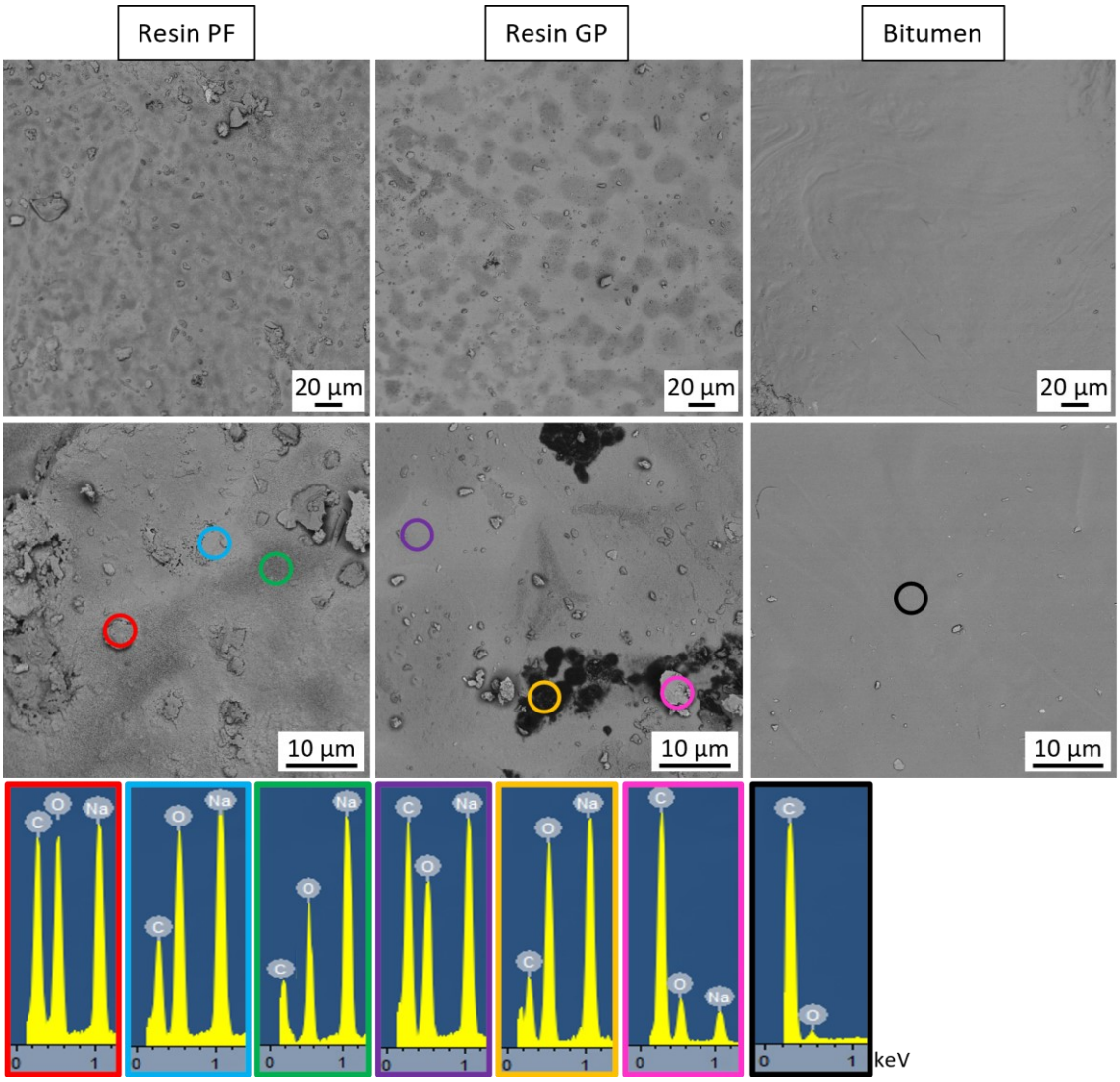

Figure 8.12. SEM images (collected by BSE detector) of the surface of resin PF, resin GP and bitumen pyrolysed at 1000 °C. At the bottom, EDS spectra (EDS spots were marked with coloured circles).

The char yields of carbon precursors were determined by weighing the remaining mass after substance pyrolysis at 1000 °C and achieved values of 38% for resin PF, 41% for resin GP and 60% for bitumen. These values were taken into account for synthesis reactions of zirconium carbide powders.

8.4.3 Polymer-derived ZrC

In order to form ZrC, two possible synthesis routes were hypothesised:

– Elemental synthesis, which can involve the following reactions:

I) $ZrCl_4 + \text{heat} \longrightarrow Zr + 2Cl_2$ (1)

II) $C_xH_yO_z + \text{heat} \longrightarrow x\text{-}(z\text{-}y/2)\ C + z\text{-}y/2\ CO + y/2\ H_2O$ (2)

III) $Zr + C \longrightarrow ZrC$ (3)

– Carbothermal reduction, where ZrO_2 reacts with C to produce ZrC, likely trough the reactions here reported:

I) $ZrCl_4 + C_xH_yO_z \longrightarrow Zr(C_xH_yO_z)\text{-complex} + 4HCl$ (4)

II) $Zr(C_xH_yO_z)\text{-complex} + heat \longrightarrow ZrO_2 + x\text{-}z\ C + z\text{-}y_{/2}\text{-}2\ CO + y_{/2}\ H_2O$ (5)

III) $ZrO_2 + 3C \longrightarrow ZrC + 2CO$ (6)

The negative values of the Gibbs free energy changes (ΔG°) indicate that reaction (3) is strongly favoured thermodynamically even at room temperature [54,55]. Conversely, under standard conditions reaction (6) has positive ΔG° and becomes favourable only at 1660 °C [56–58]. However, it was found by EDS that both types of phenolic resin and bitumen contained oxygen. Therefore, we assumed that the first reaction occurring is the ZrO_2 formation, thus consequently paving the way for the synthesis via carbothermal reduction.

Based on the above discussion of char yield of individual raw carbon sources, a molar ratio of 1:3 for $ZrCl_4$: C was set for the precursor syntheses according to reaction (6). Table 8.3 summarises the prepared samples via dry method (samples labelled as D) and previous dissolution of carbon sources into solvents, so called liquid medium method (samples labelled as S). The obtained precursors before and after pyrolysis at 1000 °C for 2 h are reported in Figure 8.13. It is worthy to note that samples PFZ_S and BZ_S after pyrolysis generated darks solid pellets, similarly to samples prepared via dry-method. Conversely, sample GPZ_S showed a porous grey structure indicating formation of foam during the conversion of the precursor into ceramic.

Table 8.3. Samples prepared using different materials via two different methods (dry method and liquid medium method) and corresponding ceramic yield after pyrolysis at temperature 1000-1800 °C.

Sample code	Materials		Solvent	Ceramic yield (%)				
	Zr source	C source		1000 °C	1400 °C	1600 °C	1800 °C	tot.
PFZ_D	$ZrCl_4$	resin PF	-	44	93	80	98	32
PFZ_S	$ZrCl_4$	resin PF	THF/cyclohexane (1:1)	39	92	74	91	24
GPZ_D	$ZrCl_4$	resin GP	-	38	92	84	96	28
GPZ_S	$ZrCl_4$	resin GP	THF	32	95	68	98	20
BZ_D	$ZrCl_4$	bitumen	-	22	94	96	97	19
BZ_S	$ZrCl_4$	bitumen	THF/cyclohexane (1:1)	42	89	76	97	27

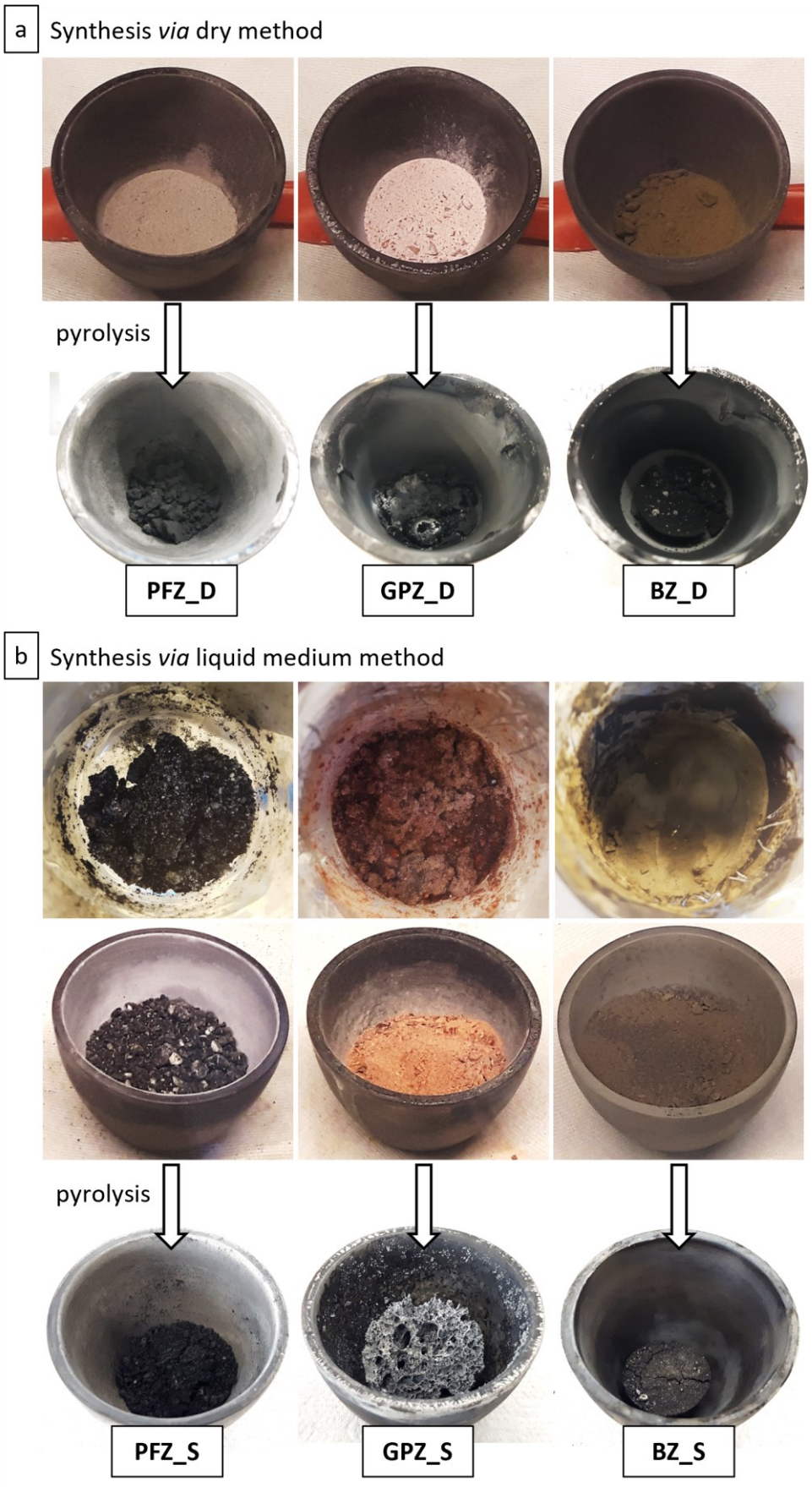

Figure 8.13. Samples prepared via (a) dry method and (b) liquid medium method, before and after pyrolysis at 1000 °C.

ATR-FT-IR Characterization: Infrared spectroscopy was used to investigate the structural modification induced by the addition of $ZrCl_4$ to C sources on the ceramic products upon pyrolysis. The synthetised polymer precursors were not analysed since they could be unstable in air and could not be preserved for long-time preventing hydrolysis [59] due to the possible presence of unreacted $ZrCl_4$.

Raw carbon sources used in this study have been widely studied in the literature. Novolac-type phenolic resin generally shows peaks at 1597 and 1506 cm^{-1} due to C=C stretching of benzene rings, peaks at 888, 821, 757 cm^{-1} due to C–H flexural vibration of benzene rings and a broad band around 3329 cm^{-1} is assigned to the –OH stretching [60–63]. In the case of bitumen, the FTIR spectra generally show band areas at 1700 cm^{-1} (C=O), 1030 cm^{-1} (S=O), and 1600 cm^{-1} (C=C) and three bands between 900 and 730 cm^{-1} (C–H aromatics) [64–67].

In the spectra of resin PF, resin GP and bitumen pyrolysed at 1000 °C almost all the absorption peaks disappeared, suggesting that nearly no residual functional groups such as alcohols, methyls or ketons remained in amorphous carbon (Figure 8.14a-c). With the addition of $ZrCl_4$ to the three C precursors, some peaks appeared in the region 700–400 cm^{-1}, which were attributed to the stretching vibration of Zr–O bonds (Figure 8.14a-c). In accordance with the literature [68–70], the backbone of the polymers was destroyed, and the networks collapsed forming a glassy carbon, during the organic-to-inorganic conversion, thus only Zr–O bonds existed after pyrolysis treatment. The appearance of Zr–O absorption peaks is believed to be caused by the incorporation of zirconium into the reaction products in the form of compounds based on Zr–O bonds [68–72]. For instance, the characteristic bands associated to monoclinic ZrO_2 are at 574 and 732 cm^{-1} and tetragonal ZrO_2 at 480 cm^{-1} [73].

The spectra of the products synthetised by dry method (i.e. PFZ_D, GPZ_D, BZ_D) and liquid medium method (i.e. PFZ_S, GPZ_S, BZ_S) appeared very similar, except for a slight higher increase in intensities of the Zr–O peaks for the latter. We can speculate that the synthesis of the polymer precursors involved the formation of a $Zr(C_xH_yO_z)$-type complex using phenolic chains and hydrocarbons both as a carbon source and a ligand, in a more effective way via the solution-based pathway.

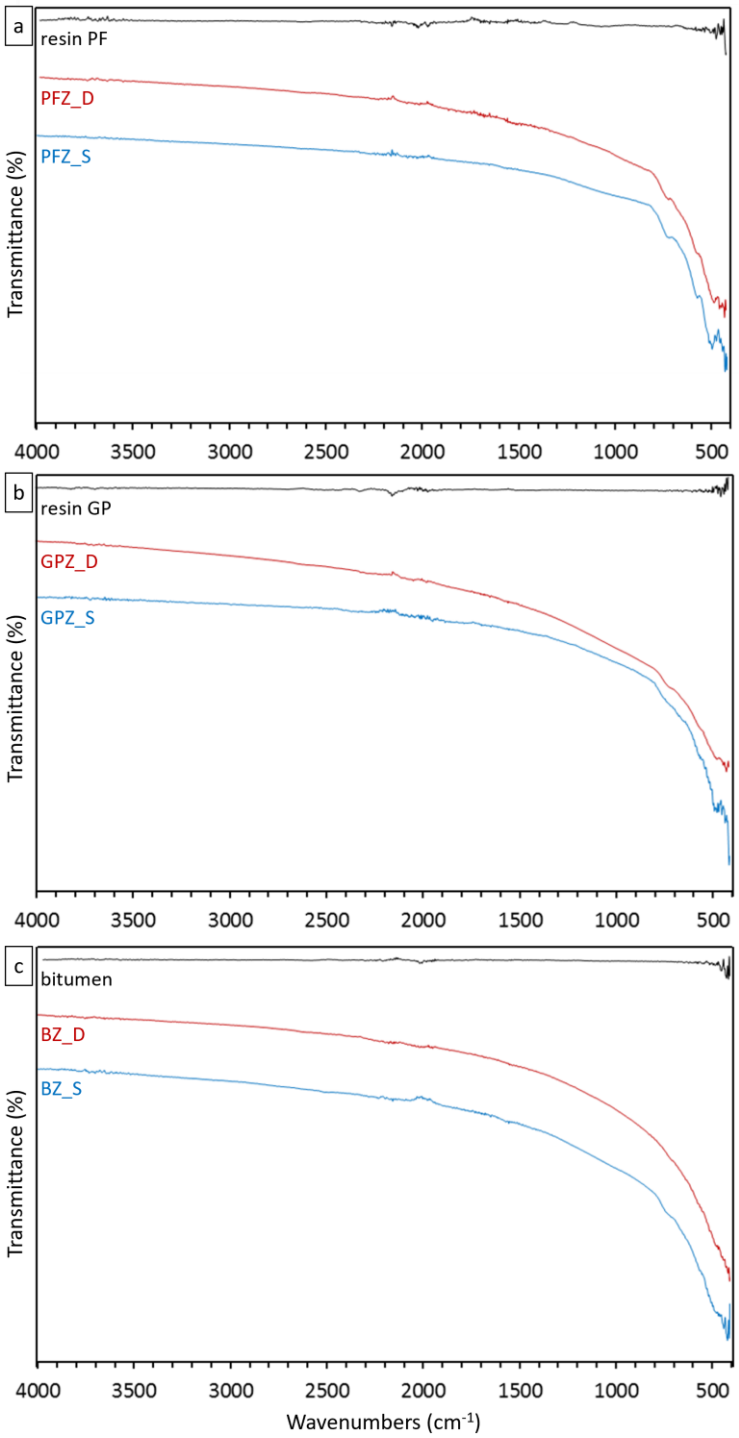

Figure 8.14. ATR-FTIR spectra of the starting materials and precursors synthetised via dry and liquid medium methods after pyrolysis: (a) resin PF and PF-based precursors PFZ_D and PFZ_S, (b) resin GP and GP-based precursors GPZ_D and GPZ_S, (c) bitumen and bitumen-based precursors BZ_D and BZ_S.

TG-DSC Analysis: Simultaneous TG-DSC analysis was conducted in Ar atmosphere to investigate the conversion process to ceramic in the range 1000–1500 °C. Analysis was performed only on the sample PFZ_S for technical reasons; on the basis of the previous analysis, similar results are expected for GP-based and bitumen-based systems. Obtained

TG-DSC curves for sample PFZ_S upon pyrolysis at 1000 °C are reported in Figure 8.15, as example of thermal behaviour for all obtained precursors. TG curve displays a low weight loss (~1,7%) below 160 °C, which corresponds to a weak endothermic peak on the DSC curve, was attributed to the evaporation of free and adsorbed water. The volatilization of the residual solvent can be excluded because the sample was previously pyrolysed up to 1000 °C. Between 160 °C and around 450 °C the TG curve is almost flat indicating a very slow weight loss. In such range the weight losses of preceramic precursors are usually caused by the decomposition of organic compounds [68,69,74]. As can be expected, the thermal decomposition of the phenolic resin was completed during pyrolysis process. In the DSC curve, the obvious peak in the range 400–450 °C corresponds to the phase formation of ZrO_2 [72,75]. Thus, the steady weight loss (~20%) registered from around 480 °C up to above 1300 °C probably corresponds to the transformation of ZrO_2 crystalline phase, besides the further ceramization process of the precursor. The weak and the broad peak at about 850 °C may be due to the phase transformation from tetragonal (t-) to monoclinic (m-) ZrO_2 or the growth of the ZrO_2 grains [72,76]. The weight loss further increased when the temperature exceeded 1300 °C, which corresponds to a clear endothermic peak at 1393 °C in DSC curve. At such temperature it is believed that carbothermal reaction between ZrO_2 and pyrolytic carbon starts [70].

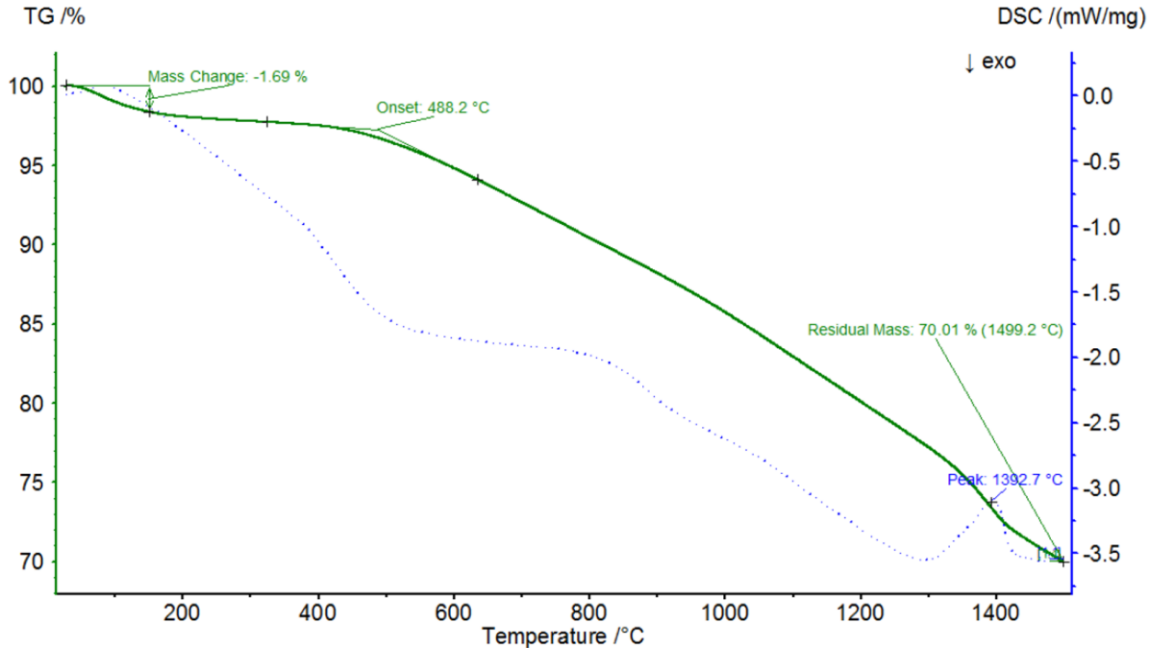

Figure 8.15. TG-DSC curves of the sample PFZ_S after pyrolysis at 1000 °C. Analysis was carried out up to 1500 C° in Ar environment.

Based on the above discussion of TG-DSC results, the heat treatments (subsequently pyrolysis up to 1000 °C) were settled at 1400 °C, and at temperatures out of TG-DSC range, for instance at 1600 °C and 1800 °C.

Ceramic yields, after each heat treatment and total, for each prepared precursor are reported in Table 8.3. The values are quite scattered, total yields range from 19 to 32%. They are undoubtedly low yields, nevertheless they are comparable or even better than those reported in previous studies concerning carbothermal synthesis of ZrC [69,74]. No correlation was observed among values, C precursor types and processes. But it can be noted a similar trend for all samples except the sample BZ_D as it registered an extremely high weight loss at 1000 °C and yield over 94% at 1400, 1600 and 1800 °C (Table 8.3).

X-Ray diffraction (XRD) was used to study the conversion of the phase composition during heat treatments at 1000–1800 °C (see XRD patterns in Figure 8.16a-c).

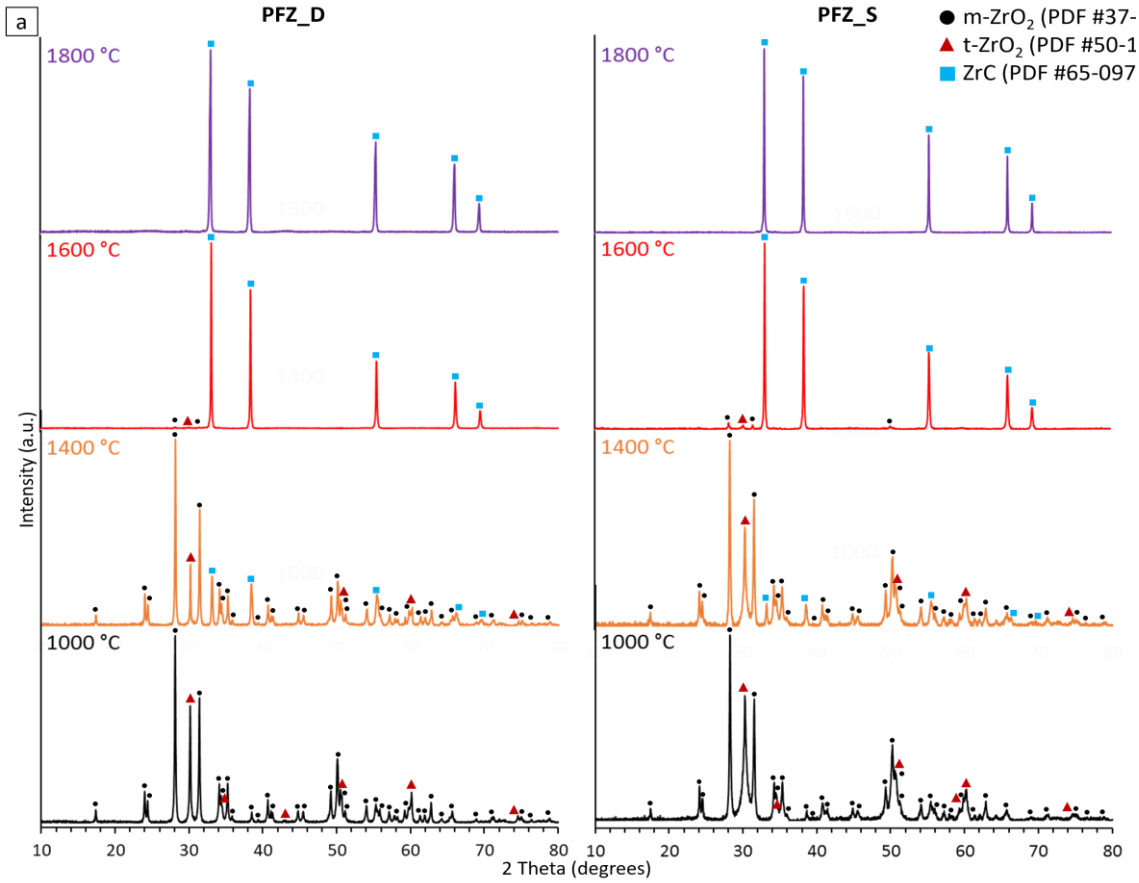

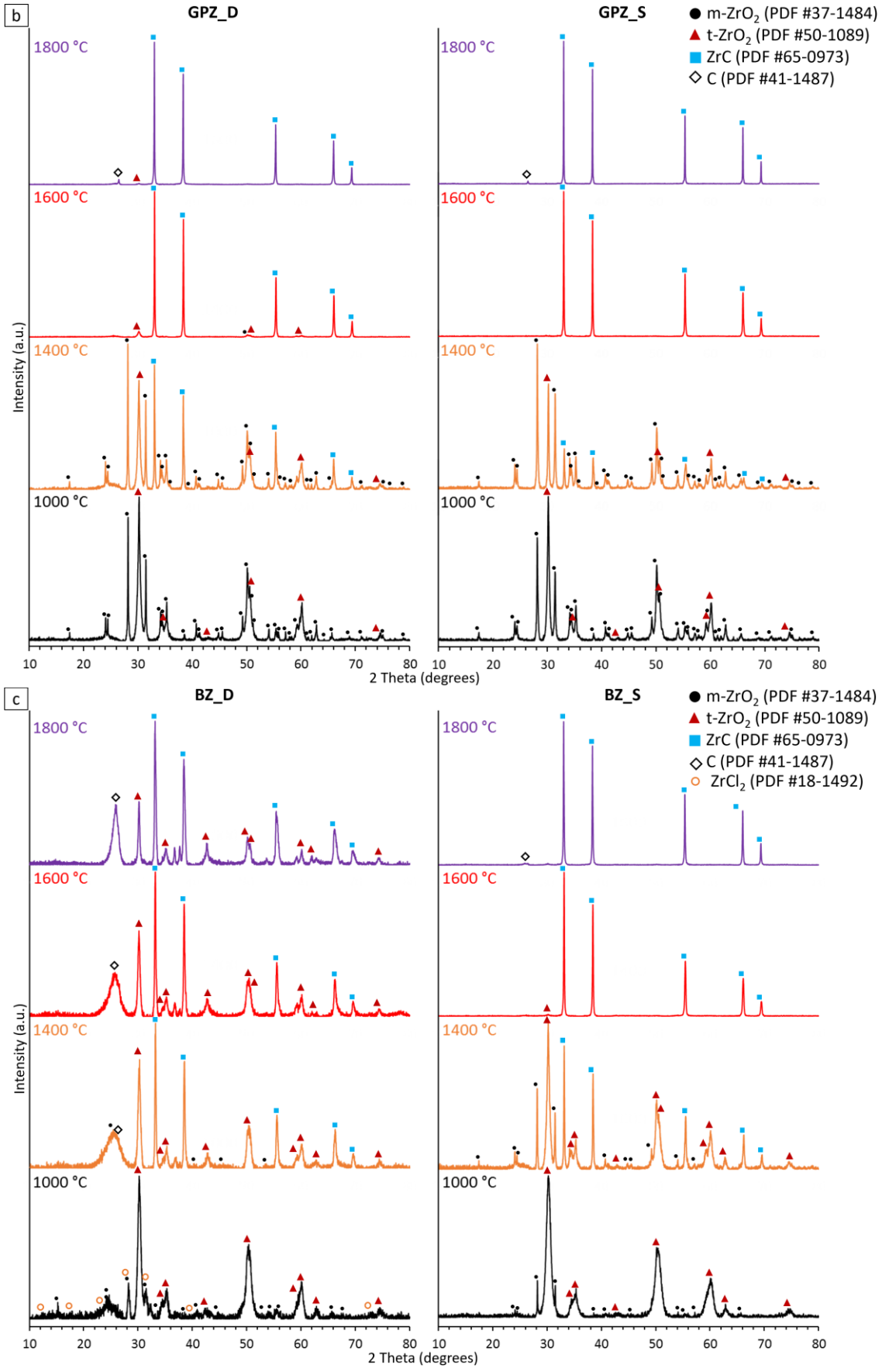

Figure 8.16. XRD patterns of precursors based on (a) resin PF, PFZ_D and PFZ_S, (b) resin GP, GPZ_D and GPZ_S, and (c) bitumen, BZ_D and BZ_S, upon pyrolysis at 1000, 1400, 1600, 1800 °C for 2 h.

As can be seen in the XRD patterns of PFZ_D and PFZ_S (Figure 8.16a), after initial pyrolysis at 1000 °C, the only crystalline phases are m-ZrO_2 (PDF #37-1484) and t-ZrO_2 (PDF #50-1089) respectively. This latter seems to be more abundant in PFZ_S. It is well known that monoclinic zirconia (also known as baddeleyte) is the most stable at temperature below 1200 °C, whereas tetragonal polymorph is stable at higher temperature (1170–2370 °C) [77,78]. The formation of t-ZrO_2 as predominant phase is commonly reported for low heat-treated ZrC precursors, since the tetragonal form can be stabilized until room temperature by carbon and tiny particle size. At 1400 °C, m-ZrO_2/t-ZrO_2 ratio increased. Also, peaks at θ = 33.1°, 38.4°, 55.4°, 65.9° and 69.3° appeared, which are associated to diffraction of cubic ZrC (PDF #65-0973). ZrC became predominant phase in the specimen heat-treated at 1600 °C. The relative amount of ZrO_2 significantly decreased due to the carbothermal reduction, but small amounts of m-ZrO_2 still existed. At 1800 °C, ZrO_2 declined to zero and only ZrC was detected.

XRD patterns of samples GPZ_D and GPZ_S (Figure 8.16b) suggested phase transformation similar to what observed for resin PF-based samples. At 1000 °C m-ZrO_2 and t-ZrO_2 formed, among them tetragonal form is the major phase similarly in both PF-based systems. Spectra upon pyrolysis at 1600 °C exhibited sharp peaks attributable to ZrC which is pure (GPZ_S) or almost pure (GPZ_D, some traces of t-ZrO_2 and m-ZrO_2 still visible). After 1800 °C, ZrO_2 was almost zero also in GPZ_D, while a broad peak indicating carbon structure (PDF #41-1487) is shown that is likely due to the crystallization of residual amorphous carbon.

XRD patterns of bitumen-based systems (Figure 8.16c) highlighted the major differences between dry and liquid methods: upon initial pyrolysis at 1000 °C, patterns showed t-ZrO_2 as major phase and broad peaks for m-ZrO_2 and carbon. Moreover, reflections attributable to traces of chloride species (e.g. $ZrCl_2$, PDF #18-1492) were revealed into sample BZ_D. BZ_S led to similar patterns to those observed for PF- and GP-based systems At 1400 °C, both t-ZrO_2 (as major phase) and ZrC (starting crystallization) were found. At 1600 °C and 1800 °C, well-crystallized ZrC and traces of ZrO_2 and C were detected. In contrast, BZ_D displayed roughly identical profiles after 1400, 1600 and 1800 °C, where are recognizable t-ZrO_2, ZrC, C and other species (some of which were not identified). Therefore, residues of ZrO_2 even after treatment at 1800 °C suggests that such synthesis pathway did not allow the carbothermal reduction of zirconia to completion.

On the basis of the collected data, the selection of the best route is not an easy task. Several considerations may be taken into account: purity of the final phases, total yield of conversion, formation of undesired foam during conversion of precursor into ceramic, availability and cost of precursors. These key features were summarized in Table 8.4 to consider all pros and cons to each precursor.

Table 8.4. Key features (total yield, conversion, formation of form, availability and costs, method application and applicability) for each of the prepared ZrC precursors.

	Total yield (%)	ZrC conversion	Formation of foam	Estimation availability and cost of C source	Application of method	Applicability
PFZ_D	32	complete 1600 °C	minimal	EU (Germany), high	powder	good
PFZ_S	24	complete 1600 °C	minimal		infiltration	excellent
GPZ_D	28	high ZrC/ZrO_2 ratio at 1400 °C	yes	US, high	powder	good
GPZ_S	20	complete 1600 °C	yes		infiltration	poor
BZ_D	19	not completed	minimal	IT, low	powder	discarded
BZ_S	27	complete 1600 °C	minimal		infiltration	good

Expect for BZ_D, crystalline ZrC was the only phase found in the samples after heat treatment at 1600 °C, consequently from this point of view no differences among carbon source were detected. On the one hand, PF resin is the best carbon source in term of yield of conversion polymer-to-ceramic; moreover, PF is a liquid resin at room temperature and the use of solvent may be avoided. On the other hand, bitumen is very cheap and a national product that can be valorized in this way for the production of ZrC and ZrC-based composites.

Concerning the powder precursors, they are not directly applicable for infiltration processing. Nevertheless, these types of products can be used as ZrC powder for the preparation of water-based powder slurry and thus applied for the preparation of ZrC-based composites through the slurry impregnation process. For this purpose, resin GP can be the most suitable as it produces a high porous material, that is characterized by a better grindability.

8.5 Conclusions

The first study investigated the effect of catalyst addition and pre-heat treatment on commercially available allyl-hydrido polycarbosilane SMP-10 on ceramic mass yield.

Catalysts and pre-curing thermal treatment before polymer curing demonstrated a net 19–20% and 11% increase in SiC mass yield compared to as-received SMP-10, respectively. The relatively little difference in mass yield between the two strategies paves the way to Si-based preceramic polymers with an enhanced ceramic yield and a chemistry not altered by the addition of a polymer catalyst. However, the addition of 1 wt% $MeCpPtMe_3$ and DCP catalysts was more effective for improved SiC mass yield. Due to their similar results, the best option may be DCP because of its lower toxicity and cheaper price (DCP € 75 per 100 g vs. $MeCpPtMe_3$ € 920 per 2 g). Overall, maximizing mass and volumetric yield leads to the potential payoff of the reduction of the numerous re-infiltration steps in PIP processing.

In the second study, a liquid single-source SIBCN(O) ceramic precursor was synthesized by a simple reaction way. The boron and nitrogen were not preferentially incorporated into the silicon carbide lattice but entered the SiC(O) forming segregated BNO-reach areas. In future work, behaviour at high temperature and performance in oxidative environment will be studied. Also, polymer-derived SiCBN(O) will be used for PIP-ed CMCs, even combining it with ultra-refractory phases with poor oxidation resistance (e.g. ZrC).

In the third study, preceramic precursors for zirconium carbide were prepared by simply mixing zirconium tetrachloride and phenolic resins or bitumen. The initial pyrolysis at 1000 °C converted the reaction products into a mixture of zirconia and amorphous carbon. ZrC was formed when the temperature of pyrolysis increased up to around 1400 °C, almost indistinctly for precursors prepared via solid-state reaction and liquid medium method. Such relatively low temperature can be attributed to the intimate mixing of the free carbon particles with ZrO_2. Formation of pure ZrC by carbothermal reduction of ZrO_2 with C was substantially completed after pyrolysis at 1600 °C.

Conventionally, solid-state reactions to synthesise ZrC require high temperatures, while solution-based processing methods can lower the temperature and shorten the reaction time, but solvents are not environmentally friendly. Also, organic reactants (e.g. organometallic compounds) are often expensive. In this work, ZrC was synthesised even without addition of solvent at relatively low temperature and using quite cheap

reactants. However, chemical rearrangements that have prevented the reduction of ZrO_2 in mixture $ZrCl_4$/bitumen (via dry method) are still unclear.

To date, the difficulties in controlling the reaction process and viscosity of the final products limit the application in PIP processing. Nevertheless, this novel way to prepare ZrC-based precursors represents a potential approach for introducing zirconium in phenolic resin and the fabrication of C/C-ZrC composites by generating in situ matrix at relatively low temperature, thus limiting the degradation of carbon fibres.

8.6 References

1. Bordia, R., Tomar, V. & Henager, C. *Precursor Derived Nanostructured Si-C-X Materials for Nuclear Applications*. http://www.osti.gov/servlets/purl/1179802/ (2015) doi:10.2172/1179802.

2. King, D., Apostolov, Z., Key, T., Carney, C. & Cinibulk, M. Novel processing approach to polymer-derived ceramic matrix composites. *Int. J. Appl. Ceram. Technol.* **15**, 399–408 (2018).

3. Key, T. S. *et al.* Process modeling of the low-temperature evolution and yield of polycarbosilanes for ceramic matrix composites. *J. Am. Ceram. Soc.* **101**, 2809–2818 (2018).

4. Riedel, R., Ruswisch, L. M., An, L. & Raj, R. Amorphous Silicoboron Carbonitride Ceramic with Very High Viscosity at Temperatures above 1500°C. *J. Am. Ceram. Soc.* **81**, 3341–3344 (1998).

5. Riedel, R. *et al.* A silicoboron carbonitride ceramic stable to 2,000°C. *Natur* **382**, 796–798 (1996).

6. Ramachandran, P. V., Drolet, M. P. & Kulkarni, A. S. A non-dissociative open-flask hydroboration with ammonia borane: Ready synthesis of ammonia-trialkylboranes and aminodialkylboranes. *Chem. Commun.* **52**, 11897–11900 (2016).

7. Jiang, J., Wang, S., Li, W. & Chen, Z. Fabrication and characterization of ZrC foam by melt infiltration. *J. Alloys Compd.* **695**, 2295–2300 (2017).

8. Katoh, Y., Vasudevamurthy, G., Nozawa, T. & Snead, L. L. Properties of zirconium carbide for nuclear fuel applications. *J. Nucl. Mater.* **441**, 718–742 (2013).

9. Starfire® Systems Inc. StarPCS SMP-10. (2018).

10. Kaur, S., Riedel, R. & Ionescu, E. Pressureless fabrication of dense monolithic SiC ceramics from a polycarbosilane. *J. Eur. Ceram. Soc.* **34**, 3571–3578 (2014).

11. Kaur, S., Mera, G., Riedel, R. & Ionescu, E. Effect of boron incorporation on the phase composition and high-temperature behavior of polymer-derived silicon

carbide. *J. Eur. Ceram. Soc.* **36**, 967–977 (2016).

12. Sreeja, R., Swaminathan, B., Painuly, A., Sebastian, T. V. & Packirisamy, S. Allylhydridopolycarbosilane (AHPCS) as matrix resin for C/SiC ceramic matrix composites. *Mater. Sci. Eng. B Solid-State Mater. Adv. Technol.* **168**, 204–207 (2010).

13. Yin, J. *et al.* The effects of SiC precursors on the microstructures and mechanical properties of SiC_f/SiC composites prepared via polymer impregnation and pyrolysis process. *Ceram. Int.* **41**, 4145–4153 (2015).

14. Zheng, J., Kramer, M. J. & Akinc, M. In situ Growth of SiC Whisker in Pyrolyzed Monolithic Mixture of AHPCS and SiC. *J. Am. Ceram. Soc.* **83**, 2961–2966 (2000).

15. Jang, Y. S. *et al.* SiC ceramic micropatterns from polycarbosilanes. *J. Eur. Ceram. Soc.* **30**, 2773–2779 (2010).

16. Süß, F. *et al.* Combination of PIP and LSI processes for SiC/SiC ceramic matrix composites. *Open Ceram.* **5**, (2021).

17. Larson, N. M. & Zok, F. W. In-situ 3D visualization of composite microstructure during polymer-to-ceramic conversion. *Acta Mater.* **144**, 579–589 (2018).

18. Konegger, T., Patidar, R. & Bordia, R. K. A novel processing approach for free-standing porous non-oxide ceramic supports from polycarbosilane and polysilazane precursors. *J. Eur. Ceram. Soc.* **35**, 2679–2683 (2015).

19. Mainzer, B. *et al.* Characterization and application of a novel low viscosity polysilazane for the manufacture of C- and SiC-fiber reinforced SiCN ceramic matrix composites by PIP process. *J. Eur. Ceram. Soc.* **39**, 212–221 (2019).

20. D'Elia, R. *et al.* Cure kinetics of a polysilazane system: Experimental characterization and numerical modelling. *Eur. Polym. J.* **76**, 40–52 (2016).

21. D'Elia, R. *et al.* Effect of dicumyl peroxide concentration on the polymerization kinetics of a polysilazane system. *Polym. Eng. Sci.* **58**, 859–869 (2018).

22. Zoli, L. *et al.* Additive Manufacturing of Ceramics Enabled by Flash Pyrolysis of Polymer Precursors with Nanoscale Layers. *J. Am. Ceram. Soc.* **99**, 57–63 (2016).

23. Ding, Q. *et al.* 3D C_f/SiBCN composites prepared by an improved polymer infiltration and pyrolysis. *J. Adv. Ceram.* **7**, 266–275 (2018).

24. Park, S. *et al.* Fabrication of three-dimensional SiC ceramic microstructures with near-zero shrinkage via dual crosslinking induced stereolithography. *Chem. Commun.* 4880–4882 (2009) doi:10.1039/b907923h.

25. Yu, Z. *et al.* Single-source-precursor synthesis of high temperature stable SiC/C/Fe nanocomposites from a processable hyperbranched polyferrocenylcarbosilane with high ceramic yield. *J. Mater. Chem. C* **2**, 1057–1067 (2014).

26. Kockrick, E. *et al.* Platinum induced crosslinking of polycarbosilanes for the

formation of highly porous CeO_2/silicon oxycarbide catalysts. *J. Mater. Chem.* **19**, 1543–1553 (2009).

27. Lukin, R. Y., Kuchkaev, A. M., Sukhov, A. V., Bekmukhamedov, G. E. & Yakhvarov, D. G. Platinum-catalyzed hydrosilylation in polymer chemistry. *Polymers (Basel).* **12**, 1–22 (2020).

28. Chalk, A. J. & Harrod, J. F. Homogeneous Catalysis. II. The Mechanism of the Hydrosilation of Olefins Catalyzed by Group VIII Metal Complexes[1]. *J. Am. Chem. Soc.* **87**, 16–21 (2002).

29. Kaur, S., Fischer, S., Falta, J., Rezwan, K. & Wilhelm, M. High surface area SiC(O)-based ceramic by pyrolysis of poly (ethylene glycol) methacrylate-modified polycarbosilane. *J. Am. Ceram. Soc.* **102**, 7187–7197 (2019).

30. Yu, Z. *et al.* Preparation of a liquid boron-modified polycarbosilane and its ceramic conversion to dense SiC ceramics. *Polym. Adv. Technol.* **22**, 2409–2414 (2011).

31. Puerta, A. R., Remsen, E. E., Bradley, M. G., Sherwood, W. & Sneddon, L. G. Synthesis and Ceramic Conversion Reactions of 9-BBN-Modified Allylhydridopolycarbosilane: A New Single-Source Precursor to Boron-Modified Silicon Carbide. *Chem. Mater.* **15**, 478–485 (2002).

32. Key, T. S., Patel, D. K., Wilks, G. B. & Cinibulk, M. K. Modeling the pyrolysis of preceramic polymers: A kinetic study of the polycarbosilane SMP-10. *J. Eur. Ceram. Soc.* **41**, 6356–6365 (2021).

33. Bird, R. B., Armstrong, R. C. & Hassager, O. *Dynamics of Polymeric Liquids, Volume 1: Fluid dynamics*. vol. 1 (Wiley, 1987).

34. Rodriguez, F., Cohen, C., Ober, C. K. & Archer, L. A. *Principles of Polymer Systems*. *Principles of Polymer Systems* (CRC Press, 2014). doi:10.1201/B17873.

35. Matthews, S., Edirisinghe, M. J. & Folkes, M. J. Effect of pre-pyrolysis heat treatment on the preparation of silicon carbide from a polycarbosilane precursor. *Ceram. Int.* **25**, 49–60 (1999).

36. Weinmann, M. *et al.* Synthesis and Thermal Behavior of Novel Si−B−C−N Ceramic Precursors. *Chem. Mater.* **12**, 623–632 (2000).

37. Yu, Z. *et al.* Modification of a liquid polycarbosilane with 9-BBN as a high-ceramic-yield precursor for SiC. *React. Funct. Polym.* **70**, 334–339 (2010).

38. Yu, Z. *et al.* Preparation, cross-linking and ceramization of AHPCS/Cp 2ZrCl 2 hybrid precursors for SiC/ZrC/C composites. *J. Eur. Ceram. Soc.* **32**, 1291–1298 (2012).

39. Lodhe, M., Babu, N., Selvam, A. & Balasubramanian, M. Synthesis and characterization of high ceramic yield polycarbosilane precursor for SiC. *J. Adv. Ceram.* **2015**, 307–311.

40. Jiao, J., Qiu, H., Li, X., Luo, J. & Wang, Y. The Pyrolysis Processing of Polycarbosilane Studied by TG, XRF, IR, XRD, and XPS. *Key Eng. Mater.* **512–515**, 965–970 (2012).

41. Ly, H. Q., Taylor, R., Day, R. J. & Heatley, F. Conversion of polycarbosilane (PCS) to SiC-based ceramic Part 1. Characterisation of PCS and curing products. *J. Mater. Sci. 2001 3616* **36**, 4037–4043 (2001).

42. Cheng, X., Xie, Z., Xiao, J. & Song, Y. Influence of Temperature on the Properties of Polycarbosilane. *J. Inorg. Organomet. Polym. Mater. 2005 152* **15**, 253–259 (2005).

43. Birot, M., Pillot, J. P. & Dunoguès, J. Comprehensive Chemistry of Polycarbosilanes, Polysilazanes, and Polycarbosilazanes as Precursors of Ceramics. *Chem. Rev.* **95**, 1443–1477 (2002).

44. Jash, P., Meux, K. & Trenary, M. Transmission Infrared Spectroscopy of Ammonia Borane. *J. Undergrad. Res. Univ. Illinois Chicago* **5**, 1–5 (2012).

45. Paolone, A., Teocoli, F., Sanna, S., Palumbo, O. & Autrey, T. Temperature dependence of the infrared spectrum of ammonia borane: Librations, rotations, and molecular vibrations. *J. Phys. Chem. C* **117**, 729–734 (2013).

46. Frueh, S. *et al.* Pyrolytic decomposition of ammonia borane to boron nitride. *Inorg. Chem.* **50**, 783–792 (2011).

47. Babenko, V. *et al.* Time dependent decomposition of ammonia borane for the controlled production of 2D hexagonal boron nitride. *Sci. Rep.* **7**, 1–12 (2017).

48. Wang, X., Wang, H. & Shi, J. Synthesis, characterization, and ceramic conversion of a liquid polymeric precursor to SiBCN ceramic via borazine-modified polymethylsilane. *J. Mater. Sci. 2018 5316* **53**, 11242–11252 (2018).

49. Zhou, C. *et al.* Dimethylaminoborane-modified copolysilazane as a novel precursor for high-temperature resistant SiBCN ceramics. *J. Eur. Ceram. Soc.* **34**, 3579–3589 (2014).

50. Huang, C. *et al.* Stable colloidal boron nitride nanosheet dispersion and its potential application in catalysis. *J. Mater. Chem. A* **1**, 12192–12197 (2013).

51. Tocha, E., Vervoort, S. & Jeltsch, K. Compatibilization of Polymer Blends. *Wiley Analytical Science* (2018).

52. Wang, T. *et al.* Solvent Extraction of Bitumen from Oil Sands. *Energy and Fuels* **28**, 2297–2304 (2014).

53. Liu, Y. *et al.* Bitumen Recovery from Crude Bitumen Samples from Halfaya Oilfield by Single and Composite Solvents-Process, Parameters, and Mechanism. *Mater. (Basel, Switzerland)* **12**, (2019).

54. Tong, Y. *et al.* Laser ablation resistance and mechanism of Si-Zr alloyed melt infiltrated C/C-SiC composite. *Ceram. Int.* **44**, 3692–3698 (2018).

55. Arai, Y., Marumo, T. & Inoue, R. Use of Zr–Ti Alloy Melt Infiltration for Fabricating Carbon-Fiber-Reinforced Ultrahigh-Temperature Ceramic Matrix Composites. *J. Compos. Sci. 2021, Vol. 5, Page 186* **5**, 186 (2021).

56. He, L. *et al.* Enhanced oxidation properties of ZrB_2–SiC composite with short carbon fibers at 1600 °C. *Ceram. Int.* **47**, 15483–15490 (2021).

57. Zhang, S. C., Hilmas, G. E. & Fahrenholtz, W. G. Zirconium Carbide–Tungsten Cermets Prepared by In Situ Reaction Sintering. *J. Am. Ceram. Soc.* **90**, 1930–1933 (2007).

58. Xu, Z., Li, F., Wang, Y., Zhao, K. & Tang, Y. Microstructure and oxidation resistance of ZrB_2–ZrC–SiC composite nanofibers fabricated via electrospinning combined with carbothermal reduction. *Ceram. Int.* **47**, 20740–20744 (2021).

59. Fang, Z. & Dixon, D. A. Hydrolysis of $ZrCl_4$ and $HfCl_4$: The initial steps in the high-temperature oxidation of metal chlorides to produce ZrO_2 and HfO_2. *J. Phys. Chem. C* **117**, 7459–7474 (2013).

60. Kumar, H., Tripathi, S. K., Mistry, S. & Bajpai, G. Synthesis, Characterization and Application of Coatings Based on Epoxy Novolac and Liquid Rubber Blend. *E-Journal Chem.* **6**, 1253–1259 (2009).

61. Yun, J., Chen, L., Zhang, X., Feng, J. & Liu, L. The Effect of Introducing B and N on Pyrolysis Process of High Ortho Novolac Resin. *Polym. 2016, Vol. 8, Page 35* **8**, 35 (2016).

62. Zhou, J. *et al.* Post-functionalization of novolac resins by introducing thermo-crosslinkable $–OCF=CF_2$ groups as the side chains: a new strategy for production of thermosetting polymers without releasing volatiles. *Polym. Chem.* **7**, 4313–4316 (2016).

63. Huang, J. *et al.* Controlled synthesis of high-ortho-substitution phenol–formaldehyde resins. *J. Appl. Polym. Sci.* **97**, 652–658 (2005).

64. Mouazen, M., Poulesquen, A. & Vergnes, B. Influence of Thermomechanical History on Chemical and Rheological Behavior of Bitumen. *Energy and Fuels* **25**, 4614–4621 (2011).

65. Weigel, S. & Stephan, D. Bitumen Characterization with Fourier Transform Infrared Spectroscopy and Multivariate Evaluation: Prediction of Various Physical and Chemical Parameters. *Energy & Fuels* **32**, 10437–10442 (2018).

66. Weigel, S. & Stephan, D. The prediction of bitumen properties based on FTIR and multivariate analysis methods. *Fuel* **208**, 655–661 (2017).

67. Hofko, B. *et al.* FTIR spectral analysis of bituminous binders: reproducibility and impact of ageing temperature. *Mater. Struct. Constr.* **51**, 1–16 (2018).

68. Wang, J. X. *et al.* Synthesis of nanocrystallized zirconium carbide based on an aqueous solution-derived precursor. *RSC Adv.* **7**, 22722–22727 (2017).

69. Li, Y. *et al.* A simple way to prepare a precursor for ZrC–SiC ceramics. *J. Mater. Sci.* **51**, 5160–5169 (2016).

70. Dong, Z. *et al.* Synthesis and pyrolysis behavior of a soluble polymer precursor for ultra-fine zirconium carbide powders. *Ceram. Int.* **41**, 7359–7365 (2015).

71. Tao, X. Y., Qiu, W. F., Li, H., Zhao, T. & Wei, X. Y. New route to synthesize preceramic polymers for zirconium carbide. *Chinese Chem. Lett.* **23**, 1075–1078 (2012).

72. Liu, C., Li, K., Li, H., Zhang, S. & Zhang, Y. The effect of zirconium incorporation on the thermal stability and carbonized product of phenol-formaldehyde resin. *Polym. Degrad. Stab.* **102**, 180–185 (2014).

73. Fernandez Lopez, E., Sanchez Escribano, V., Panizza, M., Carnasciali, M. M. & Busca, G. Vibrational and electronic spectroscopic properties of zirconia powders. *J. Mater. Chem.* **11**, 1891–1897 (2001).

74. Yan, C., Liu, R., Cao, Y., Zhang, C. & Zhang, D. Carbothermal Synthesis of Submicrometer Zirconium Carbide from Polyzirconoxane and Phenolic Resin by the Facile One-Pot Reaction. *J. Am. Ceram. Soc.* **95**, 3366–3369 (2012).

75. Dodd, A. C. & McCormick, P. G. Synthesis of nanocrystalline ZrO_2 powders by mechanochemical reaction of $ZrCl_4$ with LiOH. *J. Eur. Ceram. Soc.* **22**, 1823–1829 (2002).

76. Noda, L. K., Gonçalves, N. S., de Borba, S. M. & Silveira, J. A. Raman spectroscopy and thermal analysis of sulfated ZrO_2 prepared by two synthesis routes. *Vib. Spectrosc.* **44**, 101–107 (2007).

77. Bazhenov, A. S. & Honkala, K. Understanding Structure and Stability of Monoclinic Zirconia Surfaces from First-Principles Calculations. *Top. Catal. 2016 606* **60**, 382–391 (2016).

78. Namavar, F. *et al.* Thermal stability of nanostructurally stabilized zirconium oxide. *Nanotechnology* **18**, 415702 (2007).

9. Conclusions and outlook

The demand for advanced materials able to withstand more challenging and harsh conditions has stimulated the scientific research towards the study of a novel class of composites, so called Ultra-High Temperature Ceramic Matrix Composites (UHTCMCs). These have emerged as promising materials for application in severe environments as they combine strength, fracture toughness and strain to failure of a composite with temperature and oxidation resistance of UHTCs. They are a relatively new field and innovative manufacturing technologies are continuously being researched.

The theme of this PhD thesis was the fabrication and characterization of continuous fibre-reinforced UHTCMCs, using the Polymer Infiltration and Pyrolysis (PIP) technique re-adapted from the traditional CMC manufacturing technologies. Indeed, this technique is attractive allowing the formation of a weak fibre/matrix interface and remains one of the most viable routes for production of components, despite the lack of suitable UHTC organic/inorganic precursors in the market.

To this scope, the first parts of the thesis concerned the development of novel routes for UHTCMC manufacturing by PIP technique or a combination of it with other techniques.

In Chapters 4 and 5, carbon fibre-reinforced UHTC matrix composites were fabricated via slurry infiltration coupled with polymer infiltration and pyrolysis at relatively low temperature (i.e. 1000 °C), exploring different type (pitch-based and PAN-based) and architectures (UD, 0/90°, 2D and 2.5D) of carbon fibres.

In the following (Chapter 6), post-consolidation treatments at temperatures ranging from 1100 to 1900 °C aimed at improving thermal stability and mechanical properties at elevated temperature were discussed.

In Chapter 7, the preparation of UHTCMs by hybrid processes coupling PIP and Hot Pressing (HP) techniques was explored for a faster and cheaper manufacturing compared to the conventional PIP processes. Two different routes for the consolidation of the materials were carried out: a) pre-sintering step by HP followed by two PIP cycles with polycarbosilane, and vice versa, b) two PIP cycles followed by a cycle of HP.

The soundness of the fabricated UHTCMCs by different routes can be determined by microstructural characterisation and evaluation of mechanical and thermal properties, including elevated temperature and oxidation resistance tests, and thus allowing a general assessment of their performance. As observed, the microstructural features of the obtained materials are highly reliant on the processing method used and hence it is essential to select the correct process in order to achieve the required microstructure, which will, in turn, yield the targeted properties of the composites. UHTCMCs are designed for ultra-high temperatures applications (> 2000 °C) in harsh conditions, such as the corrosive and/or oxidizing atmospheres during Earth's re-entry of vehicles at speed above MACH 5. Hence, understanding the mechanical properties of the obtained materials at elevated temperatures is essential to foresee their performance in the service environment and CNR-ISTEC is equipped with extremely rare facilities to mechanical test materials up to 1500 °C in air and under low oxygen atmosphere and evaluate short term oxidation up to 1650 °C.

In the second half of the thesis, the work was addressed to the development of simple ways to prepare polymer-derived ceramics (PDCs) with high thermal stability, higher than that of SiC (Chapter 8). Firstly, the effect of pre-curing heat treatments and catalysts on the ceramic yield of commercial allyl-hydrido polycarbosilane was studied to understand its curing and pyrolysis behaviour. Then, a tentative of synthetise SiBCN(O) ceramic was carried out by coupling polycarbosilane, used as Si and C precursor, with ammonia borane, source of boron and nitrogen at the same time. Finally, a simple route was proposed for the synthesis of polymer precursors for zirconium carbide (ZrC), using zirconium tetrachloride ($ZrCl_4$) as zirconium source and three different carbon sources: two phenolic resins and a type of bitumen.

The main results can be summarized as below.

Preparation of polymer-derived UHTCMCs

A novel non-sintering, near-net shape processing route for the fabrication of UHTCMCs was developed. The two-step impregnation is the distinctive feature of the proposed manufacturing process, that consists of: 1) impregnation of carbon fibre cloths with a water-based slurry containing UHTC particles, followed by 2) repetitive cycles of vacuum-infiltration with commercial allyl-hydrido polycarbosilane SMP-10 and

subsequent pyrolysis. The water-based slurry infiltration step perfected at CNR-ISTEC was aimed at the introduction of UHTC particles into carbon preforms overcoming the lack of UHTC preceramic precursors on the market, the inhomogeneity typically obtained with slurries containing preceramic polymers and the ceramic powders, and in a sustainable way since no organic solvents were used. The improved yield of conversion of SMP-10 up to 80% with the addition of catalysts and pyrolysis at 1000 °C allowed to reduce the number of PIP cycles from ten or more, as reported in literatures, to just six.

The as-prepared pitch-based carbon fibres reinforced ZrB_2-enriched composites had compositions of about 30 vol% C_f, 20–30 vol% ZrB_2, 35–42 vol% SiC, a moderate density (2.7–3.2 g/cm^3) and low residual open porosity (6–10%), depending on carbon fibre architecture of the preform (0/0°, 0/90° and 2D), while PAN-based carbon fibre-reinforced ZrB_2-enriched composites had compositions of about 24–28 vol% C_f, 20–48 vol% ZrB_2, 17–46 vol% SiC and residual open porosity 5–28% depending on fibre preform.

The water-based slurry infiltration step was found effective for a good distribution of ZrB_2 and SiC phases around carbon fibres, even using complex architectures of fibres, and low defectiveness were achieved. Good homogeneity of ZrB_2 and SiC phases improved self-protection capability of the resulting materials, that showed a fast passivation of air exposed surface up to 1500 °C and low oxidation rate up to 1650 °C, with the formation of a protective borosilicate glass scale with thickness of a few tens of microns (i.e. 30–50 µm). 20–30 vol% of ZrB_2 in the material was found a good compromise between lightness and oxidation resistance, avoiding the extra cost and time to deposit an environmental thermal barrier coating on the exposed surface, e.g. ZrO_2 coating on SiC/SiC turbine blades.

UHTCMCs obtained by slurry infiltration coupled with PIP at mild conditions exhibited excellent mechanical properties, comparable or even better than those of similar CMCs produced by PIP or other more complex processes, resulting from the presence of a tailored fibre/matrix interface achieved thanks to this processing route. For instance, the flexural strength at room temperature of pitch-based C_f/ZrB_2-SiC was approaching 500 MPa for 0/0°, 370 MPa for 0/90° and 190 MPa for 2D, while fracture toughness was about 18 MPa·m$^{0.5}$ for 0/0°, 14 MPa·m$^{0.5}$ for 0/90° and 9 MPa·m$^{0.5}$ for 2D. The use of pitch-based carbon fibres, thanks to their onion-like structure, led to obtain a better mechanical transfer at fibre/matrix interphase (rather than PAN-based fibres) allowing not to resort

to the time-consuming process of CVI coating on carbon fibre. Indeed, the flexural strength at room temperature of PAN-based C_f/ZrB_2-SiC was about 325 MPa for 0/0°, 125 MPa for 2D twill, 200 MPa for 2D plain, and 120 MPa for 2.5D, while fracture toughness gave values ranging from 7 to 10 $MPa \cdot m^{0.5}$. Nevertheless, further improvements on performance can be achieved using coated PAN-based carbon fibres. Moreover, these composites kept good flexural strength up to 1400 °C (0/0° pitch-based C_f/ZrB_2-SiC reached ~550 MPa, HT strength +17%), enabling the use of low-temperature processed material at such elevated temperature for short time. However, at 1500 °C a loss of performance was observed because of the presence of oxide impurities. Post-consolidation heat treatments at temperature higher than 1400 °C caused conversion of amorphous SiC(O) into crystalline β-SiC. The higher degree of crystallinity of the polymer-derived SiC-based matrix and higher porosity (from 6 to 30–31%) led to lower flexural strength at room temperature, but also an improvement in strength at elevated temperature compared to material consolidated under mild conditions. The treatments at 1400 °C and 1700 °C were found to be the best trade-off to balance the performance in a wide range of temperature (i.e. RT strength ~300 MPa and 1500 °C strength ~210 MPa, RT strength ~200 MPa and 1500 °C strength ~1700 MPa, after treatments at 1400 °C and 1700 °C respectively).

The study aimed at further decreasing the processing time by introducing a sintering step led to alternative routes for the fabrication of UHTCMs coupling water-based powder slurry infiltration, Polymer Infiltration and Pyrolysis (PIP) and Hot Pressing (HP) techniques. By a process coupling two PIP cycles at mild conditions of 1000 °C and a cycle of HP at 1900 °C, C_f/ZrB_2-SiC composites with C_f content ~34%, ZrB_2 content ~3% and SiC content ~22% were manufactured. These composites reached flexural strengths of 167 MPa and 592 MPa at room temperature and at 1500 °C respectively, that were significantly higher than those of the composites obtained by the other route (i.e. pre-sintering step by HP followed by two PIP cycles). Moreover, they showed an improved thermal stability exhibiting a flexural strength at 1500 °C 160% higher than that of PIP-ed composites. Therefore, this proposed hybrid process was found to be effective to reduce number of treatment and enhance mechanical properties at elevated temperature compared to conventional time-consuming PIP process.

Polymer-derived Si-C-X and ZrC ceramics

Pre-treatment before polymer curing and addition of catalysts on allyl-hydrido polycarbosilane SMP-10 demonstrated an increase (~11% and ~20%, respectively) in SiC mass yield compared to as-received SMP-10. The ceramic yields due to the addition of trimethyl(methylcyclopentadienyl)platinum(IV) and dicumyl peroxide were similar (82% vs. 83%), thus preferring the latter because of lower toxicity and price.

A liquid single-source SiBCN(O) ceramic precursor was synthesised by a simple reaction between allyl-hydrido polycarbosilane and ammonia borane. The addition of boron and nitrogen demonstrated an increase in ceramic mass yield up to 88% without addition of catalyst. In the pyrolysis product, the boron and nitrogen were not preferentially incorporated into the silicon carbide lattice but entered the SiC(O) forming segregated BNO-reach areas.

Preceramic precursors for ZrC were prepared by simply mixing zirconium tetrachloride and phenolic resins or bitumen as zirconium and carbon sources, respectively. The results indicated that obtained organometallic compounds could be a Zr-O-C polymer. Pure ZrC was formed through carbothermal reduction after pyrolysis at 1600 °C. This simple reaction way paths the way to synthesize ZrC using as carbon source liquid phenolic resin, thus avoiding solvent, and bitumen, which is very cheap and a national waste material.

In the light of the results herein presented, new paths of research will be addressed to: manufacturing of UHTCMCs with tailored matrix composition, process optimization ranging from different type of reinforcement to processing parameters, synthesis of single-source polymer precursors and improvement of their viscosity for a future integration in PIP process.

In conclusion, in this Ph.D. Thesis potentialities and versatility of Polymer Infiltration and Pyrolysis (PIP) process for the manufacturing of UHTCMCs were explored and the fabrication of high-performance composites featuring high oxidation resistance and damage tolerance was accomplished. It is foreseen that the increase of knowledge on polymer-derived UHT ceramics and methods to fabricate polymer-derived UHTCMCs will push the research towards ever more challenging applications.

Acknowledgements

This dissertation represents the culmination of a project lasting three years (and three months). Thus, there are many people whom I would like to thank for their contributions, both directly and indirectly.

As for the people who specifically helped with this doctoral thesis, the first round of special thanks goes to my supervisor Dr. Diletta Sciti for giving me the opportunity to carry out the PhD project in the Structural Ceramics Group at CNR-ISTEC. Her scientific guidance and advice, energetic support, tireless efforts in reading and correcting my thesis have helped me to accomplish this goal. Secondly, I would like to thank my co-supervisor Dr. Luca Zoli for guiding me with his enthusiastic approach to science and his extraordinary help in the research activity. Inexhaustible source of ideas, fighting spirit towards my pedantry, he taught me that science is not always in black and white, but it's a million shades of colours. Also, thanks go to the other members of the Structural Ceramics Group: Dr. Antonio Vinci and Dr. Pietro Galizia for their help, tips and tricks about UHTCMC manufacturing and mechanical testing respectively; Dr. Simone Failla for his technical support in the Sintering Technologies Laboratory; Dr. Laura Silvestroni for her small but precious suggestions for INCA&Co.; almost Dr. Matteo Mor for his help in the last two years in exchange for perfect knots (beyond having endured patiently my recurring exclamation "ma chi me l'ha fatto fare, mollo tutto e vado ad allevare alpaca!" in the worst days).

I would also like to thank researchers and technicians for providing me necessary technical assistance with theoretical discussions, measurements or other aspects, in no particular order: Dr. Annalisa Natali Murri for thermal analyses; Dr. Alex Sangiorgi for the numerous thermal treatments perfectly scheduled and executed, and also for always keeping me updated on the state of health of the furnace Astro; Claudio Capiani for XRD analysis, production of silicone vessels, and for trying to kindly satisfy my requests on crucibles, bars, grinding media and whatever else; Andreana Piancastelli for mercury intrusion porosimetry analysis, both with beautiful and "leftover" samples; Mauro Mazzocchi for his teachings of scanning electron microscopy remembering me how bad my fibre-reinforced materials were; Cesare Melandri for mechanical characterization,

and investigation using digital microscope collecting representative as well as artistic images; Guia Guarini for measurements with helium pycnometer, her periodic checks on my safety when I was lonely in lab and 360° suggestions; Paola Pinasco with her tentacular presence in ISTEC and her useful suggestions in the most disparate areas. Lastly, the old wise man (but not “arzillo”) and nowadays retired Daniele Dalle Fabbriche is thanked for welcoming me in his bright office full of plants; it was a pleasure to learn the story of ISTEC and some of its ex-workers, the expansion year after year of the Sintering Technologies Laboratory, and recommendations for a tidy and peaceful space sharing.

I thank profusely all the staff of ISTEC for their kindly support and co-operation throughout my PhD period, offering me a pleasant environment to complete this research work. All that greatly helped me to grow as a researcher.

A debit of gratitude is also owed to Prof. Enrico Dalcanale, coordinator of this PhD, for his quick and concise answers to questions concerning courses, ECTS, availability of the funds, and stratagems to survive to the uprising of personal computers.

I would like to thank Francesca Carella, Lara Faccani, Nicola Gilli and Margherita Montanari, buddies in this PhD adventure, for sharing joy and difficulties, information, cars and drive to Parma/Faenza. Thanks are extended to all the colleagues at ISTEC (and also friends) Chiara, Franco, Ilaria (since Bachelor’s degree), Linda and all the others that with their suggestions, kindly support, as well as pasticcini and aperitives after work have cheered these three years.

My gratitude goes to my family, thus to: my mum, that always supports me and dispenses her practical advice for the everyday life; my dad, that does not understand what I am doing for years but he does not comment; to my uncles Emilio and Domenico, “gli aggiustatutto” par excellence that in this particular case helped me to manufacture useful contraptions for my laboratory activity. A heartfelt thanks goes to my friends, first of all to Alessandro, that confirmed that his spirit animal is a lazy calm panda bear: thank you for unfailing support and your patience during this totally absorbing period. Last but not least, I will remember this strange period also for the smart-working days at home, thus I thank also my fluffy housemate Alvin, the best companion ever, always alongside the laptop or on my books.